Modeling and uncertainty quantification in the nonlinear stochastic dynamics of horizontal drillstrings

Americo Barbosa da Cunha Junior

Université Paris-Est

École Doctorale
Sciences, Ingénierie et Environnement

Thèse

présenté et soutenue publiquement par

Americo BARBOSA DA CUNHA JUNIOR

le 11 mars 2015

pour obtenir le grade de

Docteur de l'Université Paris-Est
(Spécialité: Mécanique)

Modeling and Uncertainty Quantification in the Nonlinear Stochastic Dynamics of Horizontal Drillstrings

Jury

M.	Domingos Rade	Professeur Universidade Federal de Uberlândia	(Président)
M.	Jean-François Deü	Professeur Conservatoire National des Arts et Métiers	(Rapporteur)
M.	Fernando Rochinha	Professeur Universidade Federal do Rio de Janeiro	(Rapporteur)
M.	Thiago Ritto	Professeur Assistant Universidade Federal do Rio de Janeiro	(Examinateur)
M.	Hans Weber	Professeur PUC-Rio	(Examinateur)
M.	Rubens Sampaio	Professeur PUC-Rio	(Co-Directeur de Thèse)
M.	Christian Soize	Professeur Université Paris-Est	(Directeur de Thèse)

Université Paris-Est

École Doctorale
Sciences, Ingénierie et Environnement

Thèse

présenté et soutenue publiquement par

Americo BARBOSA DA CUNHA JUNIOR

le 11 mars 2015

pour obtenir le grade de

Docteur de l'Université Paris-Est
(Spécialité: Mécanique)

Modeling and Uncertainty Quantification in the Nonlinear Stochastic Dynamics of Horizontal Drillstrings

Jury

M.	Domingos Rade	Professeur Universidade Federal de Uberlândia	(Président)
M.	Jean-François Deü	Professeur Conservatoire National des Arts et Métiers	(Rapporteur)
M.	Fernando Rochinha	Professeur Universidade Federal do Rio de Janeiro	(Rapporteur)
M.	Thiago Ritto	Professeur Assistant Universidade Federal do Rio de Janeiro	(Examinateur)
M.	Hans Weber	Professeur PUC-Rio	(Examinateur)
M.	Rubens Sampaio	Professeur PUC-Rio	(Co-Directeur de Thèse)
M.	Christian Soize	Professeur Université Paris-Est	(Directeur de Thèse)

This page is left blank intentionally

The author graduated from PUC–Rio in Mechanical Engineering and Applied Mathematics. He also did a master in Thermal Sciences at the same university. His doctorate in Applied Mechanics was conducted in a cotutela agreement between PUC–Rio and Université Paris-Est, so that he spent a year and a half working in Paris at the *Laboratoire Modélisation et Simulation Multi–Echelle*. By the end of his doctorate the author has published 7 research articles in journals, 10 full papers in conferences, and has participated of 30 scientific events.

Acknowledgments

I start my list of acknowledgments expressing my greatest gratitude to the most important people in my life, my father Americo, my mother Heleny Gloria, and my sister Amanda Gloria. By always have been my supporters, and the people in the world who love me more. I owe to then everything!

Throughout this thesis I had two advisors. To them, now, I make my acknowledgments. The reasons are distinct, almost so distinct as the profile of each of them. Rubens Sampaio always encouraged me to go deeper and deeper in the world of mathematics/mechanics since my first class with him in the undergraduate course. I appreciate his invitation to do a doctorate in the area of stochastic mechanics, and I am gratefull for all the knowledge on mechanics/mathematics that here shared with me over the years. Christian Soize welcomed me into his laboratory and I guide myself, always in a insightful way, during the crucial stages of this thesis. With him I could learn a lot about some non-trivial aspects of scientific research, mechanics, and to give more value to my physical intuition rather than my knowledge of theorems. For all of these reasons I am grateful to both of then.

I am also grateful for the contribution on my training and/or assistance, during my academic life, to professors Carlos Tomei; Christophe Desceliers; Eduardo Cursi; Edson Cataldo; Hans Weber; Ilmar Santos; José Manoel Baltazar; Luís Fernando Figueira da Silva; Marco Antonio Grivet; Peter Hagedorn; Ricardo Sá Earp; and Sergio Belizzi. For the above reasons, and also, for the help at several moments during the development of this thesis, I would like to register a special thanks to the professors Anas Batou; Marcelo Piovan; and Thiago Ritto.

I thank the members of the jury, for having accepted to participate in the evaluation of this thesis, and for the valuable comments made on the day of the thesis defense. These comments were very relevant, and helped to improve the final version of the manuscript.

During the doctorate I had the opportunity to collaborate with researchers outside of my department, which made me evolve a lot as a professional. It was a great pleasure to work with Rafael Nasser, Hélio Lopes, and Karin Breitman in the McCloud project.

I would like to take this space to express my deepest respect and admiration for professors Fred Palmeira, José Alberto dos Reis Parise and Ricardo Sá Earp. Masters who have taught me lessons much more important than engineering and mathematics. People of noble character, which I feel very honored in be able to call friends.

Over the last years, I spent good times in company of my friends from Mechanical Engineering Department of PUC–Rio and "associated people". To these friends I express my happiness for the nice moments lived together. Thank you very much to : Abel ; Adriano ; Amparito ; André Rezende ; André Zaccur ; Bruno Cayres ; Bruno Kassar ; Carlucio ; Cesar Augusto ; Diego Garcia ; Elder ; Fernando ; Gianni ; Guilherme de Paula ; Jorge Ballaben ; Julien ; Leo Pará ; Luis Enrique ; Marcelo Pereira ; Marcelo Piovan ; Mario Escalante ; Mario Sandoval ; Maurício Gruzman ; Nattan ; Quentin ; Said ; and Wagner.

My friends and colleagues from the Department of Mathematics of PUC–Rio are also dignitary of a special acknowledgment. For the enjoyable conversations in the kitchen on the 8th floor, barbecues, birthday parties, weddings, philosophical discussions, etc. In order to does not commit the injustice of forgets someone's name, they will be remembered in group. For the same reason I apologize to the other people who were worth to be mentioned here, and were not, for my lapse of memory or lack of space.

Au Laboratoire Modélisation et Simulation Multi-Echelle, à la Résidence Internationale et à Paris, j'ai eu l'opportunité de faire des nouveaux amis (brésiliennes et étrangères). Avec eux, j'ai expérimenté des bons moments en Europe, et j'ai reçu soutien pendant les moments difficiles. Par conséquent, je me souviendrai toujours affectueusement des l'amis : Aboud ; Alejandro ; Anas ; Andréa ; Anna Maria ; An Ni ; Annia ; Ayad ; Dang Tran ; Debora ; Eliane ; Elias ; Evangéline ; Feishu ; Hadrien ; Hani ; Hussein ; Lorenzo ; Manh Tu ; Maria Emilia ; Marwa ; Mei Luo ; Naiima ; Nicolas Auffray ; Nicolas Lestoille ; Olivier ; Osamo ; Paulin ; Rania ; Roberto ; Roula ; Vartou ; Viktoria et Yaarob. Quelques amis étaient plus que des amis. Formé ma famille en France. Je serai éternellement reconnaissant aux moments de bonheur que je passai proche des chers amis : Camila ; Carmelo ; Chahinez ; Heba ; Mahran ; Mariella ; Maurício Cardoso et Nazareno. Aussi au sein de la famille, spécialement, à Davi Antônio, mon grand ami et partenaire d'aventures en Europe. Merci à toutes et à tous !

Finally, for their financial support during the years of the doctorate, I would like to thank the CNPq for the scholarship in Brazil, and the CAPES for the scholarship during my stay in France.

Abstract

Oil prospecting uses an equipment called drillstring to drill the soil until the reservoir level. This equipment is a long column under rotation, composed by a sequence of connected drill-pipes and auxiliary equipment. The dynamics of this column is very complex because, under normal operational conditions, it is subjected to longitudinal, lateral, and torsional vibrations, which presents a nonlinear coupling. Also, this structure is subjected to friction and shocks effects due to the mechanical contacts between the pairs drill-bit/soil and drill-pipes/borehole. This work presents a mechanical-mathematical model to analyze a drillstring in horizontal configuration. This model uses a beam theory which accounts rotatory inertia, shear deformation, and the nonlinear coupling between three mechanisms of vibration. The model equations are discretized using the finite element method. The uncertainties in bit-rock interaction model parameters are taken into account through a parametric probabilistic approach, and the random parameters probability distributions are constructed by means of maximum entropy principle. Numerical simulations are conducted in order to characterize the nonlinear dynamic behavior of the structure, specially, the drill-bit. Dynamical phenomena inherently nonlinear, such as slick-slip and bit-bounce, are observed in the simulations, as well as shocks. A spectral analysis shows, surprisingly, that slick-slip and bit-bounce phenomena result from the lateral vibration mechanism, and that shock phenomena comes from the torsional vibration. Seeking to increase the efficiency of the drilling process, an optimization problem that aims to maximize the rate of penetration of the column into the soil, respecting its structural limits, is proposed and solved.

Keywords

Drillstring dynamics; Nonlinear dynamics; Stochastic modeling; Uncertainty quantification; Drilling optimization;

Resumo

Prospecção de petróleo usa um equipamento chamado coluna de perfuração para escavar o solo até o nível do reservatório. Este equipamento é uma longa coluna, sob rotação, composto por uma sequência de tubos de perfuração e equipamentos auxiliares conectados. A dinâmica desta coluna é muito complexa, porque sob condições normais de operação, ela está sujeita à vibrações longitudinais, laterais e torcionais, que apresentam um acoplamento não-linear. Além disso, a estrutura está submetida a efeitos de atrito e choque devido a contatos mecânicos entre os pares broca/rocha e tubos de perfuração/parede do poço. Este trabalho apresenta um modelo mecânico-matemático para analisar uma coluna de perfuração em configuração horizontal. Este modelo usa uma teoria de viga com inércia de rotação, deformação cisalhante e acoplamento não-linear entre os três mecanismos de vibração. As equações do modelo são discretizadas utilizando o método dos elementos finitos. As incertezas dos parâmetros do modelo de interação broca-rocha são levandas em conta através de uma abordagem probabilística paramétrica, e as distribuições de probabilidades dos parâmetros aleatórios são construídas por meio do princípio da entropia máxima. Simulações numéricas são conduzidas de forma a caracterizar o comportamento dinâmico não-linear da estrutura, especialmente, da broca. Fenômenos dinâmicos inerentemente não-lineares, como *stick-slip* e *bit-bounce*, são observados nas simulações, bem como choques. Uma análise espectral mostra que, surpreendentemente, os fenômenos de *stick-slip* e *bit-bounce* são resultado do mecanismo de vibração lateral, e que os fenômenos de choque decorrem da vibração torcional. Visando aumentar a eficiência do processo de perfuração, um problema de otimização que tem como objetivo maximizar a taxa de penetração da coluna no solo, respeitando os seus limites estruturais, é proposto e resolvido.

Palavras–chave

Dinâmica da coluna de perfuração; Dinâmica não linear; Modelagem estocástica; Quantificação de incertezas; Otimização de perfuração;

Résumé

La prospection de pétrole utilise un équipement appelé tube de forage pour forer le sol jusqu'au niveau du réservoir. Cet équipement est une longue colonne rotative, composée d'une série de tiges de forage interconnectées et d'équipements auxiliaires. La dynamique de cette colonne est très complexe car dans des conditions opérationnelles normales, elle est soumise à des vibrations longitudinales, latérales et de torsion, qui présentent un couplage non linéaire. En outre, cette structure est soumise à des effets de frottement et à des chocs dûs aux contacts mécaniques entre les paires tête de forage/sol et tube de forage/sol. Ce travail présente un modèle mécanique-mathématique pour analyser un tube de forage en configuration horizontale. Ce modèle utilise la théorie des poutres qui utilise l'inertie de rotation, la déformation de cisaillement et le couplage non linéaire entre les trois mécanismes de vibration. Les équations du modèle sont discrétisées par la méthode des éléments finis. Les incertitudes des paramètres du modèle d'interaction tête de forage/sol sont prises en compte par l'approche probabiliste paramétrique, et les distributions de probabilité des paramètres aléatoires sont construites par le principe du maximum d'entropie. Des simulations numériques sont réalisées afin de caractériser le comportement dynamique non linéaire de la structure, et en particulier, de l'outil de forage. Des phénomènes dynamiques non linéaires par nature, comme le *slick-slip* et le *bit-bounce*, sont observés dans les simulations, ainsi que les chocs. Une analyse spectrale montre étonnamment que les phénomènes *slick-slip* et *bit-bounce* résultent du mécanisme de vibration latérale, et ce phénomène de choc vient de la vibration de torsion. Cherchant à améliorer l'efficacité de l'opération de forage, un problème d'optimisation, qui cherche à maximiser la vitesse de pénétration de la colonne dans le sol, sur ses limites structurelles, est proposé et résolu.

Mot–clé

Dynamique des tubes de forage; Dynamique non linéaire; Modélisation stochastique; Quantification des incertitudes; Optimisation de forage;

Table of Contents

List of Figures

List of Tables

Nomenclature

Upper-case Roman

$\mathcal{A}$	action
$[\bar{K}]$	generalized stiffness matrix
$\mathcal{C}$	damping operator
$\mathcal{D}$	energy dissipation function
$\mathcal{B}_0$	beam geometry undeformed configuration
$\mathcal{S}_0$	beam cross section undeformed configuration
$\mathcal{E}$	efficiency of the drilling process
$\mathcal{W}$	work done by the external forces
$\mathcal{W}_{\text{BR}}$	work done by the bit-rock interaction force and torque
$\mathcal{W}_{\text{FS}}$	work done by the shock force and friction torque
$\mathcal{F}$	force operator
$\mathcal{F}_{\text{BR}}$	nonlinear force due to bit-rock interaction
$\mathcal{F}_{\text{FS}}$	nonlinear force due to friction and shock
$\mathcal{F}_{\text{G}}$	linear force due to gravity
$\mathcal{F}_{\text{KE}}$	nonlinear force due to inertial effects
$\mathcal{F}_{\text{SE}}$	nonlinear force due to geometric nonlinearity
$[\hat{K}]$	effective stiffness matrix
$\mathcal{H}_m^{(1)}(x)$	shape function
$\mathcal{H}_m^{(2)}(x)$	shape function
$\mathcal{N}_m(x)$	shape function
$\mathcal{T}$	kinetic energy
$\mathcal{M}$	mass operator
$\mathscr{F}$	energy functional
$\mathscr{L}$	Lagrangian
$[\mathscr{B}]$	constraint matrix
$[\mathcal{C}]$	damping matrix
$[\mathcal{M}]$	mass matrix
$[\mathcal{K}]$	stiffness matrix
$[B]$	reduced constraint matrix
$[C]$	reduced damping matrix
$[K]$	reduced stiffness matrix

$[M]$	reduced mass matrix
$\mathbb{N}$	natural numbers set
$\mathbb{P}$	probability measure
$\mathcal{P}_{in}$	input power
$\mathcal{P}_{out}$	output power
$\mathbb{R}$	real numbers set
$\ddot{\mathbb{Q}}(t,\cdot)$	random acceleration vector at time t
$\dot{\mathbb{Q}}(t,\cdot)$	random velocity vector at time t
$\mathbb{F}$	random force vector at time t
$\mathbb{Q}(t,\cdot)$	random displacement vector at time t
$\mathbb{ROP}$	random rate of penetration
$\mathbb{U}$	random field variables vector
$\mathbb{X}$	real-valued random variable
$\mathcal{R}$	inertial frame of reference
$\mathcal{R}_n$	non-inertial frame of reference ($n = 1, 2, 3$)
$\mathcal{V}$	strain energy
$\mathrm{S}\left(p_{\mathbb{X}}\right)$	Shannon entropy of the PDF $p_{\mathbb{X}}$
$\mathcal{K}$	stiffness operator
$\mathbb{I}$	identity tensor
`UTS`	ultimate tensile strength of the material
$\ddot{\boldsymbol{Q}}(t)$	nodal acceleration vector
$\dot{\boldsymbol{Q}}(t)$	nodal velocity vector
$\dot{\boldsymbol{Q}}_0$	initial velocity vector
$\boldsymbol{\mathcal{F}}$	force vector
$\boldsymbol{Q}(t)$	nodal displacement vector
$\boldsymbol{Q}_0$	initial displacement vector
$\boldsymbol{U}$	field variables vector
A	beam cross-sectional area
E	beam material elastic modulus
F_{BR}	bit-rock force
F^a_{FS}	shock axial force
F^n_{FS}	shock normal force
G	shear modulus

I_{xx} polar moment of area

I_{yyzz} fourth product of area

I_{yy} second moment of area around the y axis

I_{zzzz} fourth moment of area around the z axis

I_{zz} second moment of area around the z axis

L beam length

N_{dofs} number of degrees of freedom

N_{elem} number of finite elements

N_{nodes} number of nodes in finite element mesh

N_{red} dimension of the reduced model

$P_{\mathbb{X}}(dx)$ probability distribution of $\mathbb{X}$

P_{risk} risk percentage acceptable to the problem

$Q_m(t)$ degree of freedom of the FEM model

R_{bh} borehole radius

R_{int} beam cross section internal radius

R_{out} beam cross section external radius

T_{BR} bit-rock torque

T_{FS} torsional frictional torque

Lower-case Roman

(x, y, z) inertial cartesian coordinate system

(x_n, y_n, z_n) non-inertial cartesian coordinate systems $(n = 1, 2, 3)$

$\bar{\boldsymbol{f}}_{n+1}$ generalized force vector

$\dot{u}_{bit}$ drill-bit axial velocity

$\hat{\boldsymbol{f}}_{n+1}$ effective force vector

$m_{\mathbb{X}}$ mean value of the random variable $\mathbb{X}$

$p_{\mathbb{X}}$ probability density function of $\mathbb{X}$

$\ddot{\mathbb{q}}(t, \cdot)$ reduced random acceleration vector at time t

$\dot{\mathbb{q}}(t, \cdot)$ reduced random velocity vector at time t

$\mathbb{f}$ reduced random force vector at time t

$\mathbb{q}(t, \cdot)$ reduced random displacement vector at time t

$\mathtt{conv}_{\mathrm{FEM}}(n)$ convergence metric of FEM approximations

$\mathtt{conv}_{\mathrm{MC}}(n_s)$ convergence metric of MC simulations

$\mathtt{energy}_{\mathrm{MECH}}(n)$ mean mechanical energy

`gap`	space between undeformed beam and borehole wall
`rop`	rate of penetration
$\ddot{\boldsymbol{q}}(t)$	reduced nodal acceleration vector
$\ddot{\boldsymbol{q}}_n$	approximation to $\ddot{\boldsymbol{q}}(t_n)$
$\dot{\boldsymbol{q}}(t)$	reduced nodal velocity vector
$\dot{\boldsymbol{q}}_0$	reduced initial velocity vector
$\dot{\boldsymbol{q}}_n$	approximation to $\dot{\boldsymbol{q}}(t_n)$
$\mathbf{v}$	beam neutral fiber point velocity vector
$\boldsymbol{f}$	reduced force vector
$\boldsymbol{h}(t)$	constraint vector
$\boldsymbol{h}_{n+1}$	approximation to $\boldsymbol{h}(t_{n+1})$
$\boldsymbol{q}(t)$	reduced nodal displacement vector
$\boldsymbol{q}_0$	reduced initial displacement vector
$\boldsymbol{q}_n$	approximation to $\boldsymbol{q}(t_n)$
$\boldsymbol{r}$	beam point position vector
$\{\boldsymbol{e}_{x_n}, \boldsymbol{e}_{y_n}, \boldsymbol{e}_{z_n}\}$	non-inertial orthonormal basis of vectors ($n = 1, 2, 3$)
$\{\boldsymbol{e}_x, \boldsymbol{e}_y, \boldsymbol{e}_z\}$	inertial orthonormal basis of vectors
c	damping constant
c_{FS}	shock damping constant of the nonlinear dashpot
c_L	longitudinal wave velocity
f	dimensional frequency (Hz)
f_{max}	maximum dimensional frequency (Hz)
g	gravity acceleration
$i = \sqrt{-1}$	imaginary unit
k_{FS_1}	shock stiffness constant of the linear spring
k_{FS_2}	shock stiffness constant of the nonlinear spring
n_s	number of MC realizations
r	lateral displacement of the neutral fiber
t	time
t_0	initial instant of time
t_f	final instant of time
t_n	n-th instant of time
u	displacement of beam neutral fiber in x direction

u_x displacement of beam section point in x direction

u_y displacement of beam section point in y direction

u_z displacement of beam section point in z direction

v displacement of beam neutral fiber in y direction

w displacement of beam neutral fiber in z direction

Upper-case Greek

Δt time step

Γ_{BR} bit-rock limit force

$[\Phi]$ projection matrix

$\mathbb{\Gamma}_{\text{BR}}$ random bit-rock limit force

$\mathbb{\Sigma}$ σ-algebra over Θ

Θ sample space

Lower-case Greek

α_{BR} rate of change of bit-rock force

β Newmark method parameter

δ_{FS} indentation

$\delta_{\mathbb{X}}$ dispersion factor of the random variable $\mathbb{X}$

δ_{nm} Kronecker delta symbol

$\dot{\theta}_x$ rate of rotation around the x axis

$\dot{\theta}_y$ rate of rotation around the y axis

$\dot{\theta}_z$ rate of rotation around the z axis

ϵ_{xx} deformation perpendicular to the x axis in the x direction

ϵ_{xy} deformation perpendicular to the x axis in the y direction

ϵ_{xz} deformation perpendicular to the x axis in the z direction

γ Newmark method parameter

κ scaling factor

κ_s shearing factor

λ first Lamé parameter

μ_{BR} bit-rock friction coefficient

μ_{FS} shock friction coefficient

ν beam material Poisson's ratio

ω^{SOR} SOR parameter

ω_{bit} drill-bit angular velocity

ω_n	n-th natural frequency
ϖ_{VM}	random von Mises equivalent stress
$\mathbb{\alpha}_{\mathrm{BR}}$	random rate of change of bit-rock force
$\mathbb{\mu}_{\mathrm{BR}}$	random bit-rock friction coefficient
ρ	beam material mass density
σ_{VM}	von Mises equivalent stress
$\sigma_{\mathbb{X}}$	standard deviation of the random variable $\mathbb{X}$
$\boldsymbol{\epsilon}$	Green-Lagrangian strain tensor
$\boldsymbol{\sigma}$	second Piola-Kirchhoff stress tensor
θ_x	rotation around the x axis
θ_y	rotation around the y axis
θ_z	rotation around the z axis
ε_1	prescribed tolerance
ε_2	prescribed tolerance
$\sigma^2_{\mathbb{X}}$	variance of the random variable $\mathbb{X}$
$\dot{\boldsymbol{\theta}}$	beam neutral fiber point rate of rotation vector
$\boldsymbol{\lambda}_{n+1}$	Lagrange multipliers vector
$\boldsymbol{\omega}$	angular velocity vector
$\boldsymbol{\phi}_n$	n-th unitary normal mode
$\boldsymbol{\psi}$	weight functions vector
ξ_{BR}	regularization function

Superscripts

$'$	space derivative
*	dimensionless quantity
$\dot{}$	time derivative
^{T}	transposition operation
$^{(n)}$	approximation constructed with n finite elements
$^+$	positive part of the function

Other Symbols

$:$	double inner product
$\cdot$	Euclidean inner product
$\mathbb{E}[\cdot]$	expected value operator
$\Gamma(\cdot)$	gamma function

$\mathbb{1}_X$	indicator function of the set X
$\mathcal{O}$	big O notation
$\|\cdot\|$	Euclidean norm
$\mathtt{sgn}\,(\cdot)$	sign function
$\mathtt{Supp}$	support of a random variable
$\otimes$	tensor product
$\mathtt{tr}\,(\cdot)$	trace operator
$\delta(\cdot)$	variation operator
$a.s.$	almost sure

Abbreviations

BHA	bottom hole assembly
FEM	finite element method
GEP	generalized eigenvalue problem
IVP	initial value problem
PDF	probability density function
PSD	power spectral density
ROP	rate of penetration
SOR	successive over-relaxation
WOB	weight on bit

There is always a well-known solution to every human problem — neat, plausible, and wrong.

Henry Louis Mencken, *The Divine Afflatus.*

1
General Introduction

Drilling of an oil well is a complex and expensive operation that uses an equipment, called drillstring, which presents a very complex dynamic behavior. The modeling of this equipment offers great challenges in terms of engineering, because it involves the handling and solution of a very complex problem of nonlinear stochastic dynamics. The subject of this thesis is the modeling and analysis of the stochastic nonlinear dynamics of a drillstring in horizontal configuration, taking into account the nonlinear coupling between the different mechanisms of vibration, the effects of friction and shock to which the equipment is subject, as well as the quantification of the physical system uncertainties.

In this chapter it is presented the motivation for this thesis, followed by the issues of scientific and technological interest associated to the subject, and finally the scope of the work.

1.1
Research motivation

1.1.1
Historical and economical aspects of oil exploration

Modern oil exploration began in the 19th century with the drilling of the earliest commercial oil wells. The petroleum extracted from those wells was mainly used for the production of paraffin and kerosene (Chisholm, 1911) [1].

Since beginning of 20th century, oil demand has been increasing due to a combination of several factors. Among these factors, one can highlight the growing need for fuel of automobiles and industrial equipment, driven by the advent of the internal combustion engine; the high energy power of a oil barrel; the relative low cost of oil production when compared with coal mining; and, perhaps the most important, a wide range of oil derivatives, which are used not only as fuel. In addition to kerosene, other fuels can obtained from petroleum, such as butane, diesel fuel, fuel oil, gasoline, jet fuel, liquefied petroleum gas, etc. Other oil by-products include alkenes, aromatic petrochemicals, asphalt, lubricants, petroleum coke, sulfuric acid, wax, etc.

Nowadays, oil and oil by-fuels are the main source of energy in Brazil and the world, as can be seen in Table 1.1, which shows the distribution of energy supply for Brazil in 2013, and for the world in 2011 (MME, 2014) [2]. Note that in the year of 2011 more than 30% of the global energy matrix was oil dependent. In the year of 2013 Brazil presented an even greater dependence, where the importance of oil in the energy matrix has reached nearly 40%.

Also, oil exploration is one of the most important economical activities developed in the planet. The oil companies handle trillions of U.S. dollars each year and generate millions of jobs worldwide, besides fomenting the development of smaller industries of service providers for oil exploration [3]. In the particular case of Brazil, the oil industry has a key role in the economic activity of oil-producing regions, such as the states of Rio de Janeiro and Espírito Santo.

Table 1.1: Distribution of energy supply, by source, for Brazil in 2013, and for the world in 2011 (MME, 2014) [2].

Source	Brazil (%)	World (%)
Biomass	24.5	10.0
Coal	5.6	28.8
Hydraulic and eletric energy	12.5	2.3
Natural gas	12.8	21.3
Oil and oil by-products	39.3	31.5
Other	4.0	1.0
Uranium	1.3	5.1

1.1.2 Oil well drilling and drillstring

Oil prospecting demands the creation of exploratory wells, which are drilled on land (onshore) or at sea (offshore) reservoirs. Usually, onshore reservoirs have a few hundred meters depth, while offshore reservoirs can achieve a few kilometers deep (Freudenrich and Strickland, 2001) [4]. For instance, in Brazilian pre-salt oil fields the average depth of a reservoir, considering the water layer, is the order of seven kilometers [5, 6].

Traditionally, an oil well configuration is vertical, but directional or even horizontal configurations, where the boreholes are drilled following a non-vertical way, are also possible (Willoughby, 2005) [7], (King, 2012) [8]. An illustration of the different types of configurations which an oil well can take is presented in Figure 1.1.

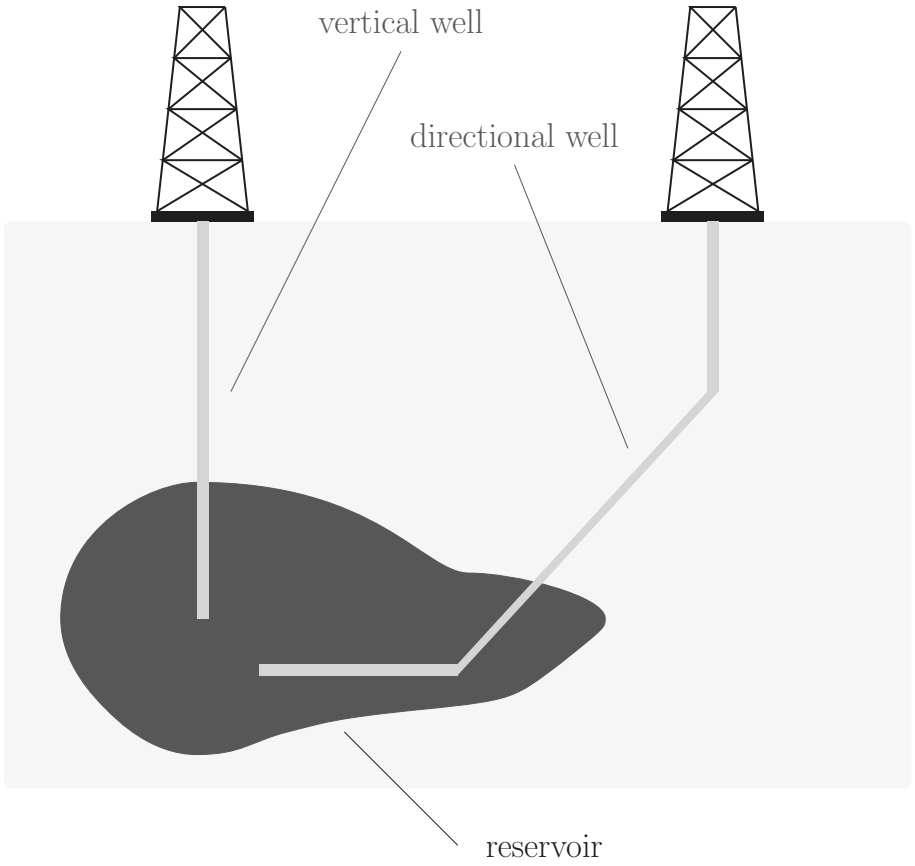

Figure 1.1: Schematic representation of two (onshore) oil wells. The left well configuration is vertical while the right one is directional.

The directional drilling allows to reach oil wells previously inaccessible by vertical drilling. Additionally, this non-conventional drilling technique should access a larger area of an oil reservoir and, thus, enhance oil production [9]. On the other hand, this non-conventional drilling technique imposes severe challenges in terms of engineering. The drilling process which follows a sinuous path requires drilling equipment with great flexibility and articulation. These devices have a complex dynamic behavior, and are more subject to damage and fatigue than the columns used in vertical drilling, once directional configuration enhances the transverse impacts between the equipment and the borehole walls (Macdonald and Bjune, 2007) [10].

The main equipment used to drill an oil well, which function is to drill the soil until the reservoir level, is called *drillstring*. This device is a long column, composed of a sequence of connected drill-pipes and auxiliary equipment. It presents stabilizers throughout its length, whose function is maintain structural integrity of borehole before cementation process. Furthermore, within the column flows a drilling mud, which is used to cool the drilling system and remove the drilling cuttings from the borehole. The bottom part of this column is called *bottom hole assembly* (BHA) and consists of a pipe of greater thickness,

named *drill-colar*, which provides the necessary weight for drilling, and a tool used to stick the rock, the *drill-bit* (Freudenrich and Strickland, 2001) [4]. A schematic representation of a typical vertical drillstring and its components is presented in Figure 1.2, but a column in horizontal configuration essentially has the same structure.

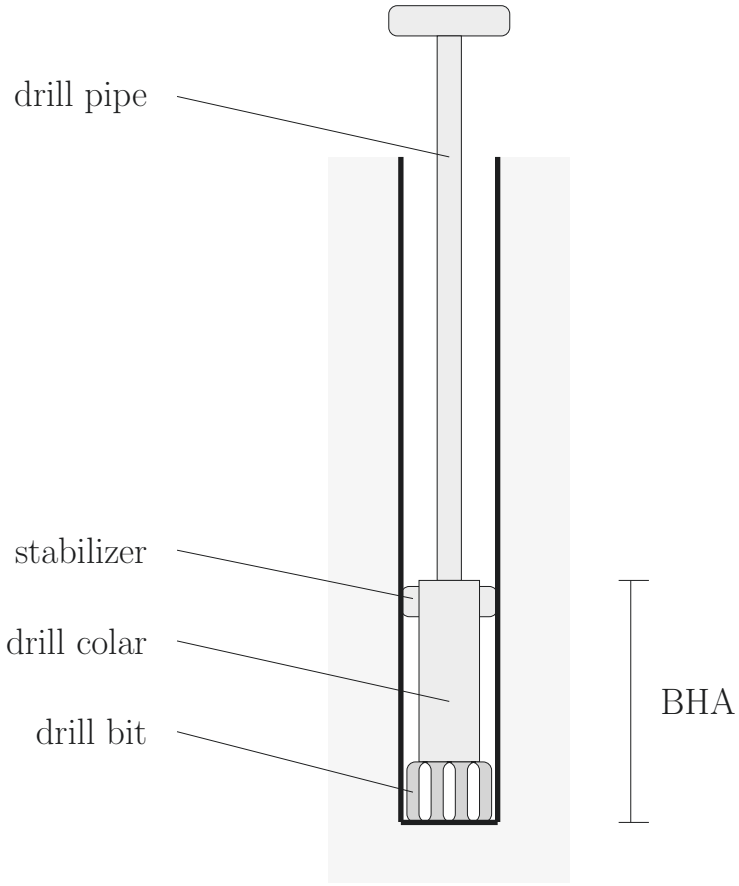

Figure 1.2: Schematic representation of a typical drillstring.

To control the drilling process, three operating parameters are used: (i) *rotation frequency* of the column, (ii) *weight on bit* (WOB), and (iii) *volumetric flow rate* of mud pumped into the column. These parameters, among many other things, control the *rate of penetration* (ROP) of the column into the soil (Jansen, 1993) [11].

Note that the rotation frequency controls the torque, which is responsible for rock penetration movement, while the WOB is a type of axial force exerted by the swivel (a type of hook) on the column top, which forces its advance. The volumetric flow rate controls the amount of drilling fluid pumped from the top of column until the borehole bottom. This fluid has the function of cool the equipment, in addition to transport, from the bottom of the well to the surface, the residues of the drilling process (Jansen, 1993) [11].

1.1.3 Uncertainties, variabilities and errors

This thesis also deals with uncertainties in the context of physical systems. To fix ideas, consider a designed system, which will give rise to a real system through a manufacturing process. This manufacturing process is subject to a series of variabilities (due to differences in the geometric dimensions of the components, variations in operating conditions, etc) that result in some differences in the parameters (geometrical dimensions, physical properties, etc) of two or more real systems manufactured. The inaccuracies on these parameters is known as *data uncertainty* (Soize, 2012) [12].

In order to make predictions about the behavior of the physical system, a computational model should be used. In the conception this model mathematical hypotheses are made. These considerations may be or not in agreement with the reality and should introduce additional inaccuracies in the model, known as *model uncertainty*. This source of uncertainty is essentially due to lack of knowledge about the phenomenon of interest and, usually, is the largest source of inaccuracy in model response (Soize, 2012) [12]. This model is also supplied with the parameters of the real system, so that it is also subjected to the data uncertainty.

A schematic representation of the conceptual process which show how uncertainties of a physical system are introduced into a computational model is shown in Figure 1.3.

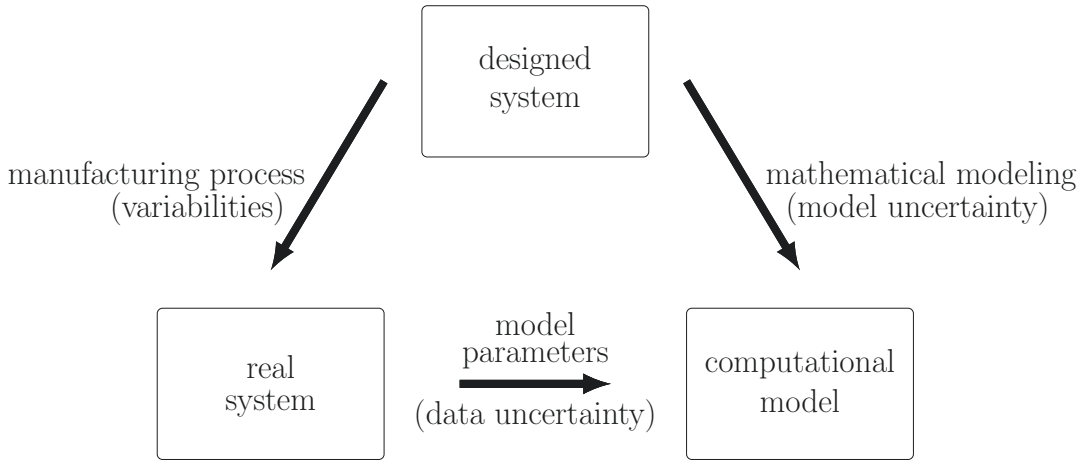

Figure 1.3: Schematic representation of the conceptual process which show how uncertainties of a physical system are introduced into a computational model.

Uncertainties affect the response of a computational model, but should not be considered errors because they are physical in nature. Errors in the model response are due to the discretization process of the equations and to the use of finite precision arithmetic to perform the calculations.

Therefore, unlike the uncertainties, that have physical origin, errors are purely mathematical in nature, and can be controlled if the numerical methods and algorithms used are well known by the analyst.

Being the uncertainties in the physical system the focus of stochastic modeling, two approaches are found in the scientific literature for the treatment of uncertainties: (i) *non-probabilistic*, and (ii) *probabilistic*.

The non-probabilistic approach uses techniques such as interval and fuzzy finite elements; imprecise probabilities; evidence theory; probability bounds analysis; fuzzy probabilities; etc, and is generally applied only when the probabilistic approach can not be used. For more details on this approach, the reader may consult the works of Moens and Vandepitte (2005) [13], Moens and Hanss (2011) [14], and Beer et al. (2013) [15].

The probabilistic approach uses probability theory to model the uncertainties of the physical system as random mathematical objects. This approach has a more well-developed and consistent mathematical framework, and, for this reason, there is a consensus among the experts that it is preferable whenever possible to use it (Soize, 2012) [12].

In the context of the probabilistic approach, when one wants to treat only the data uncertainties, the tool used is called *parametric probabilistic approach*. This procedure consists in modeling the random parameters of the computational model as random variables and/or random vectors, consistently constructing their probability distributions. Consequently, the system response becomes aleatory, and starts to be modeled by another random mathematical object, such as random variables, random vectors, stochastic processes and/or random fields, depending on the nature of the model equations. Then the system response is calculated using a stochastic solver.

For a review on the parametric probabilistic approach, the reader is encouraged to consult the works of Schuëller (1997) [16]; Schuëller (2001) [17]; Schuëller (2006) [18]; Schuëller (2007) [19]; Schuëller (2009a,b) [20, 21]; Soize (2012) [12]; and Soize (2013) [22].

Also in the context of the probabilistic approach, but when the focus are the model uncertainties, one of the tools used is called *nonparametric probabilistic approach*. This method was proposed by Soize (2000) [23], and describes the mathematical operators of the computational model, not the parameters, as random objects. The probability distribution of these objects must be constructed in a consistent manner, using the principle of maximum entropy. The methodology lumps the level of uncertainty of the model in a single parameter, which, in an ideal scenario with many experimental data available, must be identified by solving a problem of parameter identification.

The application of the nonparametric probabilistic approach in the contexts of dynamics and vibrations can be seen, for instance, in Soize (2001) [24], Soize (2003) [25], and Soize (2005) [26], and a review of the technique is presented in Soize (2012) [12] and Soize (2013) [22].

Recently Soize (2010) [27] and Batou et al. (2011) [28] published two papers combining the two probabilistic approaches in order to take into account data and model uncertainties in a single method, in what the authors called *generalized probabilistic approach*.

1.2 Issues of scientific and technological relevance

1.2.1 Study of column nonlinear dynamics

Since the axial direction of a drillstring is orders of magnitude larger than the characteristic dimension of its cross section area, the column is a long flexible structure with a very complex flexural dynamic. For sake of illustration of how flexible is such column, consider a typical 2 km long drillstring which has mean diameter of 100 mm. Herein, the drillstring *slenderness*, which is defined as the ratio between its length and diameter, is equal to 20.000. For comparison, a 300 mm long human hair, with mean diameter of 100 µm, has its slenderness equal to 3.000 (Chevallier, 2000) [29].

Furthermore, during drilling process, the drillstring is also subjected to other two mechanisms of vibration (longitudinal and torsional), which interact nonlinearly with the flexural mechanism, resulting in a further complicated dynamics. The coupling between these three mechanisms of vibration, which imposes severe complications on the drillstring dynamics modeling, come from the action of several agents, such as: structure self weight (for a vertical column); tensile and compressive loads due to the WOB and soil reaction force; dry friction and impacts with borehole walls; bit-rock interaction forces; internal flow pressure; forces induced by internal flow instabilities; etc (Spanos et. al., 2003) [30].

Thus, considering only the theoretical point of view, the study of the nonlinear dynamics of a drilling is already a rich subject. But in addition, the good understanding of its dynamics has also significance in applications. Only a few examples, it is fundamental to predict the fatigue life of the structure; to analyze the structural integrity of an oil well; and to optimize the ROP of the drill-bit into the soil, which is essential to reduce cost of production of an oil well.

1.2.2
Drilling process optimization

The task of drilling an oil well, which generally is not held by oil companies, but by service providers [31], involves immense amounts of money, since to rent a drilling rig costs on the order of some hundreds of thousands of dollars per day [32]. The process of drilling a well sometimes takes up to 3 months, so that this high daily cost has a cumulative effect, which is a major part in the final price a completed oil well. Moreover, as this drilling cost is very high and daily, all other fixed costs associated with the process become less important when one think in reduce the costs of production of an oil well.

In this sense, the strategy adopted to reduce the production cost of an oil well involves necessarily a reduction in the total number of days of operation. This is done through the maximization of the drillstring ROP into the soil, which also has a cumulative effect, that may result at the end of the operation in significant time savings.

1.3
Scope of scientific work

1.3.1
Problem definition and research objectives

Being motivated by the economic importance that oil exploration has, and will continue to have in the world for the next decades, this thesis aims to develop a study on the problematic associated with the drilling of oil wells in horizontal configuration. For this purpose, the objective is to develop a mechanical-mathematical model to describe the three-dimensional nonlinear dynamics of horizontal drillstrings, taking into account in modeling the other phenomena that affect the behavior of this system, such as friction and shocks due to the mechanical contacts between the pairs drill-bit/soil and drill-pipes/borehole. It is also intended to construct a stochastic model to take into account the uncertainties in this model that are due to the variability on its parameters. With the deterministic and stochastic models, it is intended to analyze the behavior of the mechanical system of interest, in order to obtain a better understanding of its nonlinear behavior. Indeed, the aim is to optimize the drilling process, by maximizing the ROP of the drillstring into the soil, to reduce the costs of production of an oil well.

1.3.2
Research contributions

This doctoral thesis deals with the problem defined in the previous section and presents as main contributions: (i) the development of a mechanical-mathematical model to describe the three-dimensional nonlinear dynamics of horizontal drillstrings; (ii) the development of an efficient computational model to simulate the nonlinear dynamics of interest; (iii) the implementation of this computational model in a `MATLAB` code; (iv) modeling of the bit-rock interaction model parameters uncertainties through the parametric probabilistic approach; (v) analysis of the nonlinear dynamic behavior of horizontal drillstrings, in particular the drill-bit; (vi) optimization (deterministic and robust) of the drilling process, by maximizing the drillstring ROP into the soil.

1.3.3
Manuscript outline

This manuscript is divided in seven chapters and three appendices. This introduction is the first chapter. In chapter two it is presented a review of the scientific literature concerning the nonlinear dynamics of drillstrings. Chapter three develops the deterministic modeling of a mechanical system that emulates a drillstring, in horizontal configuration, confined within an oil well. The chapter four shows the construction of a stochastic model for random parameters associated with the mechanical system of interest. In fifth chapter are presented the results of the numerical simulations performed to better understand the nonlinear behavior of the stochastic dynamical system. The chapter six concerns about the drilling process optimization, seeking to maximize the drillstring ROP into the soil. The seventh chapter reminds the thematic discussed in this thesis, the main results obtained, suggests paths for future works, and lists the authors publications along the doctorate. The appendix A presents the derivation of the weak equation of motion of the mechanical system of interest. In appendix B the reader can see the interpolation functions used by the finite element method. And finally in appendix C, are available the publications in journals that resulted from the work of this thesis.

2
Review of Scientific Literature

This chapter presents a literature review concerning the fundamental physics of drillstrings, its deterministic and stochastic modeling, and on the quantification of uncertainties intrinsic to such physical system.

2.1
Fundamental physics of drillstrings

Drillstrings have very complex physics, with three-dimensional dynamical behavior that presents longitudinal, flexural, and torsional vibrations, such as illustrated in Figure 2.1, and these mechanisms of oscillation are nonlinearly coupled in general.

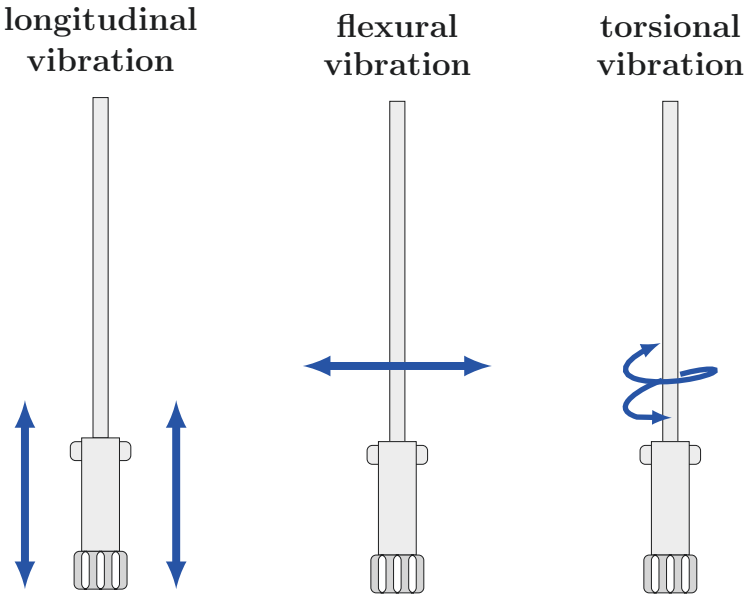

Figure 2.1: Schematic representation of the drillstring vibration mechanisms.

Moreover, these structures are subject to friction and shock effects due to transverse impacts between the structure and the borehole wall. Nonlinear effects are also introduced by the bit-rock interaction at the end of the column, and by the drilling fluid flow, that occurs in the annular space between the tube and the oil well.

Next, it is discussed in more detail each of the physical mechanisms that influence the nonlinear dynamics of a drillstring.

2.2 Longitudinal vibration: the bit-bounce phenomenon

The drillstring *longitudinal vibration* is a mechanism of axial oscillation. One of its occurrences is when drill-bit looses contact with rock and, in sequence, hits the rock sharply, a phenomenon called *bit-bounce* (Deily et al., 1968) [33]. This loss of contact may be due to irregularities in rock surface or due to an axial resonance, caused by a harmonic forcing induced by the mud pump. This phenomenon should generates some serious problems such as oscillations on WOB; decrease of ROP into the soil; fatigue of some mechanical devices; and even a possible damage to the borehole (Spanos et al., 2003) [30].

Early studies of this mechanism of vibration dates back to 1960, with the works of Bailey and Finnie [34, 35]. This phenomenon was also accessed experimentally by Cunningham (1968) [36], and Deily et al. (1968) [33], which observed that column rotation and fluctuations of pressure in drilling mud flow are sources of longitudinal vibrations on the drillstring.

Numerical studies that were conducted to understand the axial propagation of a wave in a drillstring are available in Lee (1991) [37]. More recent studies, involving numerical simulation and experimental analysis, which were conducted in order to understand how one can take advantage of the longitudinal vibrations to improve the efficiency of drilling process can be seen in Franca and Weber (2004) [38], and Franca (2004) [39], respectively.

Reviews on longitudinal vibration of drillstrings can be seen in Dykstra (1996) [40], Chevallier (2000) [29], and Spanos et al. (2003) [30].

2.3 Flexural vibration: the whirl phenomenon

The drillstring *flexural vibration* is a mechanism of transversal oscillation. For instance, this mechanism can occur due to centrifugal forces induced by rotation, a phenomenon called *whirl*. These forces can be generated by mass imbalances, a strong compressive force, etc. The phenomenon of whirling could result in damages to drill-pipes joints, drill-collars, drill-bit and borehole walls; shocks; and, reduction of ROP into the soil (Spanos et al., 2003) [30].

Historically this vibration mechanism was the last one to be observed during drillstring operation, since it occurs only in the regions of the column that are not visible from the surface. Furthermore, it is the most common mechanism of damage which the column is subjected (Chevallier, 2000) [29].

The literature presents a lot of works that investigate the phenomenon of whirl experimentally (Shyu, 1989) [41], numerically (Payne, 1992) [42], (Jansen, 1993) [11], (Kotsonis, 1994) [43], (Chevallier, 2000) [29], (Spanos et al., 2002) [44], or on both fronts (Spanos et al., 1997) [45].

For a deeper insight into whirl phenomenon of drillstrings, the interested reader is encouraged to consult Jansen (1993) [11], Chevallier (2000) [29], and Spanos et al. (2003) [30].

2.4 Torsional vibration: the stick-slip phenomenon

The drillstring *torsional vibration* is a mechanism of circumferential oscillation. In this mechanism, the vibration modes may be *transient* or *stationary*. The transient modes are encountered when drilling parameters are subjected to local variations, such as fluctuations in rotation frequency of the column or changes into soil properties. The most common occurrence of a stationary mode is when static friction between borehole wall and drill-bit is sufficient to block the rotation movement of the BHA, a phenomenon called *stick-slip*. During this block, the rotation frequency of the column, which is a structure with high torsional flexibility, is constant. In consequence, the column is twisted and potential energy of torsion is stored. When the available torque overcomes the static friction, the stored energy is released as kinetic energy of rotation and the column rotation frequency increases a lot, sometimes three times an order of magnitude above the normal. This phenomenon may result in excessive wear of the drill-bit and/or the borehole walls; can decrease the ROP into the soil; or even break the column (Spanos et al., 2003) [30].

The stick-slip phenomenon between two surfaces sliding on each other has been largely studied in the context of theoretical physics for more than seven decades (Bowden and Leben, 1939) [46], (Persson and Popov, 2000) [47].

In the context of drillstring dynamics, it is the vibration mechanism most studied, being analyzed analytically and experimentally by Bailey and Finnie (1960) [34, 35], Halsey et al. (1986) [48], Brett (1992) [49]. Other works access the phenomenon from numerical and experimental point of view, such as Lin and Wang (1991) [50], Mihajlovic et al. (2004) [51], Franca (2004) [39], or simply numerically, as is the case of Richard et al. (2004) [52], and Silveira and Wiercigroch (2009) [53].

For further information about stick-slip phenomenon in drillstring dynamics the reader can see Jansen (1993) [11], Chevallier (2000) [29], and Spanos et al., (2003) [30].

2.5 Coupling of vibration mechanisms

The individual study of each vibration mechanism that acts on a drillstring is an important task for better understanding the physical phenomena involved in the dynamics, besides being an interesting topic of academic research. But if one needs a realistic model to perform predictions about drillstring dynamics, consider an individual mechanism of vibration is of little interest, because in a real column all of these vibration mechanisms are coupled (Spanos et al., 2003) [30]. For this reason, most modeling work in this area take into account the coupling of two or three mechanisms of vibration.

Considerable effort has been developed to propose models that take into account the coupling between the different mechanisms of vibration. For example, the coupling between axial and torsional mechanisms was investigated by Sampaio et al. (2007) [54], and Germay et al. (2009) [55], both modeling the drillstring as a distributed parameters system, and by Richard et al. (2007) [56], Divenyi et al. (2012) [57], Nandakumar and Wiercigroch (2013) [58], and Depouhon and Detournay (2014)[59], which use a lumped parameters approach with two degrees of freedom. While the work of Sampaio et al. (2007) [54] aims to understand the effects introduced by the nonlinear coupling between the two mechanisms of vibration in the system response, the other works are focused on making qualitative and quantitative analyzes of the system, in order to seek configurations which reduce the stick-slip and bit-bounce phenomena during drillstring operation.

Also, studies on the coupling between longitudinal and flexural vibrations are available in Yigit and Christoforou (1996) [60], and Trindade et al. (2005) [61]. These two works show that it is necessary take into account the nonlinear coupling between longitudinal and flexural vibrations when one wants to correctly predict the transverse impacts between the drillstring and the borehole wall.

The coupling between the flexural and torsional vibrations is the central object of study in Yigit and Christoforou (1998) [62]. It is observed that, at certain frequencies, there is a large transfer of energy between the two modes of vibration. Furthermore, the model reproduces qualitatively well the stick-slip phenomenon, once the numerical values obtained with the model presented good qualitative agreement with the experimental data obtained from a test rig in laboratory.

Studies which considers the coupling between the three vibrations mechanisms also exist in the literature. For instance, Tucker and Wang (1999) [63], Coral Alamo (2006) [64], and Silveira (2011) [65], which use an exact geometric description of kinematics, through the theory of Cosserat, to model the nonlinear dynamics of a drillstring. Additionally, lumped parameters approach is used by Christoforou and Yigit (2003) [66], in a strategy to control the drillstring vibrations, and by Liu et al. (2013) [67], to conduct numerical studies that show the existence of long periods of stick-slip, besides a whirling state of the tube that periodically alternates between phases of stick and slip. The approach of distributed parameters is used by Khulief et al. (2007) [68], Ritto et al. (2009) [69], and Ritto (2010) [70]. As these models take into account the non-linear coupling between all the mechanisms of vibration, in principle, they provide a better representation of the physical phenomenon that occurs in the real system. The price one needs to pay by these nonlinearities in a distributed parameters model is the computational cost, which is much higher than the cost associated with previous models. Therefore, all these works use modal projection to obtain reduced order models.

2.6 Interaction between drill-bit and soil

The drill-bit, which is located at the end of the drillstring, has a complex geometry so that its kinematical behavior during the drilling process is extremely complicated to be described in detail. Likewise, it is also difficult to describe the forces/torques of reaction imposed by the rock formation on the drill-bit. As an alternative to describe this complex physics, Detournay and Defourny (1992) [71] established a phenomenological relationship, linking dynamic parameters into the drill-bit, such as force and torque of reaction, with kinematic quantities of the drillstring, such as angular velocity and rate of penetration.

Hence, the standard approach to model the the phenomena of interaction between the drill-bit and the rock formation became to use phenomenological equations, known as *bit-rock interaction laws*, which relate the force and the torque with the angular velocity and rate of penetration of the drillstring (Detournay et al., 2008) [72]. Such an approach lumps the dynamic effects into a force and a torque, concentrated at the end of the column, ignoring all details of the complex geometry of the drill-bit, such as illustrated in Figure 2.2.

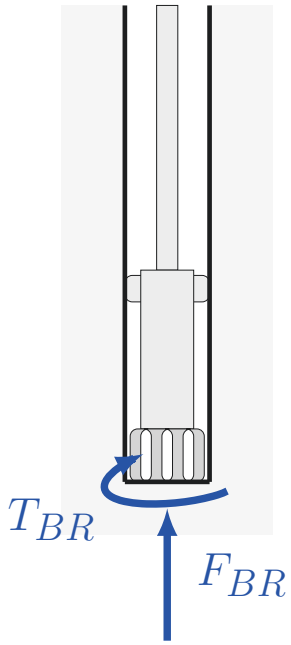

Figure 2.2: Schematic representation of the interaction between the drill-bit and the rock formation.

Assuming that two independent processes – cutting and friction – characterize the bit-rock interaction of drag bits, and the latter has three distinct phases, Detournay et al. (2008) [72] proposed a interaction law in which force and torque do not depend on two kinematic variables (angular velocity and penetration rate), but only on the ratio between them, and, of course, some constants which are function of drill-bit geometry and rock properties. Later, Franca (2010) [73] adapted this model to the context of polycrystalline-diamond-compact bits, and then to rotary-percussive drilling (Franca, 2011) [74]. All of these works combine theoretical formulation with experimental validation.

In the natural formulation, these interaction laws receive force and torque as input, and return the angular velocity and the rate of penetration as output. However, when these phenomenological equations are inverted, so that the model receives kinematics parameters and return dynamic quantities, a singularity arises, which generates infinite force and infinite torque when the rate of penetration become zero. This singularity has no justification from a physical perspective. So, a procedure of mathematical regularization, using a function that decays to zero faster than the force/torque diverges, is used in some studies, such as Tucker and Wang (2003) [75], Ritto et al. (2009) [69], Ritto et al. (2012) [76], to avoid the singularity of the model. An artificial procedure, which showed itself useful for numerical purposes.

Ritto et al. (2013) [77] proposed a phenomenological equation to describe the reaction force on the drill-bit in the context of horizontal drilling. This new interaction law, inspired by an expression used to describe friction in metal working processes (Wanheim et al., 1974) [78], models the force as an exponential decay function that is limited below. This avoids the singularity previously described. Meanwhile, the model is still purely theoretical, without any experimental validation.

A common deficiency found in all of the above models, even in those who have undergone an experimental validation process, is the absence of a static equilibrium configuration (Corben and Stehle, 1994) [79], which is not realistic from the physical point of view.

One last point, to the best of author's knowledge, there is no work in the literature that verifies if bit-rock interaction laws above, which resemble constitutive equations, were developed into a "suitable" thermodynamical framework (Rajagopal, 2003) [80].

2.7
Flow of the drilling fluid

During the drilling process, a drilling mud, which is a highly viscous fluid that presents a non-Newtonian behavior, is pumped inside the tube, leaving it by the extreme which contains the drill-bit and then flowing through the annular space between the drillstring and borehole wall. A schematic representation of this situation can be seen in Figure 2.3.

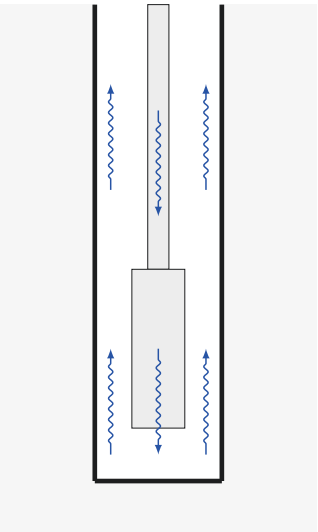

Figure 2.3: Schematic representation of the drilling fluid flow that occurs inside the drillstring and in the annular space outside of it.

In general this fluid flow is three-dimensional and turbulent, so that its physical behavior is highly nonlinear. The operation in regime of turbulence generates severe fluctuations in pressure and velocity, which induces vibrations on the drillstring. Such fluctuations are dependent on various characteristics of the fluid (viscosity, density, temperature, etc) and of the drillstring geometry (length, diameter, eccentricity, etc) (Spanos et al., 2003) [30].

The influence of eccentricity in the behavior of a fluid that flows in an annular space has been studied theoretically, numerically, and experimentally by several authors. For instance, Siginer and Bakhtiyarov (1998) [81] study the azimuthal velocity of a non-Newtonian fluid, using linear fluidity model, and compare the results obtained with an analytical expression with experimental data, obtaining good corroboration. On the other hand, a Newtonian fluid, flowing in laminar regime through an eccentric annulus, with axial bulk velocity and angular rotation of the inner cylinder, is investigated by Escudier et al., (2000) [82]. In a later work, Escudier et al. (2002) [83] studied the effect of eccentricity in case similar to the previous one, but now considering a non-Newtonian fluid. Lubrication theory was employed by Pina and Carvalho (2006) [84] to reduce computational cost of a model that describes the three-dimensional annular flow mentioned above, for a Newtonian fluid. This numerical study was conducted in order to identify the effect of eccentricity in the three-dimensional flow. Comparisons with results available in the literature showed the accuracy of the simplified model.

Another problem, where the annular flow presents a partial obstruction, which breaks its circumferential symmetry, was studied numerically and experimentally by Loureiro et al. (2006) [85]. This work identified that the width of the vortices, which are generated due to Taylor-Couette instabilities, depends on the obstruction height.

Concerning the modeling of fluid flow and drillstring structural dynamics interaction effects, the works of Ritto et al. (2009) [69], and Ritto (2010) [70], presented a simplified model for describing this flow based on the work of Païdoussis et al. (2008) [86]. This model assumes that the fluid inside the tube is inviscid, while the fluid in the annular space has viscosity. A linear variation of pressure throughout the axial direction is also supposed. The flow induced by rotation around the axial direction of the tube is disregarded. Thus, taking into account these assumptions, the fluid-structure coupling in this model is intrinsically linear (Païdoussis, 1998, 2004) [87, 88].

2.8 Directional and horizontal drillstrings

Despite the fact that directional drilling have been used in practical engineering for a few decades, and the majority of the exploratory wells drilled today be directional in configuration, most of the works find in the technical/scientific literature study vertical drillstrings only. To the best of the author's knowledge, there are very few papers in the open literature which models drillstring in directional configurations (Sahebkar et al., 2011) [89], (Hu et al., 2012) [90], and (Ritto et al., 2013) [77].

All of these works use distributed parameters approach, but while Sahebkar et al. (2011) [89] and Ritto et al. (2013) [77] only address the drillstring longitudinal dynamics, Hu et al. (2012) [90] uses generalized Euler-Bernoulli beam theory to describe the drillstring three-dimensional dynamics in a sloped directional well. In Sahebkar et al. (2011) [89], the authors study a sloped configuration for the borehole and uses a perturbation technique to compute a solution for the equations of the model. Conversely, the model equations are solved by finite element method in Ritto et al. (2013) [77].

However, regarding the physics of the directional drilling problem, none of these works examines in depth the phenomena of interest. For instance, Sahebkar et al. (2011) [89] merely analyzes the resonance frequencies of the system, while Hu et al. (2012) [90] presents a few results regarding lateral and axial dynamics, addition to a whirl orbit. It is surprising the absence of results relative to the torsional dynamics, where one would expect to observe the stick-slip phenomenon. Ritto et al. (2013) [77] are the authors who discuss the physics deeper, introducing spectral analysis of the system response, analyzing the efficiency of the drilling process, and surprisingly, identifying a type of stick-slip phenomenon in the longitudinal dynamics. However, the main objective of their work is uncertainty analysis, and not exploration of the nonlinear dynamics.

Certainly, there is a lack of works in the scientific literature dealing with the nonlinear dynamics of drillstring in directional and/or horizontal configurations. This fact, together with the engineering applications associated (fatigue life calculation; structural integrity analysis; ROP optimization; etc), make this issue a very interesting topic of research, and served as one motivation for this thesis.

2.9
Uncertainty quantification in drillstring dynamics

A drillstring is a very complex physical system, which is subject to many variabilities in its parameters. This combination of variability in physical parameters and complexity on physics leads to a computational model (prediction tool) subject to data and model uncertainties. Therefore, for a better understanding of drillstring dynamics, these uncertainties must be modeled and quantified.

In the context of vertical drillstrings dynamics, one of the first works on uncertainty quantification was the Ph.D. Thesis of Chevallier (2000) [29], giving rise to the work of Spanos et al. (2002) [44], where external forces are modeled as random objects and the method of statistical linearization is used along with the Monte Carlo method to treat the stochastic equations of the model.

Other work in this line include the D.Sc. Thesis of Ritto (2010) [70], which resulted in a series of publications. Among these publications, some of then use the nonparametric probabilistic approach to account model uncertainties, such as Ritto et al. (2009) [69], and Ritto et al. (2010a) [91]. On the other hand, the standard parametric probabilistic approach is used to take into account the data uncertainty by Ritto et al. (2010b) [92], and Ritto and Sampaio (2012) [76].

Aiming to maximize drillstring ROP into the soil, Ritto et al. (2010c) [93] solve a robust optimization problem, where the objective function is mean value of the ROP, and the restrictions are imposed by the limits of structural integrity of the system. The results show that, in some situations, it is more advantageous to solve a robust optimization problem instead of a classic optimization problem.

In the assemblies of works that deal with directional drilling, to the best of the author's knowledge, only Ritto et al. (2013) [77] considers the uncertainties, which, in this case, are related to the friction effects due to drillstring/borehole wall contact.

3
Modeling of Nonlinear Dynamical System

This chapter presents the deterministic modeling of the nonlinear dynamics of drillstrings in horizontal configuration, and is divided into four parts. The first part draws up a physical model for the problem, then, in the second part the physical model is translated into equations to obtain a mathematical model. In the third part, it is conceived a computational model to numerically approximate the solution of the mathematical model. Finally, at the end of the chapter, one finds a fourth part, that discusses the the position of the modeling presented in relation to the work that formed the basis for its development.

3.1
Physical model for the problem

The conception of a physical model for the problem includes the definition and parametrization of the mechanical system, followed by the modeling of the effects of friction and shock, as well as the effects of bit-rock interaction. As the main focus of this work is the structural part, are ignored any fluid-structure and thermal effects that may influence the dynamical system of interest.

3.1.1
Definition of the mechanical system

The mechanical system of interest in this work, which is schematically represented in Figure 3.1, consists of a horizontal rigid pipe, perpendicular to the gravity, which contains in its interior a deformable tube under rotation. This deformable tube is subjected to three dimensional displacements, which induces longitudinal, lateral, and torsional vibrations of the structure. These mechanisms of vibration are able to generate slips and shocks in random areas of the rigid tube. Also, the contact between the drill-bit, at the right extreme of the tube, with the soil generates nonlinear forces and torques on the drillstring right extreme, which may completely block the advance of the structure over the well.

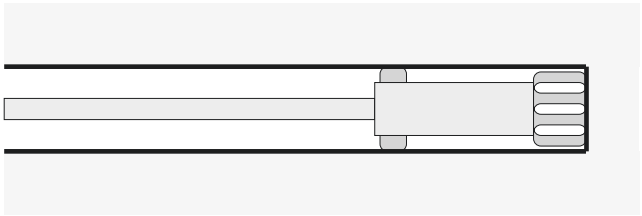

Figure 3.1: Schematic representation of the mechanical system under analysis.

3.1.2 Parameterization of the nonlinear dynamical system

For purposes of modeling, the only part of the column considered is the BHA. So, the variation of the diameter along the column is ignored. In this way, the bottom part of the deformable tube, described in the previous section, is modeled as a rotating beam in horizontal configuration, whose the transverse displacement (y and z) at both ends is blocked, as well as the transverse rotations on the left extreme. This beam is free to rotate around the x axis, and to move longitudinally. The rigid pipe described in the section 3.1.1 will be treated as a stationary cylindrical rigid wall in horizontal configuration.

As the beam is confined within the borehole, it is reasonable to assume that it undergoes small rotations in the transverse directions. By another hand, large displacements are observed in x, y, and z, as well as large rotations around the x-axis. Therefore, the analysis that follows uses a beam theory which assumes large rotation in x, large displacements in the three spatial directions, and small deformations (Bonet and Wood, 2008) [94].

Seeking not to make mathematical model excessively complex, this work will not model the fluid flow inside the beam, nor the dissipation effects induced by the flow on the system dynamics.

Due to the horizontal configuration, the beam is subject to the action of the gravitational field, which induces an acceleration g. This beam is made of an isotropic material with mass density ρ, elastic modulus E, and Poisson's ratio ν. It has length L and annular cross section, with internal radius R_{int} and external radius R_{ext}.

An illustration of the beam geometric model is presented in Figure 3.2. It is important to note that this model also ignores the mass of the drill-bit and its geometric shape.

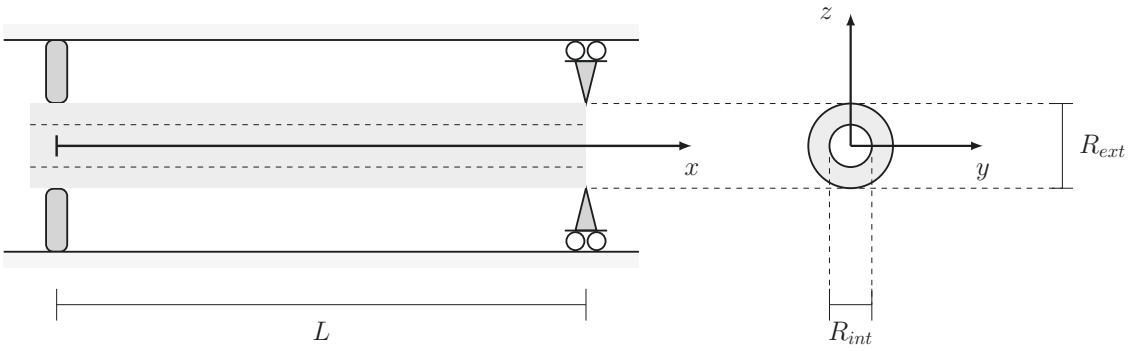

Figure 3.2: Schematic representation of the beam geometry used to model the deformable tube under rotation, and the inertial system of coordinates used.

Using the cartesian coordinate system (x, y, z), defined by the orthonormal basis $\{\boldsymbol{e}_x, \boldsymbol{e}_y, \boldsymbol{e}_z\}$, fixed in the inertial frame of reference $\mathcal{R}$, and shown in the Figure 3.2, one can describe the undeformed configuration of the beam geometry by

$$\mathcal{B}_0 = \left\{ (x, y, z) \in \mathbb{R}^3 \;\middle|\; 0 \leq x \leq L,\ (y, z) \in \mathcal{S}_0 \right\}, \tag{3.1}$$

where the undeformed configuration of the beam cross section is described by

$$\mathcal{S}_0 = \left\{ (y, z) \in \mathbb{R}^2 \;\middle|\; R_{int}^2 \leq y^2 + z^2 \leq R_{ext}^2 \right\}. \tag{3.2}$$

Once the configuration of the undeformed cross section has been characterized, one can define the cross-sectional area,

$$A = \iint_{\mathcal{S}_0} dy\, dz, \tag{3.3}$$

the second moment of area around the y axis

$$I_{yy} = \iint_{\mathcal{S}_0} z^2\, dy\, dz, \tag{3.4}$$

the second moment of area around the z axis

$$I_{zz} = \iint_{\mathcal{S}_0} y^2\, dy\, dz, \tag{3.5}$$

the polar moment of area

$$I_{xx} = \iint_{\mathcal{S}_0} \left(y^2 + z^2\right)\, dy\, dz, \tag{3.6}$$

the fourth moment of area around the z axis

$$I_{zzzz} = \iint_{\mathcal{S}_0} y^4\, dy\, dz, \tag{3.7}$$

and the fourth product of area

$$I_{yyzz} = \iint_{\mathcal{S}_0} y^2 z^2\, dy\, dz. \tag{3.8}$$

Calculating the integrals on the Eqs. (3.3) to (3.8) one can show that

$$A = \pi \left(R_{ext}^2 - R_{int}^2 \right), \tag{3.9}$$

as well as $I_{yy} = I_{zz} = I_4$, $I_{xx} = 2I_4$, $I_{yyzz} = I_6$, and $I_{zzzz} = 3I_6$, where

$$I_4 = \frac{\pi}{4} \left(R_{ext}^4 - R_{int}^4 \right), \tag{3.10}$$

and

$$I_6 = \frac{\pi}{24} \left(R_{ext}^6 - R_{int}^6 \right). \tag{3.11}$$

In this work other three coordinate systems (all of then with the same origin as the (x, y, z) coordinate system) are also used, each one fixed in a non-inertial frame of reference $\mathcal{R}_n$, where $n = 1, 2, 3$, and defined by an orthonormal basis of vectors of the form $\{\boldsymbol{e}_{x_n}, \boldsymbol{e}_{y_n}, \boldsymbol{e}_{z_n}\}$.

These systems of coordinates are related by a sequence of elementary rotations, such as follows

$$\begin{array}{ccccccc} \mathcal{R} & \xrightarrow{\theta_x} & \mathcal{R}_1 & \xrightarrow{\theta_y} & \mathcal{R}_2 & \xrightarrow{\theta_z} & \mathcal{R}_3, \\ (x, y, z) & & (x_1, y_1, z_1) & & (x_2, y_2, z_2) & & (x_3, y_3, z_3) \end{array} \tag{3.12}$$

where θ_x is the rotation between the coordinate systems (x, y, z) and (x_1, y_1, z_1), θ_y is the rotation between the coordinate systems (x_1, y_1, z_1) and (x_2, y_2, z_2), and θ_z is the rotation between the coordinate systems (x_2, y_2, z_2) and (x_3, y_3, z_3). This sequence of elementary rotations is illustrated in Figure 3.3.

Thus, with respect to the non-inertial frame of reference, the instantaneous angular velocity of the beam is written as

$$\boldsymbol{\omega} = \dot{\theta}_x \boldsymbol{e}_x + \dot{\theta}_y \boldsymbol{e}_{y_1} + \dot{\theta}_z \boldsymbol{e}_{z_2}, \tag{3.13}$$

where $\dot{\theta}_x$, $\dot{\theta}_y$, and $\dot{\theta}_z$ denote the rate of rotation around the x, y, and z directions, respectively. From now on, the upper dot $\dot{}$ will be used as an abbreviation for time derivative.

Referencing the vector $\boldsymbol{\omega}$ to the inertial frame of reference, and using the assumption of small rotations in the transversal directions, one obtains

$$\begin{aligned} \boldsymbol{\omega} = & \begin{pmatrix} \dot{\theta}_x \\ 0 \\ 0 \end{pmatrix} + \begin{pmatrix} 1 & 0 & 0 \\ 0 & \cos\theta_x & -\sin\theta_x \\ 0 & \sin\theta_x & \cos\theta_x \end{pmatrix} \begin{pmatrix} 0 \\ \dot{\theta}_y \\ 0 \end{pmatrix} + \\ & \begin{pmatrix} 1 & 0 & 0 \\ 0 & \cos\theta_x & -\sin\theta_x \\ 0 & \sin\theta_x & \cos\theta_x \end{pmatrix} \begin{pmatrix} 1 & 0 & \theta_y \\ 0 & 1 & 0 \\ -\theta_y & 0 & 1 \end{pmatrix} \begin{pmatrix} 0 \\ 0 \\ \dot{\theta}_z \end{pmatrix}, \end{aligned} \tag{3.14}$$

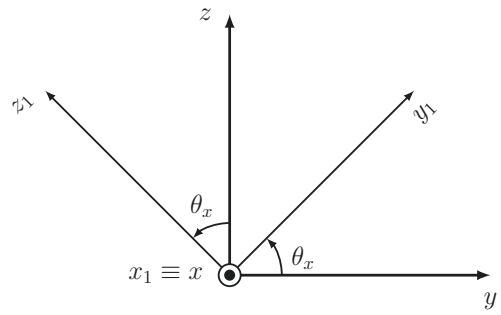

3.3(a): System of coordinates (x_1, y_1, z_1) rotates around the x axis.

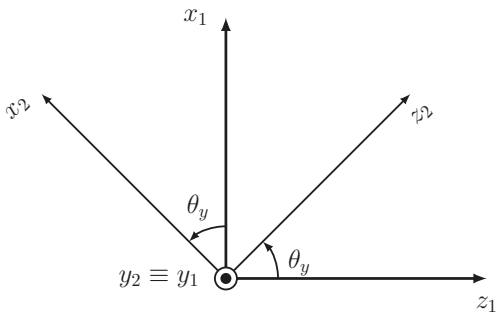

3.3(b): System of coordinates (x_2, y_2, z_2) rotates around the y_1 axis.

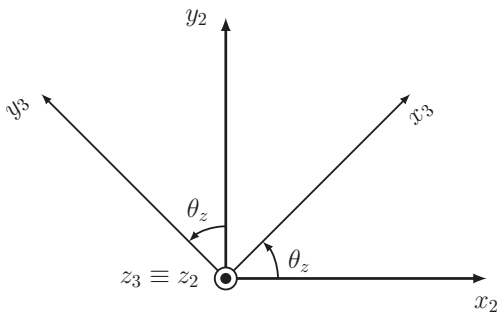

3.3(c): System of coordinates (x_3, y_3, z_3) rotates around the z_2 axis.

Figure 3.3: Sequence of elementary rotations that relates the non-inertial coordinate systems used in this work.

which is equivalent to

$$\boldsymbol{\omega} = \begin{pmatrix} \dot{\theta}_x + \dot{\theta}_z \theta_y \\ \dot{\theta}_y \cos\theta_x - \dot{\theta}_z \sin\theta_x \\ \dot{\theta}_y \sin\theta_x + \dot{\theta}_z \cos\theta_x \end{pmatrix}. \tag{3.15}$$

The kinematic hypothesis adopted for the beam theory assumes that the three-dimensional displacement of a beam point, occupying the position (x, y, z) at the instant of time t, can be written as

$$\begin{aligned} u_x(x,y,z,t) &= u - y\theta_z + z\theta_y, \\ u_y(x,y,z,t) &= v + y\left(\cos\theta_x - 1\right) - z\sin\theta_x, \\ u_z(x,y,z,t) &= w + z\left(\cos\theta_x - 1\right) + y\sin\theta_x, \end{aligned} \tag{3.16}$$

where u_x, u_y, and u_z respectively denote the displacement of a beam point in x, y, and z directions. Moreover, u, v, and w are the displacements of a beam neutral fiber point in x, y, and z directions, respectively. Remember that θ_x, θ_y, and θ_z represent rotations around axes of the non-inertial coordinate systems.

Finally, it is possible to define the vectors

$$\boldsymbol{r} = \begin{pmatrix} x \\ y \\ z \end{pmatrix}, \quad \mathbf{v} = \begin{pmatrix} \dot{u} \\ \dot{v} \\ \dot{w} \end{pmatrix}, \quad \text{and} \quad \dot{\boldsymbol{\theta}} = \begin{pmatrix} \dot{\theta}_x \\ \dot{\theta}_y \\ \dot{\theta}_z \end{pmatrix}, \tag{3.17}$$

which, respectively, represent the position of a beam point, the velocity of a neutral fiber point, and the rate of rotation of a neutral fiber point.

Note that the kinematic hypothesis of Eq.(3.16) is expressed in terms of the three spatial coordinates (x, y, and z) and six field variables, the neutral fiber displacements (u, v, and w) and the rotations around axes of the non-inertial coordinate systems (θ_x, θ_y, and θ_z). These field variables are the physical quantities of interest to describe the nonlinear dynamics of the deformable tube under rotation.

It is important to mention that, as the analysis assumed small rotations in y and z, the kinematic hypothesis of Eq.(3.16) presents nonlinearities, expressed by the trigonometric functions, only in θ_x. Besides that, since the analysis is using a beam theory, the field variables in Eq.(3.16) depend only on the spatial coordinate x and the time t, i.e., $u = u(x,t)$, $v = v(x,t)$, $w = w(x,t)$, $\theta_x = \theta_x(x,t)$, $\theta_y = \theta_y(x,t)$, and $\theta_z = \theta_z(x,t)$. Therefore, although the kinematic hypothesis of Eq.(3.16) is three-dimensional (depends on x, y, and z), the mathematical model used to describe the nonlinear dynamics of the beam is one-dimensional (depends only on x).

3.1.3 Modeling of the friction and shock effects

When a drillstring deforms laterally, there may occur a mechanical contact between the beam and the borehole wall, such as illustrated in the Figure 3.4. This mechanical contact, which generally take place via a strong impact, gives rise to effects of friction and shock (Gilardi and Sharf, 2002) [95], (Wriggers, 2006) [96].

The modeling of the phenomena of friction and shock is made in terms of a geometric parameter dubbed *indentation*, which is defined as

$$\delta_{\text{FS}} = r - \texttt{gap}, \tag{3.18}$$

where the neutral fiber lateral displacement is defined as

$$r = \sqrt{v^2 + w^2}, \tag{3.19}$$

and `gap` denotes the space between undeformed beam and borehole wall.

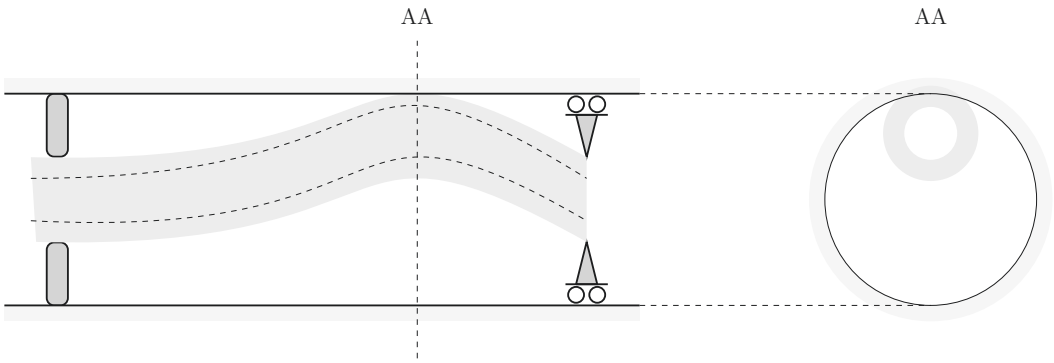

Figure 3.4: Schematic representation of the situation where there is a mechanical contact between a drillstring and the borehole wall.

Accordingly, one has $\delta_{\text{FS}} > 0$ in case of an impact, or $\delta_{\text{FS}} \leq 0$ otherwise, as can be seen in Figure 3.5. Note that the indentation corresponds to a measure of penetration in the wall of a beam cross section (Gilardi and Sharf, 2002) [95].

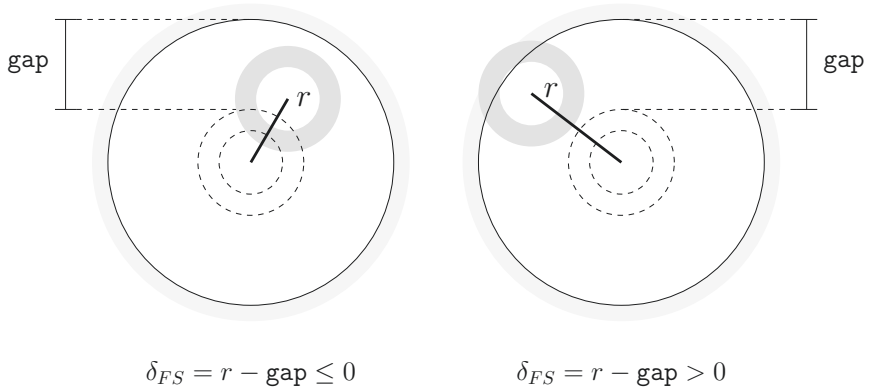

Figure 3.5: Illustration of the indentation parameter in a situation without impact (left) or with impact (right).

When the impact occurs, a normal force of the form

$$F^n_{\text{FS}} = -k_{\text{FS}_1}\,\delta_{\text{FS}} - k_{\text{FS}_2}\,\delta^3_{\text{FS}} - c_{\text{FS}}\,|\delta|^3\dot{\delta}_{\text{FS}}, \tag{3.20}$$

where k_{FS_1}, k_{FS_2} and c_{FS} are constants of the shock model, begins to act on beam cross section. In this nonlinear shock model, proposed by Hunt and Crossley (1975) [97], the first two terms correspond to a nonlinear spring, and describe the elastic deformation during the impact, while the last term is a nonlinear damper, and takes into account the loss of energy during the impact. So k_{FS_1} and k_{FS_2}, which depends on the material/geometry of the impacting bodies, are types of stiffness constants, while c_{FS}, that depends on the coefficient of restitution, is a type of damping constant.

Once the column is rotating and moving axially, the impact also induces a frictional force in the axial direction, F^a_{FS}, and a torsional friction torque, T_{FS}. Both are modeled by the Coulomb friction law (Cull and Tucker, 1999) [98] so that the force is given by

$$F^a_{\text{FS}} = -\mu_{\text{FS}}\, F^n_{\text{FS}}\, \texttt{sgn}\left(\dot{u}\right), \tag{3.21}$$

whereas the torque is described by

$$T_{\text{FS}} = -\mu_{\text{FS}}\, F^n_{\text{FS}}\, R_{bh}\, \texttt{sgn}\left(\dot{\theta}_x\right), \tag{3.22}$$

being μ_{FS} the shock friction coefficient, $\texttt{sgn}\left(\cdot\right)$ the sign function, and the radius of the borehole is $R_{bh} = R_{ext} + \texttt{gap}$.

In order to find all the points of contact between the beam and the borehole wall, it is necessary to discover all the values of x where $\delta_{\text{FS}} > 0$. This is usually done by solving an optimization problem with constraints (Wriggers and Zavarise, 2004) [99].

The strategy of detection based on the optimization problem may be robust in terms of accuracy, but it is extremely complex in terms of implementation and computational cost. For this reason, this work uses an approach that introduces the forces of Eqs.(3.20) and (3.21), and the torque of Eq.(3.22), as efforts concentrated on the nodal points of the finite element mesh, defined in the section 3.3.1. This procedure sacrifices some accuracy, but simplifies the implementation of the friction and shock model.

3.1.4
Modeling of the bit-rock interaction effects

During the drilling process, in response to rotational advance of the drillstring, a force and a torque of reaction begin to act on the drill-bit, giving rise to the so-called bit-rock interaction effects (Franca, 2010) [73].

In this work, the model proposed by Ritto et al. (2013) [77] is considered to describe the bit-rock interaction force

$$F_{\text{BR}} = \begin{cases} \Gamma_{\text{BR}} \left(e^{-\alpha_{\text{BR}}\, \dot{u}_{bit}} - 1\right) & \text{for } \dot{u}_{bit} > 0, \\ 0 & \text{for } \dot{u}_{bit} \leq 0, \end{cases} \tag{3.23}$$

where Γ_{BR} is the bit-rock limit force, α_{BR} is the rate of change of bit-rock force, and $\dot{u}_{bit} = \dot{u}(L, \cdot)$. The graph of the function F_{BR} is illustrated in Figure 3.6.

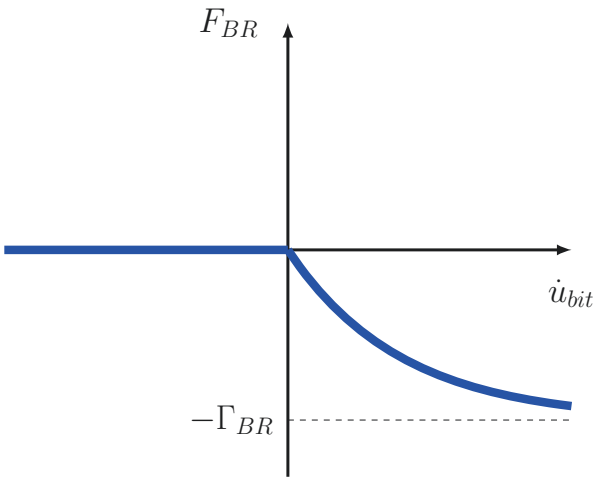

Figure 3.6: Illustration of the function used to describe the reaction force on the drill-bit, due to the bit-rock interaction effects.

Also, for the bit-rock interaction torque it is adopted the regularized Coulomb model used by Khulief et al. (2007) [68], which is expressed as

$$T_{\text{BR}} = -\mu_{\text{BR}}\, F_{\text{BR}}\, R_{bh}\, \xi_{\text{BR}}\left(\omega_{bit}\right), \tag{3.24}$$

where μ_{BR} bit-rock friction coefficient, $\omega_{bit} = \dot{\theta}_x(L, \cdot)$, and

$$\xi_{\text{BR}}\left(\omega_{bit}\right) = \tanh\left(\omega_{bit}\right) + \frac{2\,\omega_{bit}}{1+\omega_{bit}^2}, \tag{3.25}$$

is a regularization function. The graph of the regularization function ξ_{BR} is illustrated in Figure 3.7.

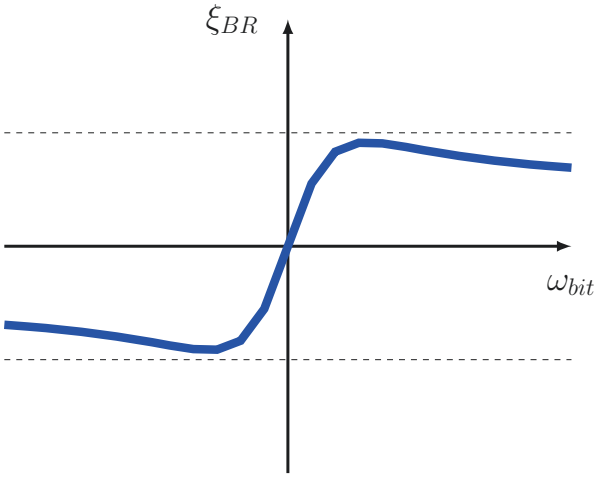

Figure 3.7: Illustration of the smooth function used to regularize the reaction torque on the drill-bit, due to the bit-rock interaction effects.

3.1.5 Kinetic energy

The kinetic energy of the beam is given by

$$\begin{aligned} \mathcal{T} &= \frac{1}{2}\iiint_{\mathcal{B}_b} \rho\, \mathbf{v}\cdot\mathbf{v}\, dx\, dy\, dz \;+ \\ &\quad \frac{1}{2}\iiint_{\mathcal{B}_b} \rho\, \boldsymbol{\omega}\cdot(\boldsymbol{r}\cdot\boldsymbol{r}\,\mathbb{I} - \boldsymbol{r}\otimes\boldsymbol{r})\,\boldsymbol{\omega}\, dx\, dy\, dz, \end{aligned} \tag{3.26}$$

where the first triple integral corresponds to the beam translational kinetic energy, and the second one is associated to the beam rotational kinetic energy. In this equation, $\mathbb{I}$ denotes the identity tensor, the symbol $\cdot$ represents the standard inner product between two Euclidean vectors, and the symbol $\otimes$ is used to designate the tensor product.

Developing the vector operations indicated in the Eq.(3.26), using (3.1) and (3.2) to define the limits of integration, using the definition of A, I_{yy}, I_{zz}, and I_{xx}, which are given by Eqs.(3.3) to (3.6), remembering that $I_{yy} = I_{zz} = I_4$, $I_{xx} = 2I_4$, and making the other calculations one can show that the Eq.(3.26) is equivalent to

$$\begin{aligned} \mathcal{T} &= \frac{1}{2}\int_{x=0}^{L} \rho\, A\left(\dot{u}^2 + \dot{v}^2 + \dot{w}^2\right) dx \;+ \\ &\quad \frac{1}{2}\int_{x=0}^{L} 2\,\rho\, I_4\left(\dot{\theta}_x + \dot{\theta}_z\theta_y\right)^2 dx \;+ \\ &\quad \frac{1}{2}\int_{x=0}^{L} \rho\, I_4\left(\dot{\theta}_y\cos\theta_x - \dot{\theta}_z\sin\theta_x\right)^2 dx \;+ \\ &\quad \frac{1}{2}\int_{x=0}^{L} \rho\, I_4\left(\dot{\theta}_y\sin\theta_x + \dot{\theta}_z\cos\theta_x\right)^2 dx. \end{aligned} \tag{3.27}$$

3.1.6 Strain energy

The analysis of the beam assumes that it is subjected to large displacements, and small deformations. In this way, its strain energy is given by

$$\mathcal{V} = \frac{1}{2}\iiint_{\mathcal{B}_0} \boldsymbol{\epsilon} : \boldsymbol{\sigma}\, dx\, dy\, dz, \tag{3.28}$$

where $\boldsymbol{\epsilon}$ denotes the Green-Lagrangian strain tensor, $\boldsymbol{\sigma}$ is the second Piola-Kirchhoff stress tensor, and the symbol $:$ represents the double inner product between two tensors.

It is further considered that the beam is made of an isotropic material, such that stress and strain are related by the following constitutive equation (Hooke's law)

$$\boldsymbol{\sigma} = 2\,G\,\boldsymbol{\epsilon} + \lambda\,\mathtt{tr}\,(\boldsymbol{\epsilon})\;\mathbb{I}, \tag{3.29}$$

where $\mathtt{tr}\,(\cdot)$ represents the trace operator, G is material shear modulus, and λ is used to designate the material first Lamé parameter. In terms of the elastic modulus E and the Poisson's ratio ν, these elastic parameters can be written as

$$G = \frac{E}{2\,(1+\nu)}, \qquad \text{and} \qquad \lambda = \frac{E\,\nu}{(1+\nu)(1-2\,\nu)}. \tag{3.30}$$

According to the beam theory used in this work, there is no tension in any cross section of the beam that is perpendicular to the x axis, i.e.,

$$\sigma_{yy} = \sigma_{zz} = \sigma_{yz} = \sigma_{zy} = 0. \tag{3.31}$$

Thus, when the hypothesis expressed by (3.31) is combined with the three-dimensional Hook's law represented by the Eq.(3.29), one can conclude

$$\sigma_{xx} = E\,\epsilon_{xx},\;\; \sigma_{xy} = 2\,G\,\epsilon_{xy},\;\; \sigma_{xz} = 2\,G\,\epsilon_{xz}, \tag{3.32}$$

which is an one-dimensional version of the Hook's law.

Combining the one-dimensional Hooke's law given by (3.32), with the symmetry of the stress tensor, one can express the double contraction between strain and stress tensors, within the integral in Eq.(3.28), as a quadratic form

$$\boldsymbol{\epsilon} : \boldsymbol{\sigma} = E\,\epsilon_{xx}^2 + 4\,G\,\epsilon_{xy}^2 + 4\,G\,\epsilon_{xz}^2, \tag{3.33}$$

which is modified, by the introduction of the shearing factor κ_s, as

$$\boldsymbol{\epsilon} : \boldsymbol{\sigma} = E\,\epsilon_{xx}^2 + 4\,\kappa_s\,G\,\epsilon_{xy}^2 + 4\,\kappa_s\,G\,\epsilon_{xz}^2. \tag{3.34}$$

This modification aims to take into account the effect of shear deformation in the beam cross section area, which is neglected when one uses the relations expressed by the Eq.(3.32).

Hence, after replace Eq.(3.34) in Eq.(3.28), one finally obtains

$$\mathcal{V} = \frac{1}{2}\iiint_{\mathcal{B}_0} \left(E\,\epsilon_{xx}^2 + 4\,\kappa_s\,G\,\epsilon_{xy}^2 + 4\,\kappa_s\,G\,\epsilon_{xz}^2\right)\,dx\,dy\,dz. \tag{3.35}$$

As the analysis is using large displacements, one has

$$\epsilon_{xx} = \frac{1}{2}\left(\frac{\partial u_x}{\partial x} + \frac{\partial u_x}{\partial x}\right) + \frac{1}{2}\left(\frac{\partial u_x}{\partial x}\frac{\partial u_x}{\partial x} + \frac{\partial u_y}{\partial x}\frac{\partial u_y}{\partial x} + \frac{\partial u_z}{\partial x}\frac{\partial u_z}{\partial x}\right), \tag{3.36}$$

$$\epsilon_{xy} = \frac{1}{2}\left(\frac{\partial u_y}{\partial x} + \frac{\partial u_x}{\partial y}\right) + \frac{1}{2}\left(\frac{\partial u_x}{\partial x}\frac{\partial u_x}{\partial y} + \frac{\partial u_y}{\partial x}\frac{\partial u_y}{\partial y} + \frac{\partial u_z}{\partial x}\frac{\partial u_z}{\partial y}\right), \tag{3.37}$$

and

$$\epsilon_{xz} = \frac{1}{2}\left(\frac{\partial u_z}{\partial x} + \frac{\partial u_x}{\partial z}\right) + \frac{1}{2}\left(\frac{\partial u_x}{\partial x}\frac{\partial u_x}{\partial z} + \frac{\partial u_y}{\partial x}\frac{\partial u_y}{\partial z} + \frac{\partial u_z}{\partial x}\frac{\partial u_z}{\partial z}\right), \tag{3.38}$$

where the quadratic terms on the right hand side of the above equations are associated to the geometric nonlinearity of the beam model.

Substituting the kinematic hypothesis of the Eq.(3.16) in Eqs.(3.36) to (3.38), and then calculating the partial derivatives, one concludes that the deformations are respectively given by

$$\begin{aligned} \epsilon_{xx} \;=\; & u' - y\,\theta'_z + z\,\theta'_y + u'\left(z\,\theta'_y - y\,\theta'_z\right) - y\,z\,\theta'_y\,\theta'_z \;+ \\ & \theta'_x\left(\left(y\,w' - z\,v'\right)\cos\theta_x - \left(y\,v' + z\,w'\right)\sin\theta_x\right) \;+ \\ & \frac{1}{2}\left(u'^2 + v'^2 + w'^2 + y^2\,\theta'^2_z + z^2\,\theta'^2_y + \left(y^2 + z^2\right)\theta'^2_x\right), \end{aligned} \tag{3.39}$$

$$\begin{aligned} \epsilon_{xy} \;=\; & \frac{1}{2}\left(v'\,\cos\theta_x + w'\sin\theta_x - z\,\theta'_x\right) \;+ \\ & \frac{1}{2}\,\theta_z\left(y\,\theta'_z - z\theta'_y - u' - 1\right), \end{aligned} \tag{3.40}$$

and

$$\begin{aligned} \epsilon_{xz} \;=\; & \frac{1}{2}\left(w'\,\cos\theta_x - v'\sin\theta_x + y\,\theta'_x\right) \;+ \\ & \frac{1}{2}\,\theta_y\left(-y\,\theta'_z + z\theta'_y + u' + 1\right), \end{aligned} \tag{3.41}$$

where $'$ is used as an abbreviation for space derivative.

3.1.7
Energy dissipation function

It is assumed that the beam under analysis loses energy through a mechanism of viscous dissipation, with a damping constant c. In this way, there is an energy dissipation function (per unit of length) associated to the system, which is given by

$$\begin{aligned} \mathcal{D} \;\; = \;\; & \frac{1}{2}\iint_{\mathcal{S}_0} c\,\rho\,\mathbf{v}\cdot\mathbf{v}\,dy\,dz \;\; + \\ & \frac{1}{2}\iint_{\mathcal{S}_0} c\,\rho\,\dot{\boldsymbol{\theta}}\cdot(\boldsymbol{r}\cdot\boldsymbol{r}\,\mathbb{I}-\boldsymbol{r}\otimes\boldsymbol{r})\,\dot{\boldsymbol{\theta}}\,dy\,dz, \end{aligned} \tag{3.42}$$

where the first term is a dissipation potential due to the translational movement, and the second term represents a dissipation potential due to the movement of rotation.

Making a development almost similar to the one performed to obtain Eq.(3.27), it can be shown that

$$\begin{aligned} \mathcal{D} \;\; = \;\; & \frac{1}{2}\,c\,\rho\,A\left(\dot{u}^2+\dot{v}^2+\dot{w}^2\right) \;\; + \\ & \frac{1}{2}\,c\,\rho\,I_4\left(2\,\dot{\theta}_x^2+\dot{\theta}_y^2+\dot{\theta}_z^2\right). \end{aligned} \tag{3.43}$$

3.1.8
External forces work

The work done by the external forces acting on the beam is given by

$$\mathcal{W} = -\iiint_{\mathcal{B}_0} \rho\,g\,w\,dx\,dy\,dz \;\; + \;\; \mathcal{W}_{\text{FS}} \;\; + \;\; \mathcal{W}_{\text{BR}}, \tag{3.44}$$

where the first term is due to the gravity, the second one is associated to the effects of friction and shock, and the last term accounts the work done by the force/torque that comes from the bit-rock interaction.

One can show that Eq.(3.44) is equivalent to

$$\mathcal{W} = -\int_{x=0}^{L} \rho\,g\,A\,w\,dx \;\; + \;\; \mathcal{W}_{\text{FS}} \;\; + \;\; \mathcal{W}_{\text{BR}}. \tag{3.45}$$

Note that, due to the non-holonomic nature (Lanczos, 1986) [100] of the forces and torques that comes from the effects of friction/shock, and bit-rock interaction, it is not possible to write explicit formulas for $\mathcal{W}_{\text{FS}}$ and $\mathcal{W}_{\text{FS}}$.

However, it is known that the virtual work of $\mathcal{W}_{\text{FS}}$, denoted by $\delta\mathcal{W}_{\text{FS}}$, is written as

$$\delta\mathcal{W}_{\text{FS}} = \sum_{m=1}^{N_{nodes}} \left(F^a_{\text{FS}}\,\delta u + F^n_{\text{FS}}\,(v\,\delta v + w\,\delta w)/r + T_{\text{FS}}\,\delta\theta_x \right)\Big|_{x=x_m}, \quad (3.46)$$

where x_m are the global coordinates of the finite element nodes, N_{nodes} is the number of nodes in the finite element mesh, and δu, δv, δw, and $\delta\theta_x$ respectively denote the variations of the fields u, v, w, and θ_x.

On the other hand, the virtual work of $\mathcal{W}_{\text{BR}}$, denoted by $\delta\mathcal{W}_{\text{BR}}$, reads as

$$\delta\mathcal{W}_{\text{BR}} = F_{\text{BR}}\,\delta u\Big|_{x=L} + T_{\text{BR}}\,\delta\theta_x\Big|_{x=L}. \quad (3.47)$$

3.2 Mathematical model for the problem

The mathematical modeling of the problem includes the derivation of the equation which describes the nonlinear dynamics of the mechanical system under study, the description of a linear conservative problem associated to the nonlinear one, and the definition of the initial conditions which the mechanical system is subjected.

3.2.1 Equation of motion of the nonlinear dynamics

The extended Hamilton's principle is employed to derive the equations which describe the nonlinear dynamics of the mechanical system under analysis. This variational principle of mechanics (Lanczos, 1986) [100] states that, among all the available paths between the configurations observed at the instants t_0 and t_f, the mechanical system of interest follows the path which minimizes the action

$$\mathcal{A} = \int_{t=t_0}^{t_f} (\mathcal{T} - \mathcal{V} + \mathcal{W})\,dt. \quad (3.48)$$

A necessary condition for minimization of the functional $\mathcal{A}$ is that its Gâteaux derivative (Sagan, 1992) [101], also called first variation, be equal to zero, i.e.

$$\delta\mathcal{A} = 0, \quad (3.49)$$

which, by using the properties of the variation operator δ, is equivalent to

$$\int_{t=t_0}^{t_f} (\delta\mathcal{T} - \delta\mathcal{V} + \delta\mathcal{W})\,dt = 0. \quad (3.50)$$

In order to include the damping effects into the system dynamics, it is necessary to rewrite the last equation as follows

$$\int_{t=t_0}^{t_f} (\delta\mathcal{T} - \delta\mathcal{V} + \delta\mathcal{W})\, dt - \int_{t=t_0}^{t_f}\int_{x=0}^{L} \delta\boldsymbol{U} \cdot \frac{\partial\mathcal{D}}{\partial\dot{\boldsymbol{U}}}\, dx\, dt = 0, \tag{3.51}$$

where the first term corresponds to the conservative part of the dynamics, and the second one is associated to the energy dissipation. In this equation, $\boldsymbol{U} = \left(u, v, w, \theta_x, \theta_y, \theta_z\right)$ is a vector field which lumps the field variables.

The development which follows is presented in detail in the Appendix A, and results in the following weak equation of motion

$$\mathcal{M}\left(\boldsymbol{\psi}, \ddot{\boldsymbol{U}}\right) + \mathcal{C}\left(\boldsymbol{\psi}, \dot{\boldsymbol{U}}\right) + \mathcal{K}\left(\boldsymbol{\psi}, \boldsymbol{U}\right) = \mathcal{F}\left(\boldsymbol{\psi}, \boldsymbol{U}, \dot{\boldsymbol{U}}, \ddot{\boldsymbol{U}}\right), \tag{3.52}$$

valid for any $\boldsymbol{\psi}$ chosen in a "suitable" space of weight functions. In this equation, $\mathcal{M}$ represents the mass operator, $\mathcal{C}$ is the damping operator, $\mathcal{K}$ is the stiffness operator, and $\mathcal{F}$ is the force operator. Also, the field variables weight functions are represented by the lumped vector $\boldsymbol{\psi} = \left(\psi_u, \psi_v, \psi_w, \psi_{\theta_x}, \psi_{\theta_y}, \psi_{\theta_z}\right)$.

The mass operators is written as

$$\begin{aligned} \mathcal{M}\left(\boldsymbol{\psi}, \ddot{\boldsymbol{U}}\right) \;=\; & \int_{x=0}^{L} \rho\, A \left(\psi_u\, \ddot{u} + \psi_v\, \ddot{v} + \psi_w\, \ddot{w}\right) dx \;+ \\ & \int_{x=0}^{L} \rho\, I_4 \left(2\,\psi_{\theta_x}\, \ddot{\theta}_x + \psi_{\theta_y}\, \ddot{\theta}_y + \psi_{\theta_z}\, \ddot{\theta}_z\right) dx, \end{aligned} \tag{3.53}$$

where the first integral is a term associated to the translational inertia, and the second one is related to the rotational inertia.

Similarly, the damping operator is defined as

$$\begin{aligned} \mathcal{C}\left(\boldsymbol{\psi}, \dot{\boldsymbol{U}}\right) \;=\; & \int_{x=0}^{L} c\,\rho\, A \left(\psi_u\, \dot{u} + \psi_v\, \dot{v} + \psi_w\, \dot{w}\right) dx \;+ \\ & \int_{x=0}^{L} c\,\rho\, I_4 \left(2\,\psi_{\theta_x}\, \dot{\theta}_x + \psi_{\theta_y}\, \dot{\theta}_y + \psi_{\theta_z}\, \dot{\theta}_z\right) dx, \end{aligned} \tag{3.54}$$

where the first term represents a dissipation mechanism that comes from the translational motion, and the second one is related with the movement of rotation.

The operator of stiffness read as

$$\begin{aligned}\mathcal{K}\left(\boldsymbol{\psi},\boldsymbol{U}\right) &= \int_{x=0}^{L} E\,A\,\psi'_u\,u'\,dx \;+ \\ &\int_{x=0}^{L} E\,I_4\left(\psi'_{\theta_y}\,\theta'_y+\psi'_{\theta_z}\,\theta'_z\right)dx \;+ \\ &\int_{x=0}^{L} 2\,\kappa_s\,G\,I_4\,\psi'_{\theta_x}\,\theta'_x\,dx \;+ \\ &\int_{x=0}^{L} \kappa_s\,G\,A\left(\left(\psi_{\theta_y}+\psi'_w\right)\left(\theta_y+w'\right)+\left(\psi_{\theta_z}-\psi'_v\right)\left(\theta_z-v'\right)\right)dx,\end{aligned} \tag{3.55}$$

where the first integral represents the axial stiffness, the second one is associated with the flexural stiffness, the third is related to the torsional stiffness, and the fourth is linked to the shear stiffness.

In the case of the force, the operator is divided into five parts

$$\begin{aligned}\mathcal{F}\left(\boldsymbol{\psi},\boldsymbol{U},\dot{\boldsymbol{U}},\ddot{\boldsymbol{U}}\right) &= \mathcal{F}_{\mathrm{G}}\left(\boldsymbol{\psi}\right)+\mathcal{F}_{\mathrm{FS}}\left(\boldsymbol{\psi},\boldsymbol{U}\right)+\mathcal{F}_{\mathrm{BR}}\left(\boldsymbol{\psi},\dot{\boldsymbol{U}}\right)+ \\ &\quad \mathcal{F}_{\mathrm{KE}}\left(\boldsymbol{\psi},\boldsymbol{U},\dot{\boldsymbol{U}},\ddot{\boldsymbol{U}}\right)+\mathcal{F}_{\mathrm{SE}}\left(\boldsymbol{\psi},\boldsymbol{U}\right),\end{aligned} \tag{3.56}$$

where the linear force

$$\mathcal{F}_{\mathrm{G}}\left(\boldsymbol{\psi}\right)=-\int_{x=0}^{L}\rho\,g\,A\,\psi_w\,dx, \tag{3.57}$$

is due to the gravity,

$$\mathcal{F}_{\mathrm{FS}}\left(\boldsymbol{\psi},\boldsymbol{U}\right) = \sum_{m=1}^{N_{nodes}}\left(F^a_{\mathrm{FS}}\,\psi_u+F^n_{\mathrm{FS}}\left(v\,\psi_v+w\,\psi_w\right)/r+T_{\mathrm{FS}}\,\psi_{\theta_x}\right)\Big|_{x=x_m} \tag{3.58}$$

is due to the nonlinear effects of friction and shock,

$$\mathcal{F}_{\mathrm{BR}}\left(\boldsymbol{\psi},\dot{\boldsymbol{U}}\right)=F_{\mathrm{BR}}\,\psi_u\Big|_{x=L}+T_{\mathrm{BR}}\,\psi_{\theta_x}\Big|_{x=L}, \tag{3.59}$$

is due to the nonlinear phenomena of bit-rock interaction,

$$\begin{aligned}\mathcal{F}_{\mathrm{KE}}\left(\boldsymbol{\psi},\boldsymbol{U},\dot{\boldsymbol{U}},\ddot{\boldsymbol{U}}\right) &= -\int_{x=0}^{L}2\,\rho\,I_4\,\psi_{\theta_x}\left(\theta_y\,\ddot{\theta}_z+\dot{\theta}_y\,\dot{\theta}_z\right)dx \\ &+\int_{x=0}^{L}2\,\rho\,I_4\,\psi_{\theta_y}\left(\theta_y\,\dot{\theta}_z^2+\dot{\theta}_x\,\dot{\theta}_z\right)dx \\ &-\int_{x=0}^{L}2\,\rho\,I_4\,\psi_{\theta_z}\left(\theta_y\,\ddot{\theta}_x+\theta_y^2\,\ddot{\theta}_z+\dot{\theta}_x\,\dot{\theta}_y+2\,\theta_y\,\dot{\theta}_y\,\dot{\theta}_z\right)dx,\end{aligned} \tag{3.60}$$

is a nonlinear inertial force that comes from the kinetic energy, and

$$\mathcal{F}_{\text{SE}}(\boldsymbol{\psi}, \boldsymbol{U}) = \int_{x=0}^{L} \left(\psi_{\theta_x}\Gamma_1 + \psi_{\theta_y}\Gamma_2 + \psi_{\theta_z}\Gamma_3\right) dx + \int_{x=0}^{L} \left(\psi'_u\Gamma_4 + \psi'_v\Gamma_5 + \psi'_w\Gamma_6 + \psi'_{\theta_x}\Gamma_7 + \psi'_{\theta_y}\Gamma_8 + \psi'_{\theta_z}\Gamma_9\right) dx, \tag{3.61}$$

is a force associated to the geometric nonlinearity, and comes from the strain energy. The nonlinear functions Γ_n, with $n = 1, \cdots, 9$, are very complex and, for sake of brevity, are not presented in this chapter. But they can be seen in the Appendix A.

Is worth noting that the nonlinear coupling between the axial, flexural and torsional mechanisms of vibration in the beam model is carried out by the inertial force $\mathcal{F}_{\text{KE}}$, and the geometric force $\mathcal{F}_{\text{SE}}$.

3.2.2 Initial conditions

With regard to the initial state of the mechanical system, it is assumed that the beam presents neither displacement nor rotations, i.e.,

$$u(x,0) = v(x,0) = w(x,0) = \theta_x(x,0) = \theta_y(x,0) = \theta_z(x,0) = 0. \tag{3.62}$$

The field variables that appear in the Eq.(3.62), except for u and θ_x, also have initial velocities and rate of rotations equal to zero. So one can write

$$\dot{v}(x,0) = \dot{w}(x,0) = \dot{\theta}_y(x,0) = \dot{\theta}_z(x,0) = 0. \tag{3.63}$$

It is also assumed that, initially, the beam moves horizontally with a constant axial velocity V_0, and rotates around the x axis with a constant angular velocity Ω. Thereby, one has that

$$\dot{u}(x,0) = V_0, \tag{3.64}$$

and

$$\dot{\theta}_x(x,0) = \Omega. \tag{3.65}$$

Projecting the Eqs.(3.62) to (3.65) in the space of weight functions one obtains the weak forms of the initial conditions, respectively, given by

$$\mathcal{M}\left(\boldsymbol{\psi}, \boldsymbol{U}(0)\right) = \mathcal{M}\left(\boldsymbol{\psi}, \boldsymbol{U}_0\right), \tag{3.66}$$

and

$$\mathcal{M}\left(\boldsymbol{\psi}, \dot{\boldsymbol{U}}(0)\right) = \mathcal{M}\left(\boldsymbol{\psi}, \dot{\boldsymbol{U}}_0\right), \tag{3.67}$$

where $\boldsymbol{U}_0 = (0,0,0,0,0,0)$ and $\dot{\boldsymbol{U}}_0 = (V_0, 0, 0, \Omega, 0, 0)$.

In formal terms, the weak formulation of the initial/boundary value problem (Hughes, 2000) [102], that describes the nonlinear dynamics of the mechanical system, consists in find a vector field $\boldsymbol{U}$, "sufficiently regular", which satisfies the weak equation of motion given by Eq.(3.52) for all "suitable" $\boldsymbol{\psi}$, as well as the weak form of the initial conditions, given by Eqs.(3.66), and (3.67).

3.2.3
Linear conservative dynamics associated

For all functions $\boldsymbol{\psi}$ in the space of weight functions, consider the linear homogeneous equation given by

$$\mathcal{M}\left(\boldsymbol{\psi}, \ddot{\boldsymbol{U}}\right) + \mathcal{K}\left(\boldsymbol{\psi}, \boldsymbol{U}\right) = 0, \tag{3.68}$$

obtained from Eq.(3.52) when one discards the damping, and the force operators.

Suppose that Eq.(3.68) has a solution of the form $\boldsymbol{U} = e^{i\omega t}\boldsymbol{\phi}$, where ω is a natural frequency (in rad/s), $\boldsymbol{\phi}$ is the associated normal mode, and $i = \sqrt{-1}$ is the imaginary unit. Replacing the expression of $\boldsymbol{U}$ above in the Eq.(3.68) and using the linearity of the operators $\mathcal{M}$, and $\mathcal{K}$, and dividing by $e^{i\omega t}$ one gets

$$-\omega^2 \mathcal{M}\left(\boldsymbol{\psi}, \boldsymbol{\phi}\right) + \mathcal{K}\left(\boldsymbol{\psi}, \boldsymbol{\phi}\right) = 0, \tag{3.69}$$

a generalized eigenvalue problem (GEP).

Since the operator $\mathcal{M}$ is positive definite, and the operator $\mathcal{K}$ is positive semi-definite, the GEP above has a denumerable number of solutions. The solutions of this eigenproblem are of the form $(\omega_n^2, \boldsymbol{\phi}_n)$, where ω_n is the n-th natural frequency and $\boldsymbol{\phi}_n$ is the n-th unitary normal mode (Hagedorn and DasGupta, 2007) [103].

Also, it should be noted that the symmetry of the operators $\mathcal{M}$, and $\mathcal{K}$ implies the following orthogonality relations

$$\mathcal{M}\left(\boldsymbol{\phi}_n, \boldsymbol{\phi}_m\right) = \delta_{nm}, \qquad \text{and} \qquad \mathcal{K}\left(\boldsymbol{\phi}_n, \boldsymbol{\phi}_m\right) = \omega_n^2\, \delta_{nm}, \tag{3.70}$$

where δ_{nm} represents the Kronecker delta symbol. For more details the reader can see Hagedorn and DasGupta (2007) [103].

3.3
Computational model for the problem

The computational modeling include the procedure of discretization of the nonlinear equations that describe the dynamics of the mechanical system, as well as a procedure to reduce the model dimension, in order to make it computationally efficient. It also includes the numerical integration of

the reduced dynamical system, the incorporation of the geometric boundary conditions of the physical problem into the formulation, and the numerical solution of the system of algebraic equations that arises from the discretization in space and time.

3.3.1 Discretization of the nonlinear dynamics

To proceed with the discretization of the initial/boundary value problem which describes the nonlinear dynamics beam, whose the weak formulation is given by Eqs.(3.52), (3.66), and (3.67), it is used the standard finite element method (FEM) [102], where the spaces of basis and weight functions are constructed by the same (finite dimensional) class of functions.

In this procedure, the beam geometry is discretized by a FEM mesh with N_{elem} finite elements. Each one of these elements is composed by two nodes, and each one of these nodes has six degrees of freedom associated, one for each field variable in the beam model described in the section 3.2.1. Thus, the number of degrees of freedom associated with the FEM model is $N_{dofs} = 6(N_{elem} + 1)$. An illustration of the FEM mesh/element can be seen in the Figure 3.8.

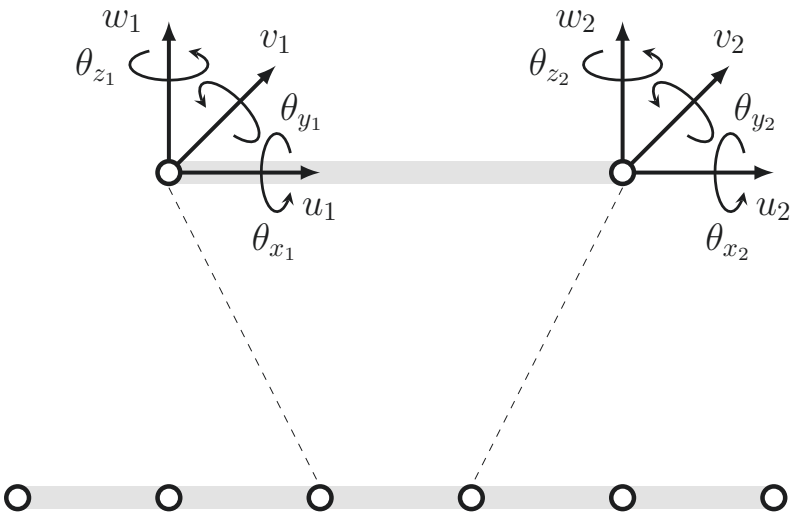

Figure 3.8: Illustration of the FEM mesh/element used to discretize the beam geometry.

Concerning the shape functions, it is adopted an interdependent interpolation scheme which avoids the shear-locking effect (Reddy, 1997) [104]. This scheme uses, for the transverse displacements/rotations, Hermite cubic polynomials, and, for the fields of axial displacement/torsional rotation, affine functions. These shape functions are presented in the Appendix B, and further details can be seen in Bazoune et al. (2003) [105] and Luo (2008) [106].

Thus, each field variable of the physical model is approximated by a linear combination of basis functions, in such way that

$$
\begin{aligned}
u(x,t) &\approx \sum_{m=1}^{N_{dofs}} Q_m(t)\,\mathcal{N}_m(x), \qquad & \theta_x(x,t) &\approx \sum_{m=1}^{N_{dofs}} Q_m(t)\,\mathcal{N}_m(x), \\
v(x,t) &\approx \sum_{m=1}^{N_{dofs}} Q_m(t)\,\mathcal{H}_m^{(1)}(x), \qquad & w(x,t) &\approx \sum_{m=1}^{N_{dofs}} Q_m(t)\,\mathcal{H}_m^{(1)}(x), \\
\theta_y(x,t) &\approx \sum_{m=1}^{N_{dofs}} Q_m(t)\,\mathcal{H}_m^{(2)}(x), \qquad & \theta_z(x,t) &\approx \sum_{m=1}^{N_{dofs}} Q_m(t)\,\mathcal{H}_m^{(2)}(x),
\end{aligned}
\tag{3.71}
$$

where $\mathcal{N}_m(x)$, $\mathcal{H}_m^{(1)}(x)$, and $\mathcal{H}_m^{(2)}(x)$ are the (position dependent) shape functions, and the (time dependent) coefficients of the linear combination, $Q_m(t)$, are the unknowns of the discretized problem. In physical terms, each one of these temporal coefficients represents a degree of freedom of the FEM model.

The result of the discretization is the following $N_{dofs} \times N_{dofs}$ nonlinear system of ordinary differential equations

$$
[\mathcal{M}]\,\ddot{\boldsymbol{Q}}(t) + [\mathcal{C}]\,\dot{\boldsymbol{Q}}(t) + [\mathcal{K}]\,\boldsymbol{Q}(t) = \boldsymbol{\mathcal{F}}\left(\boldsymbol{Q}(t), \dot{\boldsymbol{Q}}(t), \ddot{\boldsymbol{Q}}(t)\right), \tag{3.72}
$$

where $\boldsymbol{Q}(t)$ is the nodal displacement vector (translations and rotations), $\dot{\boldsymbol{Q}}(t)$ is the nodal velocity vector, and $\ddot{\boldsymbol{Q}}(t)$ is the nodal acceleration vector. The other objects in the Eq.(3.72) are the mass matrix $[\mathcal{M}]$, the damping matrix $[\mathcal{C}]$, the stiffness matrix $[\mathcal{K}]$, and the force vector $\boldsymbol{\mathcal{F}}$.

A discretization procedure similar to one presented above is applied to the initial conditions of Eqs.(3.66) and (3.67), which results in linear systems of algebraic equations given by

$$
[\mathcal{M}]\,\boldsymbol{Q}(0) = \boldsymbol{Q}_0, \qquad \text{and} \qquad [\mathcal{M}]\,\dot{\boldsymbol{Q}}(0) = \dot{\boldsymbol{Q}}_0. \tag{3.73}
$$

Note that the solution of the initial value problem (IVP), defined by differential equation of the Eq.(3.72) and the initial conditions of the Eq.(3.73), gives a finite dimensional approximation to the solution of the initial/boundary value problem of Eqs.(3.52), (3.66), and (3.67). In a sense intrinsic to the FEM, this approximation is optimal (Hughes, 2000) [102].

3.3.2
Reduction of the finite element model

In order to reduce the dimension of the finite element model developed in the section 3.3.1, it is considered a finite dimensional version of the GEP

presented in section 3.2.3, which is defined by

$$[\mathcal{K}]\,\boldsymbol{\phi}_n = \omega_n^2\,[\mathcal{M}]\,\boldsymbol{\phi}_n. \tag{3.74}$$

As a consequence of the properties of the operators $\mathcal{M}$, and $\mathcal{K}$ discussed in section 3.2.3, that are inherited by the finite dimensional operators $[\mathcal{M}]$ and $[\mathcal{K}]$, the above GEP has N_{dofs} solutions. But the Eq.(3.74) is solved only for $n = 1, 2, \cdots, N_{red}$, where the dimension of the reduced model N_{red} is an integer chosen such that $N_{red} \ll N_{dofs}$.

The procedure that follows consists in project the nonlinear dynamic, defined by the IVP of Eqs.(3.72) and (3.73), into the vector space spanned by $\{\boldsymbol{\phi}_1, \boldsymbol{\phi}_2, \cdots, \boldsymbol{\phi}_{N_{red}}\}$.

For this purpose, define the $N_{dofs} \times N_{red}$ projection matrix by

$$[\Phi] = \begin{bmatrix} | & | & & | \\ \boldsymbol{\phi}_1 & \boldsymbol{\phi}_2 & \cdots & \boldsymbol{\phi}_{N_{red}} \\ | & | & & | \end{bmatrix}, \tag{3.75}$$

make in the Eqs.(3.72) and (3.73) the change of basis defined by

$$\boldsymbol{Q}(t) = [\Phi]\,\boldsymbol{q}(t), \tag{3.76}$$

and then pre-multiply the resulting equations by the matrix $[\Phi]^T$, where the superscript ^{T} represents the transposition operation.

This development results in the reduced IVP given by

$$[M]\,\ddot{\boldsymbol{q}}(t) + [C]\,\dot{\boldsymbol{q}}(t) + [K]\,\boldsymbol{q}(t) = \boldsymbol{f}\left(\boldsymbol{q}(t), \dot{\boldsymbol{q}}(t), \ddot{\boldsymbol{q}}(t)\right), \tag{3.77}$$

and

$$\boldsymbol{q}(0) = \boldsymbol{q}_0, \qquad \text{and} \qquad \dot{\boldsymbol{q}}(0) = \dot{\boldsymbol{q}}_0, \tag{3.78}$$

where $\boldsymbol{q}(t)$ is the reduced nodal displacement vector, $\dot{\boldsymbol{q}}(t)$ is the reduced nodal velocity vector, $\ddot{\boldsymbol{q}}(t)$ is the reduced nodal acceleration vector. The reduced matrices of mass, damping, and stiffness, as well as the reduced vectors of force, initial displacement, and initial velocity are, respectively, defined by $[M] = [\Phi]^T\,[\mathcal{M}]\,[\Phi]$, $[C] = [\Phi]^T\,[\mathcal{C}]\,[\Phi]$, $[K] = [\Phi]^T\,[\mathcal{K}]\,[\Phi]$, $\boldsymbol{f} = [\Phi]^T\,\boldsymbol{\mathcal{F}}\left([\Phi]\,\boldsymbol{q}(t), [\Phi]\,\dot{\boldsymbol{q}}(t), [\Phi]\,\ddot{\boldsymbol{q}}(t)\right)$, $\boldsymbol{q}_0 = [\Phi]^T\,\boldsymbol{Q}_0$, $\dot{\boldsymbol{q}}_0 = [\Phi]^T\,\dot{\boldsymbol{Q}}_0$. These matrices are $N_{red} \times N_{red}$, while these vectors are $N_{red} \times 1$. Furthermore, due to the orthogonality properties defined by Eq.(3.70), that are inherited by the operators in finite dimension, these matrices are diagonal.

Thus, although the IVP of Eqs.(3.77) and (3.78) is apparently similar to the one defined by Eqs.(3.72) and (3.73), the former has a structure that makes it much more efficient in terms of computational cost, and so, it will be used to analyze the nonlinear dynamics under study.

3.3.3
Integration of the discretized nonlinear dynamics

In order to solve the IVP of Eqs.(3.77) and (3.78), it is employed the Newmark method (Newmark, 1959) [107], which defines the following implicit integration scheme

$$\dot{\boldsymbol{q}}_{n+1} = \dot{\boldsymbol{q}}_n + (1-\gamma)\Delta t\, \ddot{\boldsymbol{q}}_n + \gamma \Delta t\, \ddot{\boldsymbol{q}}_{n+1}, \tag{3.79}$$

$$\boldsymbol{q}_{n+1} = \boldsymbol{q}_n + \Delta t\, \dot{\boldsymbol{q}}_n + \left(\frac{1}{2} - \beta\right) \Delta t^2\, \ddot{\boldsymbol{q}}_n + \beta\, \Delta t^2\, \ddot{\boldsymbol{q}}_{n+1}, \tag{3.80}$$

where $\boldsymbol{q}_n$, $\dot{\boldsymbol{q}}_n$ and $\ddot{\boldsymbol{q}}_n$ are approximations to $\boldsymbol{q}(t_n)$, $\dot{\boldsymbol{q}}(t_n)$ and $\ddot{\boldsymbol{q}}(t_n)$, respectively, and $t_n = n\Delta t$ is an instant in a temporal mesh defined over the interval $[t_0, t_f]$, with an uniform time step Δt. This integration scheme was chosen because it is well suited to structural dynamics problems, and due to its simplicity in terms of implementation.

The parameters γ and β are associated with the accuracy and stability of the numerical scheme, in such a way that the method is unconditionally stable if the parameters respect

$$\gamma \geq \frac{1}{2}, \qquad \text{and} \qquad \beta \geq \frac{1}{4}\left(\gamma + \frac{1}{2}\right)^2. \tag{3.81}$$

If $\gamma = 1/2$ the method is stable and there is no damping of the high frequencies introduced in the system dynamics by the discretization of the model equations. Conversely, if $\gamma > 1/2$, then the high frequencies in the system response are damped. For instance, the simulations reported in this work use $\gamma = 1/2 + \alpha$, and $\beta = 1/4$, with $\alpha = 15/1000$, for which Newmark method is $\mathcal{O}(\Delta t)$. Further details about the convergence and stability of the Newmark method, can be seen in Hughes (2000) [102].

Handling up properly the Eqs.(3.79) and (3.80) one concludes that

$$\ddot{\boldsymbol{q}}_{n+1} = \frac{1}{\beta \Delta t^2}\left(\boldsymbol{q}_{n+1} - \boldsymbol{q}_n\right) - \frac{1}{\beta \Delta t}\dot{\boldsymbol{q}}_n - \frac{1}{2}\left(\frac{1}{\beta} - 2\right)\ddot{\boldsymbol{q}}_n, \tag{3.82}$$

and

$$\dot{\boldsymbol{q}}_{n+1} = \frac{\gamma}{\beta \Delta t}\left(\boldsymbol{q}_{n+1} - \boldsymbol{q}_n\right) + \left(1 - \frac{\gamma}{\beta}\right)\dot{\boldsymbol{q}}_n + \left(1 - \frac{\gamma}{2\beta}\right)\Delta t\, \ddot{\boldsymbol{q}}_n. \tag{3.83}$$

After one replaces the Eqs.(3.82) and (3.83) in the discrete version of the Eq.(3.77), which is defined by

$$[M]\, \ddot{\boldsymbol{q}}_{n+1} + [C]\, \dot{\boldsymbol{q}}_{n+1} + [K]\, \boldsymbol{q}_{n+1} = \boldsymbol{f}\left(\boldsymbol{q}_{n+1}, \dot{\boldsymbol{q}}_{n+1}, \ddot{\boldsymbol{q}}_{n+1}\right), \tag{3.84}$$

and does some manipulation, one arrives in the nonlinear system of algebraic equations, with unknown vector $\boldsymbol{q}_{n+1}$, represented by

$$[\hat{K}]\boldsymbol{q}_{n+1} = \hat{\boldsymbol{f}}_{n+1}\left(\boldsymbol{q}_{n+1}\right), \tag{3.85}$$

where the effective stiffness matrix is defined as

$$[\hat{K}] = [K] + \frac{\gamma}{\beta\Delta t}[C] + \frac{1}{\beta\Delta t^2}[M], \tag{3.86}$$

and the effective force vector is written as

$$\begin{aligned}\hat{\boldsymbol{f}}_{n+1}\left(\boldsymbol{q}_{n+1}\right) &= [M]\left(\frac{1}{\beta\Delta t^2}\boldsymbol{q}_n + \frac{1}{\beta\Delta t}\dot{\boldsymbol{q}}_n + \left(\frac{1}{2\beta} - 1\right)\ddot{\boldsymbol{q}}_n\right) + \\ &\quad [C]\left(\frac{\gamma}{\beta\Delta t}\boldsymbol{q}_n + \left(\frac{\gamma}{\beta} - 1\right)\dot{\boldsymbol{q}}_n + \frac{1}{2}\left(\frac{\gamma}{\beta} - 2\right)\Delta t\,\ddot{\boldsymbol{q}}_n\right) + \\ &\quad \boldsymbol{f}\left(\boldsymbol{q}_{n+1}, \dot{\boldsymbol{q}}_{n+1}, \ddot{\boldsymbol{q}}_{n+1}\right).\end{aligned} \tag{3.87}$$

Note that the nonlinearity of the Eq.(3.85) is on the right side, and is due to the force vector $\boldsymbol{f}$.

3.3.4
Incorporation of the boundary conditions

As can be seen in Figure 3.2, the mechanical system has the following boundary conditions: (i) left extreme with no transversal displacement, nor transversal rotation; (ii) right extreme with no transversal displacement. It is also assumed that the left end has has: (iii) constant axial and rotational velocities in x, respectively equal to V_0 and Ω.

Hence, for $x = 0$, it is true that

$$\begin{aligned} u(0,t) &= V_0\, t, \\ v(0,t) &= 0, \\ w(0,t) &= 0, \\ \theta_x(0,t) &= \Omega\, t, \\ \theta_y(0,t) &= 0, \\ \theta_z(0,t) &= 0. \end{aligned} \tag{3.88}$$

On the other hand, for $x = L$, one has

$$\begin{aligned} v(L,t) &= 0, \\ w(L,t) &= 0. \end{aligned} \tag{3.89}$$

The variational formulation presented in section 3.2.1, was made for a free-free beam, so that the above geometric boundary conditions were not included.

The most common way of impose the geometric boundary condition is require that any function in the space of base functions satisfies it, once the solution of the variational problem is sought in this space. However, this strategy is not the most interesting from the computational implementation point of view, because it requires the modification of the matrices and vectors associated to the finite element discretization after the assembly process.

Thus, this work chose to use a strategy, based on the method of Lagrange multipliers, that makes the inclusion of the geometric boundary conditions as constraints which the solution of the variational problem must satisfy (Hughes, 2000) [102]. The details of this procedure are presented below.

Note that the boundary conditions expressed in (3.88) and (3.89) can be rewritten as

$$[\mathscr{B}]\,\boldsymbol{Q}(t) = \boldsymbol{h}(t), \tag{3.90}$$

where the $8 \times N_{dofs}$ constraint matrix is defined as

$$[\mathscr{B}] = \begin{bmatrix} 1 & 0 & 0 & 0 & 0 & 0 & 0 & \cdots & 0 & 0 & 0 & 0 & 0 & 0 \\ 0 & 1 & 0 & 0 & 0 & 0 & 0 & \cdots & 0 & 0 & 0 & 0 & 0 & 0 \\ 0 & 0 & 1 & 0 & 0 & 0 & 0 & \cdots & 0 & 0 & 0 & 0 & 0 & 0 \\ 0 & 0 & 0 & 1 & 0 & 0 & 0 & \cdots & 0 & 0 & 0 & 0 & 0 & 0 \\ 0 & 0 & 0 & 0 & 1 & 0 & 0 & \cdots & 0 & 0 & 0 & 0 & 0 & 0 \\ 0 & 0 & 0 & 0 & 0 & 1 & 0 & \cdots & 0 & 0 & 0 & 0 & 0 & 0 \\ 0 & 0 & 0 & 0 & 0 & 0 & 0 & \cdots & 0 & 1 & 0 & 0 & 0 & 0 \\ 0 & 0 & 0 & 0 & 0 & 0 & 0 & \cdots & 0 & 0 & 1 & 0 & 0 & 0 \end{bmatrix}, \tag{3.91}$$

and the constraint vector is given by

$$\boldsymbol{h}(t) = \begin{pmatrix} u(0,t) \\ v(0,t) \\ w(0,t) \\ \theta_x(0,t) \\ \theta_y(0,t) \\ \theta_z(0,t) \\ v(L,t) \\ w(L,t) \end{pmatrix}. \tag{3.92}$$

Making the change os basis defined by the Eq.(3.76), one can rewrite the Eq.(3.90) as

$$[B]\,\boldsymbol{q}(t) = \boldsymbol{h}(t), \tag{3.93}$$

where the $8 \times N_{red}$ reduced constraint matrix is defined by

$$[B] = [\mathscr{B}]\,[\Phi]\,. \tag{3.94}$$

The discretization of the Eq.(3.93) results in

$$[B]\,\boldsymbol{q}_{n+1} = \boldsymbol{h}_{n+1}, \tag{3.95}$$

where $\boldsymbol{h}_{n+1}$ is an approximation to $\boldsymbol{h}(t_{n+1})$. This equation defines the constraint that must be satisfied by the "approximate solution" of the variational problem.

In what follows it is helpful to think that the Eq.(3.85) comes from the minimization of a energy functional $\boldsymbol{q}_{n+1} \mapsto \mathscr{F}\left(\boldsymbol{q}_{n+1}\right)$, which is the weak form of this nonlinear system of algebraic equations.

Then, one defines the Lagrangian as

$$\mathscr{L}\left(\boldsymbol{q}_{n+1}, \boldsymbol{\lambda}_{n+1}\right) = \mathscr{F}\left(\boldsymbol{q}_{n+1}\right) + \boldsymbol{\lambda}_{n+1}^{T}\left([B]\,\boldsymbol{q}_{n+1} - \boldsymbol{h}_{n+1}\right), \tag{3.96}$$

being the (time-dependent) Lagrange multipliers vector of the form

$$\boldsymbol{\lambda}_{n+1} = \begin{pmatrix} \lambda_1(t_{n+1}) \\ \lambda_2(t_{n+1}) \\ \lambda_3(t_{n+1}) \\ \lambda_4(t_{n+1}) \\ \lambda_5(t_{n+1}) \\ \lambda_6(t_{n+1}) \\ \lambda_7(t_{n+1}) \\ \lambda_8(t_{n+1}) \end{pmatrix}. \tag{3.97}$$

Invoking the condition of stationarity for the Lagrangian one arrives in the following $(N_{red}+8) \times (N_{red}+8)$ system of nonlinear algebraic equations

$$\begin{bmatrix} [\hat{K}] & [B]^T \\ [B] & [0] \end{bmatrix} \begin{pmatrix} \boldsymbol{q}_{n+1} \\ \boldsymbol{\lambda}_{n+1} \end{pmatrix} = \begin{pmatrix} \hat{\boldsymbol{f}}_{n+1} \\ \boldsymbol{h}_{n+1} \end{pmatrix}, \tag{3.98}$$

where $[0]$ is a 8×8 null matrix. The unknowns are $\boldsymbol{q}_{n+1}$ and $\boldsymbol{\lambda}_{n+1}$, and must be solved for each instant of time in the temporal mesh, in order to construct an approximation to the dynamic response of the mechanical system under analysis.

3.3.5
Solution of the nonlinear system of algebraic equations

Before discussing the algorithm used to solve the nonlinear system of Eq.(3.98), it is appropriate to argue about the structure of the matrix on the left hand side of this equation.

Note that the nonzero elements of the matrix $[B]$ are all equal to 1. On the other hand, the elements of the matrix $[\hat{K}]$ are several orders of magnitude greater than unity. This imbalance, in the magnitude of the two matrices elements, implies that the $(N_{red}+8)\times(N_{red}+8)$ extended matrix of the Eq.(3.98) is ill-conditioned (Trefethen and Bau, 1997) [108].

To circumvent this ill-conditioning, Negrut et al. (2009) [109] suggests the introduction of the factor $\kappa = \left(\beta\Delta t^2\right)^{-1}$. This scaling factor is multiplied to both sides of Eq.(3.95), which results, after invoking the stationarity of the Lagrangian, in the following nonlinear system of algebraic equations

$$\begin{bmatrix} [\hat{K}] & \kappa\,[B]^T \\ \kappa\,[B] & [0] \end{bmatrix} \begin{pmatrix} \boldsymbol{q}_{n+1} \\ \boldsymbol{\lambda}_{n+1} \end{pmatrix} = \begin{pmatrix} \hat{\boldsymbol{f}}_{n+1} \\ \kappa\,\boldsymbol{h}_{n+1} \end{pmatrix}, \tag{3.99}$$

which is completely equivalent to the nonlinear system of the Eq.(3.98) from the theoretical point of view, but better suitable for numerical calculations.

In what follows, the first line of Eq.(3.99) is written as

$$\boldsymbol{q}_{n+1} = [\hat{K}]^{-1}\left(\hat{\boldsymbol{f}}_{n+1} - \kappa\,[B]^T\boldsymbol{\lambda}_{n+1}\right), \tag{3.100}$$

which, in combination with the second line, results in

$$[\bar{K}]\,\boldsymbol{\lambda}_{n+1} = \bar{\boldsymbol{f}}_{n+1}, \tag{3.101}$$

where the generalized stiffness matrix is defined as

$$[\bar{K}] = \kappa\,[B]\,[\hat{K}]^{-1}\kappa\,[B]^T, \tag{3.102}$$

and the generalized force vector is given by

$$\bar{\boldsymbol{f}}_{n+1} = \kappa\,[B]\,[\hat{K}]^{-1}\hat{\boldsymbol{f}}_{n+1} - \kappa\,\boldsymbol{h}_{n+1}. \tag{3.103}$$

The nonlinear system of Eq.(3.99) is solved in two steps. First, the vector $\boldsymbol{\lambda}_{n+1}$ is computed from Eq.(3.101), which is solved through a Cholesky decomposition (Golub and Van Loan, 2013) [110]. Then, a procedure of fixed point iteration (Hamming, 1987) [111] is employed to obtain the vector $\boldsymbol{q}_{n+1}$ from the nonlinear system of Eq.(3.100). This iteration procedure is initialized using the previous instant of time as initial guess for the current instant of time, and continues until a convergence criterium is achieved or the maximum number of iteration is executed.

The convergence criterium used is defined by the inequalities

$$\frac{\left\| \boldsymbol{\lambda}_{n+1}^{(k+1)} - \boldsymbol{\lambda}_{n+1}^{(k)} \right\|}{\frac{1}{2}\left\| \boldsymbol{\lambda}_{n+1}^{(k+1)} + \boldsymbol{\lambda}_{n+1}^{(k)} \right\|} < \varepsilon_1, \tag{3.104}$$

and

$$\frac{\left\| \boldsymbol{q}_{n+1}^{(k+1)} - \boldsymbol{q}_{n+1}^{(k)} \right\|}{\frac{1}{2}\left\| \boldsymbol{q}_{n+1}^{(k+1)} + \boldsymbol{q}_{n+1}^{(k)} \right\|} < \varepsilon_2, \tag{3.105}$$

where ε_1 and ε_2 are prescribed tolerances, $^{(k)}$ denotes the index of the iteration, and $\|\cdot\|$ is the standard Euclidean norm of vectors.

It is worthy of mention that convergence problems were observed during the simulations, mainly due to the nonlinearities induced by geometric and friction/shock effects. To circumvent these problems, a successive over-relaxation (SOR) procedure (Young, 2003) [112], with a heuristically chosen SOR parameter ω^{SOR}, was be employed to force the iteration convergence.

3.3.6 MATLAB code

The computational model described in this chapter was implemented in a computer code written in `MATLAB`. In the implementation of this code one has excelled by efficiency from the point of view of time processing and memory use, in order to do the numerical simulations with high performance. A flowchart representation of this computer program is presented in Figure 3.9.

All the matrices in the computational model that are associated with the discretization process by means of the finite element method have sparse structure. Thus, in order to save memory and optimize the calculations made with these matrices, the computer code implementation uses a representation scheme for sparse matrices (Saad, 2003) [113]. Still concerning the finite element matrices, an efficient assembly strategy of the global matrices is employed. This algorithm involves a single loop and uses a triple of arrays (two for the matrices indices and one for the nonzero elements) to construct a matrix sparse representation at once. In this algorithm, the overlapping of local matrices inside the global matrix are treated during the arrays list creation (Davis, 2007) [114].

The finite element matrices are constant, so that they are assembled just once. On the other hand, the forcing vector depends on the current configuration of the system, in way that it must be reassembled in each time step. Thus, in terms of time processing, the most expensive tasks in this computational model is the evaluation, via Gaussian quadrature, of the

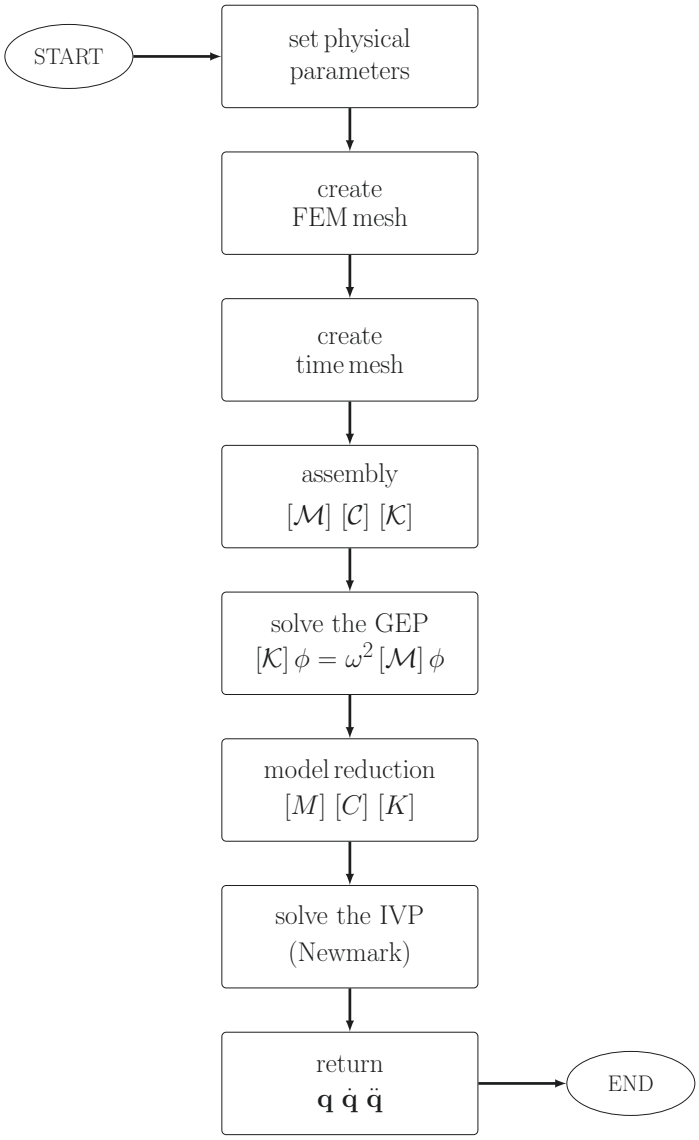

Figure 3.9: Flowchart representation of the computer program that implements the computational model developed in this work.

integral on the forcing vector, due to its highly nonlinear nature. Fortunately, this task can be optimized through the creation of a table that stores the values of the shape functions and their derivatives integrals along the finite element reference domain. As the calculation of the integral in the nonlinear vector uses the tabulated values recurrently, the use of this table allows substantial savings in terms of processing.

3.4 Remarks about the modeling

This thesis is one more work in a series of developments related to drillstring dynamics done by the Dynamics and Vibrations Group of PUC-Rio since 2005.

The first work of the group in this line was developed by Trindade et al. (2005) [61], considering the coupling between longitudinal and flexural vibrations but without regard to the rotation of the column. Followed the work of Sampaio et al. (2007) [54], that took into account the rotation of the column, studying the coupling between torsional and axial vibrations. Finally, a model taking into account the non-linear coupling between the vibrational three mechanisms proposed by Ritto et al. (2009) [69] and Ritto (2010) [70], works which also investigated issues related to uncertainties of the model.

In this thesis, the beam model proposed by Ritto et al. (2009) [69] in the context of vertical drillstrings dynamics is employed with some modifications, to adjust it to a drillstring in horizontal configuration.

First, the new direction of action of gravity is perpendicular to the drillstring axis. Therefore, the former problem is primarily a problem that addresses the dynamics of a column, while the new problem deals with the dynamics of a beam. Also, the original problem treated the nonlinear dynamics around a pre-stressed equilibrium configuration, while the new problem does not consider the dynamics around any particular configuration.

To describe the effect of shock during contact between the column and the borehole wall, Ritto et al. (2009) [69] used a linear spring to emulate the elastic deformation effects. This work added to the model a nonlinear spring to make the description of the elastic deformation more realistic, as well as a nonlinear dashpot, to take into account energy dissipation due to the impact.

With respect to the bit-rock interaction model, this thesis uses different expressions for both, the torque and the force of reaction on the bit, from those used in the reference work (Ritto et al., 2009) [69].

On the other hand, Ritto et al., (2009) [69] took into account the effects of dynamic loading induced by fluid-structure interaction, which that have been neglected in this work for simplicity.

Finally, in this thesis the boundary conditions, besides being different from those considered in Ritto et al. (2009) [69], are included in the problem formulation differently. The method of Lagrange multipliers is used to include then as restrictions, which leads to a mixed finite elements formulation (Hughes, 2000) [102].

4
Probabilistic Modeling of System Uncertanties

This chapter presents the stochastic modeling of the nonlinear dynamics. It begins with a brief discussion about the uncertainties in the mechanical system, by identifying the major source inaccuracy in the model. Then, presents the probabilistic framework and the construction of the stochastic model for the bit-rock interaction law. Finally, it presents the stochastic dynamical system associated with the mechanical system, and the strategy to compute the propagation of uncertainties.

4.1
Uncertainties in the mechanical system

The mechanical system of interest in this thesis has its physical behavior modeled by a set of equations that describe the structure nonlinear dynamics, its coupling with the phenomena of torsional friction, transverse shock, and bit-rock interaction, which the drillstring is subjected. Obviously this mathematical model is an abstraction of reality, and its use does not consider some aspects of the problem physics.

Regarding the modeling of the system, either the beam theory used to describe the structure nonlinear dynamics (Ritto et al., 2009) [69], as the friction and shock model used to describe the drillstring/borehole wall impact phenomenon (Hunt and Crossley, 1975) [97] are fairly established physical models, who have gone through several experimental tests to prove their validity, and have been used for many years in similar situations.

On the other hand, the bit-rock interaction model adopted in this work, until now was used only in a purely numeric context (Ritto et al., 2013) [77], without any experimental validation. Thus, it is natural to conclude that bit-rock interaction law is the weakness of the model proposed in this work.

In this sense, this work will focus on modeling and quantifying the uncertainties that are introduced in the mechanical system by the bit-rock interaction model. For convenience, it was chosen to use the parametric probabilistic approach (Soize, 2012) [12], where only the uncertainties of the model parameters are considered.

4.2 Probabilistic framework

Consider a probability space $(\Theta, \mathbb{\Sigma}, \mathbb{P})$, where Θ is sample space, $\mathbb{\Sigma}$ is a σ-algebra over Θ, and $\mathbb{P}$ is a probability measure. Let $\mathbb{X}$ be a real-valued random variable, defined on $(\Theta, \mathbb{\Sigma}, \mathbb{P})$, for which the probability distribution $P_{\mathbb{X}}(dx)$ on $\mathbb{R}$ admits a density $x \mapsto p_{\mathbb{X}}(x)$ with respect to dx. The support of the probability density function (PDF) $p_{\mathbb{X}}$ will be denoted by $\mathtt{Supp}\,\mathbb{X} \subset \mathbb{R}$, and any realization of random variable $\mathbb{X}$ is denoted by $\mathbb{X}(\theta)$ for $\theta \in \Theta$.

The expected value of $\mathbb{X}$ is defined as

$$\mathbb{E}\left[\mathbb{X}\right] = \int_{\mathtt{Supp}\,\mathbb{X}} x\, p_{\mathbb{X}}(x)\, dx, \tag{4.1}$$

and with the aid of expected value operator one can define some characteristic values of $\mathbb{X}$ which will be used later, such as mean value

$$m_{\mathbb{X}} = \mathbb{E}\left[\mathbb{X}\right], \tag{4.2}$$

variance

$$\sigma^2_{\mathbb{X}} = \mathbb{E}\left[\left(\mathbb{X} - m_{\mathbb{X}}\right)^2\right], \tag{4.3}$$

standard deviation

$$\sigma_{\mathbb{X}} = \sqrt{\sigma^2_{\mathbb{X}}}, \tag{4.4}$$

and the Shannon entropy of $p_{\mathbb{X}}$

$$\mathrm{S}\left(p_{\mathbb{X}}\right) = -\mathbb{E}\left[\ln p_{\mathbb{X}}(\mathbb{X})\right]. \tag{4.5}$$

In order to obtain a consistent stochastic model, one cannot arbitrarily choose the probability distribution of a random parameters, under the penalty of violating some physical principle and/or obtain an inconsistent mathematical model. It is a consensus that all information available about these parameters must be taken into account before define their distributions, i.e., specify their PDFs (Soize, 2012) [12].

The work of Soize (2000) [23] suggests the use of the *maximum entropy principle* to obtain a desired PDF. This axiom of Bayesian probability, introduced by Jaynes (1957) [115, 116], allows one to construct a coherent probability distribution in situations where little information of the random parameters are available, through the use of a function (entropy) that measures the level of uncertainty of a random parameter (Shannon, 1948) [117]. The principle can be formulated as follows:

Among all the probability distributions, consistent with the current known information of a given random parameter, the one which best represents your knowledge about this random parameter is the one which maximizes its entropy.

The idea is to choose, over all the PDFs consistent with the information that one has about the random parameter, the distribution most uninformative which is possible (the maximum entropy distribution). One can not choose a distribution with higher entropy because this would violate the constraints imposed by the known information. Conversely, choose a distribution with lower entropy involves assume information about the random parameter which are not known. Thereby, the distribution that maximizes the entropy becomes the only reasonable choice.

4.3 Probabilistic model for the bit-rock interface law

Recalling that the bit-rock interaction force and torque used in this work are respectively given by

$$F_{\mathrm{BR}} = \begin{cases} \Gamma_{\mathrm{BR}} \left(e^{-\alpha_{\mathrm{BR}} \dot{u}_{bit}} - 1 \right) & \text{for } \dot{u}_{bit} > 0, \\ 0 & \text{for } \dot{u}_{bit} \leq 0, \end{cases} \tag{4.6}$$

and

$$T_{\mathrm{BR}} = -\mu_{\mathrm{BR}} \, F_{\mathrm{BR}} \, R_{bh} \, \xi_{\mathrm{BR}} \left(\omega_{bit} \right), \tag{4.7}$$

the reader can see that this bit-rock interface law is characterized by three parameters, namely, α_{BR}, Γ_{BR}, and μ_{BR}. The construction of the probabilistic model for each one parameter of these parameters, which are respectively modeled by random variables $\mathbb{\alpha}_{\mathrm{BR}}$, $\mathbb{\Gamma}_{\mathrm{BR}}$, and $\mathbb{\mu}_{\mathrm{BR}}$, is presented below.

4.3.1 Distribution of the force rate of change

As the rate of change α_{BR} is positive, it is reasonable to assume $\mathsf{Supp}\, \mathbb{\alpha}_{\mathrm{BR}} =]0, \infty[$. Therefore, the PDF of $\mathbb{\alpha}_{\mathrm{BR}}$ is a nonnegative function $p_{\mathbb{\alpha}_{\mathrm{BR}}}$, which respects the following normalization condition

$$\int_{\alpha=0}^{+\infty} p_{\mathbb{\alpha}_{\mathrm{BR}}}(\alpha) \, d\alpha = 1. \tag{4.8}$$

It is also convenient to assume that the mean value of $\mathbb{\alpha}_{\mathrm{BR}}$ is a known positive number, denoted by $m_{\mathbb{\alpha}_{\mathrm{BR}}}$, i.e.,

$$\mathbb{E}\left[\mathbb{\alpha}_{\mathrm{BR}} \right] = m_{\mathbb{\alpha}_{\mathrm{BR}}} > 0. \tag{4.9}$$

For technical reasons, one also need to require that

$$\mathbb{E}\left[\ln \left(\mathbb{\alpha}_{\mathrm{BR}} \right) \right] = q_{\mathbb{\alpha}_{\mathrm{BR}}}, \quad |q_{\mathbb{\alpha}_{\mathrm{BR}}}| < +\infty, \tag{4.10}$$

which ensures, as can be see in Soize (2000) [23], that the inverse of α_{BR} is second order random variable. This condition is necessary to guarantee that the stochastic dynamical system associated to this random variable is of second order, i.e., it has finite variance.

Employing the principle of maximum entropy one need to maximize the entropy function $\mathrm{S}\left(p_{\alpha_{\mathrm{BR}}}\right)$, respecting the constraints imposed by (4.8), (4.9) and (4.10). The desired PDF corresponds to the gamma distribution and is given by

$$\begin{aligned} p_{\alpha_{\mathrm{BR}}}(\alpha) = \mathbb{1}_{]0,\infty[}(\alpha)\, \frac{1}{m_{\alpha_{\mathrm{BR}}}} \left(\frac{1}{\delta^2_{\alpha_{\mathrm{BR}}}}\right)^{1/\delta^2_{\alpha_{\mathrm{BR}}}} \\ \times \frac{1}{\Gamma(1/\delta^2_{\alpha_{\mathrm{BR}}})} \left(\frac{\alpha}{m_{\alpha_{\mathrm{BR}}}}\right)^{1/\delta^2_{\alpha_{\mathrm{BR}}}-1} \exp\left(\frac{-\alpha}{\delta^2_{\alpha_{\mathrm{BR}}} m_{\alpha_{\mathrm{BR}}}}\right), \end{aligned} \tag{4.11}$$

where the symbol $\mathbb{1}_{]0,\infty[}(\alpha)$ denotes the indicator function of the interval $]0,\infty[$, $0 \leq \delta_{\alpha_{\mathrm{BR}}} = \sigma_{\alpha_{\mathrm{BR}}}/m_{\alpha_{\mathrm{BR}}} < 1/\sqrt{2}$ is a type of dispersion parameter, and

$$\Gamma(z) = \int_{y=0}^{+\infty} y^{z-1}\, e^{-y}\, dy \tag{4.12}$$

is the gamma function.

An illustration for the PDF of the gamma distributed random variable α_{BR}, with mean $m_{\alpha_{\mathrm{BR}}} = 400\,1/\mathrm{m/s}$ and dispersion factor $\delta_{\alpha_{\mathrm{BR}}} = 0.5\%$, is presented in Figure 4.1.

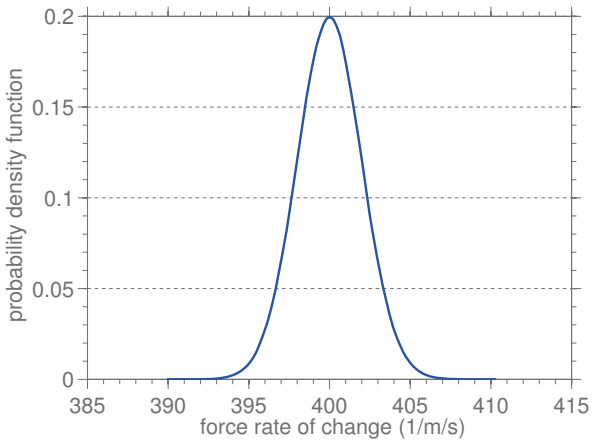

Figure 4.1: Illustration of the PDF of the gamma distributed random variable α_{BR}, with mean $m_{\alpha_{\mathrm{BR}}} = 400\,1/\mathrm{m/s}$ and dispersion factor $\delta_{\alpha_{\mathrm{BR}}} = 0.5\%$.

4.3.2 Distribution of the limit force

The parameter Γ_{BR} is also positive, in a way that $\texttt{Supp}\,\mathbb{\Gamma}_{\text{BR}} =]0, \infty[$, and consequently

$$\int_{\gamma=0}^{+\infty} p_{\mathbb{\Gamma}_{\text{BR}}}(\gamma)\, d\gamma = 1. \tag{4.13}$$

The hypothesis that the mean is a known positive number $m_{\mathbb{\Gamma}_{\text{BR}}}$ is also done, i.e.,

$$\mathbb{E}\left[\mathbb{\Gamma}_{\text{BR}}\right] = m_{\mathbb{\Gamma}_{\text{BR}}} > 0, \tag{4.14}$$

as well as that the technical condition, required for the stochastic dynamical system associated be of second order, is fulfilled, i.e.

$$\mathbb{E}\left[\ln\left(\mathbb{\Gamma}_{\text{BR}}\right)\right] = q_{\mathbb{\Gamma}_{\text{BR}}}, \quad |q_{\mathbb{\Gamma}_{\text{BR}}}| < +\infty. \tag{4.15}$$

In a similar way to the procedure presented in section 4.3.1, it can be shown that PDF of maximum entropy in this case also has gamma distribution, and is given by

$$\begin{aligned} p_{\mathbb{\Gamma}_{\text{BR}}}(\gamma) = \mathbb{1}_{]0,\infty[}(\gamma)\, \frac{1}{m_{\mathbb{\Gamma}_{\text{BR}}}} \left(\frac{1}{\delta^2_{\mathbb{\Gamma}_{\text{BR}}}}\right)^{1/\delta^2_{\mathbb{\Gamma}_{\text{BR}}}} \\ \times \frac{1}{\Gamma(1/\delta^2_{\mathbb{\Gamma}_{\text{BR}}})} \left(\frac{\gamma}{m_{\mathbb{\Gamma}_{\text{BR}}}}\right)^{1/\delta^2_{\mathbb{\Gamma}_{\text{BR}}}-1} \exp\left(\frac{-\gamma}{\delta^2_{\mathbb{\Gamma}_{\text{BR}}} m_{\mathbb{\Gamma}_{\text{BR}}}}\right). \end{aligned} \tag{4.16}$$

An illustration of this PDF, with mean $m_{\mathbb{\Gamma}_{\text{BR}}} = 30 \times 10^3\,\text{N}$ and dispersion factor $\delta_{\mathbb{\Gamma}_{\text{BR}}} = 1\%$ can be seen in Figure 4.2.

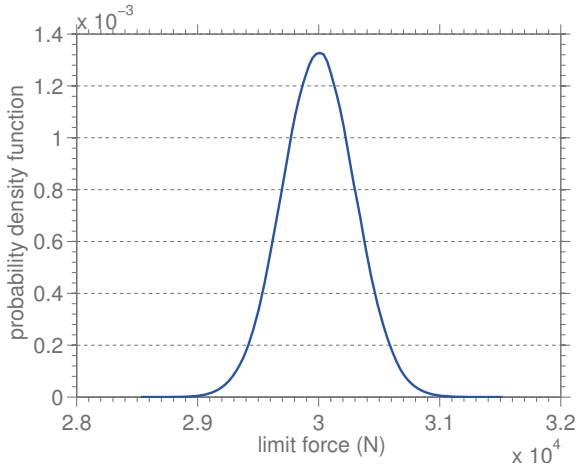

Figure 4.2: Illustration of the PDF of the gamma distributed random variable $\mathbb{\Gamma}_{\text{BR}}$, with mean $m_{\mathbb{\Gamma}_{\text{BR}}} = 30 \times 10^3\,\text{N}$ and dispersion factor $\delta_{\mathbb{\Gamma}_{\text{BR}}} = 1\%$.

4.3.3
Distribution of the friction coefficient

With respect to the parameter μ_{BR}, one know it is nonnegative and bounded above by the unity. Thus, one can safely assume that $\texttt{Supp}\, \mathbb{\mu}_{\text{BR}} = [0, 1]$, so that the normalization condition read as

$$\int_{\mu=0}^{1} p_{\mathbb{\mu}_{\text{BR}}}(\mu)\, d\mu = 1. \tag{4.17}$$

For technical reasons (Soize, 2000) [23], the following two conditions are also imposed

$$\mathbb{E}\left[\ln\left(\mathbb{\mu}_{\text{BR}}\right)\right] = q^1_{\mathbb{\mu}_{\text{BR}}}, \quad |q^1_{\mathbb{\mu}_{\text{BR}}}| < +\infty, \tag{4.18}$$

$$\mathbb{E}\left[\ln\left(1 - \mathbb{\mu}_{\text{BR}}\right)\right] = q^2_{\mathbb{\mu}_{\text{BR}}}, \quad |q^2_{\mathbb{\mu}_{\text{BR}}}| < +\infty, \tag{4.19}$$

representing a weak decay of the PDF of $\mathbb{\mu}_{\text{BR}}$ in 0^+ and 1^- respectively. A similar development is presented in Ritto et al. (2010) [92].

Evoking again the principle of maximum entropy, considering now as known information the constraints defined by (4.17), (4.18), and (4.19) one has that the desired PDF is given by

$$p_{\mathbb{\mu}_{\text{BR}}}(\mu) = \mathbb{1}_{[0,1]}(\mu)\, \frac{\Gamma(a+b)}{\Gamma(a)\,\Gamma(b)}\, \mu^{a-1}\, (1-\mu)^{b-1}, \tag{4.20}$$

which corresponds to the beta distribution. The parameters a and b are associated with the shape of the probability distribution, and can be related with $m_{\mathbb{\mu}_{\text{BR}}}$ and $\delta_{\mathbb{\mu}_{\text{BR}}}$ by

$$a = \frac{m_{\mathbb{\mu}_{\text{BR}}}}{\delta^2_{\mathbb{\mu}_{\text{BR}}}} \left(\frac{1}{m_{\mathbb{\mu}_{\text{BR}}}} - \delta^2_{\mathbb{\mu}_{\text{BR}}} - 1 \right), \tag{4.21}$$

and

$$b = \frac{m_{\mathbb{\mu}_{\text{BR}}}}{\delta^2_{\mathbb{\mu}_{\text{BR}}}} \left(\frac{1}{m_{\mathbb{\mu}_{\text{BR}}}} - \delta^2_{\mathbb{\mu}_{\text{BR}}} - 1 \right) \left(\frac{1}{m_{\mathbb{\mu}_{\text{BR}}}} - 1 \right). \tag{4.22}$$

In Figure 4.3 the reader can see the illustration a beta distributed PDF, with $m_{\mathbb{\mu}_{\text{BR}}} = 0.4$ and $\delta_{\mathbb{\mu}_{\text{BR}}} = 0.5\%$.

4.4
Stochastic initial/boundary value problem

Due to the randomness of the parameters $\mathbb{\alpha}_{\text{BR}}$, $\mathbb{\Gamma}_{\text{BR}}$, and $\mathbb{\mu}_{\text{BR}}$, the the vector field $\boldsymbol{U}$, unknown of variational problem defined by Eqs.(3.52), (3.66), and (3.67), becomes a random vector field $\mathbb{U}$, which is solution of the stochastic initial/boundary value problem defined by

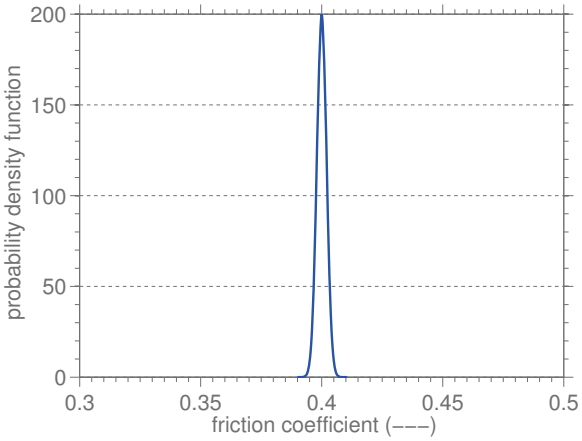

Figure 4.3: Illustration of the PDF of the beta distributed random variable $\mathbb{\mu}_{\mathrm{BR}}$, with mean $m_{\mathbb{\mu}_{\mathrm{BR}}} = 0.4$ and dispersion factor $\delta_{\mathbb{\mu}_{\mathrm{BR}}} = 0.5\%$.

$$\mathcal{M}\left(\boldsymbol{\psi}, \ddot{\mathbb{U}}\right) + \mathcal{C}\left(\boldsymbol{\psi}, \dot{\mathbb{U}}\right) + \mathcal{K}\left(\boldsymbol{\psi}, \mathbb{U}\right) = \mathcal{F}\left(\boldsymbol{\psi}, \mathbb{U}, \dot{\mathbb{U}}, \ddot{\mathbb{U}}\right), \quad a.s. \tag{4.23}$$

$$\mathcal{M}\left(\boldsymbol{\psi}, \mathbb{U}(0)\right) = \mathcal{M}\left(\boldsymbol{\psi}, \boldsymbol{U}_0\right), \quad a.s. \tag{4.24}$$

and

$$\mathcal{M}\left(\boldsymbol{\psi}, \dot{\mathbb{U}}(0)\right) = \mathcal{M}\left(\boldsymbol{\psi}, \dot{\boldsymbol{U}}_0\right). \quad a.s. \tag{4.25}$$

4.5 Stochastic nonlinear dynamical system

When the stochastic initial/boundary value problem of Eqs.(4.23), (4.24), and (4.25) is discretized in its spatial coordinate, using the standard finite element method, the result is the $N_{dofs} \times N_{dofs}$ stochastic nonlinear dynamical system defined by

$$[\mathcal{M}]\, \ddot{\mathbb{Q}}(t,\theta) + [\mathcal{C}]\, \dot{\mathbb{Q}}(t,\theta) + [\mathcal{K}]\, \mathbb{Q}(t,\theta) = \mathbb{F}\left(\mathbb{Q}, \dot{\mathbb{Q}}, \ddot{\mathbb{Q}}\right), \quad a.s. \tag{4.26}$$

$$[\mathcal{M}]\, \mathbb{Q}(0,\theta) = \boldsymbol{Q}_0, \qquad \text{and} \qquad [\mathcal{M}]\, \dot{\mathbb{Q}}(0,\theta) = \dot{\boldsymbol{Q}}_0, \quad a.s. \tag{4.27}$$

where, for a fixed t, $\mathbb{Q}(t,\cdot)$ is the random displacement vector, $\dot{\mathbb{Q}}(t,\cdot)$ is the random velocity vector, and $\ddot{\mathbb{Q}}(t,\cdot)$ is the random acceleration vector, and $\mathbb{F}$ is the random nonlinear force vector.

4.6 Reduced stochastic dynamical system

To reduce the stochastic dynamical system of Eqs.(4.26) and (4.27), the procedure is similar to that shown in section 3.3.2, once the matrices which define the associated generalized eigenvalue problem are the same as before.

In this way, using the new change of base defined by

$$\mathbb{Q}(t,\theta) = [\Phi]\, \mathbb{q}(t,\theta), \quad a.s. \tag{4.28}$$

and pre-multiplying the stochastic dynamical system by $[\Phi]^T$, one reaches its reduced form, which is defined by the following stochastic initial value problem

$$[M]\, \ddot{\mathbb{q}}(t,\theta) + [C]\, \dot{\mathbb{q}}(t,\theta) + [K]\, \mathbb{q}(t,\theta) = \mathbb{f}\left(\mathbb{q}, \dot{\mathbb{q}}, \ddot{\mathbb{q}}\right), \quad a.s. \tag{4.29}$$

$$\mathbb{q}(0,\theta) = \boldsymbol{q}_0, \qquad \text{and} \qquad \dot{\mathbb{q}}(0,\theta) = \dot{\boldsymbol{q}}_0, \quad a.s. \tag{4.30}$$

where, for a fixed t, $\mathbb{q}(t,\cdot)$ is the reduced random displacement vector, $\dot{\mathbb{q}}(t,\cdot)$ is the reduced random velocity vector, and $\ddot{\mathbb{q}}(t,\cdot)$ is the reduced random acceleration vector, and the reduced random force is given by

$$\mathbb{f} \;=\; [\Phi]^T\, \mathbb{F}\left([\Phi]\, \mathbb{q}(t,\theta), [\Phi]\, \dot{\mathbb{q}}(t,\theta), [\Phi]\, \ddot{\mathbb{q}}(t,\theta)\right). \quad a.s. \tag{4.31}$$

The methodology used to calculate the propagation of uncertainties through this stochastic dynamical system is described in the next section.

4.7 Stochastic solver: Monte Carlo method

The stochastic solver employed in this work to compute the propagation of the uncertainties through the computational model is the Monte Carlo (MC) method (Metropolis and Ulam, 1949) [118]; Liu (2001) [119]; Fishman (2003) [120]; Rubinstein and Kroese (2007) [121]; Shonkwiler and Mendivil (2009) [122]; Robert and Casella (2010) [123].

In essence, this method is an algorithm in which several realizations (samples) of the random parameters of the stochastic model are generated according to the probability distribution that was specified to them a priori. Each one of these realizations defines a new deterministic problem, which is solved (processing) using a deterministic technique, generating an amount of data. Then, all of these data are combined through statistics to access the response of the random system under analysis (Kroese et al., 2011) [124]. A general overview of the MC algorithm can be seen in the Figure 4.4.

Regarding the computational implementation, the MC method has a nonintrusive characteristic, once it does not require a new computer code to simulate a stochastic model. If a deterministic code to simulate a similar deterministic model is available, the stochastic simulation can be conducted by running the deterministic program several times, changing only the value of the parameters that are randomly generated (Kroese et al., 2011) [124].

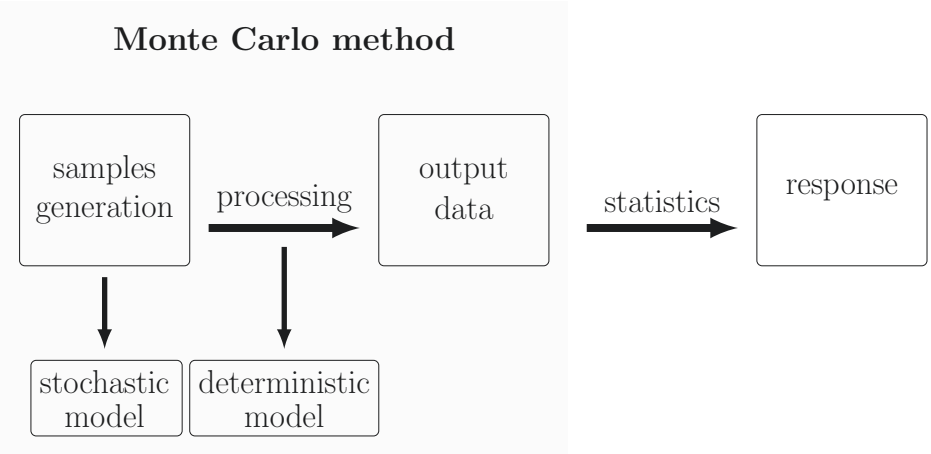

Figure 4.4: General overview of Monte Carlo algorithm.

Additionally, if the MC simulation is performed for a large number of samples, it completely describes the statistical behavior of the random system (Caflisch, 1998) [125]. Unfortunately, MC is a very time-consuming method, which makes unfeasible its use for complex simulations, when the processing time of a single realization is very large or the number of realizations to an accurate result is huge. Fortunately the algorithm is easily parallelizable, allowing circumvent this deficiency (Cunha Jr et al., 2014) [126].

5
Exploration of Nonlinear Stochastic Dynamics

This chapter deals with the numerical analysis of the nonlinear stochastic dynamical system. Here are presented numerical results related to modal analysis of the system; convergence of finite element approximation; construction of reduced order model; calculation of static equilibrium configuration; drill-bit and beam nonlinear dynamics; influence of impacts on the dynamics; spectral analysis of nonlinear dynamics; drilling process efficiency analysis; propagation of uncertainties of random parameters through nonlinear dynamical system.

5.1
Parameters for the mathematical model

In order to simulate the nonlinear dynamics of the mechanical system, the physical parameters presented in the Table 5.1 are adopted, as well as the length $L = 100\,\mathrm{m}$, the rotational and axial velocities in x, respectively given by $\Omega = 2\pi\,\mathrm{rad/s}$, and $V_0 = 1/180\,\mathrm{m/s}$. The values of these parameters do not correspond exactly to the actual values used in a real drillstring, but are of the same order of magnitude. For this configuration, the beam geometry is discretized by 500 finite elements, and the interval of integration $[t_0, t_f] = [0, 10]\,\mathrm{s}$ is considered.

Table 5.1: Physical parameters of the mechanical system.

parameter	value	unit
ρ	7900	$\mathrm{kg/m^3}$
g	9.81	$\mathrm{m/s^2}$
ν	0.3	—
c	0.01	—
E	203×10^9	Pa
R_{bh}	95×10^{-3}	m
R_{int}	50×10^{-3}	m
R_{ext}	80×10^{-3}	m

For the constants of the friction and shock model, are considered the values shown in Table 5.2, which have order of magnitude typical of a borehole wall made of steel (Zhang and Sharf, 2009) [127]. The low value for the

friction coefficient μ_{FS} is justified by the fact that in the real system, there is a fluid between the borehole wall and the column, which carries a substantial reduction in the torsional friction.

Table 5.2: Parameters of the friction and shock model.

parameter	value	unit
k_{FS_1}	1×10^{10}	N/m
k_{FS_2}	1×10^{16}	N/m^3
c_{FS}	1×10^{6}	(N/m^3)/(m/s)
μ_{FS}	0.25	—

The constants of the bit-rock interaction model can be seen in Table 5.3, and were estimated in a similar way as in Ritto et al. 2013 [77]. Besides that, trial and error numerical studies showed that $\omega^{SOR} = 0.75$, and $\varepsilon_1 = \varepsilon_2 = 10^{-2}$ are sufficient for convergence of the simulations.

Table 5.3: Parameters of the bit-rock interaction model.

parameter	value	unit
Γ_{BR}	30×10^3	N
α_{BR}	400	1/(m/s)
μ_{BR}	0.4	—

5.2 Modal analysis of the mechanical system

In this section, the modal content of the mechanical system is investigated. This investigation aims to identify the natural frequencies of the system, and, especially, to check the influence of *slenderness ratio*, defined as the ratio between beam length and external diameter, in the natural frequencies distribution.

Therefore, the dimensionless frequency band of interest in the problem is assumed as being $B = [0, 4]$, with the dimensionless frequency defined by

$$f^* = \frac{f\,L}{c_L}, \tag{5.1}$$

where f is the dimensional frequency (Hz), and $c_L = \sqrt{E/\rho}$ is the longitudinal wave velocity. As it was defined in terms of a dimensionless frequency, the band of analysis does not change when the beam length is varied. Also, the reader can check that this band is representative for the mechanical system dynamics, once the beam rotates at 2π rad/s, which means that the mechanical system is excited at 1 Hz.

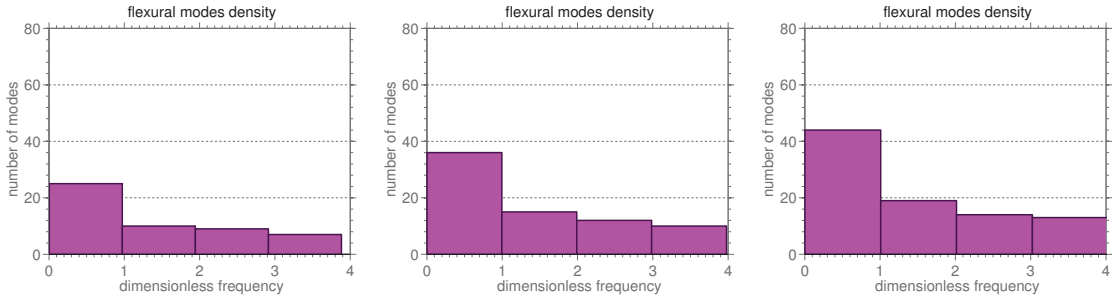

5.1(a): slenderness = 312.5 5.1(b): slenderness = 625.0 5.1(c): slenderness = 937.5

Figure 5.1: Distribution of the flexural modes as a function of dimensionless frequency, for several values of slenderness ratio.

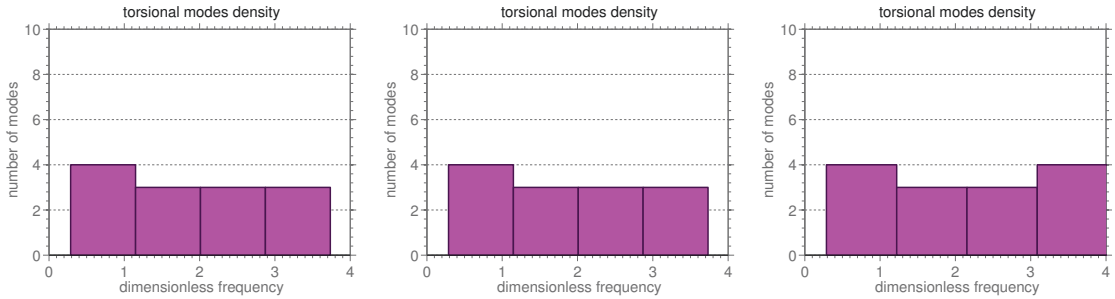

5.2(a): slenderness = 312.5 5.2(b): slenderness = 625.0 5.2(c): slenderness = 937.5

Figure 5.2: Distribution of the torsional modes as a function of dimensionless frequency, for several values of slenderness ratio.

In Figure 5.1 one can see the distribution of the flexural modes as a function of dimensionless frequency, for several values of slenderness ratio. Clearly it is observed that the flexural modes are denser in the low frequency range. Further, when the slenderness ratio increases, the modal density in the low frequencies range tend to increase.

A completely different behavior is observed for the torsional and longitudinal (traction-compression) modes of vibration, as can be seen in Figures 5.2 and 5.3, respectively. One can note that, with respect to these two modes of vibration, the modal distribution is almost uniform with respect to dimensionless frequency, and invariant to changes in the slenderness ratio.

It may also be noted from Figures 5.1 to 5.3 that, the lowest natural frequencies are associated with the flexural mechanism. This is because the flexural stiffness of the beam is much smaller than the torsional stiffness, which in turn is less than the axial stiffness. In other words, it is much easier to bend the beam than twisting it. However, twists the beam is easier than buckling it.

The dimensionless frequency band adopted in the analysis corresponds to a maximum dimensional frequency of $f_{max} = 4\,c_L/L$. In this way, a nominal time step of $\Delta t = (2\,f_{max})^{-1}$ is adopted for time integration. This time step is

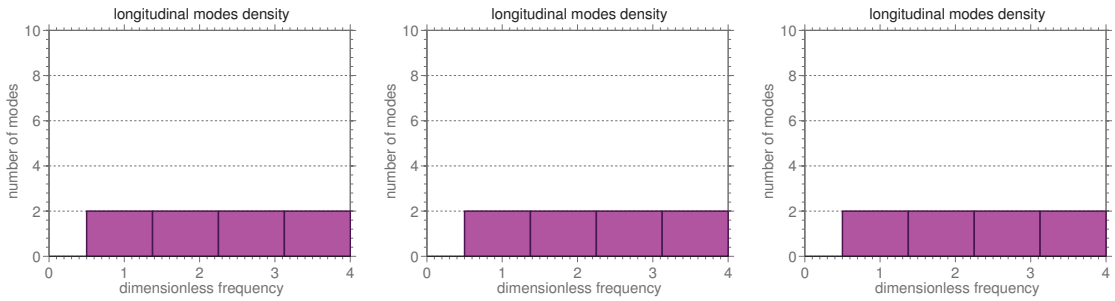

5.3(a): slenderness = 312.5 5.3(b): slenderness = 625.0 5.3(c): slenderness = 937.5

Figure 5.3: Distribution of the longitudinal modes as a function of dimensionless frequency, for several values of slenderness ratio.

automatically refined by the algorithm of integration, whenever necessary, to capture the shock effects.

5.3 Convergence of finite element approximations

Before one start to study the mechanical system of interest, it is necessary to analyze the convergence of FEM approximations used to access the nonlinear dynamics. For this purpose, it is taken into account the map $n \in \mathbb{N} \mapsto \texttt{conv}_{\text{FEM}}(n) \in \mathbb{R}$, being

$$\texttt{conv}_{\text{FEM}}(n) = \left(\int_{t=t_0}^{t_f} \int_{x=0}^{L} \left(\left\| \boldsymbol{U}^{(n)}(x,t) \right\|^2 + \left\| \dot{\boldsymbol{U}}^{(n)}(x,t) \right\|^2 \right) dx\, dt \right)^{1/2}, \quad (5.2)$$

where n denotes the number of finite elements used in the approximation, and $\|\cdot\|$ represents the standard Euclidean norm, here applied to the vector fields $\boldsymbol{U}(x,t)$ and $\dot{\boldsymbol{U}}(x,t)$. The superscript $^{(n)}$ indicates an approximation constructed with n finite elements. For details the reader is referenced to Oden and Reddy (2011) [128].

The (discrete) mean mechanical energy of the mechanical system, over the interval $[t_0, t_f]$, for an approximation constructed with n finite element is a map $n \in \mathbb{N} \mapsto \texttt{energy}_{\text{MECH}}(n) \in \mathbb{R}$, where

$$\texttt{energy}_{\text{MECH}}(n) = \frac{1}{t_f - t_0} \int_{t=t_0}^{t_f} \left(\frac{1}{2}\, \dot{\boldsymbol{Q}}^{(n)T}(t)\, [\mathcal{M}]\, \dot{\boldsymbol{Q}}^{(n)}(t) + \frac{1}{2}\, \boldsymbol{Q}^{(n)T}(t)\, [\mathcal{K}]\, \boldsymbol{Q}^{(n)}(t) \right) dt. \quad (5.3)$$

This metric also used to measure the convergence of the finite element approximations in reason of its physical appeal.

In the convergence tests reported herein, it is considered a "temporal window" defined by the interval $[t_0, t_f] = [0, 512 \times \Delta t]$, with $\Delta t = 2.5 \times 10^{-3}$ s. The number of finite elements in the mesh is increased, first by 10 units until a total of 100 elements is achieved, and then by 50 units up to a total of 800 elements.

The evolution of $\texttt{conv}_{\text{FEM}}(n)$ as a function of the number of finite elements used in the approximation can be seen in Figure 5.4. Note that for a number of elements equal to 200 or more, the metric value varies slightly.

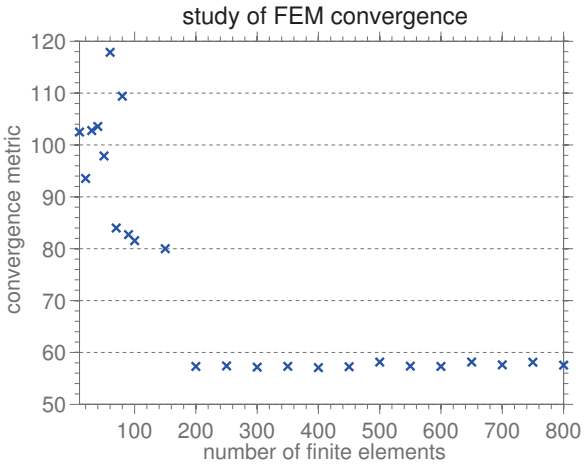

Figure 5.4: This figure illustrates the convergence metric of FEM approximations as a function of the number of finite elements.

It also noted that there is no change in the behavior of $\texttt{energy}_{\text{MECH}}(n)$ to a number of elements greater than 200, as can be see in Figure 5.5. A study of convergence which considers the first 350 natural frequencies of the system is also conducted, and shows that these frequencies converge with two decimal places of precision when 500 or more elements are used in the approximation. Accordingly, it is admitted that $N_{elem} = 500$ represents a good compromise between accuracy and computational cost, and all other simulations reported in this work use this number of elements to construct the approximation.

5.4 Construction of the reduced model

In the construction of the reduced model, are taken into account the rigid body modes of the mechanical system, as well as modes of bending, torsion and traction-compression. The construction strategy consists of including: (i) the two rigid body modes (translation and rotation); (ii) all the flexural modes such that $0 < f^* \leq 5\, L/c_L$; (iii) all the torsional modes such that $0 < f^* \leq 4$; (iv) all the longitudinal modes such that $0 < f^* \leq 4$.

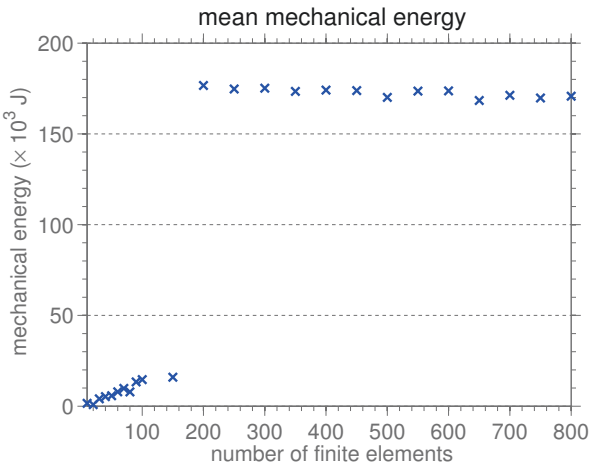

Figure 5.5: This figure illustrates the mean mechanical energy of the system as a function of the number of finite elements.

In this way, the total number of modes used in the FEM model is a function of the beam length. In Table 5.4 the reader can see a comparison, for different values of L, of the full FEM model dimension and the corresponding dimension of the reduced order model. Note that the dimension of the reduced models, constructed using the above strategy, is always much smaller than the full model dimension.

Table 5.4: Dimension of the FEM model as a function of beam length.

beam length (m)	full model DoFs	reduced model DoFs
50	306	37
100	3006	49
150	4506	60

5.5 Calculation of the static equilibrium configuration

Before the beginning of drilling operation, the drillstring is inserted into the borehole, without axial velocity and rotation imposed. Due to gravitational effects, the column deflects until it reaches a static equilibrium configuration. This configuration is calculated by the temporal integration of the dynamical system defined by the Eqs.(3.77) and (3.78), assuming zero initial conditions, i.e., $\Omega = 0\,\mathrm{rad/s}$, and $V_0 = 0\,\mathrm{m/s}$. In this way, after a short transient, the system reaches static equilibrium and remains in this configuration indefinitely.

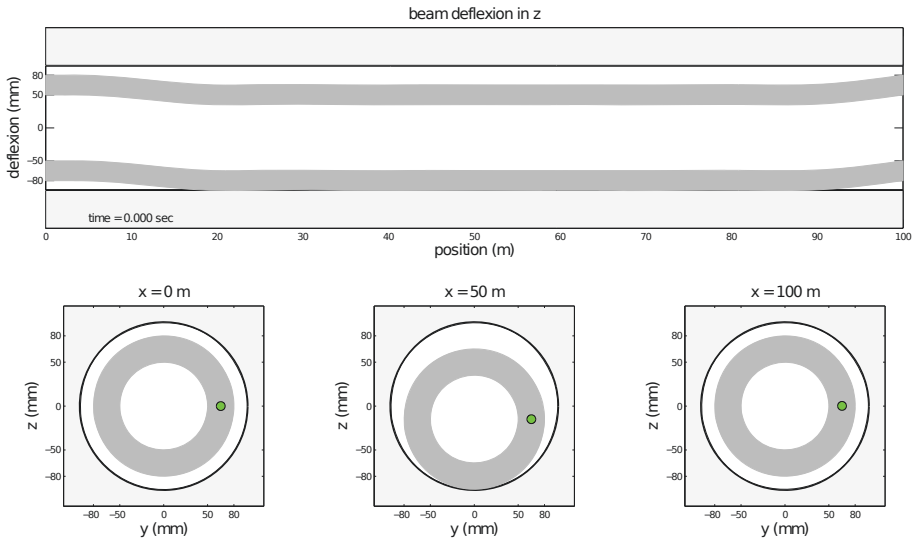

Figure 5.6: Illustration of static equilibrium configuration of a horizontal drillstring with 100 m length.

An illustration of this equilibrium configuration, for a 100 m long column is presented in Figure 5.6. In this illustration, one can see the mechanical system sectioned by the plane $y = 0\,\mathrm{m}$, as well as by the planes $x = \{0, 50, 100\}\,\mathrm{m}$. A visual inspection clearly indicates that this equilibrium is stable. Moreover, as this equilibrium configuration is the initial state of the real system, it will be used as initial condition in all other simulations reported bellow.

An animation which illustrates the calculation of the beam static equilibrium can be seen in Video 1: `http://www.youtube.com/watch?v=jJu1E19p434`.

5.6 Drill-bit nonlinear dynamic behavior

The drill-bit longitudinal displacement and velocity, can be seen in Figure 5.7. For practical reasons, some scaling factors were introduced in the units of measure of these quantities. They allow one to read the displacement in "millimeter", and the velocity in "meters per hour". Accordingly, it is noted that, during the interval of analysis, the column presents an advance in the forward direction with very small axial oscillations in the displacement. The axial oscillations in the velocity curve are more pronounced, and correspond to the vibration mechanism known as *bit-bounce*, where the drill-bit loses contact with the soil and then hits the rock abruptly. This phenomenon, which is widely observed in real systems (Spanos et at., 2003) [30], presents itself discreetly

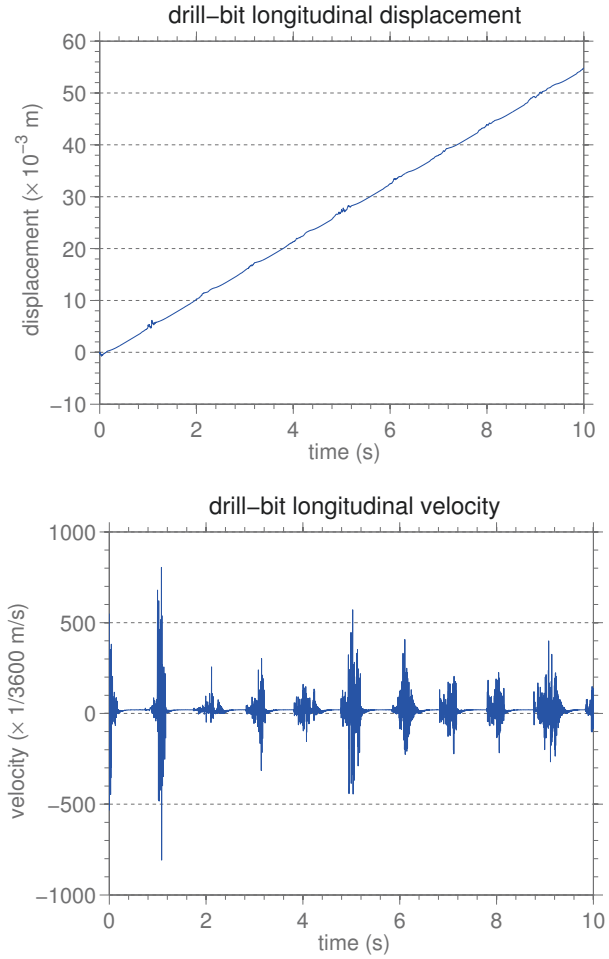

Figure 5.7: Illustration of drill-bit displacement (top) and drill-bit velocity (bottom).

in the case analyzed. Note that the velocity exhibits a mean value of 19.36 "meters per hour", close to the velocity $V_0 = 20$ "meters per hour", which is imposed on the left end of the beam. Also, throughout the "temporal window" analyzed, one can observe packages where the velocity of the drill-bit presents large fluctuations, which can reach up to 40 times the mean value.

The drill-bit rotation and angular velocity, can be seen in Figure 5.8. Now the scale factors allow one to read rotation in "revolution", and the angular velocity in "revolution per minute". Thus, what it is observed is a almost monotonic rotation. However, when one looks to the angular velocity, it is possible to see packages of fluctuations with amplitude variations that can reach up to an order of magnitude. This indicates that the drill-bit undergoes a blockage due to the torsional friction, and then it is released subtly, so that its velocity is sharply increased, in a *stick-slip* phenomenon type. This is also seen experimentally (Spanos et at., 2003) [30] in real drilling systems, and a serious consequence of this blockage is the reduction of drilling process efficiency.

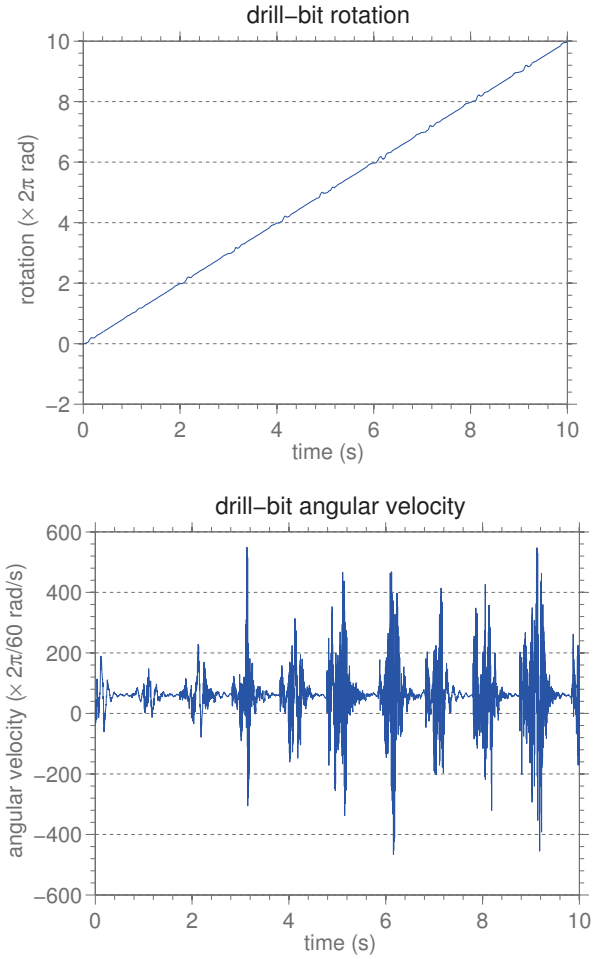

Figure 5.8: Illustration of drill-bit rotation (top) and drill-bit angular velocity (bottom).

5.7 Transverse nonlinear dynamics of the beam

Observing the cross section of the beam at $x = 50\,\text{m}$, for which the transversal displacement (top) and velocity (bottom) are shown in Figure 5.9, one can see an asymmetry of the displacement, with respect to the plane $z = 0\,\text{m}$. This is due to gravity, which favors the beam to move below this plane. Furthermore, one can note that the this signal is composed of "packages", which has a recurring oscillatory pattern. As will be seen in section 5.8, these packages present a strong correlation with the number of impacts which the mechanical system is subjected.

The evolution of the radial displacement, for $x = 50\,\text{m}$, of the beam cross-section can be seen in the Figure 5.10, which shows that several transverse impacts occur between the drillstring and the borehole wall during the drilling process. This fact is also reported experimentally (Spanos et at., 2003) [30], and is an important cause of damage to the well and to the drillstring.

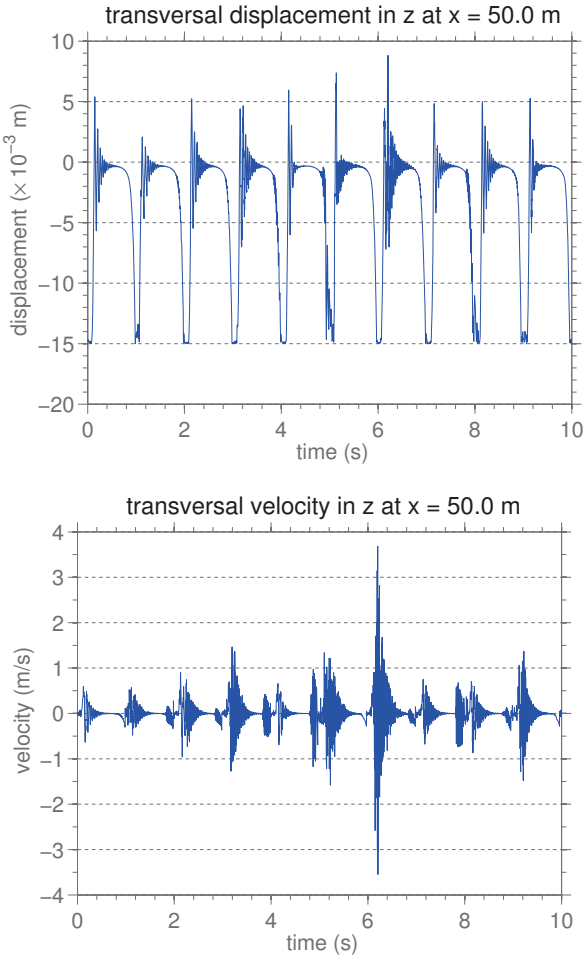

Figure 5.9: Illustration of transversal displacement (top) and velocity in z (bottom) when $x = 50\,\mathrm{m}$.

Note that, after an impact, the amplitudes of the oscillations decreases until subtly increase sharply, giving rise to a new impact, and then the entire process repeats again.

5.8 Influence of transverse impacts on the nonlinear dynamics

In Figure 5.11 it is shown the graph of the map $t \in \mathbb{R} \mapsto \texttt{number of shocks} \in \mathbb{N}$, which associates for any instant t the number of impacts suffered by the mechanical system.

The "packages of fluctuation" observed in the Figures 5.7 to 5.9 correspond to transitory periods of the dynamical system, and are highly correlated with the process of collision between beam and borehole wall. This assertion can be verified if the reader compares the graphs of Figures 5.7 to 5.9 with the graph of Figure 5.11, which shows the existence of "shock packages". The existence of a correlation is clearly evident.

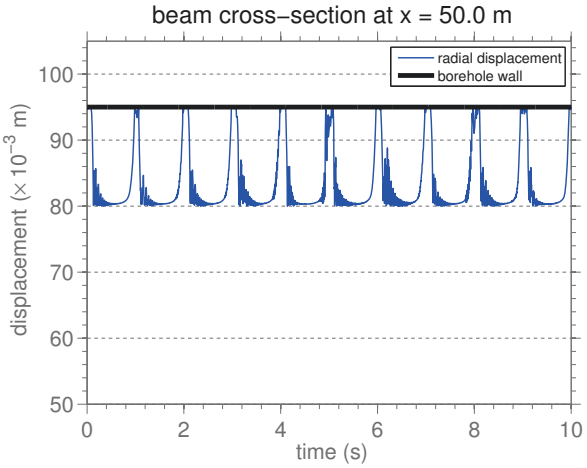

Figure 5.10: Illustration of beam radial displacement for $x = 50\,\mathrm{m}$.

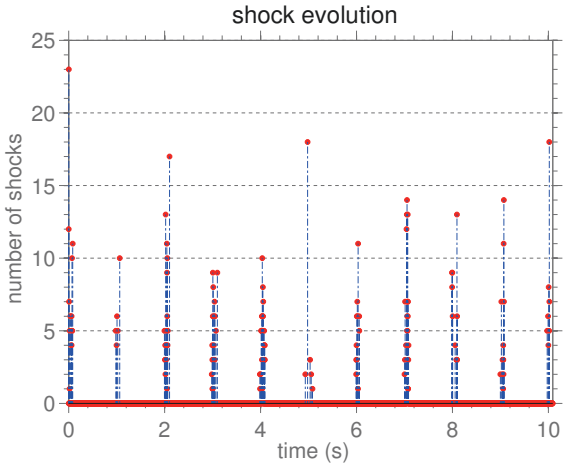

Figure 5.11: Illustration of the number of impacts suffered by the mechanical system as function of time.

Whenever there is a shock, the system "loses it memory" about the previous dynamic behavior, and undergoes a new transient period until reach a steady state again. This behavior is repeated 11 times in the "temporal window" analyzed.

Regarding the distribution of impacts along the beam, the graph of the map $x \in [0, L] \mapsto \texttt{number of shocks} \in \mathbb{N}$, which associates for any position x the number of impacts suffered by the mechanical system, is shown in Figure 5.12. It is clear that impacts do not occur near the beam ends. This is natural due to the restrictions of movement imposed by the boundary conditions.

The impacts between the drillstring and the borehole wall generate nonlinear elastic deformations in the beam, but without residual deformation effects. In this contact also occurs energy dissipation, due to the normal shock, and the torsional friction, induced by the rotation of the beam. These

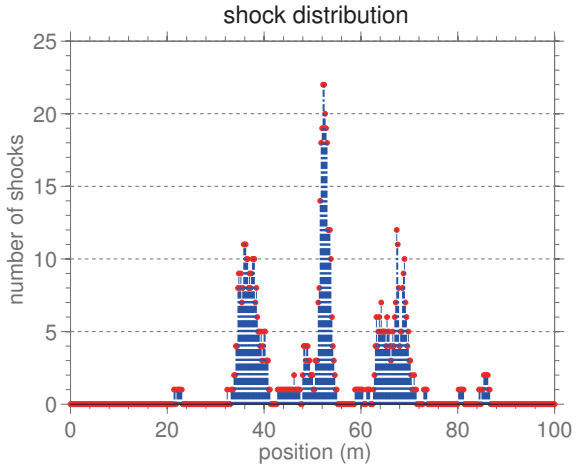

Figure 5.12: Illustration of the number of impacts suffered by the mechanical system as function of position.

mechanical contacts also activate flexural modes of vibration associated to high natural frequencies, so that the mechanical system assumes complex spatial configurations, as can be seen, for several instants, in Figure 5.13.

It is also very clear from the Figure 5.13 that, the mechanical contacts between the beam and the borehole wall, do not occur all the time among discrete points, they can also be seen along continuous line segments.

For a qualitative illustration of the nonlinear dynamics, the reader can see the Video 2: `http://www.youtube.com/watch?v=-4UVinZr4QQ`.

5.9 Spectral analysis of the nonlinear dynamics

All signals presented above, that are associated with the mechanical system response, have stochastic characteristics. Thereby, for a good understanding of them, it is necessary to analyze their spectral content through the power spectral density (PSD) function (Oppenheim and Schafer, 2009) [129].

The PSDs that are presented in this section (magenta line) were estimated using the periodogram method (Oppenheim and Schafer, 2009) [129], and the smooth curves (blue line) appearing were obtained by a filtering process, using a Savitzky-Golay filter (Savitzky and Golay, 1964) [130]. The PSDs are measured in dB/Hz, where the intensity of reference is adopted as being equal to one.

An illustration of PSD functions of drill-bit velocity and angular velocity is show in Figure 5.14. One can note that, in the case of velocity, the two peaks of highest amplitude correspond to the frequencies 84.55 Hz, and 115.20 Hz, respectively. These frequencies are very close to the flexural frequencies 84.53 Hz, and 115.29 Hz, so that the drill-bit axial dynamics is controlled by the transver-

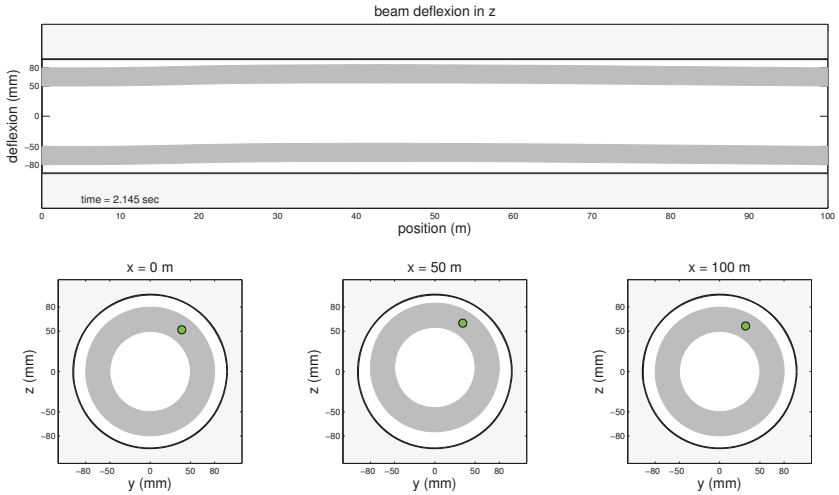

5.13(a): $t = 2.145\,\mathrm{s}$

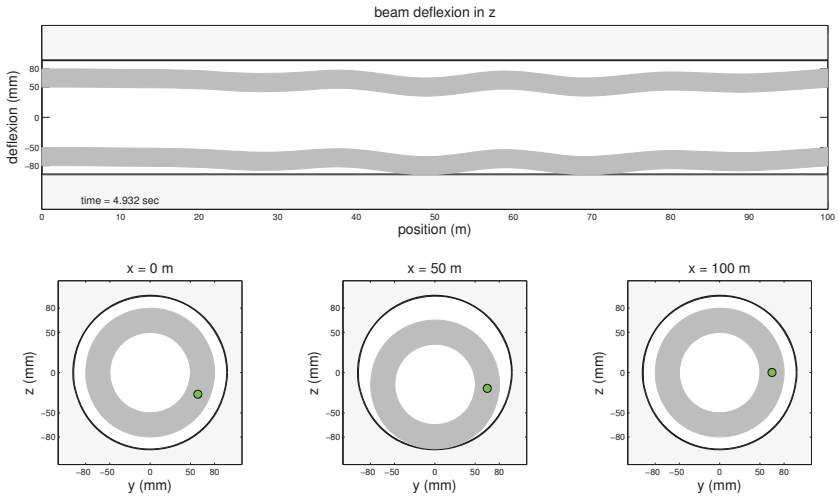

5.13(b): $t = 4.932\,\mathrm{s}$

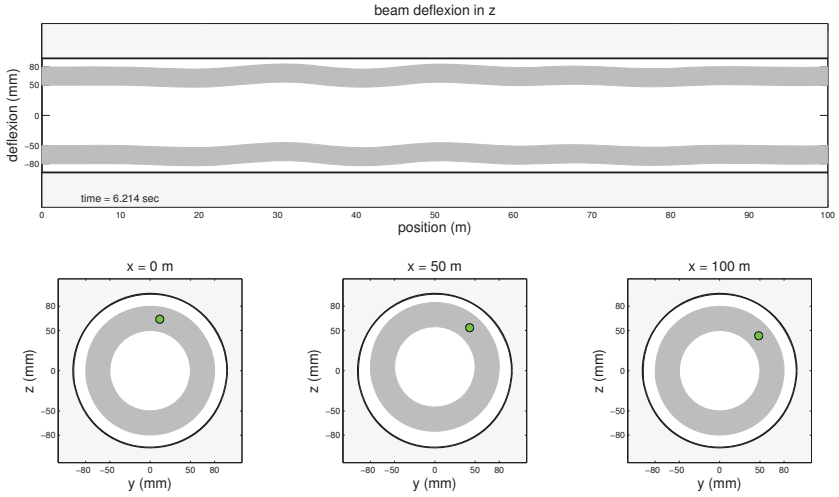

5.13(c): $t = 6.214\,\mathrm{s}$

Figure 5.13: Illustration of the mechanical system, for several instants, sectioned by the planes $y = 0\,\mathrm{m}$, and $x = \{0, 50, 100\}\,\mathrm{m}$.

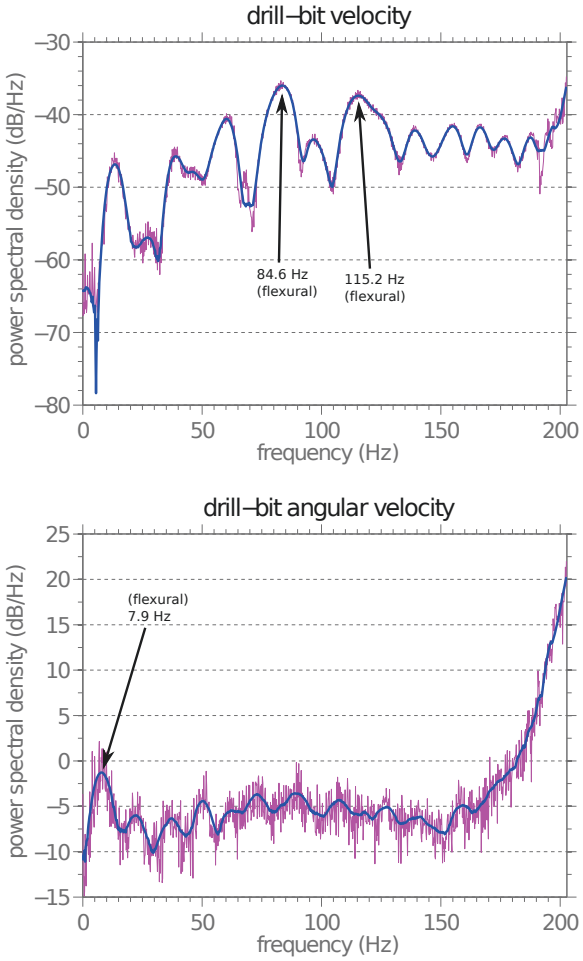

Figure 5.14: Illustration of power spectral density functions of drill-bit velocity (top) and angular velocity (bottom).

sal mechanisms of vibration. Furthermore, with respect to the angular velocity, it is noted a peak standing out in relation to the others. This peak is associated with 7.92 Hz frequency, which is very close to the flexrual frequency 7.89 Hz.

In Figure 5.15 the reader can see an illustration of PSD functions of beam transversal velocity in z and angular velocity around x when $x = 50\,\mathrm{m}$. The two peaks of highest amplitude, for the velocity in z, correspond to the frequencies 143.20 Hz, and 172.50 Hz, respectively. These frequencies are close to the torsional frequencies 145.55 Hz, and 174.67 Hz, which indicates that lateral vibrations in z, when $x = 50\,\mathrm{m}$, are induced by the torsional vibration mechanism. On the other hand, in what concerns angular velocity around x, the two peaks of largest amplitude are associated to the frequencies 6.93 Hz, and 107.10 Hz, respectively close to the flexural frequencies 6.84 Hz, and 107.16 Hz.

According to Figure 5.16, torsion is the primary mechanism of vibration that causes the impacts between the beam and borehole wall, since the highest peak of the PSD shown in this figure is associated with the frequency 57.42 Hz,

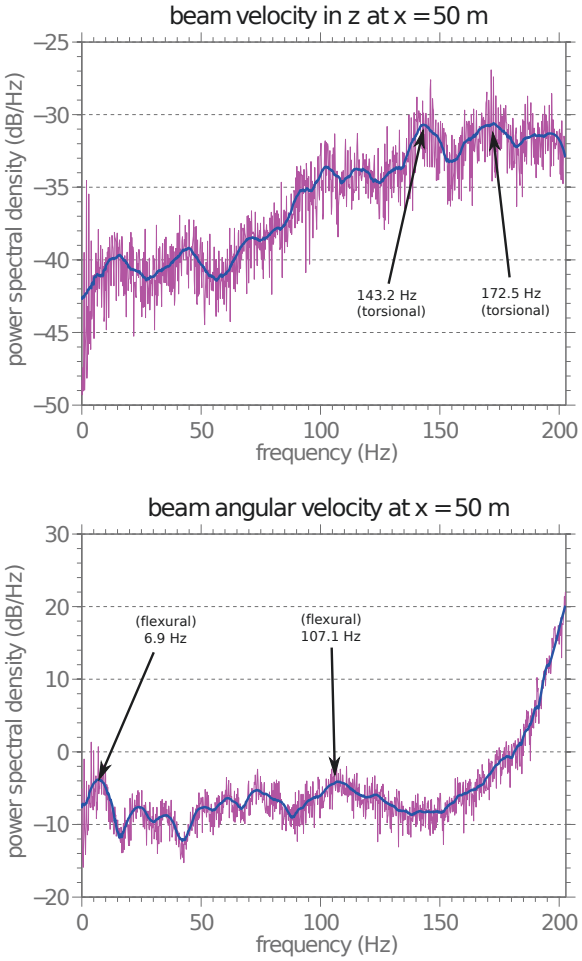

Figure 5.15: Illustration of power spectral density functions of beam transversal velocity in z (top) and angular velocity around x (bottom) when $x = 50\,\mathrm{m}$.

which is close to the torsional frequency 58.21 Hz. This result is surprising because intuition, especially when thinking about the dynamics of vertical drillstrings, suggests that lateral vibration mechanism is the mainly responsible for inducing the transverse impacts.

5.10 Analysis of the drilling process efficiency

The efficiency of the drilling process is defined as

$$\mathcal{E} = \frac{\int_{t_0}^{t_f} \mathcal{P}_{out}\, dt}{\int_{t_0}^{t_f} \mathcal{P}_{in}\, dt}, \tag{5.4}$$

where $\mathcal{P}_{out}$ is the useful (output) power used in the drilling process, and $\mathcal{P}_{in}$ is the total (input) power injected in the system, such as proposed by Ritto and Sampaio (2013) [131].

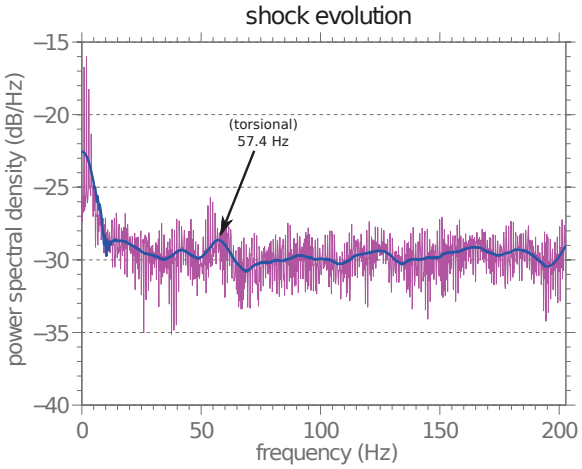

Figure 5.16: Illustration of power spectral density function of number of shocks per unit of time.

The output power is due to the drill-bit movements of translation and rotation so that

$$\mathcal{P}_{out} = \dot{u}_{bit}^{+}\,(-F_{\mathrm{BR}})^{+} \;+\; \omega_{bit}^{+}\,(-T_{\mathrm{BR}})^{+}\,, \tag{5.5}$$

where the upper script $^{+}$ means the positive part of the function. The input power is defined as

$$\mathcal{P}_{in} = \dot{u}(0,t)^{+}\,(-\lambda_1)^{+} \;+\; \dot{\theta}_x(0,t)^{+}\,(-\lambda_4)^{+}, \tag{5.6}$$

where the first and the fourth Lagrange multipliers, respectively, represent the drilling force and torque on the origin of the beam. The reason for considering, in the above definitions, only the positive part of the functions is that negative powers do not contribute to the drilling process.

One can observe the contour map of $\mathcal{E}$, for an *operating window* defined by $1/360\,\mathrm{m/s} \leq V_0 \leq 1/120\,\mathrm{m/s}$ and $3\pi/2\,\mathrm{rad/s} \leq \Omega \leq 2\pi\,\mathrm{rad/s}$, in Figure 5.17. Note that, by operating window of a drillstring, one means the subset of $\mathbb{R}^2$ that provides acceptable values for the pair $(\Omega,\, V_0)$. In order to facilitate the results interpretation, some scaling factors were introduced in the units of measure. They allow one to read the velocity in "meters per hour" and the rotation in "rotation per minute".

Accordingly, it can be noted in Figure 5.17 that the optimum operating condition is obtained at the point $(V_0, \Omega) = (1/144\,\mathrm{m/s}, 5\pi/3\,\mathrm{rad/s})$, which corresponds to an efficiency of approximately 16%, and suboptimal operation conditions occur in the vicinity of this point. Some points near the *operating window* boundary show lower efficiency.

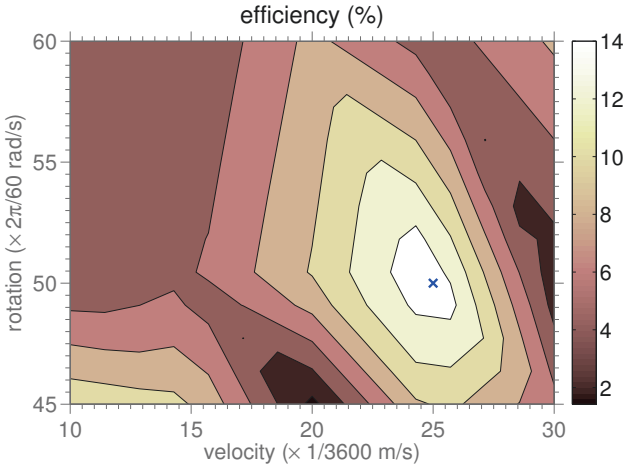

Figure 5.17: Illustration of efficiency function contour plot, for an *operating window* defined by $1/360\,\mathrm{m/s} \leq V_0 \leq 1/120\,\mathrm{m/s}$ and $3\pi/2\,\mathrm{rad/s} \leq \Omega \leq 2\pi\,\mathrm{rad/s}$.

5.11 Probabilistic analysis of the dynamics

For the probabilistic analysis of the dynamical system a parametric approach is used, where the distributions of the random parameters are constructed according to the procedure presented in chapter 4. In this case, the random variables of interest are characterized by the mean values $m_{\alpha_{\mathrm{BR}}} = 400\,1/\mathrm{m/s}$, $m_{\mathbb{\Gamma}_{\mathrm{BR}}} = 30 \times 10^3\,\mathrm{N}$, and $m_{\mathbb{\mu}_{\mathrm{BR}}} = 0.4$, and by the dispersion factors $\delta_{\alpha_{\mathrm{BR}}} = 0.5\%$, $\delta_{\mathbb{\Gamma}_{\mathrm{BR}}} = 1\%$, and $\delta_{\mathbb{\mu}_{\mathrm{BR}}} = 0.5\%$.

Initially it is necessary to analyze the convergence of MC simulations. For this purpose, it is taken into consideration the map $n_s \in \mathbb{N} \mapsto \mathtt{conv}_{\mathrm{MC}}(n_s) \in \mathbb{R}$, being

$$\mathtt{conv}_{\mathrm{MC}}(n_s) = \left(\frac{1}{n_s} \sum_{n=1}^{n_s} \int_{t=t_0}^{t_f} \left\| \mathbb{q}(t, \theta_n) \right\|^2 \, dt \right)^{1/2}, \tag{5.7}$$

where n_s is the number of MC realizations, and $\|\cdot\|$ denotes the standard Euclidean norm. This metric allows one to evaluate the convergence of the approximation $\mathbb{q}(t, \theta_n)$ in the mean-square sense. For further details the reader is encouraged to see Soize (2005) [26].

The evolution of $\mathtt{conv}(n_s)$ as a function of n_s can be seen in Figure 5.18. Note that for $n_s = 1024$ the metric value has reached a steady value. In this sense, if something is not stated otherwise, all the stochastic simulations that follows in this work use $n_s = 1024$.

An illustration of the mean value (blue line), and a confidence band (grey shadow), wherein a realization of the stochastic dynamic system has 95% of probability of being contained, for the drill-bit longitudinal displacement and

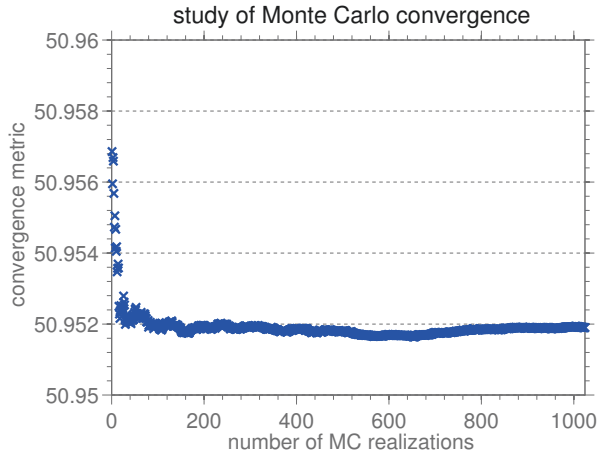

Figure 5.18: This figure illustrates the convergence metric of MC simulation as a function of the number of realizations.

velocity is shown in Figure 5.19. For sake of reference, the deterministic model, which the numerical results were presented earlier, is also presented and called the nominal model (red line). It is observed that the mean value is very similar to the nominal model for the displacement. Meanwhile, for the velocity the mean value presents oscillations that are correlated with the nominal model, but with very different amplitudes. Regarding the confidence band, there is a significant amplitude in the instants that corresponds to the packages of fluctuation and negligible amplitude in the other moments.

Fixing the time in $t = 10\,\mathrm{s}$, it is possible to analyze the behavior of the drill-bit longitudinal velocity through its normalized PDF, which is presented in Figure 5.20. In this context normalized means a distribution of probability with zero mean and unit standard deviation. It is observed a unimodal behavior, with the maximum value occurring in a neighborhood of the mean value. The narrow shape of the PDF curve shows that, at the analyzed instant, the drill-bit longitudinal velocity presents small dispersion around the mean value.

In Figure 5.21, the reader can see the nominal model, the mean value, and the 95% probability envelope of drill-bit rotation and angular velocity. A good agreement between the nominal model and the mean value of the rotation is observed, and the confidence band around it is negligible. On the other hand, with respect to the angular velocity, it is possible to see discrepancies in the amplitudes of the nominal model and the mean value. These differences occur in the instants when the system is subject to shocks, as in the case of drill-bit longitudinal velocity. The band of uncertainty shows that the dispersion around the mean increases with time due to the uncertainties of accumulation, but also in reason of the impacts, once its amplitude increases a lot near the

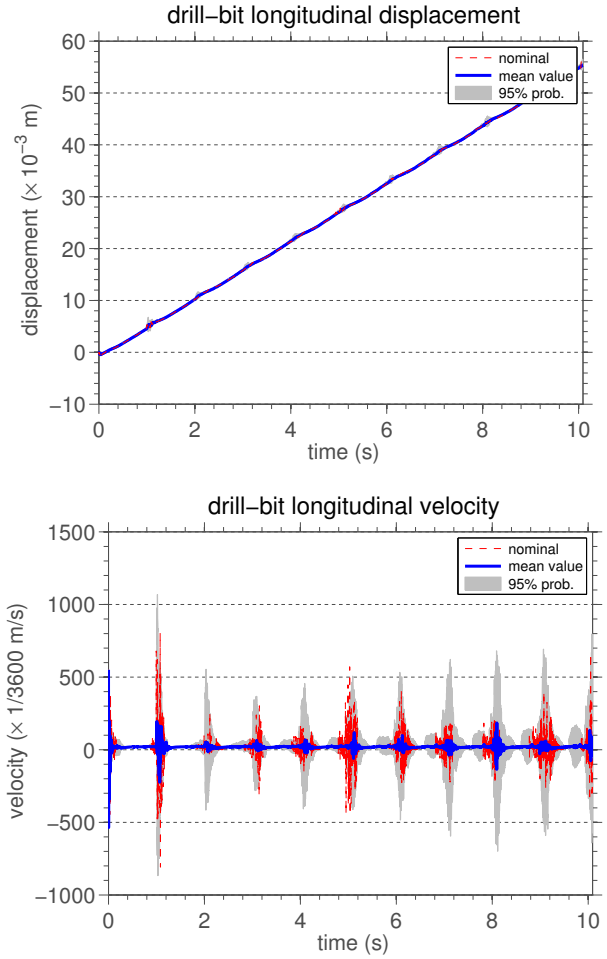

Figure 5.19: Illustration of the nominal model (red line), the mean value (blue line), and the 95% probability envelope (grey shadow) for the drill-bit longitudinal displacement (top) and velocity (bottom).

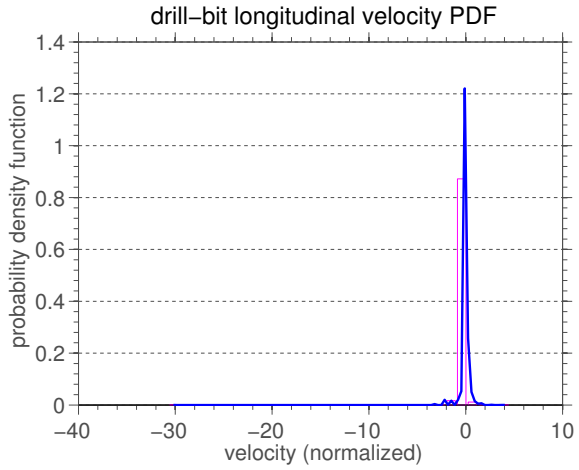

Figure 5.20: Illustration of the normalized probability density function of the drill-bit longitudinal velocity.

instants where the mean value presents large fluctuations, i.e., the instants which are correlated to the impacts between the beam and the borehole wall.

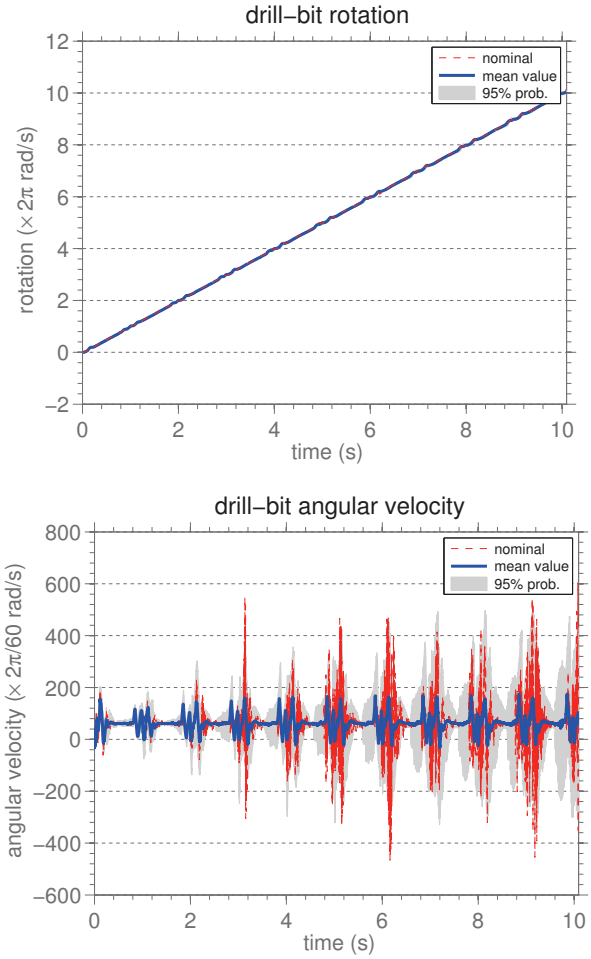

Figure 5.21: Illustration of the mean value (blue line) and the 98% probability envelope (grey shadow) for the drill-bit rotation (top) and angular velocity (bottom).

For $t = 10\,\text{s}$, the reader can see the normalized PDF of the drill-bit angular velocity in Figure 5.22. It is noted again an unimodal behavior, with the maximum again near mean value. But now the wide shape of the PDF curve shows that, at the analyzed instant, the drill-bit longitudinal angular velocity presents large dispersion around the mean value.

Moreover, in Figure 5.23 it is shown the nominal model, the mean value, and the 95% probability envelope of the beam transversal displacement and velocity in z at $x = 50\,\text{m}$. Here the mean values of both, velocity and displacement, present correlation with the nominal models. Indeed, both present discrepancies in the oscillation amplitudes, especially the velocity, discrepancies that are more pronounced, as before, in the instants wherein the system is subject to impacts. The confidence bands present meaningful amplitudes, what evidentiates a certain level of dispersion around the means, which are more significant, as expected, at the instants of impact.

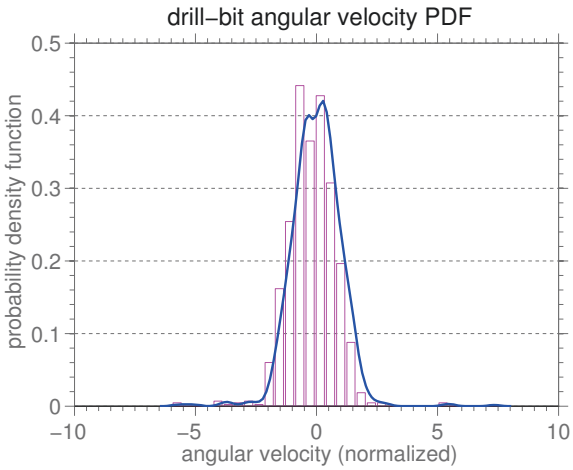

Figure 5.22: Illustration of the normalized probability density function of the drill-bit angular velocity.

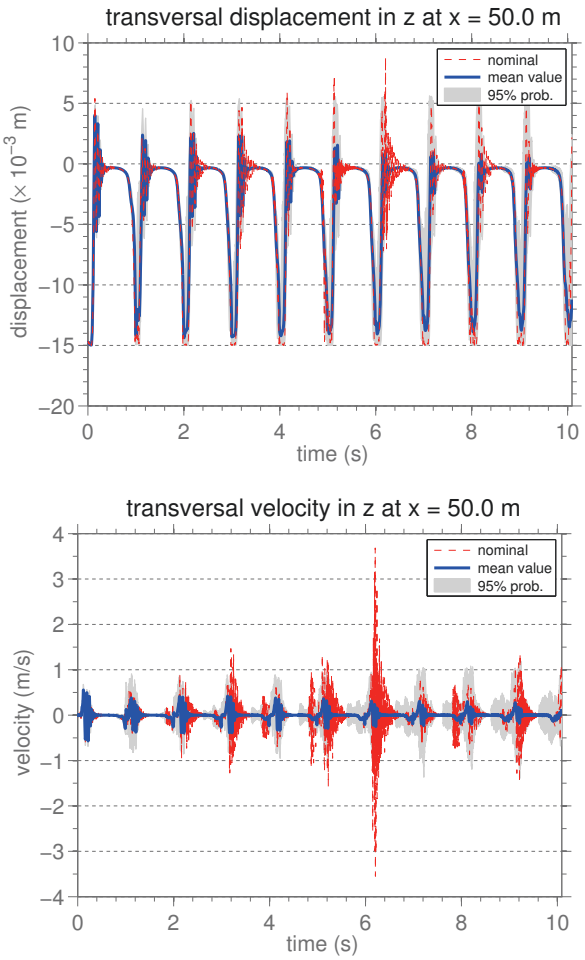

Figure 5.23: Illustration of the mean value (blue line) and the 98% probability envelope (grey shadow) for the beam transversal displacement (top) and velocity in z (bottom) at $x = 50\,\mathrm{m}$.

The PDF of the drilling process efficiency function it is shown in Figure 5.24. One can observe a unimodal distribution with the maximum around

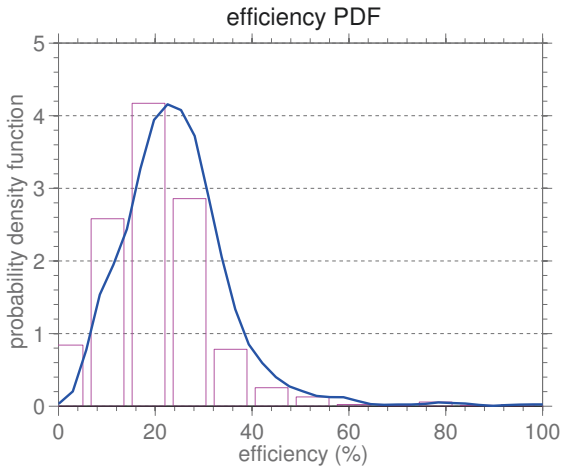

Figure 5.24: Illustration of the probability density function of the drilling process efficiency.

16% and wide dispersion between 0 and 40%, declining rapidly to negligible values outside this range. This probability distribution is compatible with a real drilling system, which is known to be extremely inefficient.

Finally, in Figure 5.25 one can see the PDF of the drillstring rate of penetration function. One notes an unimodal behavior in a narrow range between 20 and 50 "meters per hour", with the maximum around 30 "meters per hour". Once these value for the ROP are within a realistic range, the PDF may be reasonable.

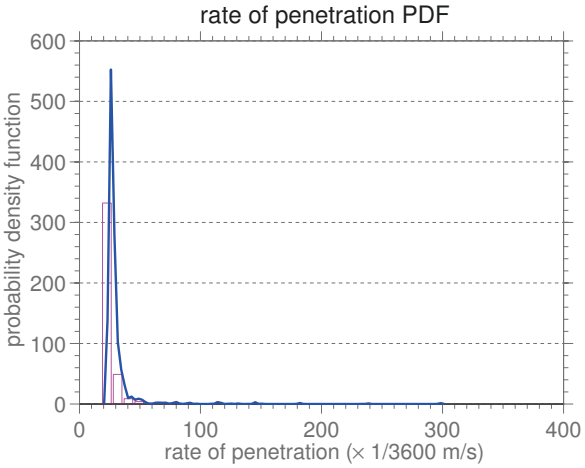

Figure 5.25: Illustration of the probability density function of the rate of penetration function.

6
Optimization of Drilling Process

This chapter concerns about the drilling process optimization. For this purpose, it presents the deterministic formulation of an optimization problem, with constraint, that seeks to maximize the drillstring ROP into the soil, the algorithm used to solve the problem, the stochastic version of the problem, by means of a robust optimization problem formulation, and numerical results.

6.1
Formulation of deterministic optimization problem

In order to optimize the drilling process of an oil well in horizontal configuration, it is necessary to maximize the drillstring ROP into the soil. To "drive" a drillstring, an operator has three parameters available (rotation frequency, WOB, and volumetric flow rate). In the model used in this thesis, the first two control parameters are respectively identified with Ω, and V_0, while the volumetric flow rate is ignored, once the flow inside the tube is not taken into account. Thus, the optimization problem that will be treated in this chapter seek to find, within the drillstring *operating window*, pairs of the form (Ω, V_0) that make drillstring penetration into the soil maximum, subject to the restrictions (imposed by structural limits) that will be defined below.

The instantaneous rate of penetration is given by the function $\dot{u}_{bit}(t)$, defined for all instants of analysis. Meanwhile, as objective function, it is more convenient to consider a scalar function. Thus, the temporal mean of $\dot{u}_{bit}(t)$ is adopted as the rate of penetration, and, consequently, objective function of the optimization problem

$$\texttt{rop}(\Omega, V_0) = \frac{1}{t_f - t_0} \int_{t=t_0}^{t_f} \dot{u}_{bit}^{+}(t)\, dt. \tag{6.1}$$

Furthermore, respect the structural limits is indispensable to avoid failures of drillstring during the drilling process. For this reason, von Mises criterion of failure is considered.

In this criterion, the von Mises equivalent stress is defined by

$$\sigma_{VM} = \sqrt{\frac{(\sigma_{xx} - \sigma_{yy})^2 + (\sigma_{yy} - \sigma_{zz})^2 + (\sigma_{zz} - \sigma_{xx})^2 + 6\,(\sigma_{xy} + \sigma_{yz} + \sigma_{zx})^2}{2}}, \tag{6.2}$$

which, after the replacement of Eqs.(3.31) and (3.32), is equivalent to

$$\sigma_{VM}(V_0,\, \Omega,\, x,\, t) = \sqrt{(E\,\epsilon_{xx})^2 + 12\,(G\,\epsilon_{xy})^2 + 12\,(G\,\epsilon_{xz})^2}, \tag{6.3}$$

a function depending on x and t, besides the operating parameters. Moreover, it is established that, for all pairs $(\Omega,\, V_0)$ in the *operating window*,

$$\texttt{UTS} - \max_{\substack{0 \le x \le L \\ t_0 \le t \le t_f}} \left\{\sigma_{VM}(V_0,\, \Omega,\, x,\, t)\right\} \ge 0, \tag{6.4}$$

where UTS is the ultimate tensile strength of the material.

In formal terms, the deterministic optimization problem of drillstring ROP can be read as follows:

Find a pair $(V_0,\, \Omega)$*, in the operating window, that maximizes the objective function given by (6.1), respecting the constraint imposed by (6.4).*

6.2 Solution algorithm for optimization problem

The first question that should be raised about this optimization problem is the existence of a solution. Since it is nonlinear and nonconvex, there is no guarantee on the existence of a global maximum. Besides that, if the global maximum exists, one can not expect to find an algorithm to search it in finite time. The best that can be done is to find a local maximum in the feasible region (Bazaraa et al. 2006) [132].

Furthermore, since the evaluation of the objective function is done through a finite element code, from the computational point of view, this optimization problem is extremely costly, making it unfeasible search for extremes candidates via gradient based methods (Nocedal and Wright 2006) [133].

In this way, to construct an approximation for the optimization problem solution, it is adopted a strategy that consists in building a surrogate surface that emulates the objective function (Queipo et al. 2005) [134]. To do this the objective function is evaluated in a structured grid of points, previously defined, in the *operating window*. Then the contour lines of the function are interpolated through these points, and, thereby, one constructs an approximation to the function contour map. The same procedure is repeated with the constraint of the optimization problem. Finally, the points that satisfy the constraint in the *operating window* are verified, and with then it is defined the *admissible*

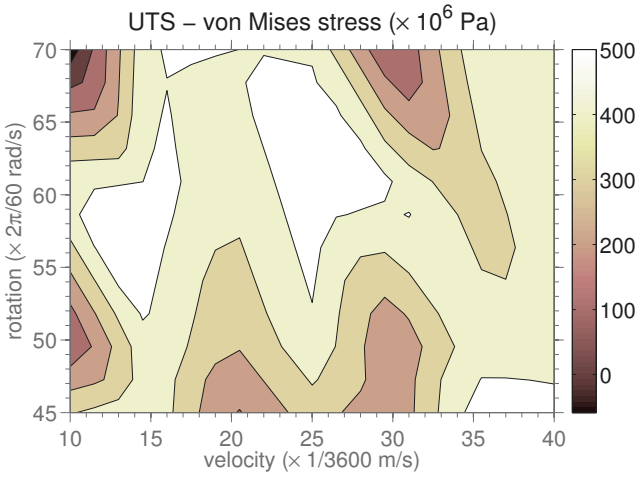

Figure 6.1: Illustration of maximum von Mises stress contour plot, for an *operating window* defined by $1/360\ m/s \leq V_0 \leq 1/90\ m/s$ and $3\pi/2\ rad/s \leq \Omega \leq 7\pi/3\ rad/s$.

region. Within the admissible region it is done the search for the point of local maximum. As the interpolation used is linear, local extremes always occur in the structured grid of points, so that only these points are evaluated to get the maximum.

6.3 Optimum value for rate of penetration

Regarding the analysis of the rate of penetration, the *operating window* is defined by the inequalities $1/360\ m/s \leq V_0 \leq 1/90\ m/s$ and $3\pi/2\ rad/s \leq \Omega \leq 7\pi/3\ rad/s$.

The contour map of the constraint (6.4), is shown in Figure 6.1. From the way constraint (6.4) is written, the Mises criterion is not satisfied when the function is negative, which occurs in a "small neighborhood" of the upper left corner of the rectangle that defines the *operating window*. It is noted that all other points respect the structural limits of the material. Then, the admissible region of the *operating window* consists of all points that satisfy the constraint.

In Figure 6.2 the reader can see the contour map of the function `rop`. Taking into account only points in the admissible region, the maximum of `rop` occurs at the point $(V_0, \Omega) = (7/720\ m/s, 2\pi\ rad/s)$, which is indicated on the graph with a blue cross. This point corresponds to a mean rate of penetration, during the time interval analyzed, approximately equal to 90 "meters per hour".

It is worth remembering that the definition of `rop` uses temporal mean of the positive part of $\dot{u}_{bit}(t)$. In such a way, it is not surprising to find the maximum value of `rop` much higher than the corresponding velocity, V_0 imposed on the left end of the column. This occurs because, by taking only

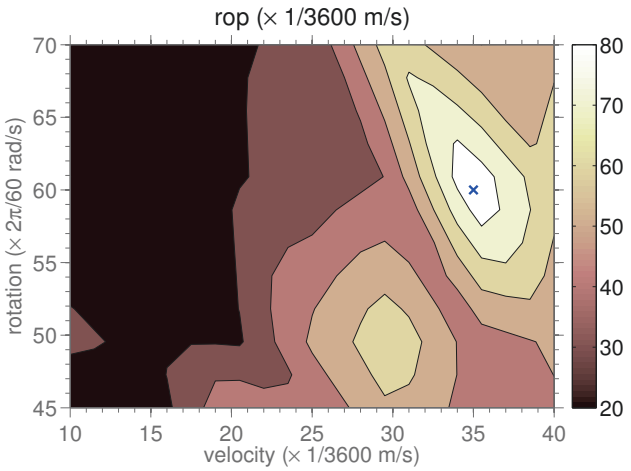

Figure 6.2: Illustration of rate of penetration function contour plot, for an *operating window* defined by $1/360\ m/s \leq V_0 \leq 1/90\ m/s$ and $3\pi/2\ rad/s \leq \Omega \leq 7\pi/3\ rad/s$. The maximum is indicated with a blue cross.

the positive part of the function, the rate of penetration value increases.

To see how significant is the inclusion of the positive part of $\dot{u}_{bit}(t)$ in the definition of `rop`, the reader can see in Figure 6.3. This Figure shows the same information as Figure 6.2, i.e., the contour map of the function `rop`, but now considering $\dot{u}_{bit}(t)$ instead of $\dot{u}^{+}_{bit}(t)$ in the definition of `rop`. Note that, in comparison with the contour map of Figure 6.2, lower values for the levels of the function are observed, and these values are now are closer to the values of V_0. Furthermore, the topology of contour lines change, so that no local extreme point can be seen isolated. This example shows the importance of considering $\dot{u}^{+}_{bit}(t)$ in the definition of `rop`.

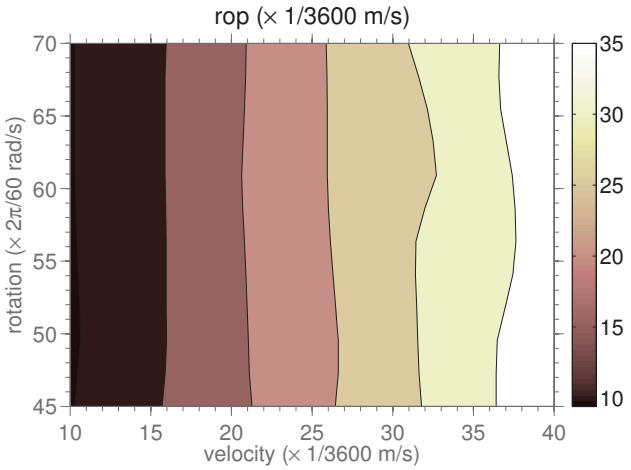

Figure 6.3: Illustration of the contour plot of the rate of penetration function, with an alternative definition, for an *operating window* defined by $1/360\ m/s \leq V_0 \leq 1/90\ m/s$ and $3\pi/2\ rad/s \leq \Omega \leq 7\pi/3\ rad/s$.

6.4 Formulation of robust optimization problem

To improve the level of confidence of the drilling process optimization, the uncertainties intrinsic to the problem should be taken into account, for instance, such as is done in Ritto et al. (2010) [93]. This leads to a robust optimization problem, i.e, optimization under uncertainty where the range of the random parameters are known, but not necessarily their distribution (Beyer and Sendhoff, 2007) [135], (Capiez-Lernout and Soize, 2008) [136, 137, 138], (Soize et al., 2008) [139], (Schuëller and Jensen, 2008) [140], (Ben-Tal et al., 2009) [141].

Taking into account the uncertainties, through the parametric approach presented in chapter 4, drill-bit velocity becomes the stochastic process $\mathbb{U}_{bit}(t,\theta)$, so that the random rate of penetration is defined by

$$\mathbb{ROP}(V_0,\,\Omega,\theta) = \frac{1}{t_f - t_0}\int_{t=t_0}^{t_f} \dot{\mathbb{U}}^{+}_{bit}(t,\theta)\,dt. \tag{6.5}$$

In the robust optimization problem, who plays the role of the objective function is not the random variable $\mathbb{ROP}(V_0,\,\Omega,\theta)$, but its expected value, i.e., $\mathbb{E}\left[\mathbb{ROP}(V_0,\,\Omega,\theta)\right]$.

Regarding the restriction imposed by the von Mises criteria, now the equivalent stress is a random field $\varpi_{VM}(V_0,\,\Omega,\,x,\,t,\theta)$, so that the inequality is written as

$$\texttt{UTS} - \max_{\substack{0\le x\le L\\ t_0\le t\le t_f}} \left\{\varpi_{VM}(V_0,\,\Omega,\,x,\,t,\theta)\right\} \ge 0. \tag{6.6}$$

However, the robust optimization problem considers as restriction the probability of the event defined by inequality (6.6),

$$\mathbb{P}\left\{\texttt{UTS} - \max_{\substack{0\le x\le L\\ t_0\le t\le t_f}} \left\{\varpi_{VM}(V_0,\,\Omega,\,x,\,t,\theta)\right\} \ge 0\right\} \ge 1 - P_{risk}, \tag{6.7}$$

where $0 < P_{risk} < 1$ is the risk percentage acceptable to the problem.

In formal terms, the robust optimization problem of drillstring ROP can be read as follows:

Find a pair $(V_0,\,\Omega)$*, in the operating window, that maximizes* $\mathbb{E}\left[\mathbb{ROP}(V_0,\,\Omega,\theta)\right]$*, respecting the probabilistic constraint imposed by (6.7).*

A robust optimization problem very similar to this one, in the context of a vertical drillstring dynamics, is considered by Ritto et al. (2010) [93]. In this work the authors also take into account as constraints the material limit of fatigue and a stability factor against stick-slip, which were not considered here for simplicity.

6.5
Robust optimum value for rate of penetration

To solve this robust optimization problem it is employed the same strategy used for the deterministic optimization problem, only considering the new objective function $\mathbb{E}\left[\mathbb{ROP}(V_0,\, \Omega, \theta)\right]$ and the probabilistic constraint (6.7).

Accordingly, it is considered the same "operating window" used in the deterministic optimization problem solved above, i.e., $1/360\ m/s \leq V_0 \leq 1/90\ m/s$ and $3\pi/2\ rad/s \leq \Omega \leq 7\pi/3\ rad/s$, in addition to $\texttt{UTS} = 650{\times}10^6\ Pa$ and $P_{risk} = 10\%$. Each MC simulation in this case used 128 realizations to compute the propagation of uncertainties.

Concerning the simulation results, the probabilistic constraint (6.7) is respected in all grid points that discretize the "operating window". Thus, the admissible region of the robust optimization problem is equal to the "operating window". In what follows, the contour map of the function $\mathbb{E}\left[\mathbb{ROP}(V_0,\, \Omega, \theta)\right]$ can be see in Figure 6.4. Note that the maximum, which is indicated on the graph with a blue cross, occurs at at the point $(V_0, \Omega) = (1/90\ m/s, 7\pi/3\ rad/s)$. This point is located in the boundary of the admissible region, in the upper right corner, and corresponds to a expected value of the mean rate of penetration, during the time interval analyzed, approximately equal to 58 "meters per hour".

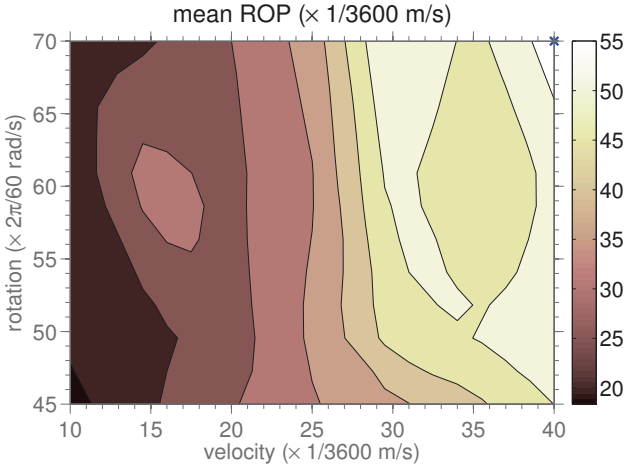

Figure 6.4: Illustration of the contour plot of the mean rate of penetration function, for an *operating window* defined by $1/360\ m/s \leq V_0 \leq 1/90\ m/s$ and $3\pi/2\ rad/s \leq \Omega \leq 7\pi/3\ rad/s$. The maximum is indicated with a blue cross in the upper right corner.

This result says that, in the *operating window* considered here, increasing the drillstring rotational and translational velocities provides the most robust strategy to maximize its ROP into the soil. This is in some ways an intuitive result, but is at odds with the result of the deterministic optimization problem, which provides another strategy to achieve optimum operating condition.

The contrast between the two results opens an interesting perspective regarding the optimization of the drilling process, since it is clearly shown that include the uncertainties in the formulation makes a big difference in the resulting optimization strategy.

7
Concluding Remarks

This chapter recalls the theme addressed in the thesis, summarizes and highlights its main conclusions and contributions, suggest some paths for future works, and list the resulting publications.

7.1
Thematic addressed in the thesis

This work was motivated by the economic importance that oil exploration has in the global scenario, looking in particular to a problem associated with the drilling of oil wells in horizontal configuration.

In this context, the thesis proposed to develop a mechanical-mathematical model to describe the three-dimensional nonlinear dynamics of horizontal drillstrings, taking into account friction and shocks phenomena that are due to the mechanical contacts between the pairs drill-bit/soil and drill-pipes/borehole. It was also objectified to construct a stochastic model to take into account the uncertainties in the mechanical-mathematical model that are due to the variability on its parameters.

Once the models have been developed, the next objective was to analyze the mechanical system of interest, in order to obtain a better understanding its nonlinear behavior. Indeed, it was intended to optimize the drilling process, by maximizing the ROP of the drillstring into the soil, to reduce the costs of production of an oil well.

7.2
Contributions and conclusions of the thesis

A mechanical-mathematical model was developed in this work to describe the nonlinear dynamics of horizontal drillstrings. The construction of this model passed through the steps of: (i) definition of the physical system of interest; (ii) parameterization of the nonlinear dynamics; and (iii) description of the physical phenomena of interest. In this context, the structure dynamic is described by a beam theory, with effects of rotatory inertia and shear deformation, which is capable of reproducing large displacements that the

beam undergoes. The model also considers the friction and shock effects due to transversal impacts, as well as, the force and torque induced by the bit-rock interaction. The model equations are deduced in a formal way, and a variational formulation for the problem is presented, where each of the mathematical operators involved is defined in infinite dimension.

It was also presented the construction of a computational model to approximate the solution of the initial/boundary value problem associated with the mechanical-mathematical model that describes the nonlinear dynamical behavior of a horizontal drillstring. This model uses the standard finite element method to discretize the model equations, and the resulting initial value problem is projected in the space spanned by the linear modes associated to the conservative part of the underlying linear dynamical system to reduce the order of the model. The reduced dynamics is integrated using the Newmark method, and the nonlinear system of algebraic equations, resulting from the time discretization, is solved by a fixed point iteration. This computational model was efficiently implemented in a `MATLAB` code.

Regarding the uncertainties treatment, this thesis presented the construction of a parametric probabilistic model for description of the uncertainties associated with the parameters of the bit-rock interaction model. These parameters were assumed to be random variables, and their distributions were specified using only the known information about them, through the principle of maximum entropy. The propagation of uncertainties of these parameters through the nonlinear dynamics was calculated using the Monte Carlo method.

Numerical simulations showed that the mechanical system of interest has a very rich nonlinear dynamics, which reproduces complex phenomena such as bit-bounce, stick-slip, and transverse impacts. The study also indicated that the large velocity fluctuations observed in the phenomena of bit-bounce and stick-slip are correlated with the transverse impacts, i.e., with the number of shocks per unit time which the system is subjected. Also, the mechanical impacts cause the beam to assume complex spatial configurations, which are formed by flexural modes associated to high natural frequencies.

A study aiming to maximize the drilling process efficiency, varying drillstring velocities of translation and rotation was presented. The optimization strategy used a trial approach to seek for a local maximum, which was located within *operating window* and corresponds to an efficiency of approximately 16%.

The probabilistic analysis of the nonlinear dynamics showed that, with respect to the velocities, the nominal model and the mean value of the stochastic model differ significantly. Furthermore, at the instants which the system was subjected to mechanical impacts, it was possible to see a more pronounced dispersion around the mean value. Regarding the probability distributions of the velocities, it was noticed a unimodal behavior essentially.

Two optimizations problems, one deterministic and one robust, where the objective was to maximize the drillstring rate of penetration into the soil respecting its structural limits were formulated and solved. The solutions of these problems provided two different strategies to optimize the ROP.

7.3 Suggestions for future works

In the simulations conducted in this study, the whirl phenomenon was not detected, although it is very common in the dynamics of vertical drillstrings. This issue has not been investigated in depth, but could have been evaluated with the model developed in this thesis, as well as the possibility of the horizontal drillstring presents mechanisms of helical/sinusoidal buckling.

Other natural suggestion for future work is to compare the predictive capacity of the beam model presented in this work with simpler models, based on the lumped parameters approach. For instance, Jansen (1993) [11] and Divenyi et al. (2012) [57]. It is of interest to determine the limitations of prediction for each model, the similarities and differences between the responses of the models, etc.

Since this work only takes into account the uncertainties of the parameters of the drill-rock interaction model, a future work on stochastic modeling can use the nonparametric probabilistic approach (Soize, 2013) [22] to address the model uncertainties.

An interesting application would be to develop a control system for the drilling process, based on the model developed in this thesis, for regulating drillstring *driving parameters* to take the ROP always close to the optimal value. This control system can also be used to avoid oscillations such as stick-slip and bit bounce, which may be harmful and lead to an early failure of the structure.

Despite being optimized, the computational model developed in this work is expensive in terms of time complexity. This opens space for a series of future work to reduce the cost of the model, either through the use of more efficient numerical algorithms, or using advanced reduction techniques, or by the use of high performance computing resources, such as GPU.

Finally, it sounds stressing the mechanical-mathematical model used in this work has not gone through any process of experimental validation (Oberkampf and Roy, 2010) [142]. This is because experimental data for this type of system is difficult to be obtained, and to construct an experimental apparatus in real scale is virtually impossible. Another interesting proposal for future work would be the construction of an experimental test rig, in reduced scale, that emulates the main aspects of a real drillstring. The model used in this study could be validated, following, for instance, the methodology presented by Batou and Soize (2009) [143], with the aid of experimental measurements taken from this reduced apparatus. The measurements obtained in this test rig could also be used to calibrate the model parameters, by solving an inverse problem of parameters identification (Allmaras et al., 2014) [144].

7.4 Publications

During his period in the doctorate, the author published, with the advisors and other collaborators, 6 research articles and submitted another one for publication in peer-reviewed journals, and presented 10 works at scientific conferences.

The articles published or submitted for publication in scientific journals are:

[J1] A. Cunha Jr, C. Soize, and R. Sampaio. Computational modeling of the nonlinear stochastic dynamics of horizontal drillstrings, (submitted for publication).

[J2] A. Cunha Jr and R. Sampaio. On the nonlinear stochastic dynamics of a continuous system with discrete attached elements. *Applied Mathematical Modelling*, 39:809—819, 2015. doi:10.1016/j.apm.2014.07.012.

[J3] A. Cunha Jr, R. Nasser, R. Sampaio, H. Lopes, and K. Breitman. Uncertainty quantification through Monte Carlo method in a cloud computing setting. *Computer Physics Communications*, 185:1355—1363, 2014. doi:10.1016/j.cpc.2014.01.006.

[J4] A. Cunha Jr and R. Sampaio. Study of the nonlinear longitudinal dynamics of a stochastic system. *MATEC Web of Conferences*, 16:05004, 2014. doi:10.1051/matecconf/20141605004.

[J5] A. Cunha Jr, C. Soize, and R. Sampaio. Exploring the nonlinear dynamics of horizontal drillstrings subjected to friction and shocks effects. *Mecánica Computacional*, 33:1517–1527, 2014. http://www.cimec.org.ar/ojs/index.php/mc/article/view/4750.

[J6] M. G. Sandoval, A. Cunha Jr, and R. Sampaio. Identification of parameters in the torsional dynamics of a drilling process through Bayesian statistics. *Mecánica Computacional*, 32:763–773, 2013. http://www.cimec.org.ar/ojs/index.php/mc/article/view/4388.

[J7] A. Cunha Jr and R. Sampaio. Effect of an attached end mass in the dynamics of uncertainty nonlinear continuous random system. *Mecánica Computacional*, 31:2676–2683, 2012. http://www.cimec.org.ar/ojs/index.php/mc/article/view/4214.

The works presented at scientific conferences are:

[C1] A. Cunha Jr, C. Soize, and R. Sampaio. Mathematical modeling of horizontal drillstrings subjected to friction and shocks effects. In *XXXV Congresso Nacional de Matemática Aplicada e Computacional*, Natal, Brazil, 2014.

[C2] A. Cunha Jr, C. Soize, and R. Sampaio. Numerical study of the nonlinear dynamics of horizontal drillings. In *8th European Nonlinear Dynamics Conference*, Vienna, Austria, 2014.

[C3] A. Cunha Jr, C. Soize, and R. Sampaio. Analysis of the nonlinear dynamics of a horizontal drillstring. In *9th International Conference on Structural Dynamics*, Porto, Portugal, 2014.

[C4] A. Cunha Jr and R. Sampaio. Effects of a random cubic spring on the longitudinal dynamics of a bar excited by a gaussian white noise. In *2nd International Symposium on Uncertainty Quantification and Stochastic Modeling*, Rouen, France, 2014.

[C5] A. Cunha Jr, C. Soize, and R. Sampaio. A deterministic approach to analyze the nonlinear dynamics of a horizontal drillstring. In *12th Conference on Dynamical Systems - Theory and Applications*, Łódź, Poland, 2013. (resume).

[C6] A. Cunha Jr, R. Nasser, R. Sampaio, H. Lopes, and K. Breitman. Uncertainty quantification using cloud computing for Monte Carlo parallelization. In *22th International Congress of Mechanical Engineering*, Ribeirão Preto, Brazil, 2013.

[C7] A. Cunha Jr and R. Sampaio. Analysis of the nonlinear stochastic dynamics of an elastic bar with an attached end mass. In *3rd South-East European Conference on Computational Mechanics*, Kos Island, Greece, 2013.

[C8] A. Cunha Jr and R. Sampaio. Uncertainty propagation in the dynamics of a nonlinear random bar. In *XV International Symposium on Dynamic Problems of Mechanics*, Armação dos Búzios, Brazil, 2013.

[C9] A. Cunha Jr and R. Sampaio. Exploring Monte Carlo method to access the dynamical behavior of a continuous random system. In *Congresso de Matemática Aplicada e Computacional - Nordeste 2012*, Natal, Brazil, 2012. (resume).

[C10] A. Cunha Jr and R. Sampaio. On the dynamics of a nonlinear continuous random system. In *1st International Symposium on Uncertainty Quantification and Stochastic Modeling*, Maresias, Brazil, 2012.

All the publications above are related to the area of stochastic modeling and uncertainty quantification, in the context of nonlinear dynamics of mechanical systems. The journal articles whose the content is directly related to the research developed in this thesis can be seen in the Appendix C.

Bibliography

[1] CHISHOLM, H. **"Petroleum" The Encyclopædia Britannica**, volume 21. 11th. ed., Cambridge: Cambridge University Press, 1911.

[2] MINISTRY OF MINES AND ENERGY – MME. **Brazilian Energy Balance 2014: Year 2013**. Rio de Janeiro: Empresa de Pesquisa Energética, 2014. 288p.

[3] THE ECONOMIST. **Cheaper oil: Winners and losers**, Oct 25th 2014. http://www.economist.com/node/21627642.

[4] FREUDENRICH, C.; STRICKLAND, J. **How Oil Drilling Works**, 2001. http://www.howstuffworks.com/oil-drilling.

[5] FOLHA DE SÃO PAULO. **Entenda o que é a camada pré-sal**, Aug 31, 2009. http://folha.com/no440468.

[6] THE ECONOMIST. **Brazil's oil boom: Filling up the future**, Nov 5, 2011. http://www.economist.com/node/21536570.

[7] WILLOUGHBY, D. **Horizontal Directional Drilling (HDD): Utility and Pipeline Applications**. New York: McGraw-Hill, 2005. 400p.

[8] KING, H. M. **Directional and Horizontal Drilling in Oil and Gas Wells**, 2012. http://geology.com/articles/horizontal-drilling.

[9] THE ECONOMIST. **Oilfield services: The unsung masters of the oil industry**, Jul 21st 2012. http://www.economist.com/node/21559358.

[10] MACDONALD, K. A.; BJUNE, J. V. Failure analysis of drillstrings. **Engineering Failure Analysis**, v.14, p. 1641–1666, 2007. doi:10.1016/j.engfailanal.2006.11.073.

[11] JANSEN, J. D. **Nonlinear Dynamics of Oilwell Drillstrings**. Amsterdam, 1993. Ph.D. Thesis, TU Delft.

[12] SOIZE, C. **Stochastic Models of Uncertainties in Computational Mechanics**. Reston: American Society of Civil Engineers, 2012. 125p.

[13] MOENS, D.; VANDEPITTE, D. A survey of non-probabilistic uncertainty treatment in finite element analysis. **Computer Methods in Applied Mechanics and Engineering**, v.194, p. 1527–1555, 2005. doi:10.1016/j.cma.2004.03.019.

[14] MOENS, D.; HANSS, M. Non-probabilistic finite element analysis for parametric uncertainty treatment in applied mechanics: Recent advances. **Finite Elements in Analysis and Design**, v.47, p. 4–16, 2011. doi:10.1016/j.finel.2010.07.010.

[15] BEER, M.; FERSON, S. ; KREINOVICH, V. Imprecise probabilities in engineering analyses. **Mechanical Systems and Signal Processing**, v.37, p. 4–29, 2013. doi:10.1016/j.ymssp.2013.01.024.

[16] SCHUËLLER, G. I. A state-of-the-art report on computational stochastic mechanics. **Probabilistic Engineering Mechanics**, v.12, p. 197–321, 1997. doi:10.1016/S0266-8920(97)00003-9.

[17] SCHUËLLER, G. I. Computational stochastic mechanics – recent advances. **Computers & Structures**, v.79, p. 2225–2234, 2001. doi:10.1016/S0045-7949(01)00078-5.

[18] SCHUËLLER, G. I. Developments in stochastic structural mechanics. **Archive of Applied Mechanics**, v.75, p. 755–773, 2006. doi:10.1007/s00419-006-0067-z.

[19] SCHUËLLER, G. I. On the treatment of uncertainties in structural mechanics and analysis. **Computers & Structures**, v.85, p. 235–243, 2007. doi:10.1016/j.compstruc.2006.10.009.

[20] SCHUËLLER, G. I.; PRADLWARTER, H. J. Uncertain linear systems in dynamics: Retrospective and recent developments by stochastic approaches. **Engineering Structures**, v.31, p. 2507–2517, 2009. doi:10.1016/j.engstruct.2009.07.005.

[21] SCHUËLLER, G. I.; PRADLWARTER, H. J. Uncertainty analysis of complex structural systems. **International Journal for Numerical Methods in Engineering**, v.80, p. 881–913, 2009. doi:10.1002/nme.2549.

[22] SOIZE, C. Stochastic modeling of uncertainties in computational structural dynamics — recent theoretical advances. **Journal of Sound and Vibration**, v.332, p. 2379—2395, 2013. doi:10.1016/j.jsv.2011.10.010.

[23] SOIZE, C. A nonparametric model of random uncertainties for reduced matrix models in structural dynamics. **Probabilistic Engineering Mechanics**, v.15, p. 277–294, 2000. doi:10.1016/S0266-8920(99)00028-4.

[24] SOIZE, C. Maximum entropy approach for modeling random uncertainties in transient elastodynamics. **Journal of the Acoustical Society of America**, v.109, p. 1979–1996, 2001. doi:10.1121/1.1360716.

[25] SOIZE, C. Random matrix theory and non-parametric model of random uncertainties in vibration analysis. **Journal of Sound and Vibration**, v.263, p. 893–916, 2003. doi:10.1016/S0022-460X(02)01170-7.

[26] SOIZE, C. A comprehensive overview of a non-parametric probabilistic approach of model uncertainties for predictive models in structural dynamics. **Journal of Sound and Vibration**, v.288, p. 623–652, 2005. doi:10.1016/j.jsv.2005.07.009.

[27] SOIZE, C. Generalized probabilistic approach of uncertainties in computational dynamics using random matrices and polynomial chaos decompositions. **International Journal for Numerical Methods in Engineering**, v.81, p. 939–970, 2010. doi:10.1002/nme.2712.

[28] BATOU, A.; SOIZE, C. ; CORUS, M. Experimental identification of an uncertain computational dynamical model representing a family of structures. **Computers & Structures**, v.89, p. 1440–1448, 2011. doi:10.1016/j.compstruc.2011.03.004.

[29] CHEVALLIER, A. **Nonlinear Stochastic Drilling Vibrations**. Houston, 2000. Ph.D. Thesis, Rice University.

[30] SPANOS, P. D.; CHEVALLIER, A. M.; POLITIS, N. P. ; PAYNE, M. L. Oil and gas well drilling: a vibrations perspective. **The Shock and Vibration Digest**, v.35, p. 85–103, 2003.

[31] THE ECONOMIST. **Oilfield-service firms: Knowing the drill**, Nov 2, 2014. `http://www.economist.com/node/21633873`.

[32] THE ECONOMIST. **The outlook for the oil price: Bust and boom**, May 21st 2009. `http://www.economist.com/node/13693010`.

[33] DEILY, F. H.; DAREING, D. W.; PAFF, G. H.; ORTLOFF, J. E. ; LYNN, R. D. Downhole measurements of drill string forces and motions. **Journal of Engineering for Industry**, v.90, p. 217–225, 1968. doi:10.1115/1.3604617.

[34] BAILEY, J. J.; FINNIE, I. An analytical study of drill-string vibration. **Journal of Engineering for Industry**, v.82, p. 122–127, 1960. doi:10.1115/1.3663017.

[35] FINNIE, I.; BAILEY, J. J. An experimental study of drill-string vibration. **Journal of Engineering for Industry**, v.82, p. 129–135, 1960. doi:10.1115/1.3663020.

[36] CUNNINGHAM, R. A. Analysis of downhole measurements of drill string forces and motions. **Journal of Engineering for Industry**, v.90, p. 208–216, 1968. doi:10.1115/1.3604616.

[37] LEE, H. Y. **Drillstring Axial Vibration and Wave Propagation in Boreholes**. Cambridge, 1991. Ph.D. Thesis, Massachusetts Institute of Technology.

[38] FRANCA, L. F. P.; WEBER, H. I. Experimental and numerical study of a new resonance hammer drilling model with drift. **Chaos, Solitons & Fractals**, v.21, p. 789–801, 2004. doi:10.1016/j.chaos.2003.12.064.

[39] FRANCA, L. F. F. M. P. **Self–Exited Percussive–Rotary Drilling in Hard Rocks**. Rio de Janeiro, 2004. D.Sc. Thesis, Pontifícia Universidade Católica do Rio de Janeiro. (in Portuguese).

[40] DYKSTRA, M. W. **Nonlinear Drill String Dynamics**. Tulsa, 1966. Ph.D. Thesis, University of Tulsa.

[41] SHYU, R. J. **Bending Vibration of Rotating Drill Strings**. Cambridge, 1989. Ph.D. Thesis, Massachusetts Institute of Technology.

[42] PAYNE, M. L. **Drilling Bottom-Hole Assembly Dynamics**. Houston, 1992. Ph.D. Thesis, Rice University.

[43] KOTSONIS, S. J. **Effects of Axial Forces on Drillstring Lateral Vibrations**. Houston, 1994. M.Sc. Thesis, Rice University.

[44] SPANOS, P. D.; CHEVALLIER, A. M. ; POLITIS, N. P. Nonlinear stochastic drill-string vibrations. **Journal of Vibration and Acoustics**, v.124, p. 512–518, 2002. doi:10.1115/1.1502669.

[45] SPANOS, P. D.; PAYNE, M. L. ; SECORA, C. K. Bottom-hole assembly modeling and dynamic response determination. **Journal of Energy Resources Technology**, v.119, p. 153–158, 1997. doi:10.1115/1.2794983.

[46] BOWDEN, F. P.; LEBEN, L. The nature of sliding and the analysis of friction. **Proceedings of the Royal Society of London. Series A, Mathematical and Physical Sciences**, v.169, p. 371–391, 1939. `http://www.jstor.org/stable/97286`.

[47] PERSSON, B. N. J.; POPOV, V. L. On the origin of the transition from slip to stick. **Solid State Communications**, v.114, p. 261–266, 2000. doi:10.1016/S0038-1098(00)00045-4.

[48] HALSEY, G. W.; KYLLINGSTAD, A.; AARRESTAD, T. V. ; LYSNE, D. **Drillstring torsional vibrations: comparison between theory and experiment on a full-scale research drilling rig**. In: SPE Annual Technical Conference and Exhibition, 1986. doi:10.2118/15564-MS.

[49] BRETT, J. F. The genesis of torsional drillstring vibrations. **Journal SPE Drilling Engineering**, v.7, p. 168–174, 1992. doi:10.2118/21943-PA.

[50] LIN, Y.-Q.; WANG, Y.-H. Stick-slip vibration of drill strings. **Journal of Engineering for Industry**, v.113, p. 38–43, 1991. doi:10.1115/1.2899620.

[51] MIHAJLOVIC, N.; VAN VEGGEL, A. A.; VAN DE WOUW, N. ; NIJMEIJER, H. **Friction-induced torsional vibrations in an experimental drill-string system**. In: 23rd IASTED Conference on Modelling, Identification and Control, 2004.

[52] RICHARD, T.; GERMAY, C. ; DETOURNAY, E. Self-excited stick–slip oscillations of drill bits. **Comptes Rendus Mécanique**, v.332, p. 619–626, 2004. doi:10.1016/j.crme.2004.01.016.

[53] SILVEIRA, M.; WIERCIGROCH, M. Low dimensional models for stick-slip vibration of drill-strings. **Journal of Physics: Conference Series**, v.181, p. 012056, 2009. doi:10.1088/1742-6596/181/1/012056.

[54] SAMPAIO, R.; PIOVAN, M. ; LOZANO, G. V. Coupled axial/torsional vibrations of drill-strings by means of non-linear model. **Mechanics Research Communications**, v.34, p. 497–502, 2007. doi:10.1016/j.mechrescom.2007.03.005.

[55] GERMAY, C.; DENOËL, V. ; DETOURNAY, E. Multiple mode analysis of the self-excited vibrations of rotary drilling systems. **Journal of Sound and Vibration**, v.325, p. 362–381, 2009. doi:10.1016/j.jsv.2009.03.017.

[56] RICHARD, T.; GERMAY, C. ; DETOURNAY, E. A simplified model to explore the root cause of stick–slip vibrations in drilling systems with drag bits. **Journal of Sound and Vibration**, v.305, p. 432–456, 2007. doi:10.1016/j.jsv.2007.04.015.

[57] DIVENYI, S.; SAVI, M. A.; WIERCIGROCH, M. ; PAVLOVSKAIA, E. Drill-string vibration analysis using non-smooth dynamics approach. **Nonlinear Dynamics**, v.70, p. 1017–1035, 2012. doi:10.1007/s11071-012-0510-3.

[58] NANDAKUMAR, K.; WIERCIGROCH, M. Stability analysis of a state dependent delayed, coupled two DOF model of drill-string vibration. **Journal of Sound and Vibration**, v.332, p. 2575–2592, 2013. doi:10.1016/j.jsv.2012.12.020.

[59] DEPOUHON, A.; DETOURNAY, E. Instability regimes and self-excited vibrations in deep drilling systems. **Journal of Sound and Vibration**, v.333, p. 2019–2039, 2014. doi:10.1016/j.jsv.2013.10.005.

[60] YIGIT, A. S.; CHRISTOFOROU, A. P. Coupled axial and transverse vibrations of oilwell drillstrings. **Journal of Sound and Vibration**, v.195, p. 617–627, 1996. doi:10.1006/jsvi.1996.0450.

[61] TRINDADE, M. A.; WOLTER, C. ; SAMPAIO, R. Karhunen–Loève decomposition of coupled axial/bending vibrations of beams subject to impacts. **Journal of Sound and Vibration**, v.279, p. 1015–1036, 2005. doi:10.1016/j.jsv.2003.11.057.

[62] YIGIT, A. S.; CHRISTOFOROU, A. P. Coupled torsional and bending vibrations of drillstrings subject to impact with friction. **Journal of Sound and Vibration**, v.215, p. 167–181, 1998. doi:10.1006/jsvi.1998.1617.

[63] TUCKER, W. R.; WANG, C. An integrated model for drill-string dynamics. **Journal of Sound and Vibration**, v.224, p. 123–165, 1999. doi:10.1006/jsvi.1999.2169.

[64] CORAL ALAMO, F. J. **Dynamics of Slender One-dimensional Structures Using Cosserat Continuum**. Rio de Janeiro, 2006. D.Sc. Thesis, Pontifícia Universidade Católica do Rio de Janeiro. (in Portuguese).

[65] SILVEIRA, M. **A comprehensive model of drill-string dynamics using Cosserat rod theory**. Aberdeen, 2011. Ph.D. Thesis, University of Aberdeen.

[66] CHRISTOFOROU, A. P.; YIGIT, A. S. Fully coupled vibrations of actively controlled drillstrings. **Journal of Sound and Vibration**, v.267, p. 1029–1045, 2003. doi:10.1016/S0022-460X(03)00359-6.

[67] LIU, X.; VLAJIC, N.; LONG, X.; MENG, G. ; BALACHANDRAN, B. Nonlinear motions of a flexible rotor with a drill bit: stick-slip and delay effects. **Nonlinear Dynamics**, v.72, p. 61–77, 2013. doi:10.1007/s11071-012-0690-x.

[68] KHULIEF, Y. A.; AL-SULAIMAN, F. A. ; BASHMAL, S. Vibration analysis of drillstrings with self-excited stick–slip oscillations. **Journal of Sound and Vibration**, v.299, p. 540–558, 2007. doi:10.1016/j.jsv.2006.06.065.

[69] RITTO, T. G.; SOIZE, C. ; SAMPAIO, R. Non-linear dynamics of a drill-string with uncertain model of the bit–rock interaction. **International Journal of Non-Linear Mechanics**, v.44, p. 865–876, 2009. doi:10.1016/j.ijnonlinmec.2009.06.003.

[70] RITTO, T. G. **Numerical Analysis of the Nonlinear Dynamics of a Drill-string with Uncertainty Modeling**. Rio de Janeiro, 2010. D.Sc. Thesis, Pontifícia Universidade Católica do Rio de Janeiro.

[71] DETOURNAY, E.; DEFOURNY, P. A phenomenological model for the drilling action of drag bits. **International Journal of Rock Mechanics and Mining Sciences & Geomechanics Abstracts**, v.29, p. 13–23, 1992. doi:10.1016/0148-9062(92)91041-3.

[72] DETOURNAY, E.; RICHARD, T. ; SHEPHERD, M. Drilling response of drag bits: Theory and experiment. **International Journal of Rock Mechanics and Mining Sciences**, v.45, p. 1347–1360, 2008. doi:10.1016/j.ijrmms.2008.01.010.

[73] FRANCA, L. F. P. Drilling action of roller-cone bits: modeling and experimental validation. **Journal of Energy Resources Technology**, v.132, p. 043101–1–043101–9, 2010. doi:10.1115/1.4003168.

[74] FRANCA, L. F. P. A bit–rock interaction model for rotary–percussive drilling. **International Journal of Rock Mechanics and Mining Sciences**, v.48, p. 827–835, 2011. doi:10.1016/j.ijrmms.2011.05.007.

[75] TUCKER, R. W.; WANG, C. Torsional vibration control and Cosserat dynamics of a drill-rig assembly. **Meccanica**, v.38, p. 145–161, 2003. doi:10.1023/A:1022035821763.

[76] RITTO, T. G.; SAMPAIO, R. Stochastic drill-string dynamics with uncertainty on the imposed speed and on the bit-rock parameters. **International Journal for Uncertainty Quantification**, v.2, p. 111–124, 2012. doi:10.1615/Int.J.UncertaintyQuantification.v2.i2.

[77] RITTO, T. G.; ESCALANTE, M. R.; SAMPAIO, R. ; ROSALES, M. B. Drill-string horizontal dynamics with uncertainty on the frictional force. **Journal of Sound and Vibration**, v.332, p. 145–153, 2013. doi:10.1016/j.jsv.2012.08.007.

[78] WANHEIM, T.; BAY, N. ; PETERSEN, A. S. A theoretically determined model for friction in metal working processes. **Wear**, v.28, p. 251–258, 1974. doi:10.1016/0043-1648(74)90165-3.

[79] CORBEN, H.; STEHLE, P. **Classical Mechanics**. 2nd. ed., New York: Dover Publications, 1994. 416p.

[80] RAJAGOPAL, K. R. On implicit constitutive theories. **Applications of Mathematics**, v.48, p. 279–319, 2003. doi:10.1023/A:1026062615145.

[81] SIGINER, D. A.; BAKHTIYAROV, S. I. Flow of drilling fluids in eccentric annuli. **Journal of Non-Newtonian Fluid Mechanics**, v.78, p. 119–132, 1998. doi:10.1016/S0377-0257(97)00101-8.

[82] ESCUDIER, M. P.; GOULDSON, I. W.; OLIVEIRA, P. J. ; PINHO, F. T. Effects of inner cylinder rotation on laminar flow of a Newtonian fluid through an eccentric annulus. **International Journal of Heat and Fluid Flow**, v.21, p. 92–103, 2000. doi:10.1016/S0142-727X(99)00059-4.

[83] ESCUDIER, M. P.; OLIVEIRA, P. J. ; PINHO, F. T. Fully developed laminar flow of purely viscous non-Newtonian liquids through annuli, including the effects of eccentricity and inner-cylinder rotation. **International Journal of Heat and Fluid Flow**, v.23, p. 52–73, 2002. doi:10.1016/S0142-727X(01)00135-7.

[84] PINA, E. P. F.; CARVALHO, M. S. Three-dimensional flow of a Newtonian liquid through an annular space with axially varying eccentricity. **Journal of Fluids Engineering**, v.128, p. 223–231, 2006. doi:10.1115/1.2170126.

[85] LOUREIRO, B. V.; DE SOUZA MENDES, P. R. ; AZEVEDO, L. F. A. Taylor-Couette instabilities in flows of Newtonian and power-law liquids in the presence of partial annulus obstruction. **Journal of Fluids Engineering**, v.128, p. 42–54, 2006. doi:10.1115/1.2136930.

[86] PAÏDOUSSIS, M. P.; LUU, T. P. ; PRABHAKAR, S. Dynamics of a long tubular cantilever conveying fluid downwards, which then flows upwards around the cantilever as a confined annular flow. **Journal of Fluids and Structures**, v.24, p. 111–128, 2008. doi:10.1016/j.jfluidstructs.2007.07.004.

[87] PAÏDOUSSIS, M. P. **Fluid-Structure Interactions: Slender Structures and Axial Flow Volume 1**. San Diego: Academic Press, 1998. 572p.

[88] PAÏDOUSSIS, M. P. **Fluid-Structure Interactions: Slender Structures and Axial Flow Volume 2**. San Diego: Academic Press, 1998. 1040p.

[89] SAHEBKAR, S. M.; GHAZAVI, M. R.; KHADEM, S. E. ; GHAYESH, M. H. Nonlinear vibration analysis of an axially moving drillstring system with time dependent axial load and axial velocity in inclined well. **Mechanism and Machine Theory**, v.46, p. 743–760, 2011. doi:10.1016/j.mechmachtheory.2010.12.003.

[90] HU, Y.; DI, Q.; ZHU, W.; CHEN, Z. ; WANG, W. Dynamic characteristics analysis of drillstring in the ultra-deep well with spatial curved beam finite element. **Journal of Petroleum Science and Engineering**, v.82—83, p. 166–173, 2012. doi:10.1016/j.petrol.2012.01.011.

[91] RITTO, T. G.; SOIZE, C. ; SAMPAIO, R. Probabilistic model identification of the bit–rock-interaction-model uncertainties in nonlinear dynamics of a drill-string. **Mechanics Research Communications**, v.37, p. 584–589, 2010. doi:10.1016/j.mechrescom.2010.07.004.

[92] RITTO, T. G.; SOIZE, C. ; SAMPAIO, R. Stochastic dynamics of a drill-string with uncertain weight-on-hook. **Journal of the Brazilian Society of Mechanical Sciences and Engineering**, v.32, p. 250–258, 2010. doi:10.1590/S1678-58782010000300008.

[93] RITTO, T. G.; SOIZE, C. ; SAMPAIO, R. Robust optimization of the rate of penetration of a drill-string using a stochastic nonlinear dynamical model. **Computational Mechanics**, v.45, p. 415–427, 2010. doi:10.1007/s00466-009-0462-8.

[94] BONET, J.; WOOD, R. D. **Nonlinear Continuum Mechanics for Finite Element Analysis**. 2nd. ed., Cambridge: Cambridge University Press, 2008. 340p.

[95] GILARDI, G.; SHARF, I. Literature survey of contact dynamics modelling. **Mechanism and Machine Theory**, v.37, p. 1213–1239, 2002. doi:10.1016/S0094-114X(02)00045-9.

[96] WRIGGERS, P. **Computational Contact Mechanics**. 2nd. ed., New York: Springer, 2006. 520p.

[97] HUNT, K. H.; CROSSLEY, F. E. Coefficient of restitution interpreted as damping in vibroimpact. **Journal of Applied Mechanics**, v.42, p. 440–445, 1975. doi:10.1115/1.3423596.

[98] CULL, S. J.; TUCKER, R. W. On the modelling of Coulomb friction. **Journal of Physics A: Mathematical and General**, v.32, p. 2103–2113, 1999. doi:10.1088/0305-4470/32/11/006.

[99] WRIGGERS, P.; ZAVARISE, G. **Computational Contact Mechanics**. In: Stein, E.; de Borst, R. ; Hughes, T. J. R., editors, Encyclopedia of Computational Mechanics, volume 2, p. 195–226. Hoboken: Wiley, 2004. doi:10.1002/0470091355.ecm033.

[100] LANCZOS, C. **The Variational Principles of Mechanics**. 4th. ed., New York: Dover Publications, 1986. 418p.

[101] SAGAN, H. **Introduction to the Calculus of Variations**. New York: Dover Publications, 1992. 449p.

[102] HUGHES, T. J. R. **The Finite Element Method**. New York: Dover Publications, 2000. 682p.

[103] HAGEDORN, P.; DASGUPTA, A. **Vibrations and Waves in Continuous Mechanical Systems**. Chichester: Wiley, 2007. 382p.

[104] REDDY, J. N. On locking-free shear deformable beam finite elements. **Computer Methods in Applied Mechanics and Engineering**, v.149, p. 113–132, 1997. doi:10.1016/S0045-7825(97)00075-3.

[105] BAZOUNE, A.; KHULIEF, Y. A. ; STEPHEN, N. G. Shape functions of three-dimensional Timoshenko beam element. **Journal of Sound and Vibration**, v.259, p. 473–480, 2003. doi:10.1006/jsvi.2002.5122.

[106] LUO, Y. An efficient 3D Timoshenko beam element with consistent shape functions. **Advances in Theoretical and Applied Mechanics**, v.1, p. 95–106, 2008.

[107] NEWMARK, N. M. A method of computation for structural dynamics. **Journal of the Engineering Mechanics Division**, v.85, p. 67–94, 1959.

[108] TREFETHEN, L. N.; BAU, D. **Numerical Linear Algebra**. Philadelphia: SIAM: Society for Industrial and Applied Mathematics, 1997. 373p.

[109] NEGRUT, D.; JAY, L. O. ; KHUDE, N. A discussion of low-order numerical integration formulas for rigid and flexible multibody dynamics. **Journal of Computational and Nonlinear Dynamics**, v.4, p. 21008–1–21008–11, 2009. doi:10.1115/1.3079784.

[110] GOLUB, G. H.; VAN LOAN, C. F. **Matrix Computations**. 4th. ed., Baltimore: The Johns Hopkins University Press, 2013. 784p.

[111] HAMMING, R. W. **Numerical Methods for Scientists and Engineers**. 2nd. ed., New York: Dover Publications, 1987. 752p.

[112] YOUNG, D. M. **Iterative Solution of Large Linear Systems**. New York: Dover Publications, 2003. 608p.

[113] SAAD, Y. **Iterative Methods for Sparse Linear Systems**. 2nd. ed., Philadelphia: SIAM: Society for Industrial and Applied Mathematics, 2003. 528p.

[114] DAVIS, T. **Creating sparse finite-element matrices in MATLAB**, 2007. `http://goo.gl/UZ4Lh`.

[115] JAYNES, E. T. Information theory and statistical mechanics. **Physical Review Series II**, v.106, p. 620–630, 1957. doi:10.1103/PhysRev.106.620.

[116] JAYNES, E. T. Information theory and statistical mechanics II. **Physical Review Series II**, v.108, p. 171–190, 1957. doi:10.1103/PhysRev.108.171.

[117] SHANNON, C. E. A mathematical theory of communication. **Bell System Technical Journal**, v.27, p. 379–423, 1948.

[118] METROPOLIS, N.; ULAM, S. The Monte Carlo method. **Journal of the American Statistical Association**, v.44, p. 335–341, 1949. doi:10.2307/2280232.

[119] LIU, J. S. **Monte Carlo Strategies in Scientific Computing**. New York: Springer, 2001. 360p.

[120] FISHMAN, G. **Monte Carlo: Concepts, Algorithms, and Applications**. Corrected edition. ed., New York: Springer, 2003. 698p.

[121] RUBINSTEIN, R. Y.; KROESE, D. P. **Simulation and the Monte Carlo Method**. 2nd. ed., New Jersey: Wiley, 2007. 372p.

[122] SHONKWILER, R. W.; MENDIVIL, F. **Explorations in Monte Carlo Methods**. New York: Springer, 2009. 243p.

[123] ROBERT, C. P.; CASELLA, G. **Monte Carlo Statistical Methods**. New York: Springer, 2010. 645p.

[124] KROESE, D. P.; TAIMRE, T. ; BOTEV, Z. I. **Handbook of Monte Carlo Methods**. New Jersey: Wiley, 2011. 772p.

[125] CAFLISCH, R. E. Monte Carlo and quasi-Monte Carlo methods. **Acta Numerica**, v.7, p. 1–49, 1998. doi:10.1017/S0962492900002804.

[126] CUNHA JR, A.; NASSER, R.; SAMPAIO, R.; LOPES, H. ; BREITMAN, K. Uncertainty quantification through Monte Carlo method in a cloud computing setting. **Computer Physics Communications**, v.185, p. 1355—1363, 2014. doi:10.1016/j.cpc.2014.01.006.

[127] ZHANG, Y.; SHARF, I. Validation of nonlinear viscoelastic contact force models for low speed impact. **Journal of Applied Mechanics**, v.76, p. 051002, 2009. doi:10.1115/1.3112739.

[128] ODEN, J. T.; REDDY, J. N. **An Introduction to the Mathematical Theory of Finite Elements**. New York: Dover Publications, 2011. 446p.

[129] OPPENHEIM, A. V.; SCHAFER, R. W. **Discrete-Time Signal Processing**. 3rd. ed., Englewood Cliffs, N.J.: Prentice Hall, 2009. 1120p.

[130] SAVITZKY, A.; GOLAY, M. J. E. Smoothing and differentiation of data by simplified least squares procedures. **Analytical Chemistry**, v.36, p. 1627–1639, 1964. doi:10.1021/ac60214a047.

[131] RITTO, T. G.; SAMPAIO, R. Measuring the efficiency of vertical drillstrings: A vibration perspective. **Mechanics Research Communications**, v.52, p. 32–39, 2013. doi:10.1016/j.mechrescom.2013.06.003.

[132] BAZARAA, M. S.; SHERALI, H. D. ; SHETTY, C. M. **Nonlinear Programming: Theory and Algorithms**. Hoboken: Wiley-Interscience, 2006. 872p.

[133] NOCEDAL, J.; WRIGHT, S. **Numerical Optimization**. 2nd. ed., New York: Springer, 2006. 664p.

[134] QUEIPO, N. V.; HAFTKA, R. T.; SHYY, W.; GOEL, T.; VAIDYANATHAN, R. ; TUCKER, P. K. Surrogate-based analysis and optimization. **Progress in Aerospace Sciences**, v.41, p. 1–28, 2005. doi:10.1016/j.paerosci.2005.02.001.

[135] BEYER, H. G.; SENDHOFF, B. Robust optimization – A comprehensive survey. **Computer Methods in Applied Mechanics and Engineering**, v.196, p. 3190–3218, 2007. doi:10.1016/j.cma.2007.03.003.

[136] CAPIEZ-LERNOUT, E.; SOIZE, C. Design optimization with an uncertain vibroacoustic model. **Journal of Vibration and Acoustics**, v.130, p. 021001, 2008. doi:10.1115/1.2827988.

[137] CAPIEZ-LERNOUT, E.; SOIZE, C. Robust design optimization in computational mechanics. **Journal of Applied Mechanics**, v.75, p. 021001, 2008. doi:10.1115/1.2775493.

[138] CAPIEZ-LERNOUT, E.; SOIZE, C. Robust updating of uncertain damping models in structural dynamics for low- and medium-frequency ranges. **Mechanical Systems and Signal Processing**, v.22, p. 1774–1792, 2008. doi:10.1016/j.ymssp.2008.02.005.

[139] SOIZE, C.; CAPIEZ-LERNOUT, E. ; OHAYON, R. Robust updating of uncertain computational models using experimental modal analysis. **AIAA Journal**, v.46, p. 2955–2965, 2008.

[140] SCHUËLLER, G. I.; JENSEN, H. A. Computational methods in optimization considering uncertainties – an overview. **Computer Methods in Applied Mechanics and Engineering**, v.198, p. 2–13, 2008. doi:10.1016/j.cma.2008.05.004.

[141] BEN-TAL, A.; GHAOUI, L. E. ; NEMIROVSKI, A. **Robust Optimization**. Princeton: Princeton University Press, 2009. 576p.

[142] OBERKAMPF, W. L.; ROY, C. J. **Verification and Validation in Scientific Computing**. Cambridge: Cambridge University Press, 2010. 784p.

[143] BATOU, A.; SOIZE, C. Identification of stochastic loads applied to a non-linear dynamical system using an uncertain computational model and experimental responses. **Computational Mechanics**, v.43, p. 559–571, 2009. doi:10.1007/s00466-008-0330-y.

[144] ALLMARAS, M.; BANGERTH, W.; LINHART, J. M.; POLANCO, J.; WANG, F.; WANG, K.; WEBSTER, J. ; ZEDLER, S. Estimating parameters in physical models through Bayesian inversion: A complete example. **SIAM Review**, v.55, p. 149–167, 2014.

[145] CUNHA JR, A.; SOIZE, C. ; SAMPAIO, R. **Computational modeling of the nonlinear stochastic dynamics of horizontal drillstrings**, (submitted for publication).

[146] CUNHA JR, A.; SAMPAIO, R. On the nonlinear stochastic dynamics of a continuous system with discrete attached elements. **Applied Mathematical Modelling**, v.39, p. 809—819, 2015. doi:10.1016/j.apm.2014.07.012.

[147] CUNHA JR, A.; SOIZE, C. ; SAMPAIO, R. Exploring the nonlinear dynamics of horizontal drillstrings subjected to friction and shocks effects. **Mecánica Computacional**, v.33, p. 1517–1527, 2014. http://www.cimec.org.ar/ojs/index.php/mc/article/view/4750.

[148] CUNHA JR, A.; SAMPAIO, R. Study of the nonlinear longitudinal dynamics of a stochastic system. **MATEC Web of Conferences**, v.16, p. 05004, 2014. doi:10.1051/matecconf/20141605004.

[149] SANDOVAL, M. G.; CUNHA JR, A. ; SAMPAIO, R. Identification of parameters in the torsional dynamics of a drilling process through Bayesian statistics. **Mecánica Computacional**, v.32, p. 763–773, 2013. http://www.cimec.org.ar/ojs/index.php/mc/article/view/4388.

[150] CUNHA JR, A.; SAMPAIO, R. Effect of an attached end mass in the dynamics of uncertainty nonlinear continuous random system. **Mecánica Computacional**, v.31, p. 2676–2683, 2012. http://www.cimec.org.ar/ojs/index.php/mc/article/view/4214.

[151] CUNHA JR, A.; SOIZE, C. ; SAMPAIO, R. **Mathematical modeling of horizontal drillstrings subjected to friction and shocks effects**. In: XXXV Congresso Nacional de Matemática Aplicada e Computacional, Natal, Brazil, 2014.

[152] CUNHA JR, A.; SOIZE, C. ; SAMPAIO, R. **Numerical study of the nonlinear dynamics of horizontal drillings**. In: 8th European Nonlinear Dynamics Conference, Vienna, Austria, 2014.

[153] CUNHA JR, A.; SOIZE, C. ; SAMPAIO, R. **Analysis of the nonlinear dynamics of a horizontal drillstring**. In: 9th International Conference on Structural Dynamics, Porto, Portugal, 2014.

[154] CUNHA JR, A.; SAMPAIO, R. **Effects of a random cubic spring on the longitudinal dynamics of a bar excited by a gaussian white noise**. In: 2nd International Symposium on Uncertainty Quantification and Stochastic Modeling, Rouen, France, 2014.

[155] CUNHA JR, A.; SOIZE, C. ; SAMPAIO, R. **A deterministic approach to analyze the nonlinear dynamics of a horizontal drill-string**. In: 12th Conference on Dynamical Systems - Theory and Applications, Łódź, Poland, 2013. (resume).

[156] CUNHA JR, A.; NASSER, R.; SAMPAIO, R.; LOPES, H. ; BREITMAN, K. **Uncertainty quantification using cloud computing for Monte Carlo parallelization**. In: 22th International Congress of Mechanical Engineering, Ribeirão Preto, Brazil, 2013.

[157] CUNHA JR, A.; SAMPAIO, R. **Analysis of the nonlinear stochastic dynamics of an elastic bar with an attached end mass**. In: 3rd South-East European Conference on Computational Mechanics, Kos Island, Greece, 2013.

[158] CUNHA JR, A.; SAMPAIO, R. **Uncertainty propagation in the dynamics of a nonlinear random bar**. In: XV International Symposium on Dynamic Problems of Mechanics, Armação dos Búzios, Brazil, 2013.

[159] CUNHA JR, A.; SAMPAIO, R. **Exploring Monte Carlo method to access the dynamical behavior of a continuous random system**. In: Congresso de Matemática Aplicada e Computacional - Nordeste 2012, Natal, Brazil, 2012. (resume).

[160] CUNHA JR, A.; SAMPAIO, R. **On the dynamics of a nonlinear continuous random system**. In: 1st International Symposium on Uncertainty Quantification and Stochastic Modeling, Maresias, Brazil, 2012.

[161] **Maple User Manual**. Toronto: Maplesoft, a division of Waterloo Maple Inc., 2005-2014.

A
Derivation of Nonlinear Equations of Motion

In this appendix it is presented the derivation of the Eq.(3.52), which is a weak equation of motion of the horizontal drillstring nonlinear dynamics. All the development is based on the modification of the extended Hamilton's principle presented in Eq.(3.51), which is equivalent to

$$\int_{t=t_0}^{t_f} \delta\mathcal{T}\, dt - \int_{t=t_0}^{t_f} \delta\mathcal{V}\, dt + \int_{t=t_0}^{t_f} \delta\mathcal{W}\, dt - \int_{t=t_0}^{t_f}\int_{x=0}^{L} \delta\boldsymbol{U}\cdot\frac{\partial\mathcal{D}}{\partial\dot{\boldsymbol{U}}}\, dx\, dt = 0. \quad \text{(A.1)}$$

The formalism that follows presents the calculation of each one of the terms in the Eq.(A.1), the correct handling of its terms, and the unfolding of the definitions presented earlier, to finally arrive at the result expressed in the Eq.(3.52).

A.1
Variation of the kinetic energy

Remembering that the kinetic energy of the mechanical system of interest in this work is given by

$$\begin{aligned}\mathcal{T} \;=\; & \frac{1}{2}\int_{x=0}^{L} \rho A\left(\dot{u}^2+\dot{v}^2+\dot{w}^2\right) dx \;+ \\ & \frac{1}{2}\int_{x=0}^{L} 2\,\rho\, I_4\left(\dot{\theta}_x+\dot{\theta}_z\theta_y\right)^2 dx \;+ \\ & \frac{1}{2}\int_{x=0}^{L} \rho\, I_4\left(\left(\dot{\theta}_y\cos\theta_x-\dot{\theta}_z\sin\theta_x\right)^2+\left(\dot{\theta}_y\sin\theta_x+\dot{\theta}_z\cos\theta_x\right)^2\right) dx,\end{aligned} \quad \text{(A.2)}$$

one has, after the calculation of the first variation, that

$$\begin{aligned}\int_{t=t_0}^{t_f}\delta\mathcal{T}\, dt \;=\; & \int_{t=t_0}^{t_f}\int_{x=0}^{L} \rho A\left(\dot{u}\,\delta\dot{u}+\dot{v}\,\delta\dot{v}+\dot{w}\,\delta\dot{w}\right) dx\, dt \;+ \\ & \int_{t=t_0}^{t_f}\int_{x=0}^{L} 2\,\rho\, I_4\left(\left(\dot{\theta}_x\,\dot{\theta}_z+\theta_y\,\dot{\theta}_z^2\right)\delta\theta_y+\left(\dot{\theta}_x+\theta_y\,\dot{\theta}_z\right)\delta\dot{\theta}_x\right) dx\, dt \;+ \\ & \int_{t=t_0}^{t_f}\int_{x=0}^{L} \rho\, I_4\left(\dot{\theta}_y\,\delta\dot{\theta}_y+\left(\dot{\theta}_z+2\,\theta_y\,\dot{\theta}_x+2\,\theta_y^2\,\dot{\theta}_z\right)\delta\dot{\theta}_z\right) dx\, dt,\end{aligned} \quad \text{(A.3)}$$

which, after the integration by parts in time, and taking into account that the variation of the field variables between the instants t_0 and t_f are zero, can be written as

$$\begin{aligned}\int_{t=t_0}^{t_f} \delta\mathcal{T}\, dt \;=\; & -\int_{t=t_0}^{t_f}\int_{x=0}^{L} \rho\, A\,(\ddot{u}\,\delta u + \ddot{v}\,\delta v + \ddot{w}\,\delta w)\, dx\, dt \\ & -\int_{t=t_0}^{t_f}\int_{x=0}^{L} \rho\, I_4 \left(2\,\ddot{\theta}_x\,\delta\theta_x + \ddot{\theta}_y\,\delta\theta_y + \ddot{\theta}_z\,\delta\theta_z\right) dx\, dt \\ & -\int_{t=t_0}^{t_f}\int_{x=0}^{L} 2\,\rho\, I_4 \left(\theta_y\,\ddot{\theta}_z + \dot{\theta}_y\,\dot{\theta}_z\right)\,\delta\theta_x\, dx\, dt \\ & +\int_{t=t_0}^{t_f}\int_{x=0}^{L} 2\,\rho\, I_4 \left(\theta_y\,\dot{\theta}_z^2 + \dot{\theta}_x\,\dot{\theta}_z\right)\,\delta\theta_y\, dx\, dt \\ & -\int_{t=t_0}^{t_f}\int_{x=0}^{L} 2\,\rho\, I_4 \left(\theta_y\,\ddot{\theta}_x + \theta_y^2\,\ddot{\theta}_z + \dot{\theta}_x\,\dot{\theta}_y + 2\,\theta_y\,\dot{\theta}_y\,\dot{\theta}_z\right)\,\delta\theta_z\, dx\, dt,\end{aligned} \tag{A.4}$$

Now, for sake of esthetic, a change in the notation of the variation of a field variable is made

$$\psi_u = \delta u, \quad \psi_v = \delta v, \quad \psi_w = \delta w, \quad \psi_{\theta_x} = \delta\theta_x, \quad \psi_{\theta_y} = \delta\theta_y, \quad \psi_{\theta_z} = \delta\theta_z, \tag{A.5}$$

so that the Eq.(A.4) now read as

$$\begin{aligned}\int_{t=t_0}^{t_f} \delta\mathcal{T}\, dt \;=\; & -\int_{t=t_0}^{t_f}\int_{x=0}^{L} \rho\, A\,(\psi_u\,\ddot{u} + \psi_v\,\ddot{v} + \psi_w\,\ddot{w})\, dx\, dt \\ & -\int_{t=t_0}^{t_f}\int_{x=0}^{L} \rho\, I_4 \left(2\,\psi_{\theta_x}\,\ddot{\theta}_x + \psi_{\theta_y}\,\ddot{\theta}_y + \psi_{\theta_z}\,\ddot{\theta}_z\right) dx\, dt \\ & -\int_{t=t_0}^{t_f}\int_{x=0}^{L} 2\,\rho\, I_4\,\psi_{\theta_x} \left(\theta_y\,\ddot{\theta}_z + \dot{\theta}_y\,\dot{\theta}_z\right) dx\, dt \\ & +\int_{t=t_0}^{t_f}\int_{x=0}^{L} 2\,\rho\, I_4\,\psi_{\theta_y} \left(\theta_y\,\dot{\theta}_z^2 + \dot{\theta}_x\,\dot{\theta}_z\right) dx\, dt \\ & -\int_{t=t_0}^{t_f}\int_{x=0}^{L} 2\,\rho\, I_4\,\psi_{\theta_z} \left(\theta_y\,\ddot{\theta}_x + \theta_y^2\,\ddot{\theta}_z + \dot{\theta}_x\,\dot{\theta}_y + 2\,\theta_y\,\dot{\theta}_y\,\dot{\theta}_z\right) dx\, dt.\end{aligned} \tag{A.6}$$

According to the Eqs.(3.53), and (3.60), the operators that come from the kinetic energy are

$$\begin{aligned}\mathcal{M}\left(\boldsymbol{\psi}, \ddot{\boldsymbol{U}}\right) \;=\; & \int_{x=0}^{L} \rho\, A\,(\psi_u\,\ddot{u} + \psi_v\,\ddot{v} + \psi_w\,\ddot{w})\, dx \;+ \\ & \int_{x=0}^{L} \rho\, I_4 \left(2\,\psi_{\theta_x}\,\ddot{\theta}_x + \psi_{\theta_y}\,\ddot{\theta}_y + \psi_{\theta_z}\,\ddot{\theta}_z\right) dx,\end{aligned} \tag{A.7}$$

and

$$\begin{aligned}\mathcal{F}_{KE}\left(\boldsymbol{\psi},\boldsymbol{U},\dot{\boldsymbol{U}},\ddot{\boldsymbol{U}}\right) &= -\int_{x=0}^{L} 2\,\rho\,I_4\,\psi_{\theta_x}\left(\theta_y\,\ddot{\theta}_z+\dot{\theta}_y\,\dot{\theta}_z\right)dx \\ &+\int_{x=0}^{L} 2\,\rho\,I_4\,\psi_{\theta_y}\left(\theta_y\,\dot{\theta}_z^2+\dot{\theta}_x\,\dot{\theta}_z\right)dx \\ &-\int_{x=0}^{L} 2\,\rho\,I_4\,\psi_{\theta_z}\left(\theta_y\,\ddot{\theta}_x+\theta_y^2\,\ddot{\theta}_z+\dot{\theta}_x\,\dot{\theta}_y+2\,\theta_y\,\dot{\theta}_y\,\dot{\theta}_z\right)dx,\end{aligned} \tag{A.8}$$

so that it is possible to rewrite the Eq.(A.6) as

$$\int_{t=t_0}^{t_f}\delta\mathcal{T}\,dt=\int_{t=t_0}^{t_f}\left(-\mathcal{M}\left(\boldsymbol{\psi},\ddot{\boldsymbol{U}}\right)+\mathcal{F}_{KE}\left(\boldsymbol{U},\dot{\boldsymbol{U}},\ddot{\boldsymbol{U}}\right)\right)dt. \tag{A.9}$$

A.2
Variation of the strain energy

In the case of the strain energy, after the deformations given by

$$\begin{aligned}\epsilon_{xx} &= u'-y\,\theta_z'+z\,\theta_y'+u'\left(z\,\theta_y'-y\,\theta_z'\right)-y\,z\,\theta_y'\,\theta_z'\;+ \\ &\theta_x'\left(\left(y\,w'-z\,v'\right)\cos\theta_x-\left(y\,v'+z\,w'\right)\sin\theta_x\right)\;+ \\ &\frac{1}{2}\left(u'^{\,2}+v'^{\,2}+w'^{\,2}+y^2\,\theta_z'^{\,2}+z^2\,\theta_y'^{\,2}+\left(y^2+z^2\right)\theta_x'^{\,2}\right),\end{aligned} \tag{A.10}$$

$$\begin{aligned}\epsilon_{xy} &= \frac{1}{2}\left(v'\,\cos\theta_x+w'\sin\theta_x-z\,\theta_x'\right)\;+ \\ &\frac{1}{2}\,\theta_z\left(y\,\theta_z'-z\theta_y'-u'-1\right),\end{aligned} \tag{A.11}$$

and

$$\begin{aligned}\epsilon_{xz} &= \frac{1}{2}\left(w'\,\cos\theta_x-v'\sin\theta_x+y\,\theta_x'\right)\;+ \\ &\frac{1}{2}\,\theta_y\left(-y\,\theta_z'+z\theta_y'+u'+1\right),\end{aligned} \tag{A.12}$$

are substituted into

$$\mathcal{V}=\frac{1}{2}\iiint_{\mathcal{B}_0}\left(E\,\epsilon_{xx}^2+4\,\kappa_s\,G\,\epsilon_{xy}^2+4\,\kappa_s\,G\,\epsilon_{xz}^2\right)dx\,dy\,dz, \tag{A.13}$$

the right side of the last equation becomes a large and complex expression.

The manipulation of the above expression manually is an arduous task, almost certainly subjected to errors of calculation. Therefore, the calculation of the strain energy variation was performed with the aid of the computer algebra system `Maple` [161]. The spreadsheet used to make symbolic calculations can be seen in Listing A.1.

Listing A.1: `Maple` spreadsheet used to compute the strain energy variation.

```
restart:

# beam strains
Exx := (1/2)*(u7^2+u8^2+u9^2) + (1/2)*(y^2*u12^2+z^2*u11^2)+
(1/2)*(y^2+z^2)*u10^2-(1+u7)*(y*u12-z*u11)-
u10*sin(u4)*(y*u8+z*u9)+u10*cos(u4)*(y*u9-z*u8)-y*z*u11*u12+u7:

Exy := -(1/2)*u6*(u7-y*u12+z*u11+1)-(1/2)*z*u10+
       (1/2)*(u8*cos(u4)+u9*sin(u4)):

Exz := (1/2)*u5*(u7-y*u12+z*u11+1)+(1/2)*y*u10+
       (1/2)*(-u8*sin(u4)+u9*cos(u4)):

# partial derivatives of Exx
dExxdu1 := diff(Exx, u1):
dExxdu2 := diff(Exx, u2):
dExxdu3 := diff(Exx, u3):
dExxdu4 := diff(Exx, u4):
dExxdu5 := diff(Exx, u5):
dExxdu6 := diff(Exx, u6):
dExxdu7 := diff(Exx, u7):
dExxdu8 := diff(Exx, u8):
dExxdu9 := diff(Exx, u9):
dExxdu10 := diff(Exx, u10):
dExxdu11 := diff(Exx, u11):
dExxdu12 := diff(Exx, u12):

# partial derivatives of Exy
dExydu1 := diff(Exy, u1):
dExydu2 := diff(Exy, u2):
dExydu3 := diff(Exy, u3):
dExydu4 := diff(Exy, u4):
dExydu5 := diff(Exy, u5):
dExydu6 := diff(Exy, u6):
dExydu7 := diff(Exy, u7):
dExydu8 := diff(Exy, u8):
dExydu9 := diff(Exy, u9):
dExydu10 := diff(Exy, u10):
```

```
dExydu11 := diff(Exy, u11):
dExydu12 := diff(Exy, u12):

# partial derivatives of Exz
dExzdu1 := diff(Exz, u1):
dExzdu2 := diff(Exz, u2):
dExzdu3 := diff(Exz, u3):
dExzdu4 := diff(Exz, u4):
dExzdu5 := diff(Exz, u5):
dExzdu6 := diff(Exz, u6):
dExzdu7 := diff(Exz, u7):
dExzdu8 := diff(Exz, u8):
dExzdu9 := diff(Exz, u9):
dExzdu10 := diff(Exz, u10):
dExzdu11 := diff(Exz, u11):
dExzdu12 := diff(Exz, u12):

# variations Exx
dExx := dExxdu1*du1+dExxdu2*du2+dExxdu3*du3+
        dExxdu4*du4+dExxdu5*du5+dExxdu6*du6+
        dExxdu7*du7+dExxdu8*du8+dExxdu9*du9+
        dExxdu10*du10+dExxdu11*du11+dExxdu12*du12:

# variations Exy
dExy := dExydu1*du1+dExydu2*du2+dExydu3*du3+
        dExydu4*du4+dExydu5*du5+dExydu6*du6+
        dExydu7*du7+dExydu8*du8+dExydu9*du9+
        dExydu10*du10+dExydu11*du11+dExydu12*du12:

# variations Exz
dExz := dExzdu1*du1+dExzdu2*du2+dExzdu3*du3+
        dExzdu4*du4+dExzdu5*du5+dExzdu6*du6+
        dExzdu7*du7+dExzdu8*du8+dExzdu9*du9+
        dExzdu10*du10+dExzdu11*du11+dExzdu12*du12:

# variation of the strain energy density
dEhat := (1/2)*(2*E*Exx*dExx+8*ks*G*Exy*dExy+8*ks*G*Exz*dExz):

# variation of the strain energy
dE:=Int(subs(y=r*cos(t),z=r*sin(t),dEhat*r),r=RIN..REX,t=0..2*Pi):
dE1:=value(dE):

# group terms which has common factors
dE2:=collect(dE1,[du1,du2,du3,du4,du5,du6,
                  du7,du8,du9,du10,du11,du12]):


```

```
# replace by zero the variations different than du12
# (in order to compute the other terms,
#  do the same with the other variations)
dE3:=subs(du1=0,du2=0,du3=0,du4=0,du5=0,du6=0,
          du7=0,du8=0,du9=0,du10=0,du11=0,dE2):
simplify(dE3);
```

After the symbolic calculations, introducing the notation

$$\psi'_u = \delta u', \quad \psi'_v = \delta v', \quad \psi'_w = \delta w', \quad \psi'_{\theta_x} = \delta\theta'_x, \quad \psi'_{\theta_y} = \delta\theta'_y, \quad \psi'_{\theta_z} = \delta\theta'_z, \quad \text{(A.14)}$$

together with the notation given by (A.5), it is possible to show that the variation of the energy functional can be written as

$$\int_{t=t_0}^{t_f} \delta\mathcal{V} dt = \int_{t=t_0}^{t_f} \left(\mathcal{K}\left(\boldsymbol{\psi}, \boldsymbol{U}\right) - \mathcal{F}_{SE}\left(\boldsymbol{U}, \dot{\boldsymbol{U}}, \ddot{\boldsymbol{U}}\right) \right) dt, \qquad \text{(A.15)}$$

where, obviously, the following definitions are recalled

$$\begin{aligned} \mathcal{K}\left(\boldsymbol{\psi}, \boldsymbol{U}\right) \;=\; & \int_{x=0}^{L} E\,A\,\psi'_u\,u'\,dx \;+ \\ & \int_{x=0}^{L} E\,I_4\left(\psi'_{\theta_y}\,\theta'_y + \psi'_{\theta_z}\,\theta'_z\right) dx \;+ \\ & \int_{x=0}^{L} 2\,\kappa_s\,G\,I_4\,\psi'_{\theta_x}\,\theta'_x\,dx \;+ \\ & \int_{x=0}^{L} \kappa_s\,G\,A\left(\left(\psi_{\theta_y} + \psi'_w\right)\left(\theta_y + w'\right) + \left(\psi_{\theta_z} - \psi'_v\right)\left(\theta_z - v'\right)\right) dx, \end{aligned} \qquad \text{(A.16)}$$

and

$$\begin{aligned} \mathcal{F}_{SE}\left(\boldsymbol{\psi}, \boldsymbol{U}\right) \;=\; & -\int_{x=0}^{L} \left(\psi_{\theta_x}\,\Gamma_1 + \psi_{\theta_y}\,\Gamma_2 + \psi_{\theta_z}\,\Gamma_3\right) dx \\ & -\int_{x=0}^{L} \left(\psi'_u\,\Gamma_4 + \psi'_v\,\Gamma_5 + \psi'_w\,\Gamma_6 + \psi'_{\theta_x}\Gamma_7 + \psi'_{\theta_y}\,\Gamma_8 + \psi'_{\theta_z}\,\Gamma_9\right) dx, \end{aligned} \qquad \text{(A.17)}$$

whereas the Γ_n $(n = 1, \cdots, 9)$ are defined as:

$$\begin{aligned} \Gamma_1 \;=\; & E\,I_4\left(1 + u'\right)\left(\sin\theta_x\left(v'\,\theta'_y + w'\,\theta'_z\right) + \cos\theta_x\left(v'\,\theta'_z - w'\,\theta'_y\right)\right)\theta'_x \;+ \\ & k_s\,G\,A\left(1 + u'\right)\left(\sin\theta_x\left(\theta_z\,v' - \theta_y\,w'\right) - \cos\theta_x\left(\theta_y\,v' + \theta_z\,w'\right)\right), \end{aligned} \qquad \text{(A.18)}$$

$$\Gamma_2 = k_s G I_4 \left(\theta_y \left(\theta_y'^2 + \theta_z'^2\right) - \theta_x' \theta_z'\right) + k_s G A \left(-w' + u' \theta_y \left(2 + u'\right) - \left(1 + u'\right) \left(v' \sin\theta_x - w' \cos\theta_x\right)\right), \tag{A.19}$$

$$\Gamma_3 = k_s G I_4 \left(\theta_z \left(\theta_y'^2 + \theta_z'^2\right) + \theta_x' \theta_y'\right) + k_s G A \left(v' + u' \theta_z \left(2 + u'\right) - \left(1 + u'\right) \left(w' \sin\theta_x + v' \cos\theta_x\right)\right), \tag{A.20}$$

$$\begin{aligned}\Gamma_4 = {} & E A \left(\frac{1}{2} \left(1 + u'\right) \left(v'^2 + w'^2\right) + \frac{1}{2} u'^2 \left(3 + u'\right)\right) + \\ & E I_4 \left(\sin\theta_x \left(v' \theta_z' - w' \theta_y'\right) - \cos\theta_x \left(v' \theta_y' + w' \theta_z'\right)\right) \theta_x' + \\ & E I_4 \left(1 + u'\right) \left(\theta_x'^2 + \frac{3}{2} \left(\theta_y'^2 + \theta_z'^2\right)\right) + \\ & k_s G A \left(\cos\theta_x \left(\theta_y w' - \theta_z v'\right) - \sin\theta_x \left(\theta_y v' + \theta_z w'\right)\right) + \\ & k_s G A \left(1 + u'\right) \left(\theta_y^2 + \theta_z^2\right),\end{aligned} \tag{A.21}$$

$$\begin{aligned}\Gamma_5 = {} & E A \left(u' + \frac{1}{2} \left(u'^2 + v'^2 + w'^2\right)\right) v' + \\ & E I_4 \left(2 \theta_x'^2 + \frac{1}{2} \left(\theta_y'^2 + \theta_z'^2\right)\right) v' + \\ & E I_4 \left(1 + u'\right) \left(\theta_z' \sin\theta_x - \theta_y' \cos\theta_x\right) \theta_x' + \\ & k_s G A \left(1 + u'\right) \left(\theta_z - \theta_y \sin\theta_x - \theta_z \cos\theta_x\right),\end{aligned} \tag{A.22}$$

$$\begin{aligned}\Gamma_6 = {} & E A \left(u' + \frac{1}{2} \left(u'^2 + v'^2 + w'^2\right)\right) w' + \\ & E I_4 \left(2 \theta_x'^2 + \frac{1}{2} \left(\theta_y'^2 + \theta_z'^2\right)\right) w' + \\ & E I_4 \left(1 + u'\right) \left(-\theta_y' \sin\theta_x - \theta_z' \cos\theta_x\right) \theta_x' + \\ & k_s G A \left(1 + u'\right) \left(-\theta_y + \theta_y \cos\theta_x - \theta_z \sin\theta_x\right),\end{aligned} \tag{A.23}$$

$$\begin{aligned}\Gamma_7 \;=\;& E\,I_4\left(u'^2+2\left(u'+v'^2+w'^2\right)\right)\theta'_x \;+ \\ & E\,I_4\left(1+u'\right)\left(\sin\theta_x\left(v'\,\theta'_z-w'\,\theta'_y\right)-\cos\theta_x\left(v'\,\theta'_y+w'\,\theta'_z\right)\right) \;+ \\ & E\,I_6\left(4\,\theta'^2_x+2\left(\theta'^2_y+\theta'^2_z\right)\right)\theta'_x \;+ \\ & k_s\,G\,A\left(\theta_z\,\theta'_y-\theta_y\,\theta'_z\right),\end{aligned} \tag{A.24}$$

$$\begin{aligned}\Gamma_8 \;=\;& E\,I_4\left(3\,u'+\frac{1}{2}\left(3\,u'^2+v'^2+w'^2\right)\right)\theta'_y \;+ \\ & E\,I_4\left(1+u'\right)\left(-w'\,\sin\theta_x-v'\,\cos\theta_x\right)\theta'_x \;+ \\ & E\,I_6\left(2\,\theta'^2_x+\frac{3}{2}\left(\theta'^2_y+\theta'^2_z\right)\right)\theta'_y \;+ \\ & k_s\,G\,I_4\left(\theta_z\,\theta'_x+\theta'_y\left(\theta^2_y+\theta^2_z\right)\right),\end{aligned} \tag{A.25}$$

and

$$\begin{aligned}\Gamma_9 \;=\;& E\,I_4\left(3\,u'+\frac{1}{2}\left(3\,u'^2+v'^2+w'^2\right)\right)\theta'_z \;+ \\ & E\,I_4\left(1+u'\right)\left(v'\,\sin\theta_x-w'\,\cos\theta_x\right)\theta'_x \;+ \\ & E\,I_6\left(2\theta'^2_x+\frac{3}{2}\left(\theta'^2_y+\theta'^2_z\right)\right)\theta'_z \;+ \\ & k_s\,G\,I_4\left(-\theta_y\,\theta'_x+\theta'_z\left(\theta^2_y+\theta^2_z\right)\right).\end{aligned} \tag{A.26}$$

A.3
Variation of the external forces work

The external forces work acting on the mechanical system is given by

$$\mathcal{W}=-\int_{x=0}^{L}\rho\,g\,A\,w\,dx \;+\; \mathcal{W}_{\rm FS} \;+\; \mathcal{W}_{\rm BR}. \tag{A.27}$$

in way that, after the first variation, one has

$$\begin{aligned}\int_{t=t_0}^{t_f} \delta\mathcal{W}\, dt &= -\int_{t=t_0}^{t_f}\int_{x=0}^{L} \rho\, g\, A\, \delta w\, dx\, dt \\ &\quad + \int_{t=t_0}^{t_f} \delta\mathcal{W}_{\text{FS}}\, dt \\ &\quad + \int_{t=t_0}^{t_f} \delta\mathcal{W}_{\text{BR}}\, dt.\end{aligned} \tag{A.28}$$

Replacing Eqs.(3.46) and (3.47) on the right hand side of the above equation, and introducing the notation $\psi_u = \delta u$, $\psi_v = \delta v$, $\psi_w = \delta w$, and $\psi_{\theta_x} = \delta\theta_x$, one obtains

$$\begin{aligned}\int_{t=t_0}^{t_f} \delta\mathcal{W}\, dt &= -\int_{t=t_0}^{t_f}\int_{x=0}^{L} \rho\, g\, A\, \psi_w\, dx\, dt \\ &\quad + \int_{t=t_0}^{t_f} \left(\sum_{m=1}^{N_{nodes}} \left(F^a_{\text{FS}}\, \psi_u + F^n_{\text{FS}}\, (v\, \psi_v + w\, \psi_w)\, /r + T_{\text{FS}}\, \psi_{\theta_x} \right) \Big|_{x=x_m} \right) dt \\ &\quad + \int_{t=t_0}^{t_f} \left(F_{\text{BR}}\, \psi_u \Big|_{x=L} + T_{\text{BR}}\, \psi_{\theta_x} \Big|_{x=L} \right) dt.\end{aligned} \tag{A.29}$$

In accordance with the Eqs.(3.57), (3.58) and (3.59), it follows that

$$\mathcal{F}_{\text{G}}\left(\boldsymbol{\psi}\right) = -\int_{x=0}^{L} \rho\, g\, A\, \psi_w\, dx, \tag{A.30}$$

$$\mathcal{F}_{\text{FS}}\left(\boldsymbol{\psi}, \boldsymbol{U}\right) = \sum_{m=1}^{N_{nodes}} \left(F^a_{\text{FS}}\, \psi_u + F^n_{\text{FS}}\, (v\, \psi_v + w\, \psi_w)\, /r + T_{\text{FS}}\, \psi_{\theta_x} \right) \Big|_{x=x_m} \tag{A.31}$$

and

$$\mathcal{F}_{\text{BR}}\left(\boldsymbol{\psi}, \dot{\boldsymbol{U}}\right) = F_{\text{BR}}\, \psi_u \Big|_{x=L} + T_{\text{BR}}\, \psi_{\theta_x} \Big|_{x=L}, \tag{A.32}$$

so that one may write the variation of the work as

$$\int_{t=t_0}^{t_f} \delta\mathcal{W}\, dt = \int_{t=t_0}^{t_f} \left(\mathcal{F}_G\left(\boldsymbol{\psi}\right) + \mathcal{F}_{FS}\left(\boldsymbol{\psi}, \boldsymbol{U}\right) + \mathcal{F}_{BR}\left(\boldsymbol{\psi}, \dot{\boldsymbol{U}}\right) \right) dt. \tag{A.33}$$

A.4
Variation of the energy dissipation function

For the dissipation function, which is given by

$$\begin{aligned} \mathcal{D} &= \frac{1}{2}\,c\,\rho\,A\left(\dot{u}^2+\dot{v}^2+\dot{w}^2\right) + \\ &\quad \frac{1}{2}\,c\,\rho\,I_4\left(2\,\dot{\theta}_x^2+\dot{\theta}_y^2+\dot{\theta}_z^2\right), \end{aligned} \tag{A.34}$$

after calculating the inner product between the gradient of $\mathcal{D}$ and the variation vector $\delta\boldsymbol{U}$, the fourth integral of Eq.(A.1) read as

$$\begin{aligned} \int_{t=t_0}^{t_f}\int_{x=0}^{L}\delta\boldsymbol{U}\cdot\frac{\partial\mathcal{D}}{\partial\dot{\boldsymbol{U}}}\,dx\,dt &= \int_{t=t_0}^{t_f}\int_{x=0}^{L}c\,\rho\,A\left(\dot{u}\,\delta u+\dot{v}\,\delta v+\dot{w}\,\delta w\right)dx\,dt + \\ &\quad \int_{t=t_0}^{t_f}\int_{x=0}^{L}c\,\rho\,I_4\left(2\,\dot{\theta}_x\,\delta\theta_x+\dot{\theta}_y\,\delta\theta_y+\dot{\theta}_z\,\delta\theta_z\right)dx\,dt, \end{aligned} \tag{A.35}$$

which, after the introduction of the notation defined by (A.5), is rewritten as

$$\begin{aligned} \int_{t=t_0}^{t_f}\int_{x=0}^{L}\delta\boldsymbol{U}\cdot\frac{\partial\mathcal{D}}{\partial\dot{\boldsymbol{U}}}\,dx\,dt &= \int_{t=t_0}^{t_f}\int_{x=0}^{L}c\,\rho\,A\left(\psi_u\,\dot{u}+\psi_v\,\dot{v}+\psi_w\,\dot{w}\right)dx\,dt + \\ &\quad \int_{t=t_0}^{t_f}\int_{x=0}^{L}c\,\rho\,I_4\left(2\,\psi_{\theta_x}\,\dot{\theta}_x+\psi_{\theta_y}\,\dot{\theta}_y+\psi_{\theta_z}\,\dot{\theta}_z\right)dx\,dt. \end{aligned} \tag{A.36}$$

The operator associated with energy dissipation of the system is, according to the Eq.(3.54), given by

$$\begin{aligned} \mathcal{C}\left(\boldsymbol{\psi},\dot{\boldsymbol{U}}\right) &= \int_{x=0}^{L}c\,\rho\,A\left(\psi_u\,\dot{u}+\psi_v\,\dot{v}+\psi_w\,\dot{w}\right)dx + \\ &\quad \int_{x=0}^{L}c\,\rho\,I_4\left(2\,\psi_{\theta_x}\,\dot{\theta}_x+\psi_{\theta_y}\,\dot{\theta}_y+\psi_{\theta_z}\,\dot{\theta}_z\right)dx, \end{aligned} \tag{A.37}$$

so that Eq.(A.36) is equivalent to

$$\int_{t=t_0}^{t_f}\int_{x=0}^{L}\delta\boldsymbol{U}\cdot\frac{\partial\mathcal{D}}{\partial\dot{\boldsymbol{U}}}\,dx\,dt=\int_{t=t_0}^{t_f}\mathcal{C}\left(\boldsymbol{\psi},\dot{\boldsymbol{U}}\right)\,dt. \tag{A.38}$$

A.5
Weak equations of motion

Substituting the variations of the functionals given by the Eqs.(A.9), (A.15), (A.33), and (A.38), into the modified extended Hamilton's principle, represented by the Eq.(A.1), one obtains that

$$\begin{aligned}\int_{t=t_0}^{t_f} \Big(-\mathcal{M}\left(\boldsymbol{\psi}, \ddot{\boldsymbol{U}}\right) + \mathcal{F}_{KE}\left(\boldsymbol{U}, \dot{\boldsymbol{U}}, \ddot{\boldsymbol{U}}\right) \;&+ \\ -\mathcal{K}\left(\boldsymbol{\psi}, \boldsymbol{U}\right) + \mathcal{F}_{SE}\left(\boldsymbol{U}, \dot{\boldsymbol{U}}, \ddot{\boldsymbol{U}}\right) \;&+ \\ \mathcal{F}_G\left(\boldsymbol{\psi}\right) + \mathcal{F}_{FS}\left(\boldsymbol{\psi}, \boldsymbol{U}\right) + \mathcal{F}_{BR}\left(\boldsymbol{\psi}, \dot{\boldsymbol{U}}\right) \;&+ \\ -\mathcal{C}\left(\boldsymbol{\psi}, \dot{\boldsymbol{U}}\right) \Big)\, dt \;&= \; 0,\end{aligned} \tag{A.39}$$

Recalling the definition of the force operator

$$\begin{aligned}\mathcal{F}\left(\boldsymbol{\psi}, \boldsymbol{U}, \dot{\boldsymbol{U}}, \ddot{\boldsymbol{U}}\right) \;=\; &\mathcal{F}_G\left(\boldsymbol{\psi}\right) \;+\; \mathcal{F}_{FS}\left(\boldsymbol{\psi}, \boldsymbol{U}\right) \;+\; \mathcal{F}_{BR}\left(\boldsymbol{\psi}, \dot{\boldsymbol{U}}\right) \;+ \\ &\mathcal{F}_{KE}\left(\boldsymbol{\psi}, \boldsymbol{U}, \dot{\boldsymbol{U}}, \ddot{\boldsymbol{U}}\right) \;+\; \mathcal{F}_{SE}\left(\boldsymbol{\psi}, \boldsymbol{U}\right),\end{aligned} \tag{A.40}$$

and, taking into account that the term inside the integral must be zero, one can finally write the Eq.(A.39) as

$$\mathcal{M}\left(\boldsymbol{\psi}, \ddot{\boldsymbol{U}}\right) + \mathcal{C}\left(\boldsymbol{\psi}, \dot{\boldsymbol{U}}\right) + \mathcal{K}\left(\boldsymbol{\psi}, \boldsymbol{U}\right) = \mathcal{F}\left(\boldsymbol{\psi}, \boldsymbol{U}, \dot{\boldsymbol{U}}, \ddot{\boldsymbol{U}}\right), \tag{A.41}$$

the weak form of the equation of motion that describes the nonlinear dynamics of the horizontal drillstring.

B
Interpolation Functions for the Finite Element Method

This appendix presents the type of (beam) finite element used in the discretization of the nonlinear dynamical system equations, the shape functions associated to the element, and the interpolation functions used to approximate the value of the field variables throughout the domain of the element. For details, the reader is referred to Bazoune et al. (2003) [105] and Luo (2008) [106].

B.1
Timoshenko beam element

In this work, the finite element considered is the Timoshenko beam element, which has two nodes, and each node has six degrees of freedom associated (three displacements and three rotations). The degrees of freedom of the first node are called u_1, v_1, w_1, θ_{x_1}, θ_{y_1}, and θ_{z_1}. For the second node the same nomenclature applies, exchanging is only 1 for 2. An illustration of this element is presented in the Figure B.1.

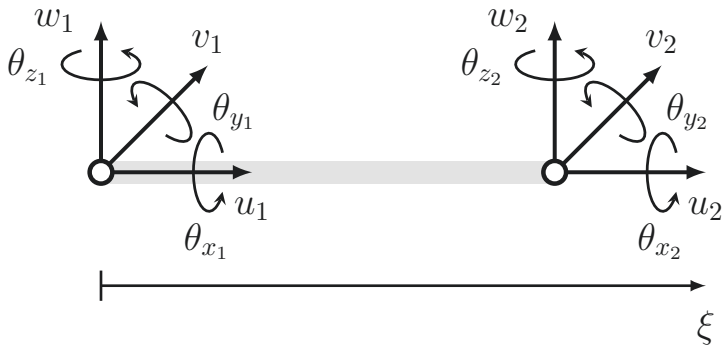

Figure B.1: Illustration of a Timoshenko beam element with two nodes and six degrees of freedom per node.

The parametrization of this element is done by the local coordinate $\xi = x/L$, in a way that the first node corresponds to $\xi = 0$, while the second node is associated to $\xi = 1$.

B.2
Shape functions

Different shape functions are used to represent the field variables associated to the degrees of freedom of the Timoshenko beam element. For instance, the axial displacement and the torsional rotation use the following affine functions

$$\begin{aligned} \mathcal{N}_1(\xi) &= 1-\xi, \\ \mathcal{N}_2(\xi) &= \xi, \end{aligned} \tag{B.1}$$

while the lateral displacements use the Hermite cubic polynomials defined by

$$\begin{aligned} \mathcal{H}_1^{(1)}(\xi) &= \frac{1}{1+\varphi}\left(1-3\,\xi^2+2\,\xi^3+\varphi\,(1-\xi)\right), \\ \mathcal{H}_2^{(1)}(\xi) &= \frac{L}{1+\varphi}\left(\xi-2\,\xi^2+\xi^3+\frac{\varphi}{2}\left(\xi-\xi^2\right)\right), \\ \mathcal{H}_3^{(1)}(\xi) &= \frac{1}{1+\varphi}\left(3\,\xi^2-2\,\xi^3+\varphi\,\xi\right), \\ \mathcal{H}_4^{(1)}(\xi) &= \frac{L}{1+\varphi}\left(-\xi^2+\xi^3+\frac{\varphi}{2}\left(-\xi+\xi^2\right)\right), \end{aligned} \tag{B.2}$$

and the lateral rotations are also represented in terms of the Hermite quadratic polynomials, defined by

$$\begin{aligned} \mathcal{H}_1^{(2)}(\xi) &= \frac{6}{L(1+\varphi)}\left(-\xi+\xi^2\right), \\ \mathcal{H}_2^{(2)}(\xi) &= \frac{1}{1+\varphi}\left(1-4\,\xi+3\,\xi^2+\varphi\,(1-\xi)\right), \\ \mathcal{H}_3^{(2)}(\xi) &= \frac{-6}{L(1+\varphi)}\left(-\xi+\xi^2\right), \\ \mathcal{H}_4^{(2)}(\xi) &= \frac{1}{1+\varphi}\left(-2\,\xi+3\,\xi^2+\varphi\,\xi\right), \end{aligned} \tag{B.3}$$

being the shear deformation parameter, which is the ratio between bending and shear stiffness, defined as

$$\varphi = \frac{12\,E\,I_4}{\kappa_s\,G\,A\,L^2}. \tag{B.4}$$

In the context of dynamic analysis of structures using finite elements, Reddy (1997) [104] suggests one to use $\varphi = 0$. This suggestion is heeded in all the analyzes reported in this thesis.

B.3
Interpolation functions

Once one has defined the shape functions, the interpolation functions of the field variables are obtained as linear combinations of then. The coefficients of these linear combinations are the degrees of freedom located at the nodes of the finite element (Hughes, 2000) [102].

Using the shape functions $\mathcal{N}_m(\xi)$, the fields of axial displacement and torsional rotation are, respectively, interpolated by the functions

$$u^h(\xi,t) = u_1(t)\,\mathcal{N}_1(\xi) + u_2(t)\,\mathcal{N}_2(\xi), \tag{B.5}$$

and

$$\theta_x^h(\xi,t) = \theta_{x_1}(t)\,\mathcal{N}_1(\xi) + \theta_{x_2}(t)\,\mathcal{N}_2(\xi). \tag{B.6}$$

Similarly, but now considering the family of shape functions $\mathcal{H}_m^{(1)}$, one has that the interpolation functions for the lateral displacement fields are given by

$$v^h(\xi,t) = v_1(t)\,\mathcal{H}_1^{(1)}(\xi) + \theta_{z_1}(t)\,\mathcal{H}_2^{(1)}(\xi) + v_2(t)\,\mathcal{H}_3^{(1)}(\xi) + \theta_{z_2}(t)\,\mathcal{H}_4^{(1)}(\xi), \tag{B.7}$$

and

$$w^h(\xi,t) = w_1(t)\,\mathcal{H}_1^{(1)}(\xi) - \theta_{y_1}(t)\,\mathcal{H}_2^{(1)}(\xi) + w_2(t)\,\mathcal{H}_3^{(1)}(\xi) - \theta_{y_2}(t)\,\mathcal{H}_4^{(1)}(\xi). \tag{B.8}$$

Considering now the family of shape functions $\mathcal{H}_m^{(2)}$, one has that the interpolation functions for the lateral rotation fields are

$$\theta_y^h(\xi,t) = -w_1(t)\,\mathcal{H}_1^{(2)}(\xi) + \theta_{y_1}(t)\,\mathcal{H}_2^{(2)}(\xi) - w_2(t)\,\mathcal{H}_3^{(2)}(\xi) + \theta_{y_1}(t)\,\mathcal{H}_4^{(2)}(\xi), \tag{B.9}$$

and

$$\theta_z^h(\xi,t) = v_1(t)\,\mathcal{H}_1^{(2)}(\xi) + \theta_{z_1}(t)\,\mathcal{H}_2^{(2)}(\xi) + v_2(t)\,\mathcal{H}_3^{(2)}(\xi) + \theta_{z_1}(t)\,\mathcal{H}_4^{(2)}(\xi). \tag{B.10}$$

C
Publications in Journals

According with the norms of the Postgraduate Program in Mechanical Engineering from PUC-Rio, all articles published or submitted for publication in scientific journals, whose content is related to the thesis, must be included at the end of the manuscript as an attachment.

Therefore, this appendix includes the following publications which are related to the thesis:

[P1] A. Cunha Jr, C. Soize, and R. Sampaio. Computational modeling of the nonlinear stochastic dynamics of horizontal drillstrings, (submitted for publication).

[P2] A. Cunha Jr, C. Soize, and R. Sampaio. Exploring the nonlinear dynamics of horizontal drillstrings subjected to friction and shocks effects. *Mecánica Computacional*, 33:1517–1527, 2014. `http://www.cimec.org.ar/ojs/index.php/mc/article/view/4750`.

manuscript No.
(will be inserted by the editor)

Computational modeling of the nonlinear stochastic dynamics of horizontal drillstrings

Americo Cunha Jr · Christian Soize · Rubens Sampaio

Received: date / Accepted: date

Abstract This work intends to analyze the nonlinear stochastic dynamics of drillstrings in horizontal configuration. For this purpose, it considers a beam theory, with effects of rotatory inertia and shear deformation, which is capable of reproducing the large displacements that the beam undergoes. The friction and shock effects, due to beam/borehole wall transversal impacts, as well as the force and torque induced by the bit-rock interaction, are also considered in the model. Uncertainties of the bit-rock interaction model are taken into account using a parametric probabilistic approach. Numerical simulations have shown that the mechanical system of interest has a very rich nonlinear stochastic dynamics, which generate phenomena such as bit-bounce, stick-slip, and transverse impacts. A study aiming to maximize the drilling process efficiency, varying drillstring velocities of translation and rotation is presented. Also, the work presents the definition and the solution of two optimizations problems, one deterministic and one robust, where the objective is to maximize the drillstring rate of penetration into the soil respecting its structural limits.

Keywords nonlinear dynamics · horizontal drillstring · uncertainty quantification · parametric probabilistic approach · robust optimization

A. Cunha Jr (corresponding author) · R. Sampaio
PUC–Rio, Departamento de Engenharia Mecânica, Rua M. de São Vicente, 225 - Rio de Janeiro, 22451-900, Brasil
E-mail: americo.cunhajr@gmail.com
E-mail: rsampaio@puc-rio.br

A. Cunha Jr · C. Soize
Université Paris-Est, Laboratoire Modélisation et Simulation Multi Echelle, MSME UMR 8208 CNRS, 5, Boulevard Descartes 77454, Marne-la-Vallée, France
E-mail: christian.soize@univ-paris-est.fr

1 Introduction

High energy demands of the 21st century make that fossil fuels, like oil and shale gas, still have a great importance in the energy matrix of several countries. Prospection of these fossil fuels demands the creation of exploratory wells. Traditionally, an exploratory well configuration is vertical, but directional or even horizontal configurations, where the boreholes are drilled following a non-vertical way, are also possible [61]. An illustration of the different types of configurations which an exploratory well can take is presented in Figure 1.

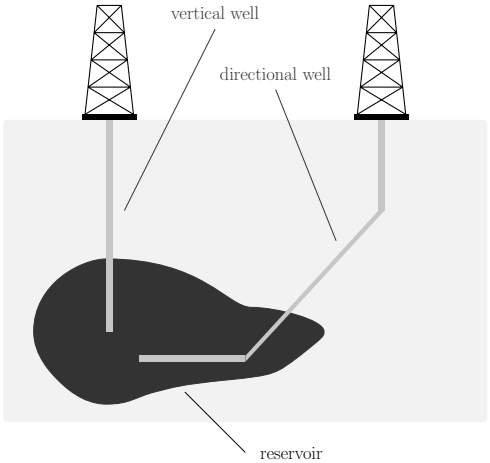

Fig. 1 Schematic representation of two exploratory wells. The left well configuration is vertical while the right one is directional.

The equipment used to drill the soil until the reservoir level is called *drillstring*. This device is a long column, composed of a sequence of connected drill-pipes and auxiliary equipment. It presents stabilizers through-

out its length, whose function is to maintain structural integrity of the borehole before cementation process. Furthermore, within the column flows drilling mud, which is used to cool the drilling system and to remove the drilling cuttings from the borehole. The bottom part of this column is called *bottom hole assembly* (BHA) and consists of a pipe of greater thickness, named *drill-colar*, and a tool used to stick the rock, the *drill-bit* [20]. A schematic representation of a typical vertical drillstring and its components is presented in Figure 2, but a column in horizontal configuration essentially has the same structure.

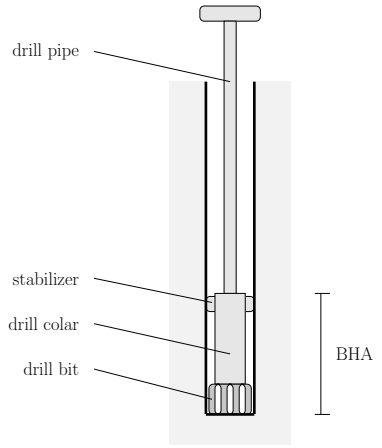

Fig. 2 Schematic representation of a typical drillstring.

Since the axial dimension of a drillstring is orders of magnitude larger than the characteristic dimension of its cross section area, the column is a long flexible structure with a very complex flexural dynamic. Furthermore, during drilling process, the drillstring is also subjected to other two mechanisms of vibration (longitudinal and torsional), which interact nonlinearly with the flexural mechanism, resulting in a further complicated dynamics [59]. The coupling between these three mechanisms of vibration, which imposes severe complications on the drillstring dynamics modeling, comes from the action of several agents, such as: structure self weight (for a vertical column); tensile and compressive loads due to the *weight on bit* (WOB) and soil reaction force; dry friction and impacts with borehole wall; bit-rock interaction forces; internal flow pressure; forces induced by internal flow instabilities; etc [59].

The dynamics of a drillstring is not a new subject in the technical/scientific literature. Works on this subject, covering experimental analysis, numerical and/or analytical modeling, can be seen since the 1960s. Most of the numerical works developed between 1960s and 1990s, have used lumped parameters approach to gain insight about drillstrings dynamical behavior. On the other hand, the analytical works focused on simple distributed parameters models. Little has been done using finite element-based approaches until the beginning of 1990s. A comprehensive literature survey of the research work produced until 2000 can be found in [10] and [59].

In recent studies, the lumped parameters approach have been used, for example, to seek configurations which reduce the stick-slip occurrence during drillstring operation [51]; to identify suitable values for the drilling system operational parameters [32]; to analyze the coupling between axial and torsional vibrations and its stability [19, 17, 34, 15]. On the other hand, approaches based on distributed parameters models have been used to: investigate drillstring failure mechanisms [27]; better understand the transversal impacts between the column and the borehole wall [60]; study the effects induced by the nonlinear coupling between the longitudinal and torsional dynamics the drillstring [46]; describe the dynamic behavior of the column taking into account the coupling between the three mechanisms of vibration [40, 38]; investigate the chaotic regime which the mechanism of drillstring transverse vibrations is subjected [9].

Despite the fact that directional drilling has been used in practical engineering for a few decades, and most of the exploratory wells drilled today be directional in configuration, all the works mentioned above model vertical drillstrings only. To the best of the authors' knowledge, there are very few papers in the open literature which models drillstring in directional configurations [45, 24, 43]. All of these works use a distributed parameters approach, but while [45, 43] only address the drillstring longitudinal dynamics, [24] uses generalized Euler-Bernoulli beam theory to describe the drillstring three-dimensional dynamics in a sloped directional well. In [45], the authors study a sloped configuration for the borehole and uses a perturbation technique to discretize the model equations. Conversely, the model equations are discretized by finite element in [43].

In addition to the difficulties inherent to the nonlinear dynamics, drillstrings are subjected to randomness on their geometrical dimensions, physical properties, external forcing, etc. The lack of knowledge on these parameters, known as *system-parameter uncertainty*, is a source of inaccuracies in drillstring modeling, which may, in an extreme case, completely compromise the model predictability [48, 49]. Furthermore, during the modeling process, hypotheses about the drillstring physical behavior are made. These considerations may be or not be in agreement with reality and should introduce additional inaccuracies in the model, known as *model uncertainty* induced by modeling errors [55, 56].

This source of uncertainty is essentially due to the use of simplified computational model for describing the phenomenon of interest and, usually, is the largest source of inaccuracy in computational model responses [55, 56].

Therefore, for a better understanding of the drillstring dynamics, these uncertainties must be modeled and quantified. In terms of quantifying these uncertainties for vertical drillstrings, the reader can see [58], where external forces are modeled as random objects and the method of statistical linearization is used along with the Monte Carlo (MC) method to treat the stochastic equations of the model. Other works in this line include: [40, 38], where system-parameter and model uncertainties are considered using a nonparametric probabilistic approach; and [42, 39], which use a standard parametric probabilistic approach to take into account the uncertainties of the system parameters. Regarding the works that model the directional configurations, only [43] considers the uncertainties, which, in this case, are related to the friction effects due to drillstring/borehole wall contact.

From what is observed above, considering only the theoretical point of view, the study of the drillstring nonlinear dynamics is already a rich subject. But in addition, a good understanding of its dynamics has also significance in applications. Only a few examples, it is fundamental to predict the fatigue life of the column structure [33] and the drill-bit wear [67]; to analyze the structural integrity of an exploratory well [14]; and to optimize the *rate of penetration* (ROP) of the drill-bit into the soil [41], and the last is essential to reduce cost of production of an exploratory well.

In this sense, this study aims to analyze the three-dimensional nonlinear dynamics of a drillstring in horizontal configuration, taking into account the system-parameter uncertainties. Through this study it is expected to gain a better understanding of drillstring physics and, thus, improve the drilling process efficiency, and maximize the column ROP accordingly. All results presented here were developed in the thesis of [12].

The rest of this work is organized as follows. The section 2 presents the mechanical system of interest in this work, its parametrization and modeling from the physical point of view. In section 3 the reader can see the mathematical formulation of the initial/boundary value problem that describes the behavior of the mechanical system of interest, as well as the conservative dynamics associated. The computational modeling of the problem, which involves the discretization of the model equations, reduction of order of the discretized dynamics, the algorithms for numerical integration and solution of nonlinear system of algebraic equations, can be seen in section 4. The probabilistic modeling of uncertainties is presented in section 5. Results of numerical simulations are presented and discussed in section 6. Finally, in the section 7, the main conclusions are emphasized, and some paths to future works are pointed out.

2 Physical model for the problem

2.1 Definition of the mechanical system

The mechanical system of interest in this work, which is schematically represented in Figure 3, consists of a horizontal rigid pipe, perpendicular to gravity, which contains in its interior a deformable tube under rotation. This deformable tube is subjected to three dimensional displacements, which induces longitudinal, lateral, and torsional vibrations of the structure. These mechanisms of vibration are able to generate slips and shocks in random areas of the rigid tube. Also, the contact between the drill-bit, at the right extreme of the tube, with the soil generates nonlinear forces and torques on the drillstring right extreme, which may completely block the advance of the structure over the well.

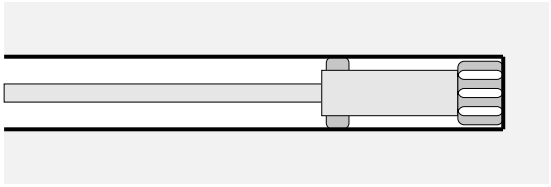

Fig. 3 Schematic representation of the mechanical system under analysis.

2.2 Nonlinear dynamical system parameterization

For purposes of modeling, the only part of the column considered is the BHA. So, the variation of the diameter along the column is being ignored. In this way, the bottom part of the deformable tube described, in the section 2.1, is modeled as a rotating beam in horizontal configuration, whose the transverse displacement (y and z) at both ends is blocked, as well as the transverse rotations on the left extreme. It looks like the left end of the system is a stabilizer and the right one a support. This beam is free to rotate around the x axis, and to move longitudinally. The rigid pipe is treated as a stationary cylindrical rigid wall in horizontal configuration.

As the beam is confined within the borehole, it is reasonable to assume that it undergoes small rotations

in the transverse directions. On the other hand, large displacements are observed in x, y, and z, as well as large rotations around the x-axis. Therefore, the analysis that follows uses a beam theory which assumes large rotation in x, large displacements in the three spatial directions, and small deformations [5].

Seeking not to make the mathematical model excessively complex, this work will not model the fluid flow inside the beam, nor the dissipation effects induced by the flow on the system dynamics.

Due to the horizontal configuration, the beam is subject to the action of the gravitational field, which induces an acceleration g. The beam is made of an isotropic material with mass density ρ, elastic modulus E, and Poisson's ratio ν. It has length L and annular cross section, with internal radius R_{int} and external radius R_{ext}.

An illustration of the beam geometric model is presented in Figure 4. It is important to note that this model also ignores the mass of the drill-bit and its geometric shape.

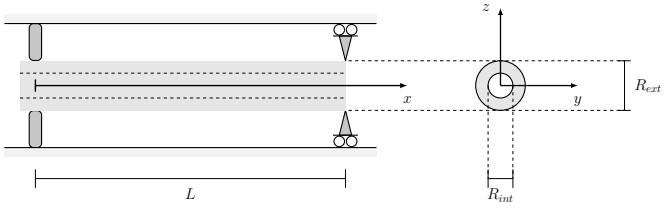

Fig. 4 Schematic representation of the beam geometry used to model the deformable tube under rotation, and the inertial system of coordinates used.

Using the cartesian coordinate system (x, y, z), defined by the orthonormal basis $\{\boldsymbol{e}_x, \boldsymbol{e}_y, \boldsymbol{e}_z\}$, fixed in the inertial frame of reference $\mathcal{R}$, and shown in the Figure 4, one can describe the undeformed configuration of the beam geometry by

$$\mathcal{B}_b = \left\{ (x, y, z) \in \mathbb{R}^3 \;\middle|\; 0 \leq x \leq L,\ (y, z) \in \mathcal{S}_b \right\}, \tag{1}$$

where the undeformed configuration of the beam cross section is described by

$$\mathcal{S}_b = \left\{ (y, z) \in \mathbb{R}^2 \;\middle|\; R_{int}^2 \leq y^2 + z^2 \leq R_{ext}^2 \right\}. \tag{2}$$

Once the configuration of the undeformed cross section has been characterized, one can define and compute the cross-sectional area,

$$A = \iint_{\mathcal{S}_b} dy\, dz = \pi \left(R_{ext}^2 - R_{int}^2 \right), \tag{3}$$

the second moment of area around the y axis

$$I_{yy} = \iint_{\mathcal{S}_b} z^2\, dy\, dz = I_4, \tag{4}$$

the second moment of area around the z axis

$$I_{zz} = \iint_{\mathcal{S}_b} y^2\, dy\, dz = I_4, \tag{5}$$

the polar moment of area

$$I_{xx} = \iint_{\mathcal{S}_b} \left(y^2 + z^2 \right) dy\, dz = 2\, I_4, \tag{6}$$

the fourth moment of area around the z axis

$$I_{zzzz} = \iint_{\mathcal{S}_b} y^4\, dy\, dz = 3\, I_6, \tag{7}$$

and the fourth product of area

$$I_{yyzz} = \iint_{\mathcal{S}_b} y^2 z^2\, dy\, dz = I_6, \tag{8}$$

where

$$I_4 = \frac{\pi}{4} \left(R_{ext}^4 - R_{int}^4 \right), \tag{9}$$

and

$$I_6 = \frac{\pi}{24} \left(R_{ext}^6 - R_{int}^6 \right). \tag{10}$$

In this work other three coordinate systems (all of then with the same origin as the (x, y, z) coordinate system) are also used, each one fixed in a non-inertial frame of reference $\mathcal{R}_n$, where $n = 1, 2, 3$, and defined by an orthonormal basis of vectors of the form $\{\boldsymbol{e}_{x_n}, \boldsymbol{e}_{y_n}, \boldsymbol{e}_{z_n}\}$.

These systems of coordinates are related by a sequence of elementary rotations, such as follows

$$\underset{(x,y,z)}{\mathcal{R}} \xrightarrow{\theta_x} \underset{(x_1,y_1,z_1)}{\mathcal{R}_1} \xrightarrow{\theta_y} \underset{(x_2,y_2,z_2)}{\mathcal{R}_2} \xrightarrow{\theta_z} \underset{(x_3,y_3,z_3)}{\mathcal{R}_3}, \tag{11}$$

where θ_x is the rotation between the coordinate systems (x, y, z) and (x_1, y_1, z_1), θ_y is the rotation between the coordinate systems (x_1, y_1, z_1) and (x_2, y_2, z_2), and θ_z is the rotation between the coordinate systems (x_2, y_2, z_2) and (x_3, y_3, z_3).

Thus, with respect to the non-inertial frame of reference, the instantaneous angular velocity of the rotating beam is written as

$$\boldsymbol{\omega} = \dot{\theta}_x \boldsymbol{e}_x + \dot{\theta}_y \boldsymbol{e}_{y_1} + \dot{\theta}_z \boldsymbol{e}_{z_2}, \tag{12}$$

where $\dot{\theta}_x$, $\dot{\theta}_y$, and $\dot{\theta}_z$ denote the rate of rotation around the x, y, and z directions, respectively. From now on, the upper dot $\dot{}$ will be used as an abbreviation for time derivative.

Referencing the vector $\boldsymbol{\omega}$ to the inertial frame of reference, and using the assumption of small rotations in the transversal directions, one obtains

$$\boldsymbol{\omega} = \begin{pmatrix} \dot{\theta}_x + \dot{\theta}_z \theta_y \\ \dot{\theta}_y \cos\theta_x - \dot{\theta}_z \sin\theta_x \\ \dot{\theta}_y \sin\theta_x + \dot{\theta}_z \cos\theta_x \end{pmatrix}. \tag{13}$$

Regarding the kinematic hypothesis adopted for the beam theory, it is assumed that the three-dimensional displacement of a beam point, occupying the position (x, y, z) at the instant of time t, can be written as

$$\begin{aligned} u_x(x,y,z,t) &= u - y\theta_z + z\theta_y, \\ u_y(x,y,z,t) &= v + y\,(\cos\theta_x - 1) - z\sin\theta_x, \\ u_z(x,y,z,t) &= w + z\,(\cos\theta_x - 1) + y\sin\theta_x, \end{aligned} \tag{14}$$

where u_x, u_y, and u_z respectively denote the displacement of a beam point in x, y, and z directions. Moreover, u, v, and w are the displacements of a beam neutral fiber point in x, y, and z directions, respectively. Remember that θ_x, θ_y, and θ_z were previously defined above, and represent rotations around axes of the non-inertial coordinate systems.

Finally, it is possible to define the vectors

$$\boldsymbol{r} = \begin{pmatrix} x \\ y \\ z \end{pmatrix}, \quad \mathbf{v} = \begin{pmatrix} \dot{u} \\ \dot{v} \\ \dot{w} \end{pmatrix}, \quad \text{and} \quad \dot{\boldsymbol{\theta}} = \begin{pmatrix} \dot{\theta}_x \\ \dot{\theta}_y \\ \dot{\theta}_z \end{pmatrix}, \tag{15}$$

which, respectively, represent the position of a beam point, the velocity of a neutral fiber point, and the rate of rotation of a neutral fiber point.

2.3 Modeling of the friction and shock effects

When a drillstring deforms laterally, there may occur a mechanical contact between the rotating beam and the borehole wall, such as illustrated in the Figure 5. This mechanical contact, which generally take place via a strong impact, gives rise to friction and shock [21, 62, 31].

The modeling of the phenomena of friction and shock is made in terms of a geometric parameter dubbed *indentation*, which is defined as

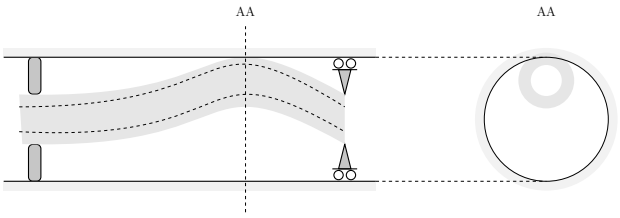

Fig. 5 Schematic representation of the situation where there is a mechanical contact between a drillstring and the borehole wall.

$$\delta_{\text{FS}} = r - \texttt{gap}, \tag{16}$$

where $r = \sqrt{v^2 + w^2}$ is the lateral displacement of the neutral fiber, and $\texttt{gap}$ denotes the spacing between the undeformed beam and the borehole wall. One has that $\delta_{\text{FS}} > 0$ in case of an impact, or $\delta_{\text{FS}} \leq 0$ otherwise, as can be seen in Figure 6. Note that the indentation corresponds to a measure of penetration in the wall of a beam cross section [21].

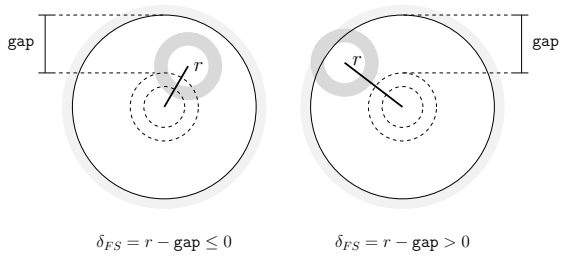

Fig. 6 Illustration of the indentation parameter in a situation without impact (left) or with impact (right).

When the impact occurs, a normal force of the form

$$F^n_{\text{FS}} = -k_{\text{FS}_1}\,\delta_{\text{FS}} - k_{\text{FS}_2}\,\delta^3_{\text{FS}} - c_{\text{FS}}\,|\delta|^3 \dot{\delta}_{\text{FS}}, \tag{17}$$

where k_{FS_1}, k_{FS_2} and c_{FS} are constants of the shock model, begins to act on the beam cross section. In this nonlinear shock model, proposed by Hunt and Crossley [26], the first (a linear spring) and the second (a nonlinear spring) terms describe the elastic deformation during the impact, while the third term (a nonlinear damper) takes into account the loss of energy during the impact.

Once the column is rotating and moving axially, the impact also induces a frictional force in the axial direction, F^a_{FS}, and a torsional friction torque, T_{FS}. Both are modeled by the Coulomb friction law [11], so that the force is given by

$$F^a_{\text{FS}} = -\mu_{\text{FS}}\,F^n_{\text{FS}}\,\texttt{sgn}\,(\dot{u})\,, \tag{18}$$

where the torque is described by

$$T_{\text{FS}} = -\mu_{\text{FS}}\, F_{\text{FS}}^{n}\, R_{bh}\, \texttt{sgn}\left(\dot{\theta}_x\right), \tag{19}$$

being μ_{FS} the friction coefficient, $\texttt{sgn}\,(\cdot)$ the sign function, and the radius of the borehole is $R_{bh} = R_{ext} + \texttt{gap}$.

In order to find all the points of contact between the beam and the borehole wall, it is necessary to discover all the values of x where $\delta_{\text{FS}} > 0$. This is usually done by solving an an optimization problem with constraints [64, 63].

Although the strategy of detection based on the optimization problem is robust in terms of accuracy, it is extremely complex in terms of implementation and computational cost. For this reason, this work uses an approach that introduces the forces of Eqs.(17) and (18), and the torque of Eq.(19), as efforts concentrated on the nodes of the finite element mesh, defined in the section 4.1. This procedure sacrifices accuracy, but simplifies the implementation of the friction and shock model.

2.4 Modeling of the bit-rock interaction effects

During the drilling process, in response to rotational advance of the drillstring, a force and a torque of reaction begin to act on the drill-bit , giving rise to the so-called bit-rock interaction effects [16, 18].

In this work, the model proposed by [43] is considered to describe the bit-rock interaction force

$$F_{\text{BR}} = \begin{cases} \Gamma_{\text{BR}}\left(e^{-\alpha_{\text{BR}}\,\dot{u}_{bit}} - 1\right) & \text{for } \dot{u}_{bit} > 0, \\ 0 & \text{for } \dot{u}_{bit} \leq 0, \end{cases} \tag{20}$$

where Γ_{BR} is the bit-rock limit force, α_{BR} is the rate of change of bit-rock force, and $\dot{u}_{bit} = \dot{u}(L,\cdot)$. The graph of the function F_{BR} is illustrated in Figure 7.

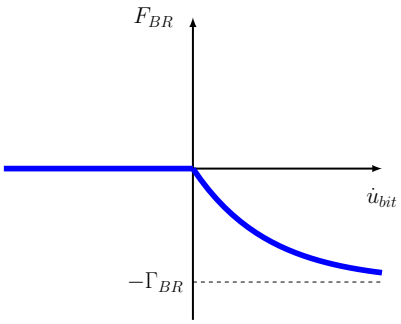

Fig. 7 Illustration of the function used to describe the reaction force on the drill-bit, due to the bit-rock interaction effects.

Also, for the bit-rock interaction torque it is adopted the regularized Coulomb model used by [28], which is expressed as

$$T_{\text{BR}} = -\mu_{\text{BR}}\, F_{\text{BR}}\, R_{bh}\, \xi_{\text{BR}}\left(\omega_{bit}\right), \tag{21}$$

where μ_{BR} bit-rock friction coefficient, $\omega_{bit} = \dot{\theta}_x(L,\cdot)$, and

$$\xi_{\text{BR}}\left(\omega_{bit}\right) = \tanh\left(\omega_{bit}\right) + \frac{2\,\omega_{bit}}{1+\omega_{bit}^{2}}, \tag{22}$$

is a regularization function. The graph of the regularization function ξ_{BR} is illustrated in Figure 8.

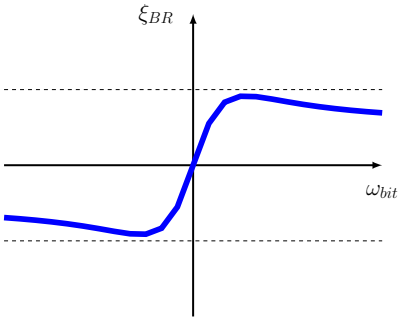

Fig. 8 Illustration of the smooth function used to regularize the reaction torque on the drill-bit, due to the bit-rock interaction effects.

2.5 Kinetic energy

The kinetic energy of the rotating beam is given by

$$\begin{aligned} \mathcal{T} = \frac{1}{2}\iiint_{\mathcal{B}_b} \rho\, \mathbf{v}\cdot\mathbf{v}\, dx\, dy\, dz \;+ \\ \frac{1}{2}\iiint_{\mathcal{B}_b} \rho\, \boldsymbol{\omega}\cdot\left(\boldsymbol{r}\cdot\boldsymbol{r}\,\mathbb{I} - \boldsymbol{r}\otimes\boldsymbol{r}\right)\boldsymbol{\omega}\, dx\, dy\, dz, \end{aligned} \tag{23}$$

where the first triple integral corresponds to the beam translational kinetic energy, and the second one is associated to the beam rotational kinetic energy. In this equation, $\mathbb{I}$ denotes the identity tensor, the symbol $\cdot$ represents the standard inner product between two Euclidean vectors, and the symbol $\otimes$ is used to designate the tensor product.

Developing the vector operations indicated in the Eq.(23), using (1) and (2) to define the limits of integration, using the definitions of A, I_{yy}, I_{zz}, and I_{xx}, and making the other calculations one can show that the Eq.(23) is equivalent to

$$\mathcal{T} = \frac{1}{2}\int_{x=0}^{L} \rho\, A \left(\dot{u}^2 + \dot{v}^2 + \dot{w}^2\right) dx \; + \tag{24}$$
$$\frac{1}{2}\int_{x=0}^{L} 2\,\rho\, I_4 \left(\dot{\theta}_x + \dot{\theta}_z\theta_y\right)^2 dx \; +$$
$$\frac{1}{2}\int_{x=0}^{L} \rho\, I_4 \left(\dot{\theta}_y \cos\theta_x - \dot{\theta}_z \sin\theta_x\right)^2 dx \; +$$
$$\frac{1}{2}\int_{x=0}^{L} \rho\, I_4 \left(\dot{\theta}_y \sin\theta_x + \dot{\theta}_z \cos\theta_x\right)^2 dx.$$

2.6 Strain energy

The analysis of the beam assumes that it is subjected to large displacements, and small deformations. In this way, its strain energy is given by

$$\mathcal{V} = \frac{1}{2}\iiint_{\mathcal{B}_b} \boldsymbol{\epsilon} : \boldsymbol{\sigma}\, dx\, dy\, dz, \tag{25}$$

where $\boldsymbol{\epsilon}$ denotes the Green-Lagrangian strain tensor, $\boldsymbol{\sigma}$ is the second Piola-Kirchhoff stress tensor, and the symbol $:$ represents the double inner product between two tensors.

It is further considered that the beam is made of an isotropic material, such that stress and strain are related by the following constitutive equation (Hooke's law)

$$\boldsymbol{\sigma} = 2\,G\,\boldsymbol{\epsilon} + \lambda\, \mathtt{tr}\,(\boldsymbol{\epsilon})\, \mathbb{I}, \tag{26}$$

where $\mathtt{tr}\,(\cdot)$ represents the trace operator, G is material shear modulus, and λ is used to designate the material first Lamé parameter. In terms of the elastic modulus E and the Poisson's ratio ν, these elastic parameters can be written as

$$G = \frac{E}{2\,(1+\nu)}, \qquad \text{and} \qquad \lambda = \frac{E\,\nu}{(1+\nu)(1-2\,\nu)}. \tag{27}$$

According to the beam theory used in this work, there is no tension in any cross section of the beam that is perpendicular to the x axis, i.e., $\sigma_{yy} = 0$, $\sigma_{zz} = 0$, $\sigma_{yz} = 0$, and $\sigma_{zy} = 0$. When this hypothesis is combined with the tri-dimensional Hooke's law, represented by the Eq.(26), one can conclude that $\sigma_{xx} = E\,\epsilon_{xx}$, $\sigma_{xy} = 2\,G\,\epsilon_{xy}$, and $\sigma_{xz} = 2\,G\,\epsilon_{xz}$, which is an one-dimensional version of the Hooke's law.

Combining this one-dimensional Hooke's law with the symmetry of the stress tensor, one can express the double contraction between strain and stress tensors, within the integral in Eq.(25), as a quadratic form

$$\boldsymbol{\epsilon} : \boldsymbol{\sigma} = E\,\epsilon_{xx}^2 + 4\,G\,\epsilon_{xy}^2 + 4\,G\,\epsilon_{xz}^2, \tag{28}$$

which is modified, by the introduction of the shearing factor κ_s, as

$$\boldsymbol{\epsilon} : \boldsymbol{\sigma} = E\,\epsilon_{xx}^2 + 4\,\kappa_s\,G\,\epsilon_{xy}^2 + 4\,\kappa_s\,G\,\epsilon_{xz}^2. \tag{29}$$

This modification aims to take into account the effect of shear deformation in the beam cross section area, which is neglected when one uses the one-dimensional Hooke's law.

Hence, after replace Eq.(29) in Eq.(25), one finally obtains

$$\mathcal{V} = \frac{1}{2}\iiint_{\mathcal{B}_b} \left(E\,\epsilon_{xx}^2 + 4\,\kappa_s\,G\,\epsilon_{xy}^2 + 4\,\kappa_s\,G\,\epsilon_{xz}^2\right) dx\, dy\, dz. \tag{30}$$

As the analysis is using large displacements, one has

$$\epsilon_{xx} = \frac{1}{2}\left(\frac{\partial u_x}{\partial x} + \frac{\partial u_x}{\partial x}\right) \; + \tag{31}$$
$$\frac{1}{2}\left(\frac{\partial u_x}{\partial x}\frac{\partial u_x}{\partial x} + \frac{\partial u_y}{\partial x}\frac{\partial u_y}{\partial x} + \frac{\partial u_z}{\partial x}\frac{\partial u_z}{\partial x}\right),$$

$$\epsilon_{xy} = \frac{1}{2}\left(\frac{\partial u_y}{\partial x} + \frac{\partial u_x}{\partial y}\right) \; + \tag{32}$$
$$\frac{1}{2}\left(\frac{\partial u_x}{\partial x}\frac{\partial u_x}{\partial y} + \frac{\partial u_y}{\partial x}\frac{\partial u_y}{\partial y} + \frac{\partial u_z}{\partial x}\frac{\partial u_z}{\partial y}\right),$$

and

$$\epsilon_{xz} = \frac{1}{2}\left(\frac{\partial u_z}{\partial x} + \frac{\partial u_x}{\partial z}\right) \; + \tag{33}$$
$$\frac{1}{2}\left(\frac{\partial u_x}{\partial x}\frac{\partial u_x}{\partial z} + \frac{\partial u_y}{\partial x}\frac{\partial u_y}{\partial z} + \frac{\partial u_z}{\partial x}\frac{\partial u_z}{\partial z}\right),$$

where the quadratic terms on the right hand side of the above equations are associated to the geometric nonlinearity of the beam model.

Substituting the kinematic hypothesis of the Eq.(14) in Eqs.(31) to (33), and then calculating the partial derivatives, one concludes that the deformations are respectively given by

$$\epsilon_{xx} = u' - y\,\theta_z' + z\,\theta_y' + u'\left(z\,\theta_y' - y\,\theta_z'\right) - y\,z\,\theta_y'\,\theta_z' \; + \tag{34}$$
$$\theta_x'\left(\left(y\,w' - z\,v'\right)\cos\theta_x - \left(y\,v' + z\,w'\right)\sin\theta_x\right) \; +$$
$$\frac{1}{2}\left(u'^2 + v'^2 + w'^2 + y^2\,\theta_z'^2 + z^2\,\theta_y'^2 + \left(y^2+z^2\right)\theta_x'^2\right),$$

$$\epsilon_{xy} = \frac{1}{2}\left(v'\,\cos\theta_x + w'\sin\theta_x - z\,\theta'_x\right) \; + \; \frac{1}{2}\,\theta_z\left(y\,\theta'_z - z\theta'_y - u' - 1\right), \tag{35}$$

and

$$\epsilon_{xz} = \frac{1}{2}\left(w'\,\cos\theta_x - v'\sin\theta_x + y\,\theta'_x\right) \; + \; \frac{1}{2}\,\theta_y\left(-y\,\theta'_z + z\theta'_y + u' + 1\right), \tag{36}$$

where $'$ is used as an abbreviation for space derivative.

2.7 Energy dissipation function

It is assumed that the beam loses energy through a mechanism of viscous dissipation, with a (dimensionless) damping constant c. In this way, there is an energy dissipation function (per unit of length) associated to the system, which is given by

$$\mathcal{D} = \frac{1}{2}\iint_{\mathcal{S}_b} c\,\rho\,\mathbf{v}\cdot\mathbf{v}\,dy\,dz \; + \; \frac{1}{2}\iint_{\mathcal{S}_b} c\,\rho\,\dot{\boldsymbol{\theta}}\cdot\left(\boldsymbol{r}\cdot\boldsymbol{r}\,\mathbb{I} - \boldsymbol{r}\otimes\boldsymbol{r}\right)\dot{\boldsymbol{\theta}}\,dy\,dz, \tag{37}$$

where the first term is a dissipation potential due to the translational movement, and the second term represents a dissipation potential due to the movement of rotation.

Making a development almost similar to the one performed to obtain Eq.(24), it can be shown that

$$\mathcal{D} = \frac{1}{2}\,c\,\rho\,A\left(\dot{u}^2 + \dot{v}^2 + \dot{w}^2\right) \; + \; \frac{1}{2}\,c\,\rho\,I_4\left(2\,\dot{\theta}_x^2 + \dot{\theta}_y^2 + \dot{\theta}_z^2\right). \tag{38}$$

2.8 External forces work

The work done by the external forces acting on the beam is given by

$$\mathcal{W} = -\int_{x=0}^{L} \rho\,A\,g\,w\,dx + \mathcal{W}_{\text{FS}} + \mathcal{W}_{\text{BR}}. \tag{39}$$

where the first term is due to the gravity, the second one is associated to the effects of friction and shock, and the last term accounts the work done by the force/torque that comes from the bit-rock interaction.

Note that, due to the non-holonomic nature of the forces and torques that comes from the effects of friction/shock, and bit-rock interaction, it is not possible to write explicit formulas for $\mathcal{W}_{\text{FS}}$ and $\mathcal{W}_{\text{FS}}$ [30].

However, it is known that the virtual work of $\mathcal{W}_{\text{FS}}$, denoted by $\delta\mathcal{W}_{\text{FS}}$, is written as

$$\delta\mathcal{W}_{\text{FS}} = \sum_{m=1}^{N_{nodes}} \left(F^a_{\text{FS}}\,\delta u + F^n_{\text{FS}}\left(v\,\delta v + w\,\delta w\right)/r + T_{\text{FS}}\,\delta\theta_x\right)\Big|_{x=x_m} \tag{40}$$

where x_m are the global coordinates of the finite element nodes, N_{nodes} is the number of nodes in the finite element mesh, and δu, δv, δw, and $\delta\theta_x$ respectively denote the variations of the fields u, v, w, and θ_x.

On the other hand, the virtual work of $\mathcal{W}_{\text{BR}}$, denoted by $\delta\mathcal{W}_{\text{BR}}$, reads as

$$\delta\mathcal{W}_{\text{BR}} = F_{\text{BR}}\,\delta u\Big|_{x=L} + T_{\text{BR}}\,\delta\theta_x\Big|_{x=L}. \tag{41}$$

3 Mathematical model for the problem

3.1 Equation of motion of the nonlinear dynamics

A modified version of the extended Hamilton's principle [30] is employed to derive the equations which describe the nonlinear dynamics of the mechanical system, so that the first variation is expressed as

$$\int_{t=t_0}^{t_f}\left(\delta\mathcal{T} - \delta\mathcal{V} + \delta\mathcal{W}\right)dt \; - \; \int_{t=t_0}^{t_f}\int_{x=0}^{L}\delta\boldsymbol{U}\cdot\frac{\partial\mathcal{D}}{\partial\dot{\boldsymbol{U}}}\,dx\,dt = 0, \tag{42}$$

where the first term corresponds to the conservative part of the dynamics, the second one is associated to the energy dissipation. Also, $\boldsymbol{U}$ is a vector field which lumps the field variables, the initial and final instants of observation are respectively denoted by t_0 and t_f, and the symbol δ represents the variation operator [44].

The development of Eq.(42) results in the following weak equation of motion

$$\mathcal{M}\left(\boldsymbol{\psi},\ddot{\boldsymbol{U}}\right) + \mathcal{C}\left(\boldsymbol{\psi},\dot{\boldsymbol{U}}\right) + \mathcal{K}\left(\boldsymbol{\psi},\boldsymbol{U}\right) = \mathcal{F}\left(\boldsymbol{\psi},\boldsymbol{U},\dot{\boldsymbol{U}},\ddot{\boldsymbol{U}}\right), \tag{43}$$

valid for any $\boldsymbol{\psi}$ chosen in a "suitable" space of weight functions, where the field variables and their corresponding weight functions are represented by the vector fields $\boldsymbol{U} = \left(u, v, w, \theta_x, \theta_y, \theta_z\right)$, and $\boldsymbol{\psi} = \left(\psi_u, \psi_v, \psi_w, \psi_{\theta_x}, \psi_{\theta_y}, \psi_{\theta_z}\right)$.

Furthermore,

$$\mathcal{M}\left(\boldsymbol{\psi},\ddot{\boldsymbol{U}}\right) = \int_{x=0}^{L}\rho\,A\left(\psi_u\,\ddot{u} + \psi_v\,\ddot{v} + \psi_w\,\ddot{w}\right)dx \; + \; \int_{x=0}^{L}\rho\,I_4\left(2\,\psi_{\theta_x}\,\ddot{\theta}_x + \psi_{\theta_y}\,\ddot{\theta}_y + \psi_{\theta_z}\,\ddot{\theta}_z\right)dx, \tag{44}$$

represents the mass operator,

$$\mathcal{C}\left(\boldsymbol{\psi},\dot{\boldsymbol{U}}\right) = \int_{x=0}^{L} c\,\rho\,A\left(\psi_u\,\dot{u} + \psi_v\,\dot{v} + \psi_w\,\dot{w}\right)dx \;+ \int_{x=0}^{L} c\,\rho\,I_4\left(2\,\psi_{\theta_x}\,\dot{\theta}_x + \psi_{\theta_y}\,\dot{\theta}_y + \psi_{\theta_z}\,\dot{\theta}_z\right)dx, \tag{45}$$

is the damping operator,

$$\begin{aligned}\mathcal{K}\left(\boldsymbol{\psi},\boldsymbol{U}\right) = &\int_{x=0}^{L} E\,A\,\psi_u'\,u'\,dx \;+ \\ &\int_{x=0}^{L} E\,I_4\left(\psi_{\theta_y}'\,\theta_y' + \psi_{\theta_z}'\,\theta_z'\right)dx \;+ \\ &\int_{x=0}^{L} 2\,\kappa_s\,G\,I_4\,\psi_{\theta_x}'\,\theta_x'\,dx \;+ \\ &\int_{x=0}^{L} \kappa_s\,G\,A\left(\psi_{\theta_y} + \psi_w'\right)\left(\theta_y + w'\right)dx \;+ \\ &\int_{x=0}^{L} \kappa_s\,G\,A\left(\psi_{\theta_z} - \psi_v'\right)\left(\theta_z - v'\right)dx,\end{aligned} \tag{46}$$

is the stiffness operator, and

$$\begin{aligned}\mathcal{F}\left(\boldsymbol{\psi},\boldsymbol{U},\dot{\boldsymbol{U}},\ddot{\boldsymbol{U}}\right) = &\mathcal{F}_{\text{KE}}\left(\boldsymbol{\psi},\boldsymbol{U},\dot{\boldsymbol{U}},\ddot{\boldsymbol{U}}\right) + \\ &\mathcal{F}_{\text{SE}}\left(\boldsymbol{\psi},\boldsymbol{U}\right) \;+\; \mathcal{F}_{\text{FS}}\left(\boldsymbol{\psi},\boldsymbol{U}\right) \;+ \\ &\mathcal{F}_{\text{BR}}\left(\boldsymbol{\psi},\dot{\boldsymbol{U}}\right) \;+\; \mathcal{F}_{\text{G}}\left(\boldsymbol{\psi}\right),\end{aligned} \tag{47}$$

is the force operator, which is divided into five parts. A nonlinear force due to inertial effects

$$\begin{aligned}\mathcal{F}_{\text{KE}} = &-\int_{x=0}^{L} 2\,\rho\,I_4\,\psi_{\theta_x}\left(\theta_y\,\ddot{\theta}_z + \dot{\theta}_y\,\dot{\theta}_z\right)dx \\ &+\int_{x=0}^{L} 2\,\rho\,I_4\,\psi_{\theta_y}\left(\theta_y\,\dot{\theta}_z^2 + \dot{\theta}_x\,\dot{\theta}_z\right)dx \\ &-\int_{x=0}^{L} 2\,\rho\,I_4\,\psi_{\theta_z}\left(\theta_y\,\ddot{\theta}_x + \theta_y^2\,\ddot{\theta}_z\right)dx \\ &-\int_{x=0}^{L} 2\,\rho\,I_4\,\psi_{\theta_z}\left(\dot{\theta}_x\,\dot{\theta}_y + 2\,\theta_y\,\dot{\theta}_y\,\dot{\theta}_z\right)dx,\end{aligned} \tag{48}$$

a nonlinear force due to geometric nonlinearity

$$\begin{aligned}\mathcal{F}_{\text{SE}} = &\int_{x=0}^{L}\left(\psi_{\theta_x}\,\Gamma_1 + \psi_{\theta_y}\,\Gamma_2 + \psi_{\theta_z}\,\Gamma_3\right)dx \;+ \\ &\int_{x=0}^{L}\left(\psi_u'\,\Gamma_4 + \psi_v'\,\Gamma_5 + \psi_w'\,\Gamma_6\right)dx \;+ \\ &\int_{x=0}^{L}\left(\psi_{\theta_x}'\Gamma_7 + \psi_{\theta_y}'\,\Gamma_8 + \psi_{\theta_z}'\,\Gamma_9\right)dx,\end{aligned} \tag{49}$$

a nonlinear force due to the effects of friction and shock

$$\mathcal{F}_{\text{FS}} = \sum_{m=1}^{N_{nodes}}\left(F_{\text{FS}}^{a}\,\psi_u + F_{\text{FS}}^{n}\left(v\,\psi_v + w\,\psi_w\right)/r + T_{\text{FS}}\,\psi_{\theta_x}\right)\Big|_{x=x_m} \tag{50}$$

a nonlinear force due to the bit-rock interaction

$$\mathcal{F}_{\text{BR}} = F_{\text{BR}}\,\psi_u\Big|_{x=L} + T_{\text{BR}}\,\psi_{\theta_x}\Big|_{x=L}, \tag{51}$$

and a linear force due to the gravity

$$\mathcal{F}_{\text{G}} = -\int_{x=0}^{L}\rho\,A\,g\,\psi_w\,dx. \tag{52}$$

The nonlinear functions Γ_n, with $n = 1,\cdots,9$, in Eq.(49) are very complex and, for sake of space limitation, are not presented in this section. But they can be seen in the Appendix A.

The model presented above is an adaptation, for the case of horizontal drillstrings, with some variations in the friction and shock treatment, of the model proposed by [40, 38] to describe the nonlinear dynamics of vertical drillstrings.

3.2 Initial conditions

With regard to the initial state of the mechanical system, it is assumed that the beam presents neither displacement nor rotations, i.e., $u(x,0) = 0$, $v(x,0) = 0$, $w(x,0) = 0$, $\theta_x(x,0) = 0$, $\theta_y(x,0) = 0$, and $\theta_z(x,0) = 0$. These field variables, except for u and θ_x, also have initial velocities and rate of rotations equal to zero, i.e. $\dot{v}(x,0) = 0$, $\dot{w}(x,0) = 0$, $\dot{\theta}_y(x,0) = 0$, and $\dot{\theta}_z(x,0) = 0$.

It is also assumed that, initially, the beam moves horizontally with a constant axial velocity V_0, and rotates around the x axis with a constant angular velocity Ω. Thereby, one has that $\dot{u}(x,0) = V_0$, and $\dot{\theta}_x(x,0) = \Omega$.

Projecting the initial conditions above in the space of weight functions one obtains the weak forms of the initial conditions, respectively, given by

$$\mathcal{M}\left(\boldsymbol{\psi},\boldsymbol{U}(0)\right) = \mathcal{M}\left(\boldsymbol{\psi},\boldsymbol{U}_0\right), \tag{53}$$

and

$$\mathcal{M}\left(\boldsymbol{\psi},\dot{\boldsymbol{U}}(0)\right) = \mathcal{M}\left(\boldsymbol{\psi},\dot{\boldsymbol{U}}_0\right), \tag{54}$$

where $\boldsymbol{U}_0 = (0,0,0,0,0,0)$ and $\dot{\boldsymbol{U}}_0 = (V_0,0,0,\Omega,0,0)$.

In formal terms, the weak formulation of the initial/boundary value problem that describes the nonlinear dynamics of the mechanical system consists in find a vector field $\boldsymbol{U}$, "sufficiently regular", which satisfies the weak equation of motion given by Eq.(43) for all "suitable" $\boldsymbol{\psi}$, as well as the weak form of the initial conditions, given by Eqs.(53), and (54) [25].

3.3 Associated linear conservative dynamics

Consider the linear homogeneous equation given by

$$\mathcal{M}\left(\boldsymbol{\psi}, \ddot{\boldsymbol{U}}\right) + \mathcal{K}\left(\boldsymbol{\psi}, \boldsymbol{U}\right) = 0, \tag{55}$$

obtained from Eq.(43) when one discards the damping, and the force operators, and which is valid for all $\boldsymbol{\psi}$ in the space of weight functions.

Suppose that Eq.(55) has a solution of the form $\boldsymbol{U} = e^{i\omega t}\boldsymbol{\phi}$, where ω is a natural frequency (in rad/s), $\boldsymbol{\phi}$ is the associated normal mode, and $i = \sqrt{-1}$ is the imaginary unit. Replacing this expression of $\boldsymbol{U}$ in the Eq.(55) and using the linearity of the operators $\mathcal{M}$, and $\mathcal{K}$, one gets

$$\left(-\omega^2 \mathcal{M}\left(\boldsymbol{\psi}, \boldsymbol{\phi}\right) + \mathcal{K}\left(\boldsymbol{\psi}, \boldsymbol{\phi}\right)\right) e^{i\omega t} = 0, \tag{56}$$

which is equivalent to

$$-\omega^2 \mathcal{M}\left(\boldsymbol{\psi}, \boldsymbol{\phi}\right) + \mathcal{K}\left(\boldsymbol{\psi}, \boldsymbol{\phi}\right) = 0, \tag{57}$$

a generalized eigenvalue problem.

Since the operator $\mathcal{M}$ is positive-definite, and the operator $\mathcal{K}$ is positive semi-definite, the generalized eigenvalue problem above has a denumerable number of solutions. The solutions of this eigenproblem are of the form $(\omega_n^2, \boldsymbol{\phi}_n)$, where ω_n is the n-th natural frequency and $\boldsymbol{\phi}_n$ is the n-th normal mode [23].

Also, it should be noted that the symmetry of the operators $\mathcal{M}$, and $\mathcal{K}$ implies the following orthogonality relations

$$\mathcal{M}\left(\boldsymbol{\phi}_n, \boldsymbol{\phi}_m\right) = \delta_{nm}, \quad \text{and} \quad \mathcal{K}\left(\boldsymbol{\phi}_n, \boldsymbol{\phi}_m\right) = \omega_n^2\, \delta_{nm}, \tag{58}$$

where δ_{nm} represents the Kronecker delta symbol. See [23] for more details.

The generalized eigenvalue problem of Eq.(57), as well as the properties of (58), will be useful for the construction of a reduced order model for the discretized dynamical system which approximates the solution of the weak boundary-initial value problem of Eqs.(43), (53), and (54).

4 Computational model for the problem

4.1 Discretization of the nonlinear dynamics

To proceed with the discretization of the initial/boundary value problem which describes the nonlinear dynamics rotating beam, whose the weak formulation is given by Eqs.(43), (53), and (54), it is used the standard finite element method (FEM) [25], where the spaces of basis and weight functions are constructed by the same (finite dimensional) class of functions.

In this procedure, the beam geometry is discretized by a FEM mesh with N_{elem} finite elements. Each one of these elements is composed by two nodes, and each one of these nodes has six degrees of freedom associated, one for each field variable in the beam model described in the section 3.1. Thus, the number of degrees of freedom associated with the FEM model is $N_{dofs} = 6(N_{elem}+1)$. An illustration of the FEM mesh/element can be seen in the Figure 9.

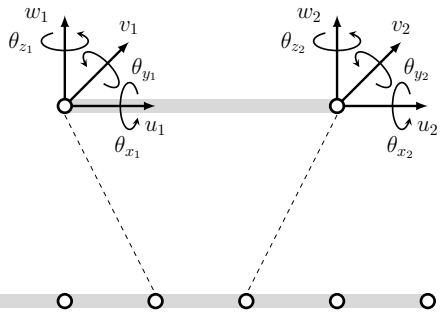

Fig. 9 Illustration of the FEM mesh/element used to discretize the beam geometry.

Concerning the shape functions, it is adopted an interdependent interpolation scheme which avoids the shear-locking effect [37]. This scheme uses, for the transverse displacements/rotations, Hermite cubic polynomials, and, for the fields of axial displacement/torsional rotation, affine functions [2].

Thus, each field variable of the physical model is approximated by a linear combination of basis functions, in such way that

$$u(x,t) \approx \sum_{m=1}^{N_{dofs}} Q_m(t)\, \mathcal{N}_m(x), \tag{59}$$

$$\theta_x(x,t) \approx \sum_{m=1}^{N_{dofs}} Q_m(t)\, \mathcal{N}_m(x),$$

$$v(x,t) \approx \sum_{m=1}^{N_{dofs}} Q_m(t)\, \mathcal{H}_m^{(1)}(x),$$

$$w(x,t) \approx \sum_{m=1}^{N_{dofs}} Q_m(t)\, \mathcal{H}_m^{(1)}(x),$$

$$\theta_y(x,t) \approx \sum_{m=1}^{N_{dofs}} Q_m(t)\, \mathcal{H}_m^{(2)}(x),$$

$$\theta_z(x,t) \approx \sum_{m=1}^{N_{dofs}} Q_m(t)\, \mathcal{H}_m^{(2)}(x),$$

where $\mathcal{N}_m(x)$, $\mathcal{H}_m^{(1)}(x)$, and $\mathcal{H}_m^{(2)}(x)$ are the (position dependent) shape functions, and the (time dependent) coefficients of the linear combination, $Q_m(t)$, are the unknowns of the discretized problem. In physical terms, each one of these temporal coefficients represents a degree of freedom of the FEM model.

The discretization results is the $N_{dofs} \times N_{dofs}$ nonlinear system of ordinary differential equations given by

$$[\mathcal{M}]\,\ddot{\boldsymbol{Q}}(t) + [\mathcal{C}]\,\dot{\boldsymbol{Q}}(t) + [\mathcal{K}]\,\boldsymbol{Q}(t) = \boldsymbol{\mathcal{F}}\left(\boldsymbol{Q}, \dot{\boldsymbol{Q}}, \ddot{\boldsymbol{Q}}\right), \quad (60)$$

where $\boldsymbol{Q}(t)$ is the nodal displacement vector (translations and rotations), $\dot{\boldsymbol{Q}}(t)$ is the nodal velocity vector, and $\ddot{\boldsymbol{Q}}(t)$ is the nodal acceleration vector. The other objects in the Eq.(60) are the mass matrix $[\mathcal{M}]$, the damping matrix $[\mathcal{C}]$, the stiffness matrix $[\mathcal{K}]$, and the force vector $\boldsymbol{\mathcal{F}}$.

A discretization procedure similar to one presented above is applied to the initial conditions of Eqs.(53) and (54), which results in linear systems of algebraic equations given by

$$[\mathcal{M}]\,\boldsymbol{Q}(0) = \boldsymbol{Q}_0, \qquad \text{and} \qquad [\mathcal{M}]\,\dot{\boldsymbol{Q}}(0) = \dot{\boldsymbol{Q}}_0. \quad (61)$$

4.2 Reduction of the finite element model

In order to reduce the dimension of the finite element model developed in the section 4.1, it is considered a finite dimensional version of the generalized eigenvalue problem presented in section 3.3, which is defined by

$$[\mathcal{K}]\,\boldsymbol{\phi}_n = \omega_n^2\,[\mathcal{M}]\,\boldsymbol{\phi}_n. \quad (62)$$

As a consequence of the properties of the operators $\mathcal{M}$, and $\mathcal{K}$ discussed in section 3.3, that are inherited by the finite dimensional operators $[\mathcal{M}]$ and $[\mathcal{K}]$, the above eigenvalue problem has N_{dofs} solutions. But the Eq.(62) is solved only for $n = 1, 2, \cdots, N_{red}$, where the dimension of the reduced model N_{red} is an integer chosen such that $N_{red} \ll N_{dofs}$.

The procedure that follows consists in project the nonlinear dynamic, defined by the initial value problem of Eqs.(60) and (61), into the vector space spanned by $\{\boldsymbol{\phi}_1, \boldsymbol{\phi}_2, \cdots, \boldsymbol{\phi}_{N_{red}}\}$.

For this purpose, define the $N_{dofs} \times N_{red}$ projection matrix by

$$[\Phi] = \begin{bmatrix} | & | & & | \\ \boldsymbol{\phi}_1 & \boldsymbol{\phi}_2 & \cdots & \boldsymbol{\phi}_{N_{red}} \\ | & | & & | \end{bmatrix}, \quad (63)$$

make in the Eqs.(60) and (61) the change of basis defined by

$$\boldsymbol{Q}(t) = [\Phi]\,\boldsymbol{q}(t), \quad (64)$$

and then pre-multiply the resulting equations by the matrix $[\Phi]^T$, where the superscript ^{T} represents the transposition operation.

This development results in the reduced initial value problem given by

$$[M]\,\ddot{\boldsymbol{q}}(t) + [C]\,\dot{\boldsymbol{q}}(t) + [K]\,\boldsymbol{q}(t) = \boldsymbol{f}\left(\boldsymbol{q}(t), \dot{\boldsymbol{q}}(t), \ddot{\boldsymbol{q}}(t)\right), \quad (65)$$

and

$$\boldsymbol{q}(0) = \boldsymbol{q}_0, \qquad \text{and} \qquad \dot{\boldsymbol{q}}(0) = \dot{\boldsymbol{q}}_0, \quad (66)$$

where $\boldsymbol{q}(t)$ is the reduced displacement vector, $\dot{\boldsymbol{q}}(t)$ is the reduced velocity vector, $\ddot{\boldsymbol{q}}(t)$ is the reduced acceleration vector. The reduced matrices of mass, damping, and stiffness, as well as the reduced vectors of force, initial displacement, and initial velocity are, respectively, defined by $[M] = [\Phi]^T\,[\mathcal{M}]\,[\Phi]$, $[C] = [\Phi]^T\,[\mathcal{C}]\,[\Phi]$, $[K] = [\Phi]^T\,[\mathcal{K}]\,[\Phi]$, $\boldsymbol{f} = [\Phi]^T\,\boldsymbol{\mathcal{F}}\left([\Phi]\,\boldsymbol{q}(t), [\Phi]\,\dot{\boldsymbol{q}}(t), [\Phi]\,\ddot{\boldsymbol{q}}(t)\right)$, $\boldsymbol{q}_0 = [\Phi]^T\,\boldsymbol{Q}_0$, $\dot{\boldsymbol{q}}_0 = [\Phi]^T\,\dot{\boldsymbol{Q}}_0$. These matrices are $N_{red} \times N_{red}$, while these vectors are $N_{red} \times 1$. Furthermore, due to the orthogonality properties defined by Eq.(58), that are inherited by the operators in finite dimension, these matrices are diagonal.

Thus, although the initial value problem of Eqs.(65) and (66) is apparently similar to the one defined by Eqs.(60) and (61), the former has a structure that makes it much more efficient in terms of computational cost, and so, it will be used to analyze the nonlinear dynamics under study.

4.3 Integration of the discretized nonlinear dynamics

In order to solve the initial value problem of Eqs.(65) and (66), it is employed the Newmark method [35], which defines the following implicit integration scheme

$$\dot{\boldsymbol{q}}_{n+1} = \dot{\boldsymbol{q}}_n + (1-\gamma)\Delta t\,\ddot{\boldsymbol{q}}_n + \gamma\Delta t\,\ddot{\boldsymbol{q}}_{n+1}, \quad (67)$$

$$\boldsymbol{q}_{n+1} = \boldsymbol{q}_n + \Delta t\,\dot{\boldsymbol{q}}_n + \left(\frac{1}{2} - \beta\right)\Delta t^2\,\ddot{\boldsymbol{q}}_n + \beta\,\Delta t^2\,\ddot{\boldsymbol{q}}_{n+1}, \quad (68)$$

where $\boldsymbol{q}_n$, $\dot{\boldsymbol{q}}_n$ and $\ddot{\boldsymbol{q}}_n$ are approximations to $\boldsymbol{q}(t_n)$, $\dot{\boldsymbol{q}}(t_n)$ and $\ddot{\boldsymbol{q}}(t_n)$, respectively, and $t_n = n\Delta t$ is an instant in a temporal mesh defined over the interval $[t_0, t_f]$,

with an uniform time step Δt. The parameters γ and β are associated with the accuracy and stability of the numerical scheme [25], and for the simulations reported in this work they are assumed as $\gamma = 1/2 + \alpha$, and $\beta = 1/4\left(1/2 + \gamma\right)^2$, with $\alpha = 15/1000$.

Handling up properly the Eqs.(67) and (68), and the discrete version of Eq.(65), one arrives in a nonlinear system of algebraic equations, with unknown vector $\boldsymbol{q}_{n+1}$, which is represented by

$$[\hat{K}]\boldsymbol{q}_{n+1} = \hat{\boldsymbol{f}}_{n+1}\left(\boldsymbol{q}_{n+1}\right), \tag{69}$$

where $[\hat{K}]$ is the effective stiffness matrix, and $\hat{\boldsymbol{f}}_{n+1}$ is the (nonlinear) effective force vector.

4.4 Incorporation of the boundary conditions

As can be seen in Figure 4, the mechanical system has the following boundary conditions: (i) left extreme with no transversal displacement, nor transversal rotation; (ii) right extreme with no transversal displacement. It is also assumed that the left end has has: (iii) constant axial and rotational velocities in x, respectively equal to V_0 and Ω.

Hence, for $x = 0$, it is true that $u(0,t) = V_0\, t$, $v(0,t) = 0$, $w(0,t) = 0$, $\theta_x(0,t) = \Omega\, t$, $\theta_y(0,t) = 0$, and $\theta_z(0,t) = 0$. On the other hand, for $x = L$, one has $v(L,t) = 0$, and $w(L,t) = 0$.

The variational formulation presented in section 3.1, was made for a free-free beam, so that the above geometric boundary conditions were not included. For this reason, they are included in the formulation as constraints using the Lagrange multipliers method [25]. The details of this procedure are presented below.

Observe that the boundary conditions can be rewritten in matrix form as

$$[\mathscr{B}]\,\boldsymbol{Q}(t) = \boldsymbol{h}(t), \tag{70}$$

where the constraint matrix $[\mathscr{B}]$ is $8 \times N_{dofs}$ and has almost all the entries equal to zero. The exceptions are $[\mathscr{B}]_{ii} = 1$ for $i = \{1, \cdots, 6\}$, $[\mathscr{B}]_{7(N_{dofs}-5)} = 1$, and $[\mathscr{B}]_{8(N_{dofs}-4)} = 1$. The constraint vector is given by

$$\boldsymbol{h}(t) = \begin{pmatrix} u(0,t) \\ v(0,t) \\ w(0,t) \\ \theta_x(0,t) \\ \theta_y(0,t) \\ \theta_z(0,t) \\ v(L,t) \\ w(L,t) \end{pmatrix}. \tag{71}$$

Making the change of basis defined by Eq.(64), one can rewrite Eq.(70) as

$$[B]\,\boldsymbol{q}(t) = \boldsymbol{h}(t), \tag{72}$$

where the $8 \times N_{red}$ reduced constraint matrix is defined by $[B] = [\mathscr{B}]\,[\Phi]$.

The discretization of the Eq.(72) results in

$$[B]\,\boldsymbol{q}_{n+1} = \boldsymbol{h}_{n+1}, \tag{73}$$

where $\boldsymbol{h}_{n+1}$ is an approximation to $\boldsymbol{h}(t_{n+1})$. This equation defines the constraint that must be satisfied by the "approximate solution" of the variational problem.

In what follows it is helpful to think that the Eq.(69) comes from the minimization of a energy functional $\boldsymbol{q}_{n+1} \mapsto \mathscr{F}\left(\boldsymbol{q}_{n+1}\right)$, which is the weak form of this nonlinear system of algebraic equations.

Then, one defines the Lagrangian as

$$\mathscr{L}\left(\boldsymbol{q}_{n+1}, \boldsymbol{\lambda}_{n+1}\right) = \mathscr{F}\left(\boldsymbol{q}_{n+1}\right) + \boldsymbol{\lambda}_{n+1}^T\left([B]\,\boldsymbol{q}_{n+1} - \boldsymbol{h}_{n+1}\right), \tag{74}$$

being the (time-dependent) Lagrange multipliers vector of the form

$$\boldsymbol{\lambda}_{n+1} = \begin{pmatrix} \lambda_1(t_{n+1}) \\ \lambda_2(t_{n+1}) \\ \lambda_3(t_{n+1}) \\ \lambda_4(t_{n+1}) \\ \lambda_5(t_{n+1}) \\ \lambda_6(t_{n+1}) \\ \lambda_7(t_{n+1}) \\ \lambda_8(t_{n+1}) \end{pmatrix}. \tag{75}$$

Invoking the stationarity condition of the Lagrangian one arrives in the following $(N_{red}+8) \times (N_{red}+8)$ system of nonlinear algebraic equations

$$\begin{bmatrix} [\hat{K}] & [B]^T \\ [B] & [0] \end{bmatrix} \begin{pmatrix} \boldsymbol{q}_{n+1} \\ \boldsymbol{\lambda}_{n+1} \end{pmatrix} = \begin{pmatrix} \hat{\boldsymbol{f}}_{n+1} \\ \boldsymbol{h}_{n+1} \end{pmatrix}, \tag{76}$$

where $[0]$ is a 8×8 null matrix. The unknowns are $\boldsymbol{q}_{n+1}$ and $\boldsymbol{\lambda}_{n+1}$, and must be solved for each instant of time in the temporal mesh, in order to construct an approximation to the dynamic response of the mechanical system under analysis.

The solution of the nonlinear system of algebraic equations, defined by Eq.(76), is carried out first obtaining and solving a discrete Poisson equation for $\boldsymbol{\lambda}_{n+1}$ [22], and then using the first line of (76) to obtain $\boldsymbol{q}_{n+1}$. To solve these equations, a procedure of fixed point iteration is used in combination with a process of successive over relaxation [65].

5 Probabilistic modeling of system-parameter uncertainties

The mathematical model used to describe the physical behavior of the mechanical system is an abstraction of reality, and its use does not consider some aspects of the problem physics. Regarding the modeling of the system, either the beam theory used to describe the structure dynamics [40], as the friction and shock model used [26] are fairly established physical models, who have gone through several experimental tests to prove their validity, and have been used for many years in similar situations. On the other hand, the bit-rock interaction model adopted in this work, until now was used only in a purely numeric context [43], without any experimental validation. Thus, it is natural to conclude that bit-rock interaction law is the weakness of the model proposed in this work.

In this sense, this work will focus on modeling and quantifying the uncertainties that are introduced in the mechanical system by the bit-rock interaction model. For convenience, it was chosen to use the parametric probabilistic approach [55], where only the uncertainties of the system parameters are considered, and the maximum entropy principle is employed to construct the probability distributions.

5.1 Probabilistic framework

Let $\mathbb{X}$ be a real-valued random variable, defined on a probability space $(\Theta, \mathbb{\Sigma}, \mathbb{P})$, for which the probability distribution $P_{\mathbb{X}}(dx)$ on $\mathbb{R}$ admits a density $x \mapsto p_{\mathbb{X}}(x)$ with respect to dx. The support of the probability density function (PDF) $p_{\mathbb{X}}$ will be denoted by $\mathtt{Supp}\,\mathbb{X} \subset \mathbb{R}$. The mathematical expectation of $\mathbb{X}$ is defined by

$$\mathbb{E}\left[\mathbb{X}\right] = \int_{\mathtt{Supp}\,\mathbb{X}} x\, p_{\mathbb{X}}(x)\, dx\,, \tag{77}$$

and any realization of random variable $\mathbb{X}$ will be denoted by $\mathbb{X}(\theta)$ for $\theta \in \Theta$. Let $m_{\mathbb{X}} = \mathbb{E}\left[\mathbb{X}\right]$ be the mean value, $\sigma_{\mathbb{X}}^2 = \mathbb{E}\left[\left(\mathbb{X} - m_{\mathbb{X}}\right)^2\right]$ be the variance, and $\sigma_{\mathbb{X}} = \sqrt{\sigma_{\mathbb{X}}^2}$ be the standard deviation of $\mathbb{X}$. The Shannon entropy of PDF $p_{\mathbb{X}}$ is defined by $\mathrm{S}\left(\mathbb{X}\right) = -\mathbb{E}\left[\ln p_{\mathbb{X}}(\mathbb{X})\right]$.

5.2 Probabilistic model for the bit-rock interface law

Recalling that the bit-rock interaction force and torque are, respectively, given by Eqs.(20) and (21), the reader can see that this bit-rock interface law is characterized by three parameters, namely, α_{BR}, $\mathit{\Gamma}_{\mathrm{BR}}$, and μ_{BR}. The construction of the probabilistic model for each one parameter of these parameters, which are respectively modeled by random variables $\mathbb{\alpha}_{\mathrm{BR}}$, $\mathbb{\Gamma}_{\mathrm{BR}}$, and $\mathbb{\mu}_{\mathrm{BR}}$, is presented below.

5.3 Distribution of the force rate of change

As the rate of change α_{BR} is positive, it is reasonable to assume $\mathtt{Supp}\,\mathbb{\alpha}_{\mathrm{BR}} =]0, \infty[$. Therefore, the PDF of $\mathbb{\alpha}_{\mathrm{BR}}$ is a nonnegative function $p_{\mathbb{\alpha}_{\mathrm{BR}}}$, such that

$$\int_{\alpha=0}^{+\infty} p_{\mathbb{\alpha}_{\mathrm{BR}}}(\alpha)\, d\alpha = 1. \tag{78}$$

It is also convenient to assume that the mean value of $\mathbb{\alpha}_{\mathrm{BR}}$ is a known positive number, denoted by $m_{\mathbb{\alpha}_{\mathrm{BR}}}$, i.e.,

$$\mathbb{E}\left[\mathbb{\alpha}_{\mathrm{BR}}\right] = m_{\mathbb{\alpha}_{\mathrm{BR}}} > 0. \tag{79}$$

One also need to require that

$$\mathbb{E}\left[\ln\left(\mathbb{\alpha}_{\mathrm{BR}}\right)\right] = q_{\mathbb{\alpha}_{\mathrm{BR}}}, \quad |q_{\mathbb{\alpha}_{\mathrm{BR}}}| < +\infty, \tag{80}$$

which ensures, as can be see in [52, 53, 54], that the inverse of $\mathbb{\alpha}_{\mathrm{BR}}$ is second order random variable. This condition is necessary to guarantee that the stochastic dynamical system associated to this random variable is of second order, i.e., it has finite variance. Employing the principle of maximum entropy one need to maximize the entropy function $\mathrm{S}\left(\mathbb{\alpha}_{\mathrm{BR}}\right)$, respecting the constraints imposed by (78), (79) and (80).

The desired PDF corresponds to the gamma distribution and is given by

$$p_{\mathbb{\alpha}_{\mathrm{BR}}}(\alpha) = \mathbb{1}_{]0,\infty[}(\alpha)\, \frac{1}{m_{\mathbb{\alpha}_{\mathrm{BR}}}} \left(\frac{1}{\delta_{\mathbb{\alpha}_{\mathrm{BR}}}^2}\right)^{1/\delta_{\mathbb{\alpha}_{\mathrm{BR}}}^2} \times \frac{1}{\mathit{\Gamma}(1/\delta_{\mathbb{\alpha}_{\mathrm{BR}}}^2)} \left(\frac{\alpha}{m_{\mathbb{\alpha}_{\mathrm{BR}}}}\right)^{1/\delta_{\mathbb{\alpha}_{\mathrm{BR}}}^2 - 1} \exp\left(\frac{-\alpha}{\delta_{\mathbb{\alpha}_{\mathrm{BR}}}^2 m_{\mathbb{\alpha}_{\mathrm{BR}}}}\right), \tag{81}$$

where the symbol $\mathbb{1}_{]0,\infty[}(\alpha)$ denotes the indicator function of the interval $]0, \infty[$, $0 \leq \delta_{\mathbb{\alpha}_{\mathrm{BR}}} = \sigma_{\mathbb{\alpha}_{\mathrm{BR}}}/m_{\mathbb{\alpha}_{\mathrm{BR}}} < 1/\sqrt{2}$ is a type of dispersion parameter, and

$$\mathit{\Gamma}(z) = \int_{y=0}^{+\infty} y^{z-1}\, e^{-y}\, dy, \tag{82}$$

is the gamma function.

5.4 Distribution of the limit force

The parameter Γ_{BR} is also positive, in a way that $\mathtt{Supp}\,\mathbb{\Gamma}_{\mathrm{BR}} =]0,\infty[$, and consequently

$$\int_{\gamma=0}^{+\infty} p_{\mathbb{\Gamma}_{\mathrm{BR}}}(\gamma)\,d\gamma = 1. \tag{83}$$

The hypothesis that the mean is a known positive number $m_{\mathbb{\Gamma}_{\mathrm{BR}}}$ is also done, i.e.,

$$\mathbb{E}\left[\mathbb{\Gamma}_{\mathrm{BR}}\right] = m_{\mathbb{\Gamma}_{\mathrm{BR}}} > 0, \tag{84}$$

as well as that the technical condition, required for the stochastic dynamical system associated be of second order, is fulfilled, i.e.

$$\mathbb{E}\left[\ln\left(\mathbb{\Gamma}_{\mathrm{BR}}\right)\right] = q_{\mathbb{\Gamma}_{\mathrm{BR}}}, \quad |q_{\mathbb{\Gamma}_{\mathrm{BR}}}| < +\infty. \tag{85}$$

In a similar way to the procedure presented in section 5.3, it can be shown that PDF of maximum entropy is also gamma distributed, and given by

$$p_{\mathbb{\Gamma}_{\mathrm{BR}}}(\gamma) = \mathbb{1}_{]0,\infty[}(\gamma)\,\frac{1}{m_{\mathbb{\Gamma}_{\mathrm{BR}}}}\left(\frac{1}{\delta^2_{\mathbb{\Gamma}_{\mathrm{BR}}}}\right)^{1/\delta^2_{\mathbb{\Gamma}_{\mathrm{BR}}}} \times\frac{1}{\Gamma(1/\delta^2_{\mathbb{\Gamma}_{\mathrm{BR}}})}\left(\frac{\gamma}{m_{\mathbb{\Gamma}_{\mathrm{BR}}}}\right)^{1/\delta^2_{\mathbb{\Gamma}_{\mathrm{BR}}}-1}\exp\left(\frac{-\gamma}{\delta^2_{\mathbb{\Gamma}_{\mathrm{BR}}}m_{\mathbb{\Gamma}_{\mathrm{BR}}}}\right). \tag{86}$$

5.5 Distribution of the friction coefficient

With respect to the parameter μ_{BR}, one know it is non-negative and bounded above by the unity. Thus, one can safely assume that $\mathtt{Supp}\,\mathbb{\mu}_{\mathrm{BR}} = [0,1]$, so that the normalization condition read as

$$\int_{\mu=0}^{1} p_{\mathbb{\mu}_{\mathrm{BR}}}(\mu)\,d\mu = 1. \tag{87}$$

For technical reasons [52, 53, 54], the following two conditions are also imposed

$$\mathbb{E}\left[\ln\left(\mathbb{\mu}_{\mathrm{BR}}\right)\right] = q^1_{\mathbb{\mu}_{\mathrm{BR}}}, \quad |q^1_{\mathbb{\mu}_{\mathrm{BR}}}| < +\infty, \tag{88}$$

$$\mathbb{E}\left[\ln\left(1-\mathbb{\mu}_{\mathrm{BR}}\right)\right] = q^2_{\mathbb{\mu}_{\mathrm{BR}}}, \quad |q^2_{\mathbb{\mu}_{\mathrm{BR}}}| < +\infty, \tag{89}$$

representing a weak decay of the PDF of $\mathbb{\mu}_{\mathrm{BR}}$ in 0^+ and 1^- respectively. Evoking again the principle of maximum entropy considering now as known information the constraints defined by (87), (88), and (89) one has that the desired PDF is given by

$$p_{\mathbb{\mu}_{\mathrm{BR}}}(\mu) = \mathbb{1}_{[0,1]}(\mu)\,\frac{\Gamma(a+b)}{\Gamma(a)\,\Gamma(b)}\,\mu^{a-1}\,(1-\mu)^{b-1}, \tag{90}$$

which corresponds to the beta distribution

The parameters a and b are associated with the shape of the probability distribution, and can be related with $m_{\mathbb{\mu}_{\mathrm{BR}}}$ and $\delta_{\mathbb{\mu}_{\mathrm{BR}}}$ by

$$a = \frac{m_{\mathbb{\mu}_{\mathrm{BR}}}}{\delta^2_{\mathbb{\mu}_{\mathrm{BR}}}}\left(\frac{1}{m_{\mathbb{\mu}_{\mathrm{BR}}}} - \delta^2_{\mathbb{\mu}_{\mathrm{BR}}} - 1\right), \tag{91}$$

and

$$b = \frac{m_{\mathbb{\mu}_{\mathrm{BR}}}}{\delta^2_{\mathbb{\mu}_{\mathrm{BR}}}}\left(\frac{1}{m_{\mathbb{\mu}_{\mathrm{BR}}}} - \delta^2_{\mathbb{\mu}_{\mathrm{BR}}} - 1\right)\left(\frac{1}{m_{\mathbb{\mu}_{\mathrm{BR}}}} - 1\right). \tag{92}$$

5.6 Stochastic nonlinear dynamical system

Due to the randomness of the parameters $\mathbb{\alpha}_{\mathrm{BR}}$, $\mathbb{\Gamma}_{\mathrm{BR}}$, and $\mathbb{\mu}_{\mathrm{BR}}$, the physical behavior of the mechanical system is now described, for all θ in Θ, by the stochastic nonlinear dynamical system defined by

$$[M]\,\ddot{\mathbb{q}}(t,\theta) + [C]\,\dot{\mathbb{q}}(t,\theta) + [K]\,\mathbb{q}(t,\theta) = \mathbb{f}\left(\mathbb{q},\dot{\mathbb{q}},\ddot{\mathbb{q}}\right), \tag{93}$$

$$\mathbb{q}(0,\theta) = \boldsymbol{q}_0, \qquad \text{and} \qquad \dot{\mathbb{q}}(0,\theta) = \dot{\boldsymbol{q}}_0, \quad a.s. \tag{94}$$

where $\mathbb{q}(t)$ is the random reduced displacement vector, $\dot{\mathbb{q}}(t)$ is the random reduced velocity vector, and $\ddot{\mathbb{q}}(t)$ is the random reduced acceleration vector, and $\mathbb{f}$ is the random reduced nonlinear force vector.

The methodology used to calculate the propagation of uncertainties through this stochastic dynamical system is Monte Carlo (MC) method [29], employing a strategy of parallelization described in [13].

6 Numerical experiments and discussions

In order to simulate the nonlinear dynamics of the mechanical system, the physical parameters presented in the Table 1 are adopted, as well as the length $L = 100\ m$, the rotational and axial velocities in x, respectively given by $\Omega = 2\pi\ rad/s$, and $V_0 = 1/180\ m/s$. The values of these parameters do not correspond exactly to the actual values used in a real drillstring, but

Table 1 Physical parameters of the mechanical system that are used in the simulation.

parameter	value	unit
ρ	7900	kg/m^3
g	9.81	m/s^2
ν	0.3	—
c	0.01	—
E	203×10^9	Pa
R_{bh}	95×10^{-3}	m
R_{int}	50×10^{-3}	m
R_{ext}	80×10^{-3}	m

are of the same order of magnitude. For this configuration, the beam geometry is discretized by 500 finite elements, and the interval of integration $[t_0, t_f] = [0, 10]$ s is considered.

For the constants of the friction and shock model, are considered the values shown in Table 2, which have order of magnitude typical of a borehole wall made of steel [66]. The low value for the friction coefficient μ_{FS} is justified by the fact that in the real system, there is a fluid between the borehole wall and the column, which carries a substantial reduction in the torsional friction.

Table 2 Parameters of the friction and shock model that are used in the simulation.

parameter	value	unit
k_{FS_1}	1×10^{10}	N/m
k_{FS_2}	1×10^{16}	N/m^3
c_{FS}	1×10^6	$(N/m^3)/(m/s)$
μ_{FS}	0.25	—

The constants of the bit-rock interaction model can be seen in Table 3, and were estimated following a similar strategy as that shown in [43].

Table 3 Parameters of the bit-rock interaction model that are used in the simulation.

parameter	value	unit
Γ_{BR}	30×10^3	N
α_{BR}	400	$1/(m/s)$
μ_{BR}	0.4	—

6.1 Modal analysis of the mechanical system

In this section, the modal content of the mechanical system is investigated. This investigation aims to identify the natural frequencies of the system, and, especially, to check the influence of *slenderness ratio*, defined as the ratio between beam length and external diameter, in the natural frequencies distribution.

Therefore, the dimensionless frequency band of interest in the problem is assumed as being $B = [0, 4]$, with the dimensionless frequency defined by

$$f^* = \frac{f\,L}{c_L}, \tag{95}$$

where f is the dimensional frequency (Hz), and $c_L = \sqrt{E/\rho}$ is the longitudinal wave velocity. As it was defined in terms of a dimensionless frequency, the band of analysis does not change when the beam length is varied. Also, the reader can check that this band is representative for the mechanical system dynamics, once the beam rotates at 2π rad/s, which means that the mechanical system is excited at 1 Hz.

In Figure 10 one can see the distribution of the flexural modes as a function of dimensionless frequency, for several values of slenderness ratio. Clearly it is observed that the flexural modes are denser in the low frequency range. Further, when the slenderness ratio increases, the modal density in the low frequencies range tend to increase.

A completely different behavior is observed for the torsional and longitudinal (traction-compression) modes of vibration, as can be seen in Figures 11 and 12, respectively. One can note that, with respect to these two modes of vibration, the modal distribution is almost uniform with respect to dimensionless frequency, and invariant to changes in the slenderness ratio.

It may also be noted from Figures 10 to 12 that, the lowest natural frequencies are associated with the flexural mechanism. This is because the flexural stiffness of the beam is much smaller than the torsional stiffness, which in turn is less than the axial stiffness. In other words, it is much easier to bend the beam than twisting it. However, twists the beam is easier than buckling it.

The dimensionless frequency band adopted in the analysis corresponds to a maximum dimensional frequency of $f_{max} = 4\,c_L/L$. In this way, a nominal time step of $\Delta t = (2\,f_{max})^{-1}$ is adopted for time integration. This time step is automatically refined by the algorithm of integration, whenever necessary, to capture the shock effects.

6.2 Construction of the reduced model

In the construction of the reduced model, are taken into account the rigid body modes of the mechanical system, as well as modes of bending, torsion and traction-compression. The construction strategy consists of including: (i) the two rigid body modes (translation and

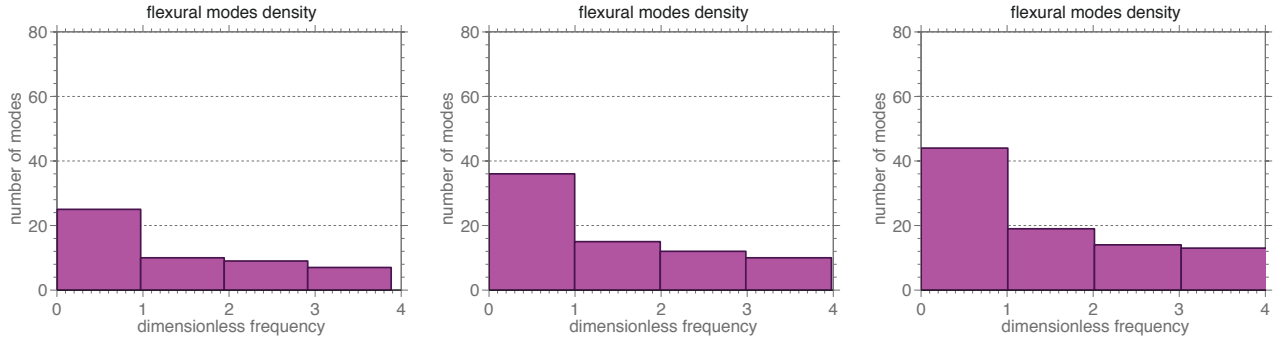

(a) slenderness = 312.5 (b) slenderness = 625.0 (c) slenderness = 937.5

Fig. 10 Distribution of the flexural modes as a function of dimensionless frequency, for several values of slenderness ratio.

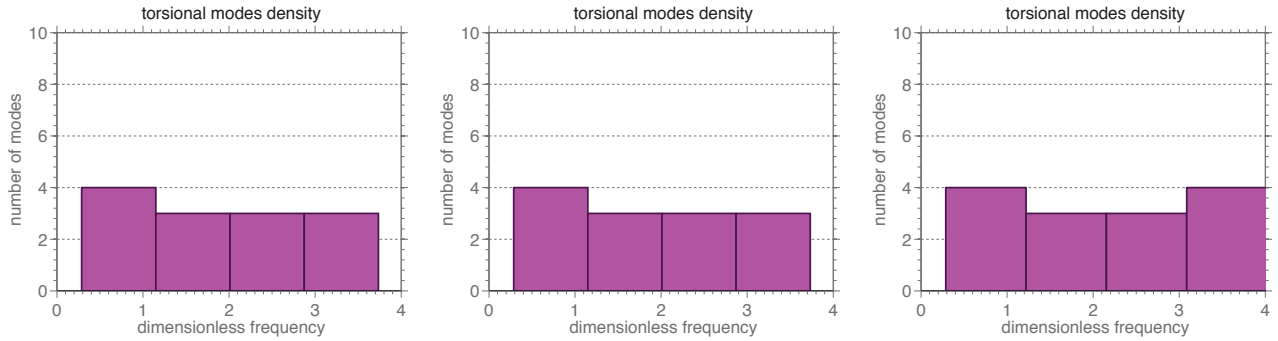

(a) slenderness = 312.5 (b) slenderness = 625.0 (c) slenderness = 937.5

Fig. 11 Distribution of the torsional modes as a function of dimensionless frequency, for several values of slenderness ratio.

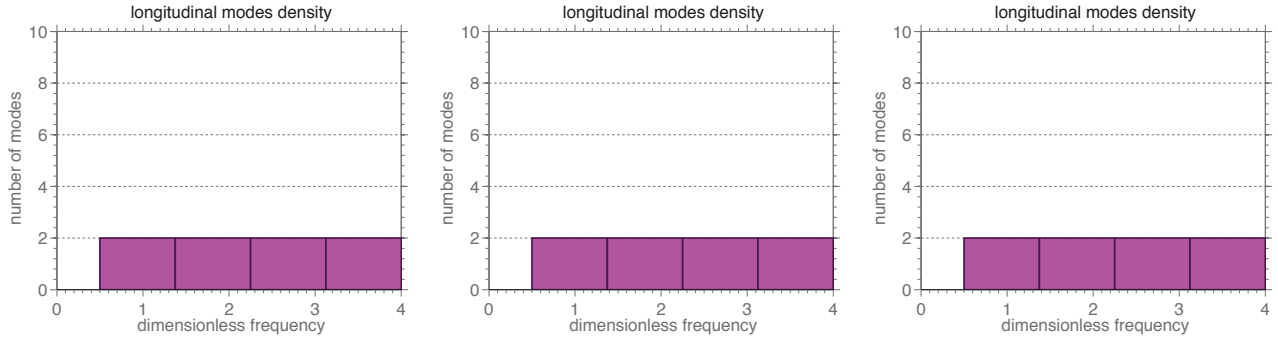

(a) slenderness = 312.5 (b) slenderness = 625.0 (c) slenderness = 937.5

Fig. 12 Distribution of the longitudinal modes as a function of dimensionless frequency, for several values of slenderness ratio.

rotation); (ii) all the flexural modes such that $0 < f^* \leq 5\,L/c_L$; (iii) all the torsional modes such that $0 < f^* \leq 4$; (iv) all the longitudinal modes such that $0 < f^* \leq 4$.

In this way, the total number of modes used in the FEM model is a function of the beam length. In Table 4 the reader can see a comparison, for different values of L, of the full FEM model dimension and the corresponding dimension of the reduced order model. Note that the dimension of the reduced models, constructed using the above strategy, is always much smaller than the full model dimension.

Table 4 Dimension of the FEM model as a function of beam length.

beam length (m)	full model DoFs	reduced model DoFs
50	306	37
100	3006	49
150	4506	60

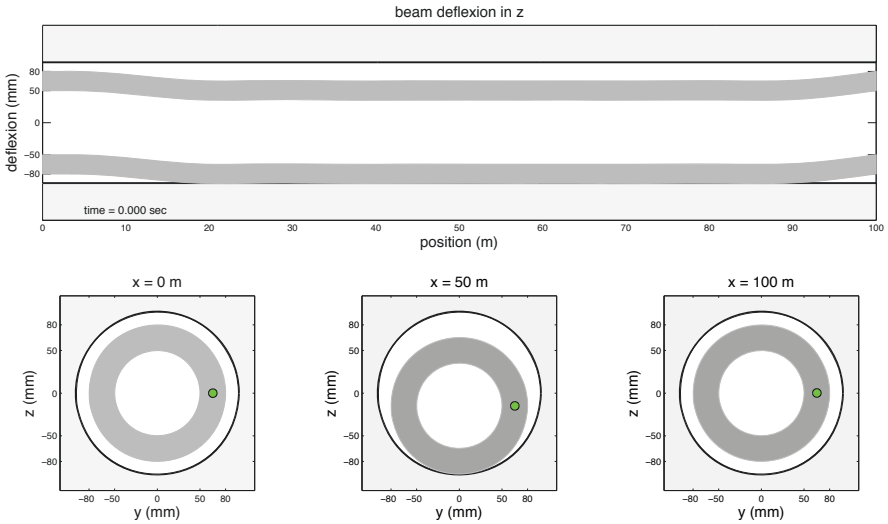

Fig. 13 Illustration of static equilibrium configuration of a horizontal drillstring with 100 m length.

6.3 Calculation of the static equilibrium configuration

Before the beginning of drilling operation, the drillstring is inserted into the borehole, without axial velocity and rotation imposed. Due to gravitational effects, the column deflects until it reaches a static equilibrium configuration. This configuration can calculated by the temporal integration of the dynamical system defined by the Eqs.(65) and (66), assuming zero initial conditions, i.e., $\Omega = 0\ rad/s$, and $V_0 = 0\ m/s$. In this way, after a short transient, the system reaches static equilibrium and remains in this configuration indefinitely.

An illustration of this equilibrium configuration, for a 100 m long column is presented in Figure 13. In this illustration, one can see the mechanical system sectioned by the plane $y = 0\ m$, as well as by the planes $x = \{0, 50, 100\}\ m$. A visual inspection clearly indicates that this equilibrium is stable. Moreover, as this equilibrium configuration is the initial state of the real system, it will be used as initial condition in all other simulations reported bellow.

An animation which illustrates the calculation of the beam static equilibrium can be seen in Online Resource 1.

6.4 Drill-bit nonlinear dynamic behavior

The drill-bit longitudinal displacement and velocity, can be seen in Figure 14. For practical reasons, some scaling factors were introduced in the units of measure of these quantities. They allow one to read the displacement in "millimeter", and the velocity in "meters per hour". Accordingly, it is noted that, during the interval of analysis, the column presents an advance in the forward direction with very small axial oscillations in the displacement. The axial oscillations in the velocity curve are more pronounced, and correspond to the vibration mechanism known as *bit-bounce*, where the drill-bit loses contact with the soil and then hits the rock abruptly. This phenomenon, which is widely observed in real systems [59], presents itself discreetly in the case analyzed. Note that the velocity exhibits a mean value of 19.36 "meters per hour", close to the velocity $V_0 = 20$ "meters per hour", which is imposed on the left end of the beam. Also, throughout the "temporal window" analyzed, one can observe packages where the velocity of the drill-bit presents large fluctuations, which can reach up to 40 times the mean value.

The drill-bit rotation and angular velocity, can be seen in Figure 15. Now the scale factors allow one to read rotation in "revolution", and the angular velocity in "revolution per minute". Thus, what it is observed is a almost monotonic rotation. However, when one looks to the angular velocity, it is possible to see packages of fluctuations with amplitude variations that can reach up to an order of magnitude. This indicates that the drill-bit undergoes a blockage due to the torsional friction, and then it is released subtly, so that its velocity is sharply increased, in a *stick-slip* phenomenon type. This is also seen experimentally [59] in real drilling systems, and a serious consequence of this blockage is the reduction of drilling process efficiency.

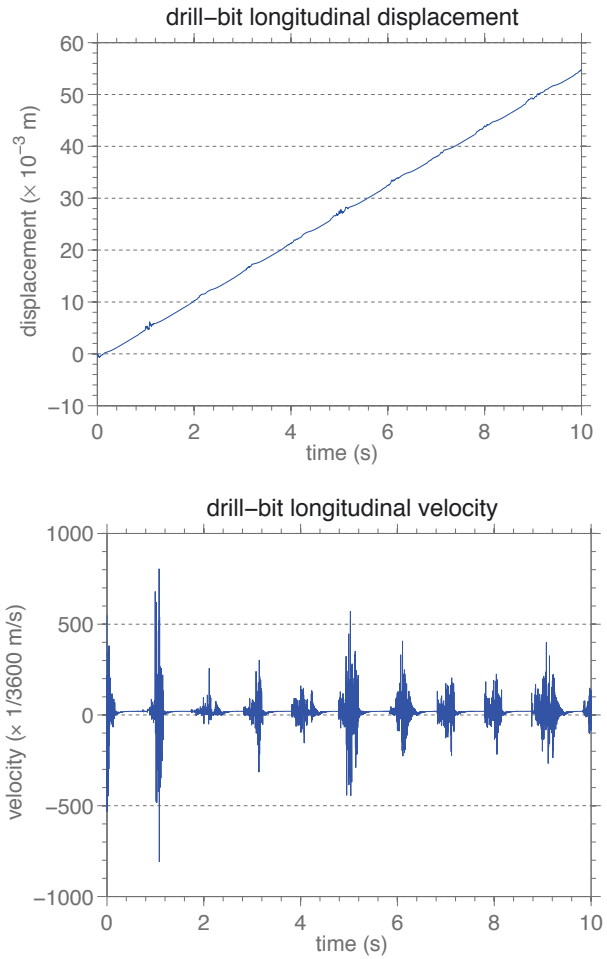

Fig. 14 Illustration of drill-bit displacement (top) and drill-bit velocity (bottom).

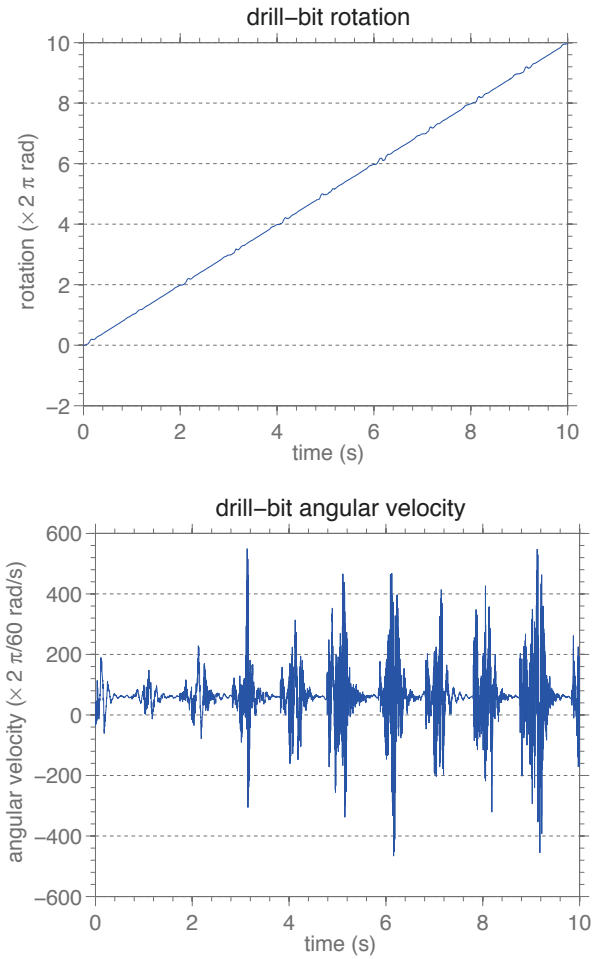

Fig. 15 Illustration of drill-bit rotation (top) and drill-bit angular velocity (bottom).

6.5 Transverse nonlinear dynamics of the beam

Observing the cross section of the beam at $x = 50\ m$, for which the transversal displacement (top) and velocity (bottom) are shown in Figure 16, one can see an asymmetry of the displacement, with respect to the plane $z = 0\ m$. This is due to gravity, which favors the beam to move below this plane. Furthermore, one can note that the this signal is composed of "packages", which has a recurring oscillatory pattern. As will be seen in section 6.6, these packages present a strong correlation with the number of impacts which the mechanical system is subjected.

The evolution of the radial displacement, for $x = 50\ m$, of the beam cross-section can be seen in the Figure 17, which shows that several transverse impacts occur between the drillstring and the borehole wall during the drilling process. This fact is also reported experimentally [59], and is an important cause of damage to the well and to the drillstring.

Note that, after an impact, the amplitudes of the oscillations decreases until subtly increase sharply, giving rise to a new impact, and then the entire process repeats again.

6.6 Influence of transverse impacts on the nonlinear dynamics

In Figure 18 it is shown the graph of the map $t \in \mathbb{R} \mapsto \texttt{number of shocks} \in \mathbb{N}$, which associates for any instant t the number of impacts suffered by the mechanical system.

The "packages of fluctuation" observed in the Figures 14 to 16 correspond to transitory periods of the dynamical system, and are highly correlated with the process of collision between beam and borehole wall. This assertion can be verified if the reader compares the graphs of Figures 14 to 16 with the graph of Figure 18, which shows the existence of "shock packages". The existence of a correlation is clearly evident.

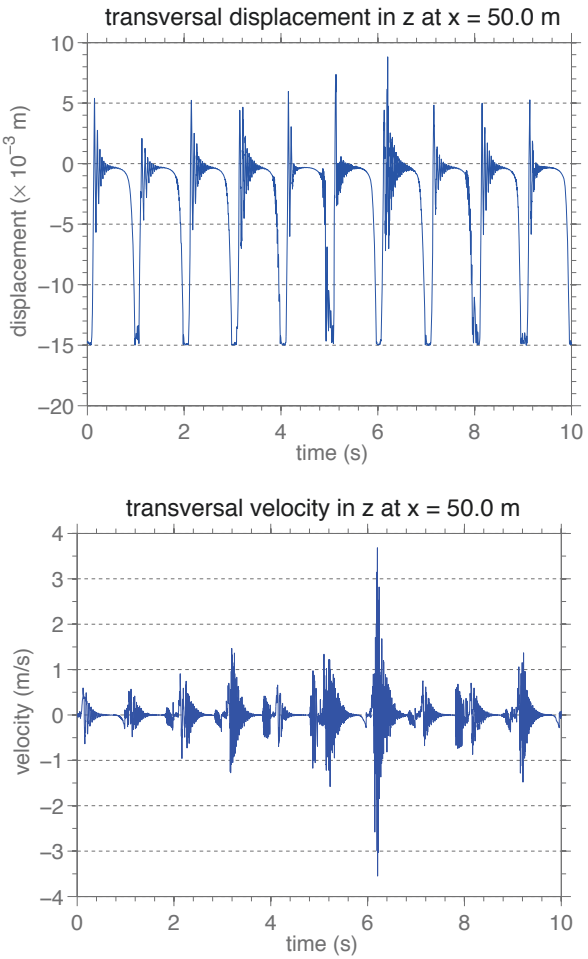

Fig. 16 Illustration of transversal displacement (top) and velocity in z (bottom) when $x = 50\ m$.

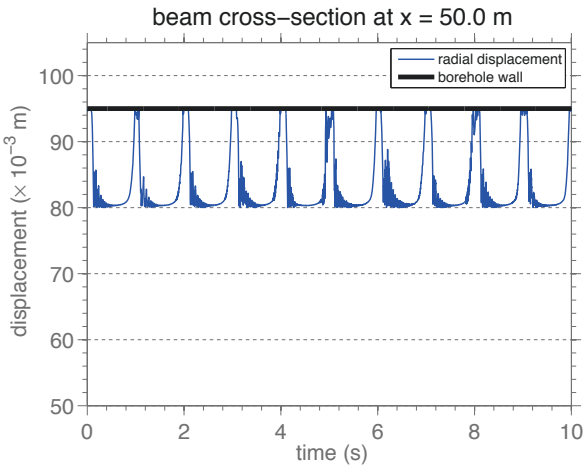

Fig. 17 Illustration of beam radial displacement for $x = 50\ m$.

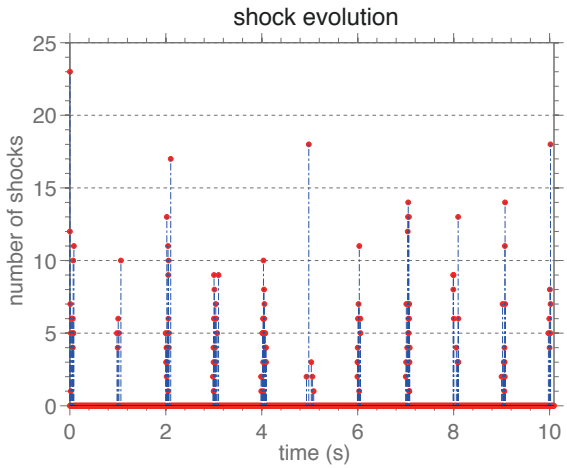

Fig. 18 Illustration of the number of impacts suffered by the mechanical system as function of time.

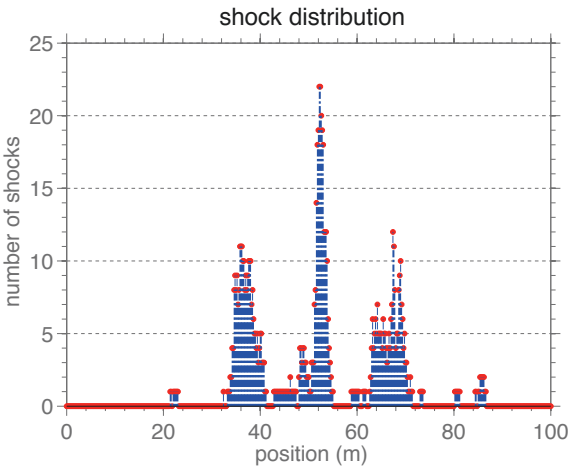

Fig. 19 Illustration of the number of impacts suffered by the mechanical system as function of position.

Whenever there is a shock, the system "loses it memory" about the previous dynamic behavior, and undergoes a new transient period until reach a steady state again. This behavior is repeated 11 times in the "temporal window" analyzed.

Regarding the distribution of impacts along the beam, the graph of the map $x \in [0, L] \mapsto \texttt{number of shocks} \in \mathbb{N}$, which associates for any position x the number of impacts suffered by the mechanical system, is shown in Figure 19. It is clear that impacts do not occur near the beam ends. This is natural due to the restrictions of movement imposed by the boundary conditions.

The impacts between the drillstring and the borehole wall generate nonlinear elastic deformations in the beam, but without residual deformation effects. In this contact also occurs energy dissipation, due to the normal shock, and the torsional friction, induced by the rotation of the beam. These mechanical contacts also activate flexural modes of vibration associated to high natural frequencies, so that the mechanical system as-

sumes complex spatial configurations, as can be seen, for several instants, in Figure 20.

It is also very clear from the Figure 20 that, the mechanical contacts between the beam and the borehole wall, do not occur all the time among discrete points, they can also be seen along continuous line segments.

For a qualitative illustration of the nonlinear dynamics, the reader can see the Online Resource 2.

6.7 Spectral analysis of the nonlinear dynamics

All signals presented above, that are associated with the mechanical system response, have stochastic characteristics. Thereby, for a good understanding of them, it is necessary to analyze their spectral content through the power spectral density (PSD) function [36].

The PSDs that are presented in this section (magenta line) were estimated using the periodogram method [36], and the smooth curves (blue line) appearing were obtained by a filtering process, using a Savitzky-Golay filter [47]. The PSDs are measured in dB/Hz, where the intensity of reference is adopted as being equal to one.

An illustration of PSD functions of drill-bit velocity and angular velocity is show in Figure 21. One can note that, in the case of velocity, the two peaks of highest amplitude correspond to the frequencies 84.55 Hz, and 115.20 Hz, respectively. These frequencies are very close to the flexural frequencies 84.53 Hz, and 115.29 Hz, so that the drill-bit axial dynamics is controlled by the transversal mechanisms of vibration. Furthermore, with respect to the angular velocity, it is noted a peak standing out in relation to the others. This peak is associated with 7.92 Hz frequency, which is very close to the flexrual frequency 7.89 Hz.

In Figure 22 the reader can see an illustration of PSD functions of beam transversal velocity in z and angular velocity around x when $x = 50\ m$. The two peaks of highest amplitude, for the velocity in z, correspond to the frequencies 143.20 Hz, and 172.50 Hz, respectively. These frequencies are close to the torsional frequencies 145.55 Hz, and 174.67 Hz, which indicates that lateral vibrations in z, when $x = 50\ m$, are induced by the torsional vibration mechanism. On the other hand, in what concerns angular velocity around x, the two peaks of largest amplitude are associated to the frequencies 6.93 Hz, and 107.10 Hz, respectively close to the flexural frequencies 6.84 Hz, and 107.16 Hz.

According to Figure 23, torsion is the primary mechanism of vibration that causes the impacts between the beam and borehole wall, since the highest peak of the PSD shown in this figure is associated with the frequency 57.42 Hz, which is close to the torsional frequency 58.21 Hz. This result is surprising because intuition, especially when thinking about the dynamics of vertical drillstrings, suggests that lateral vibration mechanism is the mainly responsible for inducing the transverse impacts.

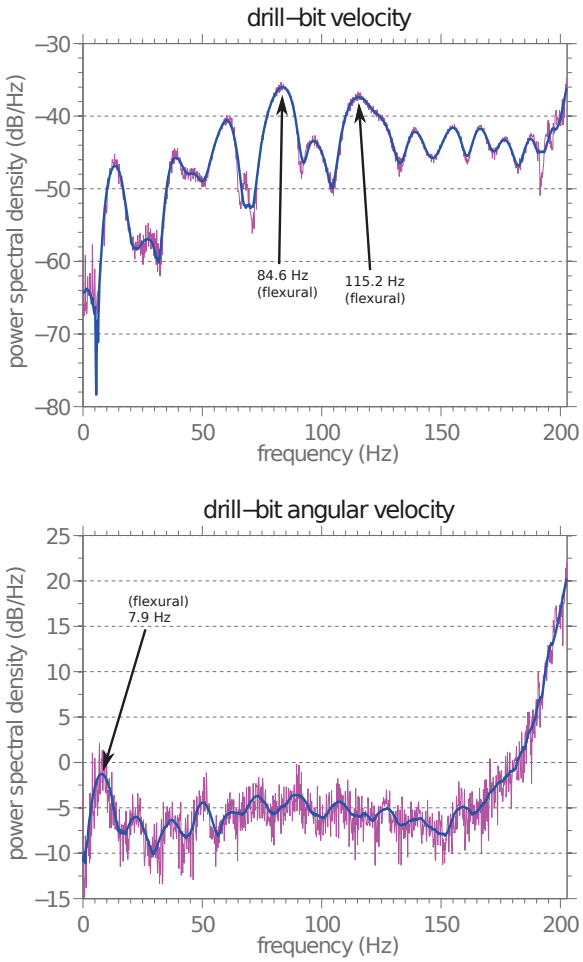

Fig. 21 Illustration of power spectral density functions of drill-bit velocity (top) and angular velocity (bottom).

6.8 Analysis of the drilling process efficiency

The efficiency of the drilling process is defined as

$$\mathcal{E} = \frac{\int_{t_0}^{t_f} \mathcal{P}_{out}\, dt}{\int_{t_0}^{t_f} \mathcal{P}_{in}\, dt}, \tag{96}$$

where $\mathcal{P}_{out}$ is the useful (output) power used in the drilling process, and $\mathcal{P}_{in}$ is the total (input) power injected in the system. The output power is due to the drill-bit movements of translation and rotation so that

$$\mathcal{P}_{out} = \dot{u}_{bit}^{+} \left(-F_{\text{BR}}\right)^{+} + \omega_{bit}^{+} \left(-T_{\text{BR}}\right)^{+}, \tag{97}$$

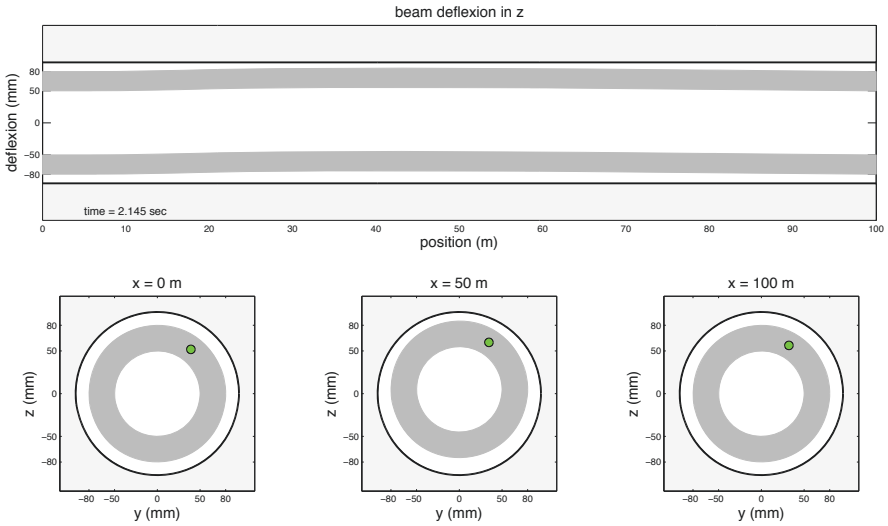

(a) $t = 2.145\ s$

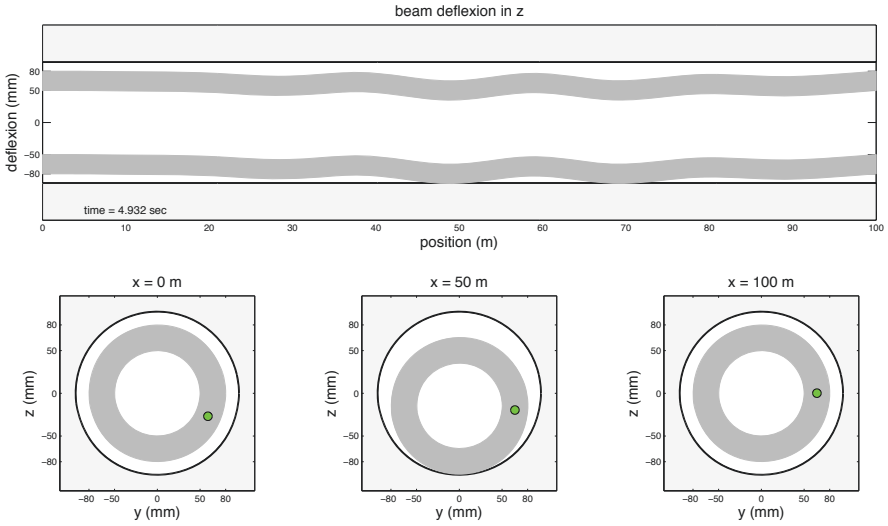

(b) $t = 4.932\ s$

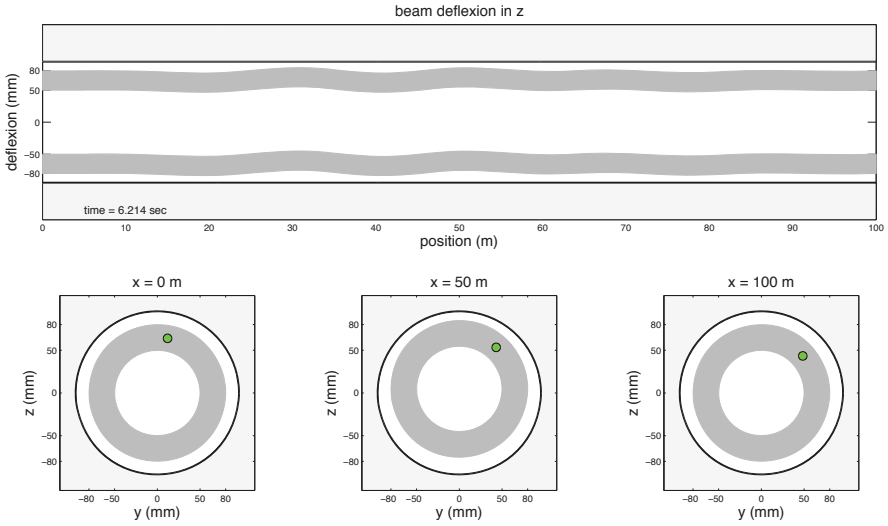

(c) $t = 6.214\ s$

Fig. 20 Illustration of the mechanical system, for several instants, sectioned by the planes $y = 0\ m$, and $x = \{0, 50, 100\}\ m$.

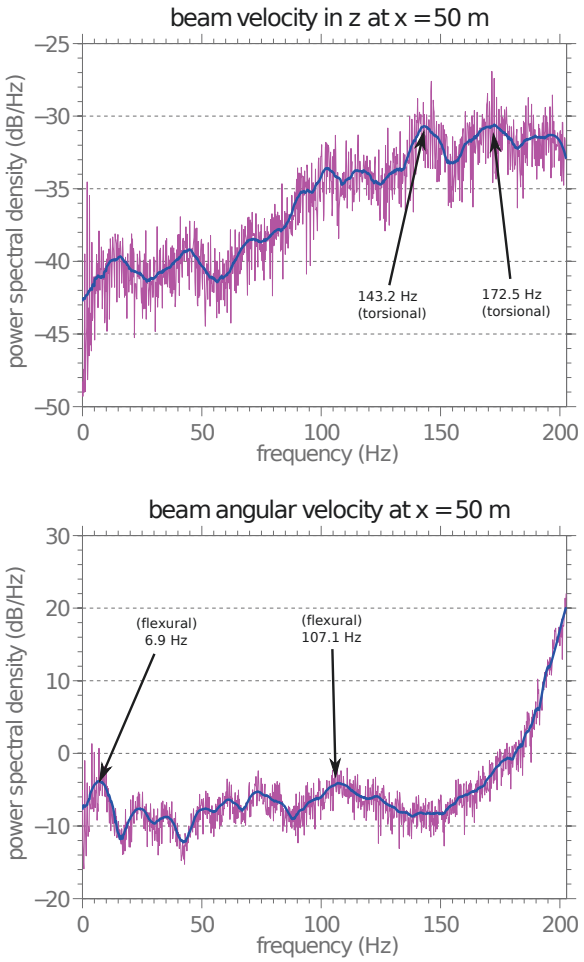

Fig. 22 Illustration of power spectral density functions of beam transversal velocity in z (top) and angular velocity around x (bottom) when $x = 50\ m$.

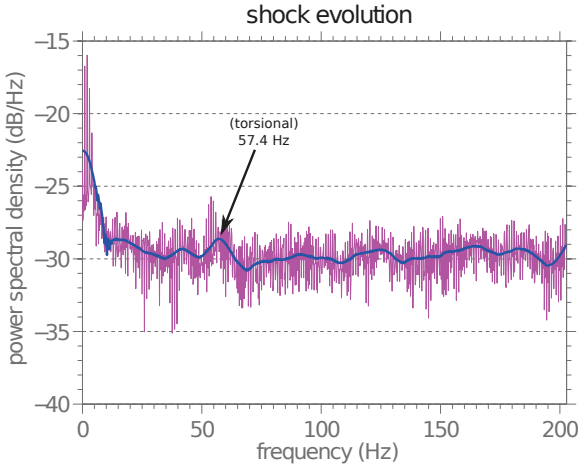

Fig. 23 Illustration of power spectral density function of number of shocks per unit of time.

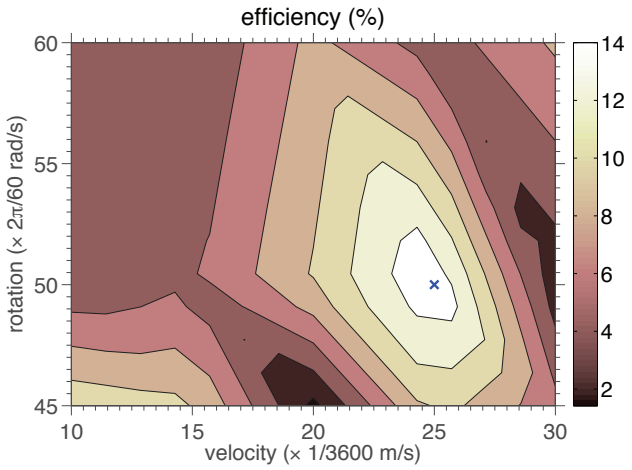

Fig. 24 Illustration of efficiency function contour plot, for an "operating window" defined by $1/360\ m/s \leq V_0 \leq 1/120\ m/s$ and $3\pi/2\ rad/s \leq \Omega \leq 2\pi\ rad/s$. The maximum is indicated with a blue cross.

where the upper script $^+$ means the positive part of the function. The input power is defined as

$$\mathcal{P}_{in} = \dot{u}(0,t)^+ (-\lambda_1)^+ \ + \ \dot{\theta}_x(0,t)^+ (-\lambda_4)^+, \tag{98}$$

where the first and the fourth Lagrange multipliers, respectively, represent the drilling force and torque on the origin of the beam. The reason for considering, in the above definitions, only the positive part of the functions is that negative powers do not contribute to the drilling process.

One can observe the contour map of $\mathcal{E}$, for an "operating window" defined by $1/360\ m/s \leq V_0 \leq 1/120\ m/s$ and $3\pi/2\ rad/s \leq \Omega \leq 2\pi\ rad/s$, in Figure 24. Note that, by operating window of a drillstring, one means the subset of $\mathbb{R}^2$ that provides acceptable values for the pair (Ω, V_0). In order to facilitate the results interpretation, some scaling factors were introduced in the units of measure. They allow one to read the velocity in "meters per hour" and the rotation in "rotation per minute".

Accordingly, it can be noted in Figure 24 that the optimum operating condition is obtained at the point $(V_0, \Omega) = (1/144\ m/s, 5\pi/3\ rad/s)$, which is indicated with a blue cross in the graph. This point corresponds to an efficiency of approximately 16%. Suboptimal operation conditions occur in the vicinity of this point, and some points near the "operating window" boundary show lower efficiency.

6.9 Optimization of drillstring rate of penetration

In order to optimize the drilling process of an oil well in horizontal configuration, it is necessary to maximize the drillstring ROP into the soil.

The instantaneous rate of penetration is given by the function $\dot{u}_{bit}(t)$, defined for all instants of analysis. Meanwhile, only contributes to the advance of the column, the positive part of this function $\dot{u}^{+}_{bit}(t)$. In addition, as objective function, it is more convenient to consider a scalar function. Thus, the temporal mean of $\dot{u}^{+}_{bit}(t)$ is adopted as rate of penetration, and, consequently, objective function of the optimization problem

$$\texttt{rop}(\Omega,\, V_0) = \frac{1}{t_f - t_0}\int_{t=t_0}^{t_f} \dot{u}^{+}_{bit}(t)\, dt. \tag{99}$$

Furthermore, respect the structural limits is indispensable to avoid failures of drillstring during the drilling process. For this reason, von Mises criterion of failure is considered, where it is established that, for all pairs $(\Omega,\, V_0)$ in the "operating window", one has

$$\texttt{UTS} - \max_{\substack{0\leq x\leq L\\ t_0\leq t\leq t_f}} \left\{\sigma_{VM}(V_0,\, \Omega,\, x,\, t)\right\} \geq 0, \tag{100}$$

where UTS is the ultimate tensile strength of the material, and σ_{VM} is the von Mises equivalent stress.

Regarding the analysis of the rate of penetration, the "operating window" is defined by the inequations $1/360\ m/s \leq V_0 \leq 1/90\ m/s$ and $3\pi/2\ rad/s \leq \Omega \leq 7\pi/3\ rad/s$, and $\texttt{UTS} = 650 \times 10^6\ Pa$.

The contour map of the constraint (100), is shown in Figure 25. From the way constraint (100) is written, the Mises criterion is not satisfied when the function is negative, which occurs in a "small neighborhood" of the upper left corner of the rectangle that defines the "operating window". It is noted that all other points respect the structural limits of the material. In this way, then, the *admissible* region of the "operating window" consists of all points that satisfy the constraint.

In Figure 26 the reader can see the contour map of the function rop. Taking into account only points in the admissible region, the maximum of rop occurs at the point $(V_0, \Omega) = (7/720\ m/s, 2\pi\ rad/s)$, which is indicated on the graph with a blue cross. This point corresponds to a mean rate of penetration, during the time interval analyzed, approximately equal to 90 "meters per hour".

It is worth remembering that the definition of rop uses temporal mean of the positive part of $\dot{u}_{bit}(t)$. In such a way, it is not surprising to find the maximum value of rop much higher than the corresponding velocity, V_0 imposed on the left end of the column. This occurs because, by taking only the positive part of the function, the rate of penetration value increases.

To see how significant is the inclusion of the positive part of $\dot{u}_{bit}(t)$ in the definition of rop, the reader can see in Figure 27. This Figure shows the same information as Figure 26, i.e., the contour map of the function rop, but now considering $\dot{u}_{bit}(t)$ instead of $\dot{u}^{+}_{bit}(t)$ in the definition of rop. Note that, in comparison with the contour map of Figure 26, lower values for the levels of the function are observed, and these values are now are closer to the values of V_0. Furthermore, the topology of contour lines change, so that no local extreme point can be seen isolated. This example shows the importance of considering $\dot{u}^{+}_{bit}(t)$ in the definition of rop.

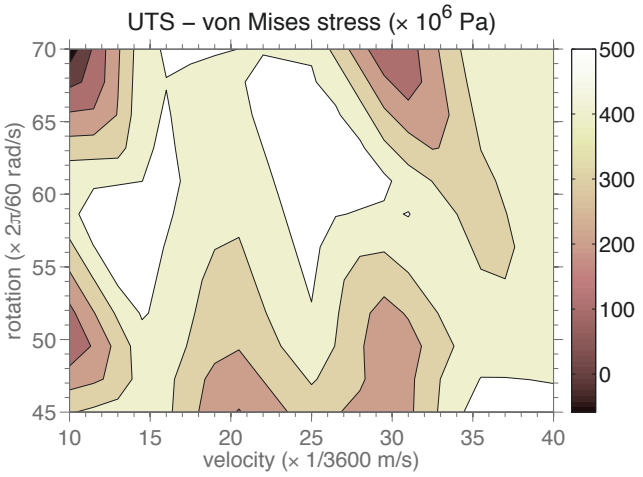

Fig. 25 Illustration of maximum von Mises stress contour plot, for an "operating window" defined by $1/360\ m/s \leq V_0 \leq 1/90\ m/s$ and $3\pi/2\ rad/s \leq \Omega \leq 7\pi/3\ rad/s$.

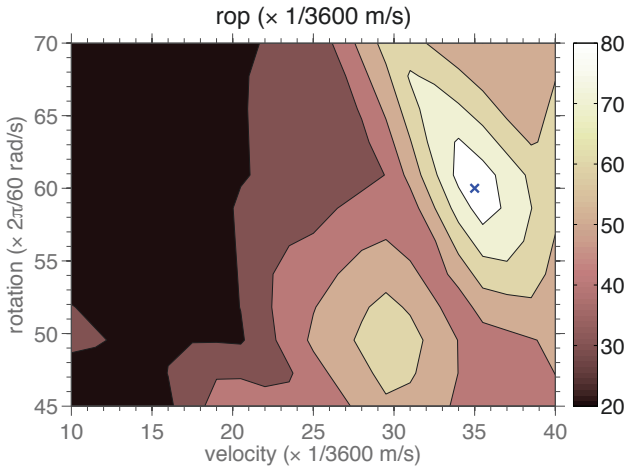

Fig. 26 Illustration of rate of penetration function contour plot, for an "operating window" defined by $1/360\ m/s \leq V_0 \leq 1/90\ m/s$ and $3\pi/2\ rad/s \leq \Omega \leq 7\pi/3\ rad/s$. The maximum is indicated with a blue cross.

6.10 Probabilistic analysis of the dynamics

For the probabilistic analysis of the dynamic system a parametric approach is used, where the distributions

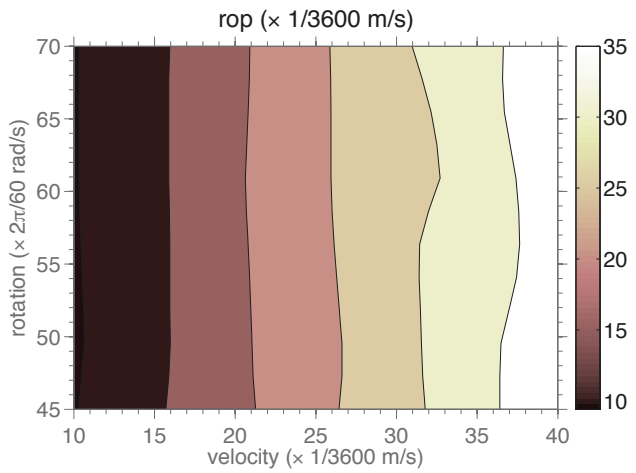

Fig. 27 Illustration of the contour plot of the rate of penetration function, with an alternative definition, for an "operating window" defined by $1/360\ m/s \leq V_0 \leq 1/90\ m/s$ and $3\pi/2\ rad/s \leq \Omega \leq 7\pi/3\ rad/s$.

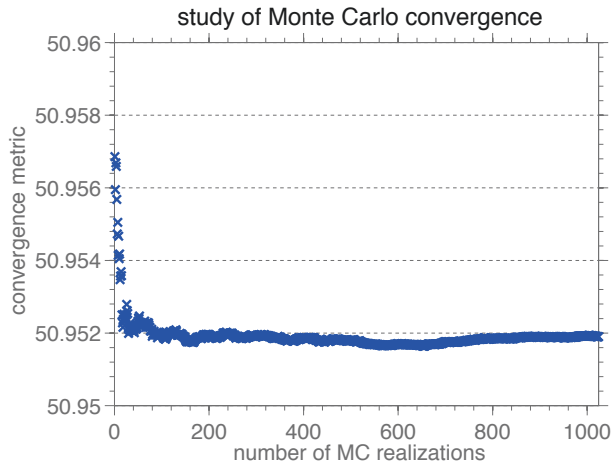

Fig. 28 This figure illustrates the convergence metric of MC simulation as a function of the number of realizations.

of the random parameters are constructed according to the procedure presented in section 5. In this case, the random variables of interest are characterized by the mean values $m_{\mathbb{\alpha}_{\mathrm{BR}}} = 400\ 1/m/s$, $m_{\mathbb{\Gamma}_{\mathrm{BR}}} = 30 \times 10^3\ N$, and $m_{\mathbb{\mu}_{\mathrm{BR}}} = 0.4$, and by the dispersion factors $\delta_{\mathbb{\alpha}_{\mathrm{BR}}} = 0.5\%$, $\delta_{\mathbb{\Gamma}_{\mathrm{BR}}} = 1\%$, and $\delta_{\mathbb{\mu}_{\mathrm{BR}}} = 0.5\%$.

To compute the propagation of the uncertainties of the parameters through the model, the MC method is employed. To analyze the convergence of MC simulations, it is taken into consideration the map $n_s \in \mathbb{N} \mapsto \mathtt{conv}_{\mathrm{MC}}(n_s) \in \mathbb{R}$, being

$$\mathtt{conv}_{\mathrm{MC}}(n_s) = \left(\frac{1}{n_s} \sum_{n=1}^{n_s} \int_{t=t_0}^{t_f} \left\| \mathbb{q}(t, \theta_n) \right\|^2 \, dt \right)^{1/2}, \quad (101)$$

where n_s is the number of MC realizations, and $\|\cdot\|$ denotes the standard Euclidean norm. This metric allows one to evaluate the convergence of the approximation $\mathbb{q}(t, \theta_n)$ in the mean-square sense. For further details the reader is encouraged to see [54].

The evolution of $\mathtt{conv}(n_s)$ as a function of n_s can be seen in Figure 28. Note that for $n_s = 1024$ the metric value has reached a steady value. In this sense, if something is not stated otherwise, all the stochastic simulations that follows in this work use $n_s = 1024$.

An illustration of the mean value (blue line), and a confidence band (grey shadow), wherein a realization of the stochastic dynamic system has 95% of probability of being contained, for the drill-bit longitudinal displacement and velocity is shown in Figure 29. For sake of reference, the deterministic model, which the numerical results were presented earlier, is also presented and called the nominal model (red line). It is observed that the mean value is very similar to the nominal model for the displacement. Meanwhile, for the velocity the mean value presents oscillations that are correlated with the nominal model, but with very different amplitudes. Regarding the confidence band, there is a significant amplitude in the instants that corresponds to the packages of fluctuation and negligible amplitude in the other moments.

Fixing the time in $t = 10\ s$, it is possible to analyze the behavior of the drill-bit longitudinal velocity through its normalized PDF, which is presented in Figure 30. In this context normalized means a distribution of probability with zero mean and unit standard deviation. It is observed an unimodal behavior, with the maximum value occurring in a neighborhood of the mean value, with small dispersion around this position.

In Figure 31, the reader can see the nominal model, the mean value, and the 95% probability envelope of drill-bit rotation and angular velocity. A good agreement between the nominal model and the mean value of the rotation is observed, and the confidence band around it is negligible. On the other hand, with respect to the angular velocity, it is possible to see discrepancies in the amplitudes of the nominal model and the mean value. These differences occur in the instants when the system is subject to shocks, as in the case of drill-bit longitudinal velocity. The band of uncertainty shows that the dispersion around the mean value increases with time due to the uncertainties of accumulation, but also in reason of the impacts, once its amplitude increases a lot near the instants where the mean value presents large fluctuations, i.e., the instants which are correlated to the impacts between the beam and the borehole wall.

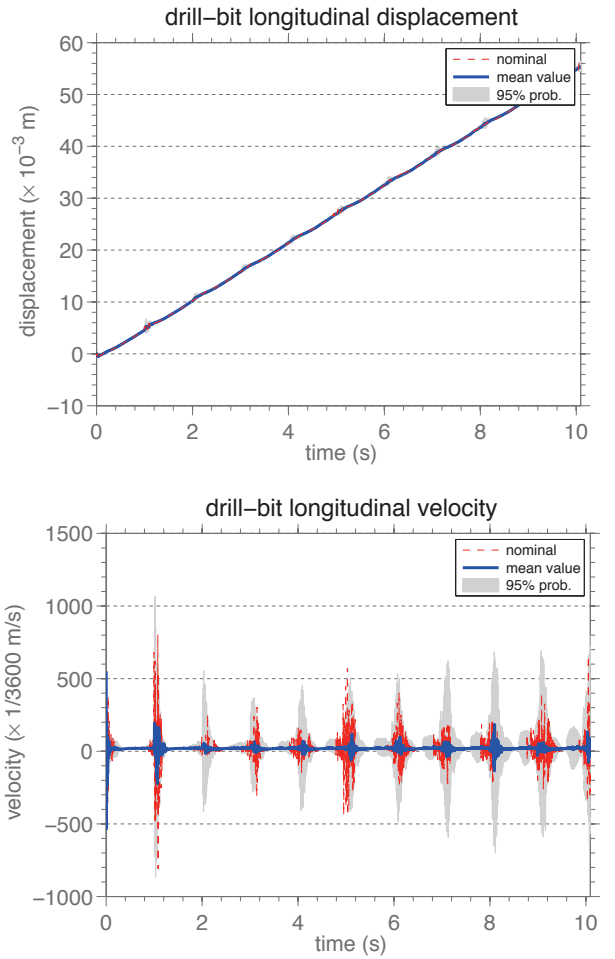

Fig. 29 Illustration of the nominal model (red line), the mean value (blue line), and the 95% probability envelope (grey shadow) for the drill-bit longitudinal displacement (top) and velocity (bottom).

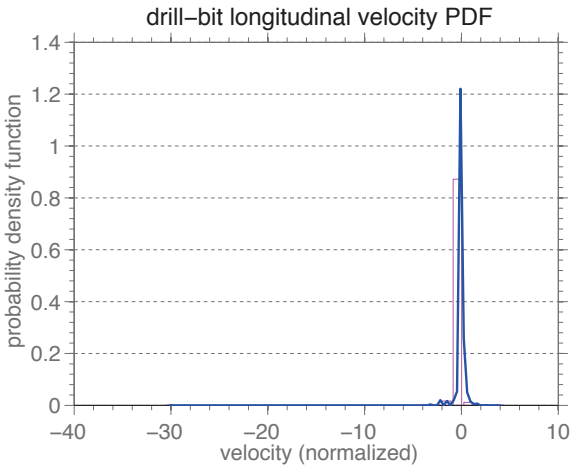

Fig. 30 Illustration of the normalized probability density function of the drill-bit longitudinal velocity.

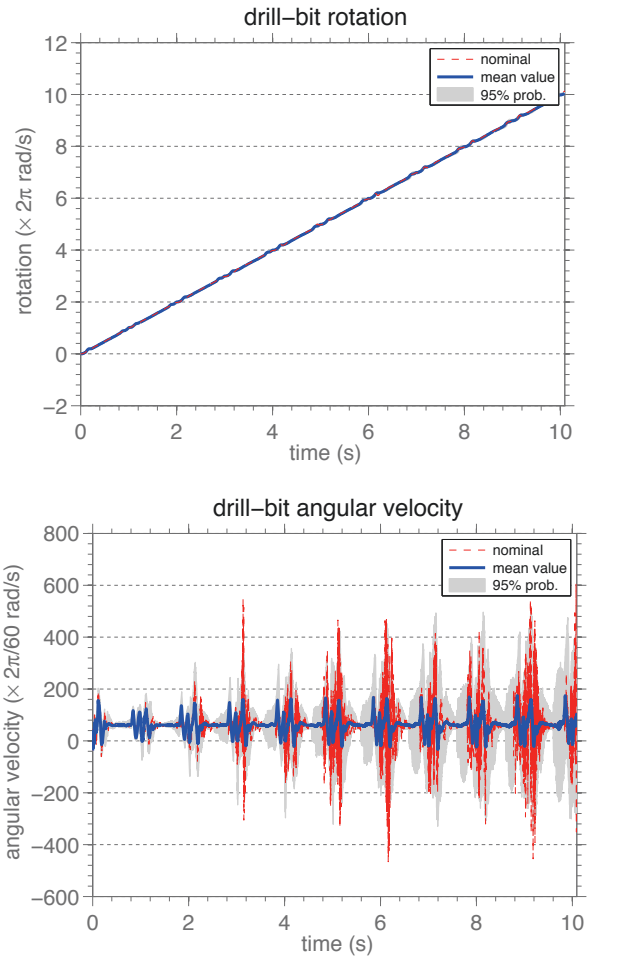

Fig. 31 Illustration of the nominal model (red line), the mean value (blue line), and the 95% probability envelope (grey shadow) for the drill-bit rotation (top) and angular velocity (bottom).

For $t = 10\ s$, the reader can see the normalized PDF of the drill-bit angular velocity in Figure 32. It is noted again an unimodal behavior, with the maximum again near mean value. But now a large dispersion around the mean can be seen.

Moreover, in Figure 33 it is shown the nominal model, the mean value, and the 95% probability envelope of the beam transversal displacement and velocity in z at $x = 50\ m$. Here the mean values of both, velocity and displacement, present correlation with the nominal models. Indeed, both present discrepancies in the oscillation amplitudes, especially the velocity, discrepancies that are more pronounced, as before, in the instants wherein the system is subject to impacts. The confidence bands present meaningful amplitudes, what evidentiates a certain level of dispersion around the means, which are more significant, as expected, at the instants of impact.

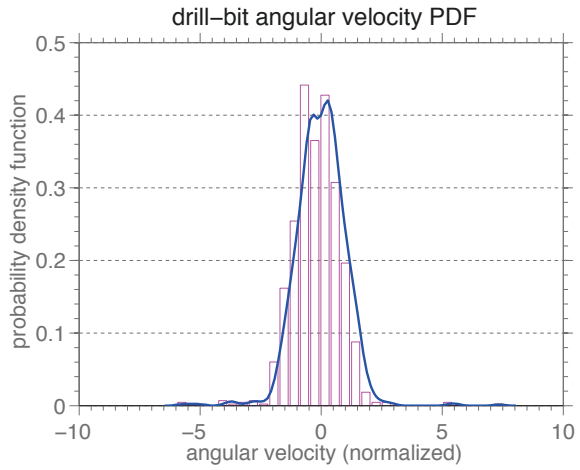

Fig. 32 Illustration of the normalized probability density function of the drill-bit angular velocity.

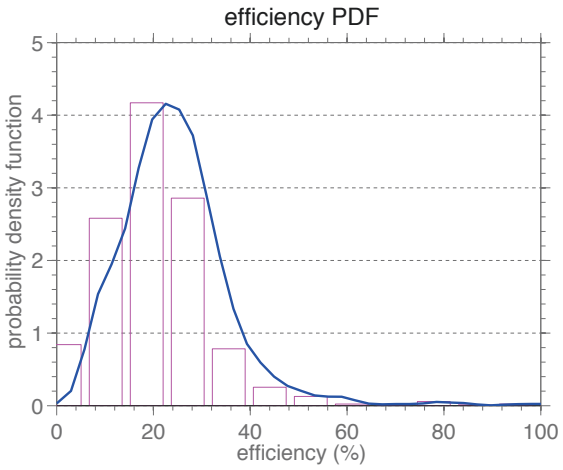

Fig. 34 Illustration of the probability density function of the drilling process efficiency.

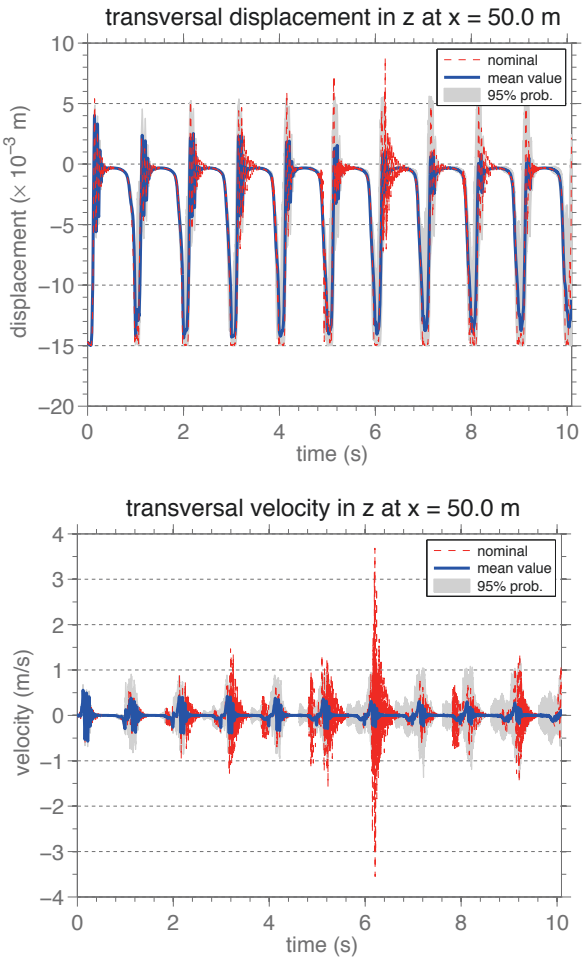

Fig. 33 Illustration of the nominal model (red line), the mean value (blue line), and the 95% probability envelope (grey shadow) for the beam transversal displacement (top) and velocity in z (bottom) at $x = 50\ m$.

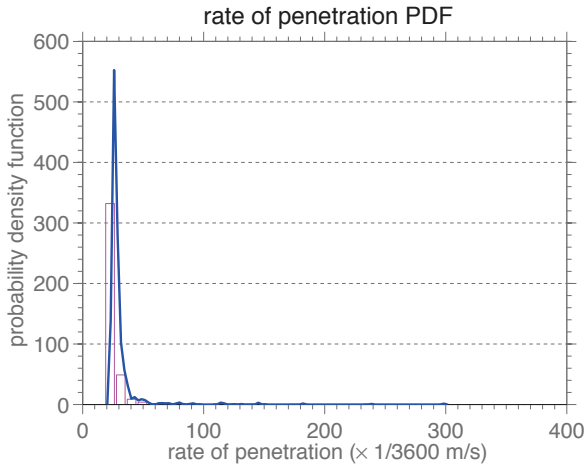

Fig. 35 Illustration of the probability density function of the rate of penetration function.

The PDF of the drilling process efficiency function it is shown in Figure 34. One can observe a unimodal distribution with the maximum around 16% and wide dispersion between 0 and 40%, declining rapidly to negligible values outside this range.

Finally, in Figure 35 one can see the PDF of the drillstring rate of penetration function. One notes an unimodal behavior in a narrow range between 20 and 50 “meters per hour”, with the maximum around 30 “meters per hour”.

6.11 Robust optimization of drillstring rate of penetration

To improve the level of confidence of the drilling process optimization, the uncertainties intrinsic to the problem should be taken into account. This leads to a robust optimization problem, i.e, optimization under uncertainty

where the range of the random parameters are known, but not necessarily their distribution [4, 50, 7, 6, 8, 57, 3].

Taking into account the uncertainties, through the parametric approach presented in section 5, drill-bit velocity becomes the stochastic process $\mathbb{U}_{bit}(t,\theta)$, so that the random rate of penetration is defined by

$$\mathbb{ROP}(V_0,\,\Omega,\theta) = \frac{1}{t_f - t_0}\int_{t=t_0}^{t_f} \dot{\mathbb{U}}^{+}_{bit}(t,\theta)\,dt. \tag{102}$$

In the robust optimization problem, who plays the role of the objective function is the expected value of the random variable $\mathbb{ROP}(V_0,\,\Omega,\theta)$, i.e., $\mathbb{E}\left[\mathbb{ROP}(V_0,\,\Omega,\theta)\right]$.

Regarding the restriction imposed by the von Mises criteria, now the equivalent stress is a random field $\varpi_{VM}(V_0,\,\Omega,\,x,\,t,\theta)$, so that the inequality is written as

$$\texttt{UTS} - \max_{\substack{0\le x\le L\\ t_0\le t\le t_f}} \left\{\varpi_{VM}(V_0,\,\Omega,\,x,\,t,\theta)\right\} \ge 0. \tag{103}$$

However, the robust optimization problem considers as restriction the probability of the event defined by inequality (103),

$$\mathbb{P}\left\{\texttt{UTS} - \max_{\substack{0\le x\le L\\ t_0\le t\le t_f}} \left\{\varpi_{VM}(V_0,\,\Omega,\,x,\,t,\theta)\right\} \ge 0\right\} \ge 1 - P_{risk}, \tag{104}$$

where $0 < P_{risk} < 1$ is the risk percentage acceptable to the problem.

A robust optimization problem very similar to this one, in the context of a vertical drillstring dynamics, is considered in [41].

To solve this robust optimization problem it is employed a trial strategy which discretizes the "operating window" in a structured grid of points and then evaluates the objective function $\mathbb{E}\left[\mathbb{ROP}(V_0,\,\Omega,\theta)\right]$ and the probabilistic constraint (104) in these points.

Accordingly, it is considered the same "operating window" used in the deterministic optimization problem solved above, i.e., $1/360\ m/s \le V_0 \le 1/90\ m/s$ and $3\pi/2\ rad/s \le \Omega \le 7\pi/3\ rad/s$, in addition to $\texttt{UTS} = 650\times 10^6\ Pa$ and $P_{risk} = 10\%$. Each MC simulation in this case used 128 realizations to compute the propagation of uncertainties.

Concerning the simulation results, the probabilistic constraint (104) is respected in all grid points that discretize the "operating window". Thus, the admissible region of the robust optimization problem is equal to the "operating window". In what follows, the contour map of the function $\mathbb{E}\left[\mathbb{ROP}(V_0,\,\Omega,\theta)\right]$ can be see in Figure 36. Note that the maximum, which is indicated on the graph with a blue cross, occurs at at the point $(V_0,\Omega) = (1/90\ m/s, 7\pi/3\ rad/s)$. This point is located in the boundary of the admissible region, in the upper right corner, and corresponds to a expected value of the mean rate of penetration, during the time interval analyzed, approximately equal to 58 "meters per hour".

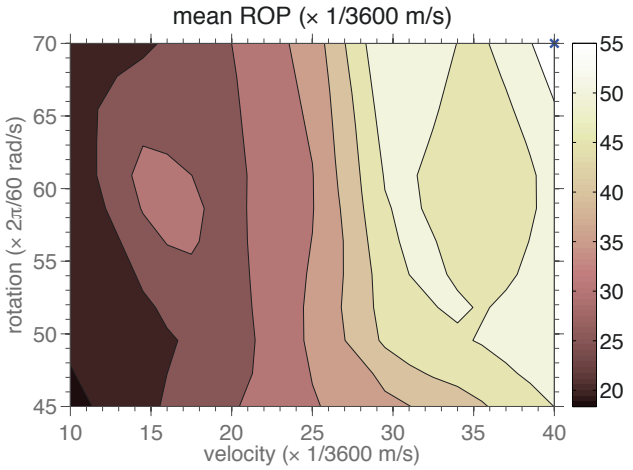

Fig. 36 Illustration of the contour plot of the mean rate of penetration function, for an "operating window" defined by $1/360\ m/s \le V_0 \le 1/90\ m/s$ and $3\pi/2\ rad/s \le \Omega \le 7\pi/3\ rad/s$. The maximum is indicated with a blue cross in the upper right corner.

This result says that, in the "operating window" considered here, increasing the drillstring rotational and translational velocities provides the most robust strategy to maximize its ROP into the soil. This is in some ways an intuitive result, but is at odds with the result of the deterministic optimization problem, which provides another strategy to achieve optimum operating condition.

7 Concluding remarks

A model was developed in this work to describe the nonlinear dynamics of horizontal drillstrings. The model uses a beam theory, with effects of rotatory inertia and shear deformation, which is capable of reproducing large displacements that the beam undergoes. This model also considers the friction and shock effects due to transversal impacts, as well as, the force and torque induced by the bit-rock interaction.

Numerical simulations showed that the mechanical system of interest has a very rich nonlinear dynamics, which reproduces complex phenomena such as bit-

bounce, stick-slip, and transverse impacts. The study also indicated that the large velocity fluctuations observed in the phenomena of bit-bounce and stick-slip are correlated with the transverse impacts, i.e., with the number of shocks per unit time which the system is subjected. Also, the mechanical impacts cause the beam to assume complex spatial configurations, which are formed by flexural modes associated to high natural frequencies.

A study aiming to maximize the drilling process efficiency, varying drillstring velocities of translation and rotation was presented. The optimization strategy used a trial approach to seek for a local maximum, which was located within "operating window" and corresponds to an efficiency of approximately 16%.

The probabilistic analysis of the nonlinear dynamics showed that, with respect to the velocities, the nominal model and the mean value of the stochastic model differ significantly. Furthermore, at the instants which the system was subjected to mechanical impacts, it was possible to see a more pronounced dispersion around the mean value. Regarding the probability distributions of the velocities, it was noticed a unimodal behavior essentially.

Two optimizations problems, one deterministic and one robust, where the objective was to maximize the drillstring rate of penetration into the soil respecting its structural limits were formulated and solved. The solutions of these problems provided two different strategies to optimize the ROP.

Finally, it sounds stressing the mathematical model used in this work has not gone through any process of experimental validation. This is because experimental data for this type of system is difficult to be obtained, and to construct an experimental apparatus in real scale is virtually impossible. An interesting proposal for future work would be the construction of an experimental test rig, in reduced scale, that emulates the main aspects of a real drillstring. The model used in this study could be validated, following, for instance, the methodology presented in [1], with the aid of experimental measurements taken from this reduced apparatus.

A Geometric nonlinearly force coefficients

This appendix presents the coefficients which appears in the geometric nonlinearity force of Eq.(49). For the sake of saving space, in the following lines it is used the abbreviations: $S_{\theta_x} = \sin\theta_x$, and $C_{\theta_x} = \cos\theta_x$.

$$\begin{aligned}\Gamma_1 = {} & E\,I_4\,(1+u')\left(v'\,\theta_y' + w'\,\theta_z'\right) S_{\theta_x}\,\theta_x' \; + \\ & E\,I_4\,(1+u')\left(v'\,\theta_z' - w'\,\theta_y'\right) C_{\theta_x}\,\theta_x' \; + \\ & k_s\,G\,A\,(1+u')\left(\theta_z\,v' - \theta_y\,w'\right) S_{\theta_x} \; - \\ & k_s\,G\,A\,(1+u')\left(\theta_y\,v' + \theta_z\,w'\right) C_{\theta_x},\end{aligned} \tag{105}$$

$$\begin{aligned}\Gamma_2 = {} & k_s\,G\,I_4\left(\theta_y\left(\theta_y'^{\,2} + \theta_z'^{\,2}\right) - \theta_x'\,\theta_z'\right) \; + \\ & k_s\,G\,A\left(-w' + u'\,\theta_y\,(2+u')\right) \; - \\ & k_s\,G\,A\,(1+u')\left(v'\,S_{\theta_x} - w'\,C_{\theta_x}\right),\end{aligned} \tag{106}$$

$$\begin{aligned}\Gamma_3 = {} & k_s\,G\,I_4\left(\theta_z\left(\theta_y'^{\,2} + \theta_z'^{\,2}\right) + \theta_x'\,\theta_y'\right) \; + \\ & k_s\,G\,A\left(v' + u'\,\theta_z\,(2+u')\right) \; - \\ & k_s\,G\,A\,(1+u')\left(w'\,S_{\theta_x} + v'\,C_{\theta_x}\right),\end{aligned} \tag{107}$$

$$\begin{aligned}\Gamma_4 = {} & E\,A\left(\frac{1}{2}\,(1+u')\left(v'^{\,2} + w'^{\,2}\right) + \frac{1}{2}u'^{\,2}\,(3+u')\right) \; + \\ & E\,I_4\left(S_{\theta_x}\left(v'\,\theta_z' - w'\,\theta_y'\right) - C_{\theta_x}\left(v'\,\theta_y' + w'\,\theta_z'\right)\right)\theta_x' \; + \\ & E\,I_4\,(1+u')\left(\theta_x'^{\,2} + \frac{3}{2}\left(\theta_y'^{\,2} + \theta_z'^{\,2}\right)\right) \; + \\ & k_s\,G\,A\left(C_{\theta_x}\left(\theta_y\,w' - \theta_z\,v'\right) - S_{\theta_x}\left(\theta_y\,v' + \theta_z\,w'\right)\right) \; + \\ & k_s\,G\,A\,(1+u')\left(\theta_y^2 + \theta_z^2\right),\end{aligned} \tag{108}$$

$$\begin{aligned}\Gamma_5 = {} & E\,A\left(u' + \frac{1}{2}\left(u'^{\,2} + v'^{\,2} + w'^{\,2}\right)\right) v' \; + \\ & E\,I_4\left(2\,\theta_x'^{\,2} + \frac{1}{2}\left(\theta_y'^{\,2} + \theta_z'^{\,2}\right)\right) v' \; + \\ & E\,I_4\,(1+u')\left(\theta_z' S_{\theta_x} - \theta_y' C_{\theta_x}\right)\theta_x' \; + \\ & k_s\,G\,A\,(1+u')\left(\theta_z - \theta_y\,S_{\theta_x} - \theta_z\,C_{\theta_x}\right),\end{aligned} \tag{109}$$

$$\begin{aligned}\Gamma_6 = {} & E\,A\left(u' + \frac{1}{2}\left(u'^{\,2} + v'^{\,2} + w'^{\,2}\right)\right) w' \; + \\ & E\,I_4\left(2\,\theta_x'^{\,2} + \frac{1}{2}\left(\theta_y'^{\,2} + \theta_z'^{\,2}\right)\right) w' \; + \\ & E\,I_4\,(1+u')\left(-\theta_y'\,S_{\theta_x} - \theta_z'\,C_{\theta_x}\right)\theta_x' \; + \\ & k_s\,G\,A\,(1+u')\left(-\theta_y + \theta_y\,C_{\theta_x} - \theta_z\,S_{\theta_x}\right),\end{aligned} \tag{110}$$

$$\begin{aligned}\Gamma_7 = {} & E\,I_4\left(u'^{\,2} + 2\left(u' + v'^{\,2} + w'^{\,2}\right)\right)\theta_x' \; + \\ & E\,I_4\,(1+u')\left(v'\,\theta_z' - w'\,\theta_y'\right) S_{\theta_x} \; - \\ & E\,I_4\,(1+u')\left(v'\,\theta_y' + w'\,\theta_z'\right) C_{\theta_x} \; + \\ & E\,I_6\left(4\,\theta_x'^{\,2} + 2\left(\theta_y'^{\,2} + \theta_z'^{\,2}\right)\right)\theta_x' \; + \\ & k_s\,G\,A\left(\theta_z\,\theta_y' - \theta_y\,\theta_z'\right),\end{aligned} \tag{111}$$

$$\Gamma_8 = E\,I_4\left(3\,u' + \frac{1}{2}\left(3\,u'^{\,2} + v'^{\,2} + w'^{\,2}\right)\right)\theta'_y \; + \tag{112}$$
$$E\,I_4\left(1+u'\right)\left(-w'\,S_{\theta_x} - v'\,C_{\theta_x}\right)\theta'_x \; +$$
$$E\,I_6\left(2\,\theta'^{\,2}_x + \frac{3}{2}\left(\theta'^{\,2}_y + \theta'^{\,2}_z\right)\right)\theta'_y \; +$$
$$k_s\,G\,I_4\left(\theta_z\,\theta'_x + \theta'_y\left(\theta_y^2 + \theta_z^2\right)\right),$$

and

$$\Gamma_9 = E\,I_4\left(3\,u' + \frac{1}{2}\left(3\,u'^{\,2} + v'^{\,2} + w'^{\,2}\right)\right)\theta'_z \; + \tag{113}$$
$$E\,I_4\left(1+u'\right)\left(v'\,S_{\theta_x} - w'\,C_{\theta_x}\right)\theta'_x \; +$$
$$E\,I_6\left(2\theta'^{\,2}_x + \frac{3}{2}\left(\theta'^{\,2}_y + \theta'^{\,2}_z\right)\right)\theta'_z \; +$$
$$k_s\,G\,I_4\left(-\theta_y\,\theta'_x + \theta'_z\left(\theta_y^2 + \theta_z^2\right)\right).$$

Acknowledgements The authors are indebted to the Brazilian agencies CNPq, CAPES, and FAPERJ, and the French agency COFECUB for the financial support given to this research.

References

1. Batou A, Soize C (2009) Identification of stochastic loads applied to a non-linear dynamical system using an uncertain computational model and experimental responses. Computational Mechanics 43:559–571, DOI 10.1007/s00466-008-0330-y
2. Bazoune A, Khulief YA, Stephen NG (2003) Shape functions of three-dimensional Timoshenko beam element. Journal of Sound and Vibration 259:473–480, DOI 10.1006/jsvi.2002.5122
3. Ben-Tal A, Ghaoui LE, Nemirovski A (2009) Robust Optimization. Princeton University Press, Princeton
4. Beyer HG, Sendhoff B (2007) Robust optimization – A comprehensive survey. Computer Methods in Applied Mechanics and Engineering 196:3190–3218, DOI 10.1016/j.cma.2007.03.003
5. Bonet J, Wood RD (2008) Nonlinear Continuum Mechanics for Finite Element Analysis, 2nd edn. Cambridge University Press, Cambridge
6. Capiez-Lernout E, Soize C (2008) Design optimization with an uncertain vibroacoustic model. Journal of Vibration and Acoustics 130:021,001, DOI 10.1115/1.2827988
7. Capiez-Lernout E, Soize C (2008) Robust design optimization in computational mechanics. Journal of Applied Mechanics 75:021,001, DOI 10.1115/1.2775493
8. Capiez-Lernout E, Soize C (2008) Robust updating of uncertain damping models in structural dynamics for low- and medium-frequency ranges. Mechanical Systems and Signal Processing 22:1774–1792, DOI 10.1016/j.ymssp.2008.02.005
9. Chatjigeorgiou IK (2013) Numerical simulation of the chaotic lateral vibrations of long rotating beams. Applied Mathematics and Computation 219:5592–5612, DOI 10.1016/j.amc.2012.11.076
10. Chevallier A (2000) Nonlinear Stochastic Drilling Vibrations. Ph.D Thesis, Rice University, Houston
11. Cull SJ, Tucker RW (1999) On the modelling of Coulomb friction. Journal of Physics A: Mathematical and General 32:2103–2113, DOI 10.1088/0305-4470/32/11/006
12. Cunha Jr A (2015) Modeling and Uncertainty Quantification in the Nonlinear Stochastic Dynamics of a Horizontal Dsrillstrings. D.Sc. Thesis, Pontifícia Universidade Católica do Rio de Janeiro / Université Paris-Est
13. Cunha Jr A, Nasser R, Sampaio R, Lopes H, Breitman K (2014) Uncertainty quantification through Monte Carlo method in a cloud computing setting. Computer Physics Communications 185:1355—1363, DOI 10.1016/j.cpc.2014.01.006, DOI 10.1016/j.cpc.2014.01.006
14. Davies RJ, Almond S, Ward RS, Jackson RB, Adams C, Worrall F, Herringshaw LG, Gluyas JG, Whitehead MA (in press) Oil and gas wells and their integrity: Implications for shale and unconventional resource exploitation. Marine and Petroleum Geology DOI http://dx.doi.org/10.1016/j.marpetgeo.2014.03.001
15. Depouhon A, Detournay E (2014) Instability regimes and self-excited vibrations in deep drilling systems. Journal of Sound and Vibration 333:2019–2039, DOI 10.1016/j.jsv.2013.10.005
16. Detournay E, Richard T, Shepherd M (2008) Drilling response of drag bits: Theory and experiment. International Journal of Rock Mechanics & Mining Sciences 45:1347–1360, DOI 10.1016/j.ijrmms.2008.01.010
17. Divenyi S, Savi MA, Wiercigroch M, Pavlovskaia E (2012) Drill-string vibration analysis using non-smooth dynamics approach. Nonlinear Dynamics 70:1017–1035, DOI 10.1007/s11071-012-0510-3
18. Franca LFP (2010) Drilling action of roller-cone bits: modeling and experimental validation. Journal of Energy Resources Technology 132:043,101–1–043,101–9, DOI 10.1115/1.4003168
19. Franca LFP, Weber HI (2004) Experimental and numerical study of a new resonance hammer drilling model with drift. Chaos, Solitons & Fractals 21:789–801, DOI 10.1016/j.chaos.2003.12.064
20. Freudenrich C, Strickland J (2001) How Oil Drilling Works. http://www.howstuffworks.com/oil-drilling
21. Gilardi G, Sharf I (2002) Literature survey of contact dynamics modelling. Mechanism and Machine Theory 37:1213–1239, DOI 10.1016/S0094-114X(02)00045-9
22. Golub GH, Van Loan CF (2013) Matrix Computations, 4th edn. The Johns Hopkins University Press, Baltimore
23. Hagedorn P, DasGupta A (2007) Vibrations and Waves in Continuous Mechanical Systems. Wiley, Chichester
24. Hu Y, Di Q, Zhu W, Chen Z, Wang W (2012) Dynamic characteristics analysis of drillstring in the ultra-deep well with spatial curved beam finite element. Journal of Petroleum Science and Engineering 82—83:166–173, DOI 10.1016/j.petrol.2012.01.011
25. Hughes TJR (2000) The Finite Element Method. Dover Publications, New York
26. Hunt KH, Crossley FE (1975) Coefficient of restitution interpreted as damping in vibroimpact. Journal of Applied Mechanics 42:440–445, DOI 10.1115/1.3423596
27. Jansen JD (1993) Nonlinear Dynamics of Oilwell Drillstrings. Ph.D Thesis, TU Delft, Amsterdam
28. Khulief YA, Al-Sulaiman FA, Bashmal S (2007) Vibration analysis of drillstrings with self-excited stick–slip oscillations. Journal of Sound and Vibration 299:540–558, DOI 10.1016/j.jsv.2006.06.065

29. Kroese DP, Taimre T, Botev ZI (2011) Handbook of Monte Carlo Methods. Wiley, New Jersey
30. Lanczos C (1986) The Variational Principles of Mechanics, 4th edn. Dover Publications, New York
31. Litewka P, Wriggers P (2002) Frictional contact between 3D beams. Computational Mechanics 28:26–39, DOI 10.1007/s004660100266
32. Liu X, Vlajic N, Long X, Meng G, Balachandran B (2013) Nonlinear motions of a flexible rotor with a drill bit: stick-slip and delay effects. Nonlinear Dynamics 72:61–77, DOI 10.1007/s11071-012-0690-x
33. Macdonald KA, Bjune JV (2007) Failure analysis of drillstrings. Engineering Failure Analysis 14:1641–1666, DOI 10.1016/j.engfailanal.2006.11.073
34. Nandakumar K, Wiercigroch M (2013) Stability analysis of a state dependent delayed, coupled two DOF model of drill-stringvibration. Journal of Sound and Vibration 332:2575–2592, DOI 10.1016/j.jsv.2012.12.020
35. Newmark NM (1959) A method of computation for structural dynamics. Journal of the Engineering Mechanics Division 85:67–94
36. Oppenheim AV, Schafer RW (2009) Discrete-Time Signal Processing, 3rd edn. Prentice Hall, Englewood Cliffs, N.J.
37. Reddy JN (1997) On locking-free shear deformable beam finite elements. Computer Methods in Applied Mechanics and Engineering 149:113–132, DOI 10.1016/S0045-7825(97)00075-3
38. Ritto TG (2010) Numerical Analysis of the Nonlinear Dynamics of a Drill-string with Uncertainty Modeling. D.Sc. Thesis, Pontifícia Universidade Católica do Rio de Janeiro / Université Paris-Est
39. Ritto TG, Sampaio R (2012) Stochastic drill-string dynamics with uncertainty on the imposed speed and on the bit-rock parameters. International Journal for Uncertainty Quantification 2:111–124, DOI 10.1615/Int.J.UncertaintyQuantification.v2.i2
40. Ritto TG, Soize C, Sampaio R (2009) Non-linear dynamics of a drill-string with uncertain model of the bit–rock interaction. International Journal of Non-Linear Mechanics 44:865–876, DOI 10.1016/j.ijnonlinmec.2009.06.003
41. Ritto TG, Soize C, Sampaio R (2010) Robust optimization of the rate of penetration of a drill-string using a stochastic nonlinear dynamical model. Computational Mechanics 45:415–427, DOI 10.1007/s00466-009-0462-8
42. Ritto TG, Soize C, Sampaio R (2010) Stochastic dynamics of a drill-string with uncertain weight-on-hook. Journal of the Brazilian Society of Mechanical Sciences and Engineering 32:250–258, DOI 10.1590/S1678-58782010000300008
43. Ritto TG, Escalante MR, Sampaio R, Rosales MB (2013) Drill-string horizontal dynamics with uncertainty on the frictional force. Journal of Sound and Vibration 332:145–153, DOI 10.1016/j.jsv.2012.08.007
44. Sagan H (1992) Introduction to the Calculus of Variations. Dover Publications, New York
45. Sahebkar SM, Ghazavi MR, Khadem SE, Ghayesh MH (2011) Nonlinear vibration analysis of an axially moving drillstring system with time dependent axial load and axial velocity in inclined well. Mechanism and Machine Theory 46:743–760, DOI 10.1016/j.mechmachtheory.2010.12.003
46. Sampaio R, Piovan M, Lozano GV (2007) Coupled axial/torsional vibrations of drill-strings by means of non-linear model. Mechanics Research Communications 34:497–502, DOI 10.1016/j.mechrescom.2007.03.005
47. Savitzky A, Golay MJE (1964) Smoothing and differentiation of data by simplified least squares procedures. Analytical Chemistry 36:1627–1639, DOI 10.1021/ac60214a047
48. Schuëller GI (1997) A state-of-the-art report on computational stochastic mechanics. Probabilistic Engineering Mechanics 12:197–321, DOI 10.1016/S0266-8920(97)00003-9
49. Schuëller GI (2007) On the treatment of uncertainties in structural mechanics and analysis. Computers & Structures 85:235–243, DOI 10.1016/j.compstruc.2006.10.009
50. Schuëller GI, Jensen HA (2008) Computational methods in optimization considering uncertainties – an overview. Computer Methods in Applied Mechanics and Engineering 198:2–13, DOI 10.1016/j.cma.2008.05.004
51. Silveira M, Wiercigroch M (2009) Low dimensional models for stick-slip vibration of drill-strings. Journal of Physics: Conference Series 181:012,056, DOI 10.1088/1742-6596/181/1/012056
52. Soize C (2000) A nonparametric model of random uncertainties for reduced matrix models in structural dynamics. Probabilistic Engineering Mechanics 15:277–294, DOI 10.1016/S0266-8920(99)00028-4
53. Soize C (2001) Maximum entropy approach for modeling random uncertainties in transient elastodynamics. Journal of the Acoustical Society of America 109:1979–1996, DOI 10.1121/1.1360716
54. Soize C (2005) A comprehensive overview of a nonparametric probabilistic approach of model uncertainties for predictive models in structural dynamics. Journal of Sound and Vibration 288:623–652, DOI 10.1016/j.jsv.2005.07.009
55. Soize C (2012) Stochastic Models of Uncertainties in Computational Mechanics. Amer Society of Civil Engineers, Reston
56. Soize C (2013) Stochastic modeling of uncertainties in computational structural dynamics — recent theoretical advances. Journal of Sound and Vibration 332:2379––2395, DOI 10.1016/j.jsv.2011.10.010
57. Soize C, Capiez-Lernout E, Ohayon R (2008) Robust updating of uncertain computational models using experimental modal analysis. AIAA Journal 46:2955–2965
58. Spanos PD, Chevallier AM, Politis NP (2002) Nonlinear stochastic drill-string vibrations. Journal of Vibration and Acoustics 124:512–518, DOI 10.1115/1.1502669
59. Spanos PD, Chevallier AM, Politis NP, Payne ML (2003) Oil and gas well drilling: a vibrations perspective. The Shock and Vibration Digest 35:85–103
60. Trindade MA, Wolter C, Sampaio R (2005) Karhunen–Loève decomposition of coupled axial/bending vibrations of beams subject to impacts. Journal of Sound and Vibration 279:1015–1036, DOI 10.1016/j.jsv.2003.11.057
61. Willoughby D (2005) Horizontal Directional Drilling (HDD): Utility and Pipeline Applications. McGraw-Hill, New York
62. Wriggers P (2006) Computational Contact Mechanics, 2nd edn. Springer, New York
63. Wriggers P, Zavarise G (2004) Computational Contact Mechanics. In: Stein E, de Borst R, Hughes TJR (eds) Encyclopedia of Computational Mechanics, vol 2, Wiley, Hoboken, pp 195–226, DOI 10.1002/0470091355.ecm033
64. Wriggers P, Wagner W, Stein E (1987) Algorithms for non-linear contact constraints with application to stability problems of rods and shells. Computational Mechanics 2:215–230, DOI 10.1007/BF00571026

65. Young DM (2003) Iterative Solution of Large Linear Systems. Dover Publications, New York
66. Zhang Y, Sharf I (2009) Validation of nonlinear viscoelastic contact force models for low speed impact. Journal of Applied Mechanics 76:051,002, DOI 10.1115/1.3112739
67. Zhu X, Liu Y, Tong H (2014) Analysis of reamer failure based on vibration analysis of the rock breaking in horizontal directional drilling. Engineering Failure Analysis 37:64 – 74, DOI 10.1016/j.engfailanal.2013.11.016

Asociación Argentina
de Mecánica Computacional

Mecánica Computacional Vol XXXIII, págs. 1517-1527 (artículo completo)
Graciela Bertolino, Mariano Cantero, Mario Storti y Federico Teruel (Eds.)
San Carlos de Bariloche, 23-26 Setiembre 2014

EXPLORING THE NONLINEAR DYNAMICS OF HORIZONTAL DRILLSTRINGS SUBJECTED TO FRICTION AND SHOCKS EFFECTS

Americo Cunha Jr[a,b], **Christian Soize**[b] **and Rubens Sampaio**[a]

[a] *PUC–Rio, Departamento de Engenharia Mecânica*
Rua Marquês de São Vicente, 225, Gávea, Rio de Janeiro - RJ, Brasil.
americo.cunhajr@gmail.com *rsampaio@puc-rio.br*

[b] *Université Paris-Est, Laboratoire Modélisation et Simulation Multi Echelle,*
MSME UMR 8208 CNRS, 5, Boulevard Descartes 77454, Marne-la-Vallée, France.
christian.soize@univ-paris-est.fr

Keywords: nonlinear dynamics, drillstring dynamics, stick-slip, bit-bounce

Abstract. This paper presents a model to describe the nonlinear dynamics of a drillstring in horizontal configuration, which is intended to correctly predict the three-dimensional dynamics of this complex structure. This model uses a beam theory, with effects of rotatory inertia and shear deformation, which is capable of reproducing the large displacements that the beam undergoes. Also, it considers the effects of torsional friction and normal shock due to the transversal impacts between the rotating beam and the borehole wall, as well as, the force and the torque induced by the bit-rock interaction. This is done as a first effort to solve a robust optimization problem, which seeks to maximize the rate of penetration of the drillstring into the soil, to reduce the drilling process costs. Numerical simulations reported in this work shown that the developed computational model is able to quantitatively well describe the dynamical behavior of a horizontal drillstring, once its reproduces some phenomena observed in real drilling systems, such as bit-bounce, stick-slip, and transverse impacts.

1 INTRODUCTION

A drillstring is a device, used to drill oil wells, which presents an extremely complex three-dimensional nonlinear dynamics. The dynamical system associated with this physical system involves the nonlinear coupling between three different mechanisms of vibration (longitudinal, transverse, and torsional), as well as lateral and frontal shocks, due to drill-pipes/borehole and drill-bit/soil and impacts respectively (Spanos et al., 2003). Traditionally, a drillstring configuration is vertical, but directional or even horizontal configurations, where the boreholes are drilled following a non-vertical way, are also possible.

Once oil drilling a topic of great relevance in the context of engineering, the dynamics of a vertical drillstring has been studied in several works (Chevallier, 2000; Ritto et al., 2009, 2010; Chatjigeorgiou, 2013; Liu et al., 2013; Depouhon and Detournay, 2014). However, although of most of the oil wells today be drilled with columns using non-vertical configurations, very few papers in the open literature models drillstring in directional configurations (Sahebkar et al., 2011; Hu et al., 2012; Ritto et al., 2013).

Aiming to fill the gap in the scientific literature on horizontal drillstring dynamics, this work presents the modeling of a drillstring in a horizontal configuration. This model takes into account the three-dimensional dynamics of the structure, as well as the transversal/torsional effects of shock, which the structure is subject due to the impact with the borehole wall. Also, the model considers the bit-rock interaction effects, and the weight of the drilling fluid.

This rest of this paper is organized as follows. The mathematical modeling of the nonlinear dynamics appears in section 2. Then, in section 3, the results of numerical simulations are presented and discussed. Finally, in section 4, the main conclusions are emphasized and some directions for future work outlined.

2 MATHEMATICAL MODELING

2.1 Mechanical system of interest

The mechanical system of interest in this work is sketched in Figure 1. It consists of a horizontal rigid pipe (illustrated as the pair of stationary rigid walls), perpendicular to gravity acceleration g, which contains in its interior a deformable tube under rotation (rotating beam), subjected to three-dimensional displacements. This deformable tube has a length L, cross section area A, and is made of a material with mass density ρ, elastic modulus E, and Poisson ratio ν. It loses energy through a mechanism of viscous dissipation, proportional to the mass operator, with damping coefficient c. Inside the tube there is a fluid without viscosity, with mass density ρ_f. Concerning the boundary conditions, the rotating beam is blocked for transversal displacements in both extremes; blocked to transversal rotations on the left extreme; and, on the left extreme, has a constant angular velocity around x equal to Ω, and an imposed longitudinal velocity V_0.

2.2 Beam theory

The beam theory adopted takes into account the rotatory inertia and shear deformation of the beam cross section. Also, as the beam is confined within the borehole, it is reasonable to assume that it is undergoing small rotations in the transverse directions.

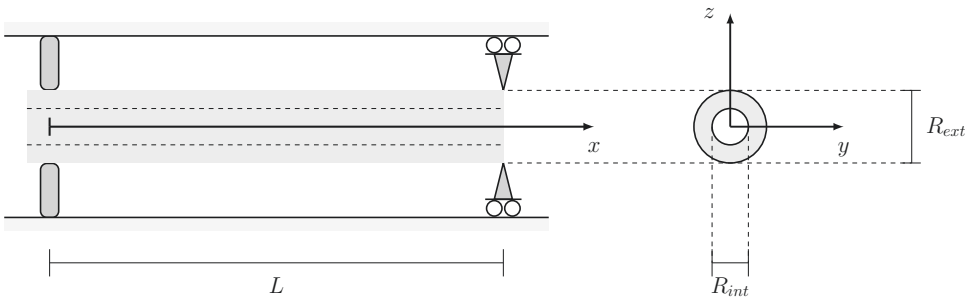

Figure 1: Schematic representation of the rotating beam which models the horizontal drillstring.

By another hand, large displacements are observed in x, y, and z. Therefore, the analysis that follows uses a beam theory which assumes large rotation in x, and large displacements the three spatial directions, which couples the longitudinal, transverse and torsional vibrations (Bonet and Wood, 2008).

Regarding the kinematic hypothesis adopted for the beam theory, it is assumed that the three-dimensional displacement of a beam point, occupying the position (x, y, z) at the instant of time t, can be written as

$$\begin{aligned} u_x(x,y,z,t) &= u - y\theta_z + z\theta_y, \\ u_y(x,y,z,t) &= v + y\left(\cos\theta_x - 1\right) - z\sin\theta_x, \\ u_z(x,y,z,t) &= w + z\left(\cos\theta_x - 1\right) + y\sin\theta_x, \end{aligned} \tag{1}$$

where letters u, v, and w are used to denote the displacements of a beam neutral fiber point in x, y, and z directions, respectively, while θ_x, θ_y, and θ_z represent rotations of the beam around the x, y, and z axes respectively. Note that these quantities depend on the position x and the time t.

2.3 Friction and shock effects

This rotating beam is also able to generate normal shocks and torsional friction in random areas of the rigid tube, which are respectively described by the Hunt and Crossley shock model Hunt and Crossley (1975), and the standard Coulomb friction model. Therefore, the force of normal shock is given by

$$F_{FS} = -k_{FS_1}\,\delta_{FS} - k_{FS_2}\,\delta_{FS}^3 - c_{FS}\,|\delta|^3\dot{\delta}_{FS}, \tag{2}$$

and the Coulomb frictional torque by

$$T_{FS} = -\mu_{FS}\,F_{FS}\,R_{bh}\,\mathtt{sgn}\left(\dot{\theta}_x\right). \tag{3}$$

In the above equations, k_{FS_1}, k_{FS_2} and c_{FS} are constants of the shock model, while μ_{FS} is a friction coefficient, R_{bh} is the borehole radius, and $\mathtt{sgn}\,(\cdot)$ the sign function. The $\dot{}$ is an abbreviation for time derivative, and the parameter $\delta_{FS} = r - \mathtt{gap}$, where $r = \sqrt{v^2 + w^2}$, is dubbed *indentation*, and is a measure of penetration in the wall of a beam cross section, such as illustrated in Figure 2.

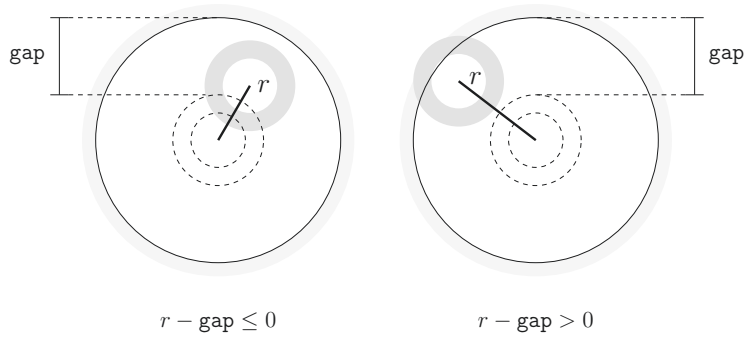

Figure 2: Illustration of the indentation parameter in a situation without impact (left) or with impact (right).

2.4 Bit-rock interaction effects

At the right extreme of the rotating beam act a force and a torque, which emulate the effects of interaction between the drill-bit and the soil. They are respectively given by

$$F_{BR} = \begin{cases} \Gamma_{BR} \left(\exp\left(-\alpha_{BR} \dot{u}(L,\cdot)\right) - 1 \right), & \text{for} \quad \dot{u}(L,\cdot) > 0 \\ 0, & \text{for} \quad \dot{u}(L,\cdot) \leq 0 \end{cases} \tag{4}$$

and

$$T_{BR} = -\mu_{BR}\, F_{BR}\, \xi_{BR} \left(\dot{\theta}_x \right), \tag{5}$$

where Γ_{BR} is the bit-rock limit force; α_{BR} is the rate of change of bit-rock force; μ_{BR} bit-rock friction coefficient; and ξ_{BR} is a regularization function, which takes into account the dimension of length, to the Eq.(5) gives a torque. The expression for the bit-rock interaction models above were, respectively, proposed by Ritto et al. (2013) and Khulief et al. (2007).

2.5 Variational formulation of the nonlinear dynamics

Using a modified version of the extended Hamilton's principle, to include the effects of dissipation, one can write the weak form of the nonlinear equation of motion of the mechanical system as

$$\mathcal{M}\left(\boldsymbol{\psi}, \ddot{\boldsymbol{U}}\right) + \mathcal{C}\left(\boldsymbol{\psi}, \dot{\boldsymbol{U}}\right) + \mathcal{K}\left(\boldsymbol{\psi}, \boldsymbol{U}\right) = \mathcal{F}_{NL}\left(\boldsymbol{\psi}, \boldsymbol{U}, \dot{\boldsymbol{U}}, \ddot{\boldsymbol{U}}\right), \tag{6}$$

where $\mathcal{M}$ represents the mass operator, $\mathcal{C}$ is the damping operator, $\mathcal{K}$ is the stiffness operator, and $\mathcal{F}_{NL}$ is the nonlinear force operator. Also, the field variables and their weight functions are lumped in the vectors fields $\boldsymbol{U} = \left(u, v, w, \theta_x, \theta_y, \theta_z\right)$, and $\boldsymbol{\psi} = \left(\psi_u, \psi_v, \psi_w, \psi_{\theta_x}, \psi_{\theta_y}, \psi_{\theta_z}\right)$.

The above operators are respectively defined by

$$\begin{aligned}\mathcal{M}\left(\boldsymbol{\psi},\ddot{\boldsymbol{U}}\right) &= \int_{x=0}^{L}\rho\,A\left(\psi_u\,\ddot{u}+\psi_v\,\ddot{v}+\psi_w\,\ddot{w}\right)dx\;+\\ &\int_{x=0}^{L}\rho_f\,A_f\left(\psi_v\,\ddot{v}+\psi_w\,\ddot{w}\right)dx\;+\\ &\int_{x=0}^{L}\rho\,I_4\left(2\,\psi_{\theta_x}\,\ddot{\theta}_x+\psi_{\theta_y}\,\ddot{\theta}_y+\psi_{\theta_z}\,\ddot{\theta}_z\right)dx,\end{aligned}\tag{7}$$

$$\begin{aligned}\mathcal{C}\left(\boldsymbol{\psi},\dot{\boldsymbol{U}}\right) &= \int_{x=0}^{L}c\,\rho\,A\left(\psi_u\,\dot{u}+\psi_v\,\dot{v}+\psi_w\,\dot{w}\right)dx\;+\\ &\int_{x=0}^{L}c\,\rho\,I_4\left(2\,\psi_{\theta_x}\,\dot{\theta}_x+\psi_{\theta_y}\,\dot{\theta}_y+\psi_{\theta_z}\,\dot{\theta}_z\right)dx,\end{aligned}\tag{8}$$

$$\begin{aligned}\mathcal{K}\left(\boldsymbol{\psi},\boldsymbol{U}\right) &= \int_{x=0}^{L}E\,A\,\psi_u'\,u'\,dx\;+\\ &\int_{x=0}^{L}E\,I_4\left(\psi_{\theta_y}'\,\theta_y'+\psi_{\theta_z}'\,\theta_z'\right)dx\;+\\ &\int_{x=0}^{L}2\,\kappa_s\,G\,I_4\,\psi_{\theta_x}'\,\theta_x'\,dx\;+\\ &\int_{x=0}^{L}\kappa_s\,G\,A\left(\left(\psi_{\theta_y}+\psi_w'\right)\left(\theta_y+w'\right)+\left(\psi_{\theta_z}-\psi_v'\right)\left(\theta_z-v'\right)\right)dx,\end{aligned}\tag{9}$$

and

$$\begin{aligned}\mathcal{F}_{NL}\left(\boldsymbol{\psi},\boldsymbol{U},\dot{\boldsymbol{U}},\ddot{\boldsymbol{U}}\right) &= \mathcal{F}_{\text{KE}}\left(\boldsymbol{\psi},\boldsymbol{U},\dot{\boldsymbol{U}},\ddot{\boldsymbol{U}}\right)+\mathcal{F}_{\text{SE}}\left(\boldsymbol{\psi},\boldsymbol{U}\right)\;+\\ &\mathcal{F}_{\text{FS}}\left(\boldsymbol{\psi},\boldsymbol{U}\right)+\mathcal{F}_{\text{BR}}\left(\boldsymbol{\psi},\dot{\boldsymbol{U}}\right)+\mathcal{F}_{\text{G}}\left(\boldsymbol{\psi}\right),\end{aligned}\tag{10}$$

where

$$\begin{aligned}\mathcal{F}_{\text{KE}} &= -\int_{x=0}^{L}2\,\rho\,I_4\,\psi_{\theta_x}\left(\theta_y\,\ddot{\theta}_z+\dot{\theta}_y\,\dot{\theta}_z\right)dx\\ &+\int_{x=0}^{L}2\,\rho\,I_4\,\psi_{\theta_y}\left(\theta_y\,\dot{\theta}_z^2+\dot{\theta}_x\,\dot{\theta}_z\right)dx\\ &-\int_{x=0}^{L}2\,\rho\,I_4\,\psi_{\theta_z}\left(\theta_y\,\ddot{\theta}_x+\theta_y^2\,\ddot{\theta}_z\right)dx\\ &-\int_{x=0}^{L}2\,\rho\,I_4\,\psi_{\theta_z}\left(\dot{\theta}_x\,\dot{\theta}_y+2\,\theta_y\,\dot{\theta}_y\,\dot{\theta}_z\right)dx\end{aligned}\tag{11}$$

is a nonlinear force due to inertial effects;

$$\mathcal{F}_{\text{SE}} = \int_{x=0}^{L} \left(\psi_{\theta_x}\,\Gamma_1 + \psi_{\theta_y}\,\Gamma_2 + \psi_{\theta_z}\,\Gamma_3\right) dx \; + \int_{x=0}^{L} \left(\psi'_u\,\Gamma_4 + \psi'_v\,\Gamma_5 + \psi'_w\,\Gamma_6\right) dx \; + \int_{x=0}^{L} \left(\psi'_{\theta_x}\,\Gamma_7 + \psi'_{\theta_y}\,\Gamma_8 + \psi'_{\theta_z}\,\Gamma_9\right) dx, \tag{12}$$

is a nonlinear force due to geometric nonlinearity;

$$\mathcal{F}_{\text{FS}} = \sum_{m=1}^{N_{nodes}} \left(F_{\text{FS}}\left(v\,\psi_v + w\,\psi_w\right)/r + T_{\text{FS}}\,\psi_{\theta_x}\right)\Big|_{x=x_m}, \tag{13}$$

is a nonlinear force due to the effects of friction and shock;

$$\mathcal{F}_{\text{BR}} = F_{\text{BR}}\,\psi_u\Big|_{x=L} + T_{\text{BR}}\,\psi_{\theta_x}\Big|_{x=L}, \tag{14}$$

is a nonlinear force due to the bit-rock interaction; and

$$\mathcal{F}_{\text{G}} = -\int_{x=0}^{L} \left(\rho\,A + \rho_f\,A_f\right)\,g\,\psi_w\,dx, \tag{15}$$

is a linear force due to the gravity. The nonlinear functions Γ_n, with $n = 1, \cdots, 9$, in Eq.(12) are very complex and, for sake of space limitation, are not presented here. See Cunha Jr (2015) for details.

The weak form of the initial conditions reads

$$\mathcal{M}\left(\boldsymbol{\psi}, \boldsymbol{U}(0)\right) = \mathcal{M}\left(\boldsymbol{\psi}, \boldsymbol{U}_0\right), \tag{16}$$

and

$$\mathcal{M}\left(\boldsymbol{\psi}, \dot{\boldsymbol{U}}(0)\right) = \mathcal{M}\left(\boldsymbol{\psi}, \dot{\boldsymbol{U}}_0\right), \tag{17}$$

where $\boldsymbol{U}_0$ and $\dot{\boldsymbol{U}}_0$, respectively, denote the initial displacement, and the initial velocity fields.

The model presented above is an adaptation, for the case of horizontal drillstrings, with some variations in the friction and shock treatment, of the model proposed by Ritto et al. (2009) to describe the nonlinear dynamics of vertical drillstrings.

2.6 Discretization of the model equations

The Eqs.(6), (16) and (17) are discretized by means of the standard finite element method (Hughes, 2000), using an interdependent interpolation scheme (Reddy, 1997), which adopts affine functions for the axial displacement/torsional rotation, and Hermite cubic polynomials for the transverse displacements/rotations.

Therefore, one arrives in the following initial value problem

$$[M]\,\ddot{\boldsymbol{Q}}(t) + [C]\,\dot{\boldsymbol{Q}}(t) + [K]\,\boldsymbol{Q}(t) = \boldsymbol{\mathcal{F}}\left(\boldsymbol{Q}(t), \dot{\boldsymbol{Q}}(t), \ddot{\boldsymbol{Q}}(t)\right), \tag{18}$$

and

$$[M]\,\boldsymbol{Q}(0) = \boldsymbol{Q}_0, \qquad \text{and} \qquad [M]\,\dot{\boldsymbol{Q}}(0) = \dot{\boldsymbol{Q}}_0, \tag{19}$$

where $\boldsymbol{Q}(t)$ is the nodal displacement vector (translations and rotations), $\dot{\boldsymbol{Q}}(t)$ is the nodal velocity vector, $\ddot{\boldsymbol{Q}}(t)$ is the nodal acceleration vector, $[M]$ is the mass matrix, $[C]$ is the damping matrix, $[K]$ is the stiffness matrix, and $\boldsymbol{\mathcal{F}}$ is a nonlinear force vector, which contains contributions of an inertial force and a force of geometric stiffness.

The geometric boundary conditions are included as constraints, via the method of Lagrange multipliers. Nominally, they are the velocity of translation, V_0, and the velocity of rotation, Ω, which are imposed at the left end of the beam.

2.7 Reduction of the nonlinear dynamics

To reduce the computational cost of the simulations, the initial value problem of Eqs.(18) and (19) is projected in a vector space of dimension N_{red}, spanned by the linear modes associated to the conservative part of the underlying linear dynamical system. This results in the reduced initial value problem given by

$$[M]\,\ddot{\boldsymbol{q}}(t) + [C]\,\dot{\boldsymbol{q}}(t) + [K]\,\boldsymbol{q}(t) = \boldsymbol{f}\left(\boldsymbol{q}(t), \dot{\boldsymbol{q}}(t), \ddot{\boldsymbol{q}}(t)\right), \tag{20}$$

and

$$\boldsymbol{q}(0) = \boldsymbol{q}_0, \qquad \text{and} \qquad \dot{\boldsymbol{q}}(0) = \dot{\boldsymbol{q}}_0, \tag{21}$$

which is integrated using the Newmark method (Newmark, 1959), and the nonlinear system of algebraic equations, resulting from the time discretization, is solved by a fixed point iteration.

3 RESULTS AND DISCUSSION

In order to simulate the nonlinear dynamics of the mechanical system, the physical parameters presented in the Table 1 are adopted, as well as the length $L = 35\ m$, the rotational and axial velocities in x, respectively given by $\Omega = 2\pi\ rad/s$, and $V_0 = 1/720\ m/s$. For the geometry discretization, 105 finite elements are used. This results in FEM model with 636 degrees of freedom. In the reduced order model, 51 DOF are considered.

The dynamics is investigated for a "temporal window" of $90s$, with a nominal time step $\Delta t = 69\ ms$, which is refined whenever necessary to capture the effects of shock. For the initial conditions, the static equilibrium configuration of the beam is adopted.

The drill-bit longitudinal displacement and velocity, can be seen in Figure 3. It is noted that, during the interval of analysis, the column presents an advance in the forward direction with small axial oscillations. These axial oscillations, which are more pronounced in the velocity curve, correspond to the vibration mechanism known as *bit-bounce*, where the drill-bit loses contact with the soil and then hits the rock abruptly. This phenomenon is widely observed in real systems (Spanos et al., 2003).

Table 1: Physical parameters of the mechanical system that are used in the simulation.

parameter	value	unit
ρ	7900	kg/m^3
ρ_f	1200	kg/m^3
E	203	GPa
ν	0.3	—
R_{int}	40	mm
R_{ext}	60	mm
R_{bh}	70	mm
c	0.03	—
g	9.81	m/s^2
k_{FS_1}	1×10^{10}	N/m
k_{FS_2}	1×10^{16}	N/m^3
c_{FS}	1×10^{9}	$(N/m^3)/(m/s)$
μ_{FS}	1×10^{-5}	—
Γ_{BR}	250	kN
α_{BR}	180	$1/(m/s)$
μ_{BR}	400×10^{-4}	—

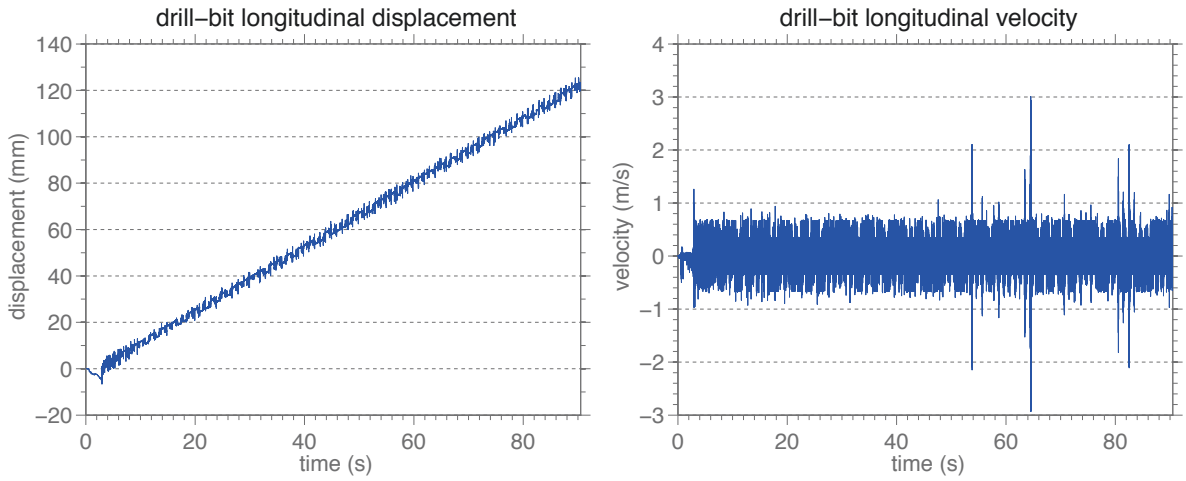

Figure 3: Illustration of the drill-bit displacement (left) and of the drill-bit velocity (right).

The drill-bit rotation and angular velocity, can be seen in Figure 4. What it is observed now is a almost monotonic rotation. However, when one looks to the angular velocity, it is possible to see packages of fluctuations with amplitude variations that can reach up to four orders of magnitude. This indicates that the drill-bit undergoes a blockage due to the torsional friction, and then it is released subtly, so that its velocity is sharply increased, in a *stick-slip* phenomenon type. This is also seen experimentally (Spanos et al., 2003) in real drilling systems.

The evolution of the radial displacement, for $x = 20$, of the beam cross-section can be seen in the Figure 5. Analyzing this figure it is clear that transverse impacts between the drillstring and the borehole wall occur during the drilling process, which is also reported experimentally (Spanos et al., 2003).

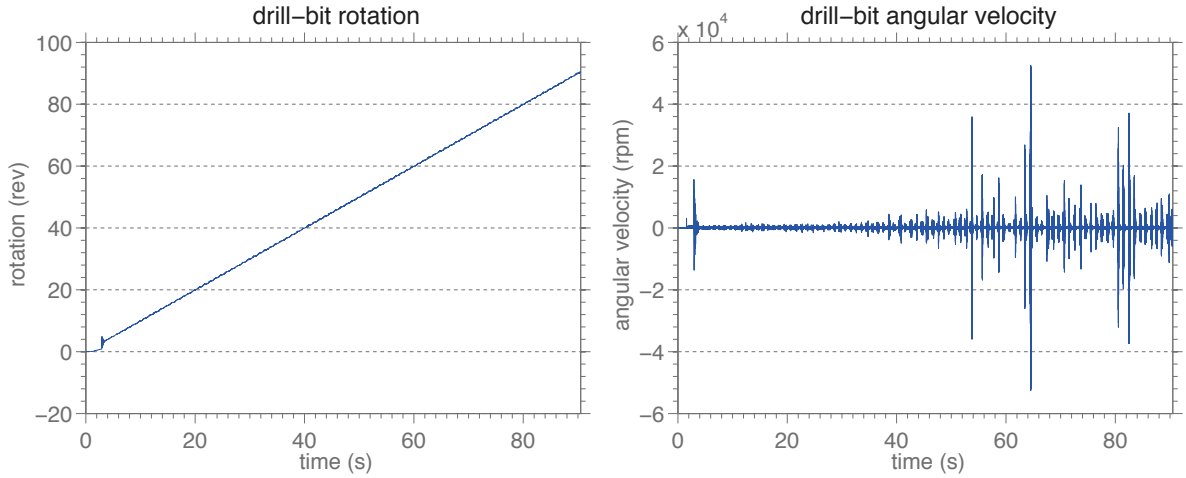

Figure 4: Illustration of the drill-bit rotation (left) and of the drill-bit angular velocity (right).

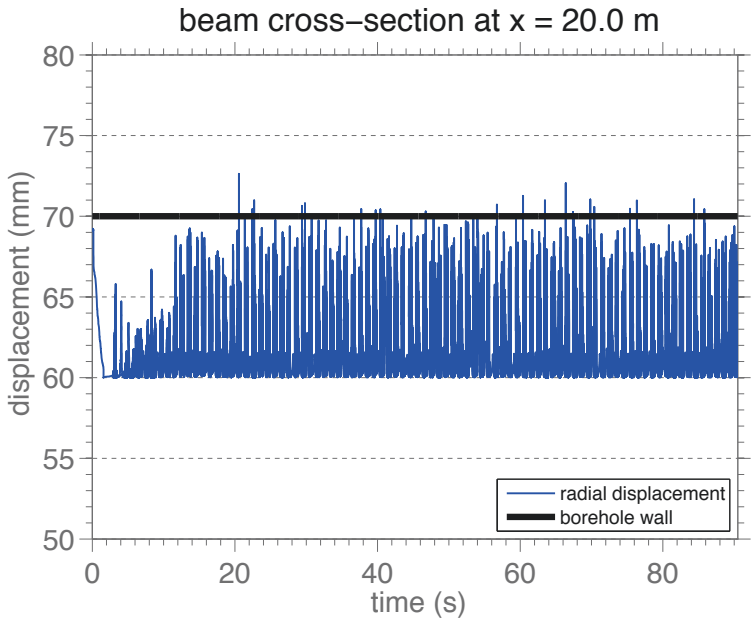

Figure 5: Illustration of the beam radial displacement for $x = 20\ m$.

4 CONCLUDING REMARKS

A model was developed in this work to describe the nonlinear dynamics of horizontal drillstrings. The model uses a beam theory, with effects of rotatory inertia and shear deformation, which is capable of reproducing the large displacements that the beam undergoes. This model also considers the effects of friction and shock due to the transversal impacts between the beam and the borehole wall, as well as, the force and the torque induced by the bit-rock interaction.

Numerical simulations reported in this work shown that the developed computational model is able to quantitatively well describe the dynamical behavior of a horizontal drillstring, once its reproduces some phenomena observed in real drilling systems, such as bit-bounce, stick-slip, and transverse impacts.

In a future work, the authors intend to develop a stochastic modeling of the nonlinear dynamics of horizontal drillstrings, in order to quantify the uncertainties associated with this problem, which are due to the variability of its parameters (Schuëller, 2007), and/or epistemic in nature, i.e., result of the ignorance about the physics of the problem (Soize, 2013). Also, in a next step, they want to solve an robust optimization problem, which seeks to maximize the rate of penetration of the column into the soil (Ritto et al., 2010).

ACKNOWLEDGMENTS

The authors are indebted to the Brazilian agencies CNPq, CAPES, and FAPERJ, and the French agency COFECUB for the financial support given to this research. They would also like to acknowledge professors Anas Batou and Thiago Ritto for valuable discussions on this work.

REFERENCES

Bonet J. and Wood R.D. *Nonlinear Continuum Mechanics for Finite Element Analysis*. Cambridge University Press, Cambridge, 2nd edition, 2008.

Chatjigeorgiou I.K. Numerical simulation of the chaotic lateral vibrations of long rotating beams. *Applied Mathematics and Computation*, 219:5592–5612, 2013. doi:10.1016/j.amc.2012.11.076.

Chevallier A. *Nonlinear Stochastic Drilling Vibrations*. Ph.D Thesis, Rice University, Houston, 2000.

Cunha Jr A. *Modeling and Uncertainty Quantification in the Nonlinear Stochastic Dynamics of a Horizontal Dsrillstrings*. D.Sc. Thesis, Pontifícia Universidade Católica do Rio de Janeiro / Université Paris-Est, 2015.

Depouhon A. and Detournay E. Instability regimes and self-excited vibrations in deep drilling systems. *Journal of Sound and Vibration*, 333:2019–2039, 2014. doi:10.1016/j.jsv.2013.10.005.

Hu Y., Di Q., Zhu W., Chen Z., and Wang W. Dynamic characteristics analysis of drillstring in the ultra-deep well with spatial curved beam finite element. *Journal of Petroleum Science and Engineering*, 82—83:166–173, 2012. doi:10.1016/j.petrol.2012.01.011.

Hughes T.J.R. *The Finite Element Method*. Dover Publications, New York, 2000.

Hunt K.H. and Crossley F.E. Coefficient of restitution interpreted as damping in vibroimpact. *Journal of Applied Mechanics*, 42:440–445, 1975. doi:10.1115/1.3423596.

Khulief Y.A., Al-Sulaiman F.A., and Bashmal S. Vibration analysis of drillstrings with self-excited stick–slip oscillations. *Journal of Sound and Vibration*, 299:540–558, 2007. doi:10.1016/j.jsv.2006.06.065.

Liu X., Vlajic N., Long X., Meng G., and Balachandran B. Nonlinear motions of a flexible rotor with a drill bit: stick-slip and delay effects. *Nonlinear Dynamics*, 72:61–77, 2013. doi:10.1007/s11071-012-0690-x.

Newmark N.M. A method of computation for structural dynamics. *Journal of the Engineering Mechanics Division*, 85:67–94, 1959.

Reddy J.N. On locking-free shear deformable beam finite elements. *Computer Methods in Applied Mechanics and Engineering*, 149:113–132, 1997. doi:10.1016/S0045-7825(97)00075-3.

Ritto T.G., Escalante M.R., Sampaio R., and Rosales M.B. Drill-string horizontal dynamics with uncertainty on the frictional force. *Journal of Sound and Vibration*, 332:145–153, 2013. doi:10.1016/j.jsv.2012.08.007.

Ritto T.G., Soize C., and Sampaio R. Non-linear dynamics of a drill-string with uncertain model of the bit–rock interaction. *International Journal of Non-Linear Mechanics*, 44:865–876, 2009. doi:10.1016/j.ijnonlinmec.2009.06.003.

Ritto T.G., Soize C., and Sampaio R. Robust optimization of the rate of penetration of a drill-string using a stochastic nonlinear dynamical model. *Computational Mechanics*, 45:415–427, 2010. doi:10.1007/s00466-009-0462-8.

Sahebkar S.M., Ghazavi M.R., Khadem S.E., and Ghayesh M.H. Nonlinear vibration analysis of an axially moving drillstring system with time dependent axial load and axial velocity in inclined well. *Mechanism and Machine Theory*, 46:743–760, 2011. doi:10.1016/j.mechmachtheory.2010.12.003.

Schuëller G.I. On the treatment of uncertainties in structural mechanics and analysis. *Computers & Structures*, 85:235–243, 2007. doi:10.1016/j.compstruc.2006.10.009.

Soize C. Stochastic modeling of uncertainties in computational structural dynamics — recent theoretical advances. *Journal of Sound and Vibration*, 332:2379—2395, 2013. doi:10.1016/j.jsv.2011.10.010.

Spanos P.D., Chevallier A.M., Politis N.P., and Payne M.L. Oil and gas well drilling: a vibrations perspective. *The Shock and Vibration Digest*, 35:85–103, 2003.